ACCELERATED QUANTITATIVE MAPPING AND ANGIOGRAPHY FOR CEREBRAL AND CARDIOVASCULAR MAGNETIC RESONANCE IMAGING

by
Dan Zhu

A dissertation submitted to Johns Hopkins University in conformity

with the requirements for the degree of Doctor of Philosophy

Baltimore, Maryland
December 2020

Abstract

Magnetic resonance imaging (MRI) produces images with anatomical and functional information. These images can be obtained without the use of contrast agents, which generally require long scan times. This dissertation investigates existing techniques for accelerating such functional MRI methods, contributes novel fast acquisition and reconstruction techniques, and proposes new ways of analyzing real-time MRI data.

First, we aim to determine an advantageous approach for accelerating high spatial resolution 3D cardiac T2 relaxometry data by comparing the performance of different data undersampling patterns and reconstruction methods over a range of acceleration rates. Quantitative results on healthy and edematous hearts reveal that the relaxometry maps are more sensitive to undersampling than anatomical images. The 3-fold variable density random undersampling with model-based or joint-sparsity sensitivity encoding (SENSE) is recommended.

Second, we develop a rapid T2 mapping protocol using spiral acquisition and novel model-based approach joined with compressed sensing (CS) and model-based reconstruction. We also develop a sequence that suppresses cerebrospinal fluid (CSF). Quantitative evaluation on digital phantoms and healthy volunteers demonstrates the feasibility of T2 quantification with 3D high-resolution and whole-brain coverage in 2-3 min.

Third, we propose a Golden Angle (GA) rotated Spiral Sparse Parallel imaging

(GASSP) method for high spatial (0.8mm) and high temporal (<21ms) resolution for measuring coronary blood flow in a single breath-hold. We reduce k-space gaps using novel binning and triggered GA schemes. Velocity and flow metrics are validated against two existing methods and show high reproducibility.

Fourth, we construct an abdominal non-contrast-enhanced magnetic resonance angiography (MRA) protocol with a large spatial coverage at 3.0T. The protocol uses advanced velocity-selective (VS) pulse trains. MRA with a large spatial coverage is slow and accelerated using CS. The VS-MRA sequences generate high-quality angiograms and arteriograms with high blood contrast.

Finally, physiological changes in real-time (RT) MRI (30-100 frames/sec) are explored using Fourier transform (FT), principal component analyses (PCA), and perfusion modeling. We detect spectral patterns in pharyngeal images acquired during speaking and obtain T1-weighted, pulsation-weighted, and respiration-weighted images in healthy volunteers and heart patients with wall motion abnormalities with FT and PCA. RT perfusion maps are estimated from a proposed perfusion model in ongoing work in progress.

Advisor and first reader: Paul A. Bottomley

Russell H. Morgan Professor, Radiology and Radiological Science, Johns Hopkins University

Second reader: J. Webster Stayman

Associate Professor, Biomedical Engineering, Johns Hopkins University

Acknowledgments

Throughout my Ph.D. training, I have received a great deal of support and assistance.

I would first like to express my deep and sincere gratitude to my research supervisor, Dr. Paul A. Bottomley. He has 45 years' expertise and pioneered MRI, which was invaluable for my academic training. His intelligence and creativity helped my research with many novel ideas and thoughts. I would not be able to succeed with my Ph.D. training without his strong support and patient guidance. I learned a lot from him that brought my work to a higher level: thinking, experiment designing, writing and presentation skill, etc. I received much support from him and his collaborators, most of which are crucial for the research. He is also humorous and brings a lot of fun to the group.

I would also like to thank Dr. Daniel A. Herzka, my former advisor during the first two years of my Ph.D. training. Though he left the institution, his support and guidance was a meaningful experience.

Besides the advisor, I thank Dr. J. Webster Stayman, as the chair of my thesis committee for his assistance, encouragement, and critical reviews.

Then I will give my thanks to Dr. Michael Schär, Dr. Qin Qin, Dr. Robert G. Weiss, and Dr. Michael A. Jacobs, excellent professors and scientists, for their wonderful collaboration. Dr. Schär has shared with me his rich experience in cardiovascular imaging and in operating Philips scanner. I received much support from Dr. Qin for his expertise in pulse sequence design and perfusion imaging. Dr. Weiss, a leading cardiologist, helped a lot with cardiac patient studies, with his rich experience in cardiac pathology. I also gained experience in pelvic imaging when collaboration with Dr. Jacobs.

My thanks also go to Dr. Nicole Seiberlich for offering me internship opportunities in her group at Case Western Reserve University. She is a leading scientist in accelerated cardiac imaging and significantly broadened my knowledge of fast MRI.

Next, I would like to thank Dr. Wenbo Li, Dr. Gabriele Bonanno, Dr. Dapeng Liu, Dr. Feng Xu, Ruoxun Zi, Dr. Allison G Hays, Dr. M. Muz Zviman, Dr. Henry Halperin, and Dr. Farzad Sedaghat for their collaboration. Their works on coding, data acquiring, image reconstruction, data processing, and manuscript drafting are super helpful to my Ph.D. training.

I would like to thank lab members Xiaoyang Liu, Dr. Parag Karmarkar, Dr. Yi Zhang and Meiyappan Solaiyappan for their encouragement and help with my work. I thank Dr. Li Pan, Dr. Shanshan Jiang and Dr. Deng Mao for patiently answering my questions. I would like to thank Lin Chen, my college and roommate, for her accompany and encouragement during busy and hard times. I thank Peggy Herman, Mary Price, Joseph Gillen, Terri Brawner, Kathleen Kahl, Cindy Maranto and Hugh Wall for their help on documents and scanners.

I am also grateful for other visible and invisible help from all other members in Radiology and Kirby Center, the source and education from the university and teachers, and the encouragement from my family and friends.

Yours Sincerely,

Dan Zhu

November 2020

Contents

List of Tables

List of Figures

Chapter 1 Introduction

1.1 Overview of the thesis

Magnetic resonance imaging (MRI) is a widely used clinical imaging technique because it is free of ionizing radiation and enjoys the advantages of high spatial resolution, high signal-to-noise-ratio (SNR), multiple contrast mechanisms, and high soft-tissue sensitivity. Besides the typical spin-lattice relaxation time (T1)-weighted (T1w) images, spin-spin relaxation time (T2)-weighted (T2w) images, proton density (PD)-weighted (PDw) images as well as absolute T1 and T2 mapping, images whose contrasts reflect physiological functions can also be provided by MRI. These include angiography, perfusion, diffusion, velocity mapping, and magnetic resonance (MR) spectroscopy, with quantitative measurements obtainable in most cases. MRI can benefit from abundant controllable parameters and the extra dimension of phase information. With such complex functional information MRI can avoid the use of contrast agents and can be encoded for screening, diagnosis, and follow-up studies after treatment. These techniques show promise in clinical applications. Quantitative MRI "relaxometry" (T1 and T2) mapping is sensitive to acute myocardial edema (1,2) and brain lesions (3,4). Phase contrast (PC) MRI (5) can provide velocity maps to analyze the spatial and temporal flow pattern and flow reserve, and can reveal the severity of coronary stenoses (6). MR angiography (MRA) (7) is widely used for diagnosing vascular aneurysms, plaques, vessel malformations, dissections, and stenoses. MRA may also aid in evaluating kidney transplants, the patency of coronary bypass vessels, and tumor surgery.

Despite its potential diagnostic advantages, MRI’s long acquisition time can limit its clinical application. Quantitative MRI is typically slower because extra scans are required for parameter calculation, and sometimes repeated scans must be added to increase SNR. Accelerating MRI may not only reduce scan time but also reduce artifacts caused by motion and improve the clinical utility of the images. Various fast MRI sequences and methods have been reported (8–18). These include: fast spin-echo (i.e. FSE, TSE or RARE) (9); spoiled gradient-echo (i.e. SPGR, FLASH, FFE) (10); balanced or unbalanced steady-state-free-precession (bSSFP, SSFP) (11); echo-planar imaging (EPI) (12,13); and some non-Cartesian sampling methods (like spiral) (14) that increase the efficiency of data acquisition. Fast MRI based on data handling such as parallel imaging (PI) (15), compressed sensing (CS) (16), low-rank (17), and principal component analysis (PCA) (18) makes use of data redundancy to reduce the total amount of data required for image reconstruction and thus reduce data acquisition time. To achieve even faster MRI, current techniques often combine multiple fast imaging techniques.

This dissertation evaluates existing methods and contributes novel techniques that speed up and optimize cardiovascular and cerebral MRI acquisition and reconstruction, as well as new data analysis methods.

This first chapter gives a brief introduction to this dissertation and provides some MRI background related to the techniques described in the following chapters.

These include some basics of MRI, some fast imaging methods, and some quantitative and functional MR techniques.

Chapter 2 is focused on acceleration strategies of whole-heart three-dimensional (3D) T2 mapping methods. This chapter compares a wide range of acceleration factors, different undersampling patterns, and some existing multi-contrast reconstruction methods on swine and human datasets. The aim is to determine an optimal strategy for accelerated high-resolution ($1.25 \times 1.25 \times 5$ mm^3) T2 mapping that can also be applicable for mapping other parameters and different organ systems. The tradeoff between scan time and the quality of parametric maps is evaluated.

In chapter 3, a new rapid and accurate method was developed for high-resolution whole-brain 3D T2 mapping. While chapter 2 compares existing methods, novel protocols, and a new reconstruction method were proposed and evaluated in this chapter. We made use of the high acquisition efficiency of spiral trajectories and combined model-based T2 reconstruction with spatial sparsity constraints. The new parametric mapping methods were not limited to T2 mapping and allow the MRI signal from CSF to be suppressed to enhance contrast, using a magnetization preparation.

Chapter 4 introduces new methods to achieve high-quality coronary PC MRI with both high spatial and high temporal resolution, combining spiral trajectory and CS reconstruction. New protocols and data handling schemes were proposed to reduce undersampling artifacts and to improve image quality. Advanced reconstruction approaches that combine PI and CS were modified to adapt coronary PC MRI that is phase-sensitive and requires an additional velocity-encoding dimension beyond typical dynamic MRI. This new method obtains high quality dynamic cardiac images with 0.8 mm spatial resolution and <21 ms temporal resolution in a single breath-hold and can measure coronary blood velocity and flow parameters with high reproducibility.

As well as velocity measurements, PC MRI can also generate angiograms by subtracting the velocity encoded images (19). The PC module can be improved to create a velocity-selective module to perform MRA directly without subtraction. In Chapter 5, a velocity-selective MRI technique is used to saturate the MRI signal in static tissue to achieve 3D MRA of the whole abdomen without using contrast agents. MRA data are acquired during free breathing. Because vascularity in the abdomen is complicated, we optimized the direction of the selective velocity encoding, the number of velocity-selective modules, and the delay time to improve the quality of the angiograms. The new protocol was combined with bSSFP acquisition, PI, and CS to obtain high resolution ($1.4 \times 1.4 \times 2$ mm^3) MRA with a large spatial coverage.

Chapter 6 explores physiological changes within real-time (RT) structural MRI acquired at up to 100 frames/sec using a highly-undersampled radial acquisition and graphics processing units obtained via a collaboration with the Max Planck Institute. Spectral analysis, principal component analysis (PCA), and perfusion models were applied to RT datasets to extract physiological information reflecting kinetics and perfusion in the heart, speech in the pharynx, and blood flow to the brain. The methods were tested on healthy subjects and cardiac patients with wall motion abnormalities.

Chapter 7 summarizes the previous chapters and introduces some ongoing and future works related to this dissertation.

1.2 Basics of MRI

1.2.1 Spins and magnetization

The phenomenon of Nuclear Magnetic Resonance (NMR) was first discovered by Felix Bloch and Edward Purcell in 1946. Some Nuclei can absorb radiation at specific frequencies when placed in an external magnetic field (B_0) and emit detectable radiation after returning to equilibrium.

Nuclei that are suitable for NMR contain at least one unpaired nucleon. Unpaired nucleons possess spin angular momentum, which endows the nucleus with a magnetic moment and is key for NMR. Despite the many eligible nuclear isotopes that are suitable for NMR, such as ^{13}C, ^{14}N, ^{31}P, and ^{19}F, the most commonly used nucleus in MRI is ^{1}H owing to its substantial biological abundance. The ^{1}H nucleus is usually referred to as the ‘proton’ because it is composed of a single proton. When B_0 is present, the proton spins will align with the external field in two allowed energy states, roughly parallel and antiparallel to B_0, with a slight excess in the low energy state, depending on thermal motion in the sample. The energy of the radiation that can be absorbed by protons under this situation has to be exactly the same as the energy difference between the parallel and the antiparallel states (ΔE). The frequency of this radiation, called the Larmor frequency (ν), is proportional to B_0. The constant of proportionality is called the gyromagnetic ratio (γ) and is specific to the nucleus. Values of $\bar{\gamma} = \gamma/2\pi$ are often quoted instead of γ. The equations for the Larmor frequency and the energy difference are given by Eq. 1.1 and Eq. 1.2, respectively:

$$\nu = \bar{\gamma}B_0 \qquad 1.1$$

$$\Delta E = h\nu = h\bar{\gamma}B_0 \qquad 1.2$$

For protons, $\bar{\gamma}$ = 42.58 MHz / T. h = 6.626×10^{-34} J·s is Planck's constant.

The ratio of spins in each state in a sample in B_0 subject to no other excitation fields is in a constant equilibrium state at room temperature. The ratio of antiparallel (N^-) and parallel spins (N^+) follows the Boltzmann distribution:

$$N^-/N^+ = e^{-\Delta E/kT} \qquad 1.3$$

Here k = 1.3805x10-23 J / K is the Boltzmann constant, and T is the temperature in Kelvin.

Since the net magnetic moment of a sample of antiparallel and parallel spins will, in part, cancel, a macroscopic bulk magnetization only arises when there is a net difference in the number of spins occupying the two energy states. This is given by Eq. 1.3 and is generally very small compared to the total number of spins (N^++N^-). The bulk magnetization in this situation is referred to as M^0, which, at equilibrium, is parallel to B_0.

When radiation at the Larmor frequency (usually called a ‘radiofrequency pulse’ or ‘RF pulse’) is applied, spins in the parallel energy state can absorb the radiation and transit to the antiparallel (higher energy) state. The component of the bulk magnetization that is oriented parallel to B_0, i.e., the longitudinal magnetization (M_z), will generally decrease in this situation. At the same time, a component of the magnetization (M_{xy}) transverse to B_0 is generated. M_{xy} is perpendicular to B_0 and rotates about the z-axis in the xy plane at the Larmor frequency, which is called ‘precession.’ But if the exciting ration is continued, it is a possible to cause rotation of the bulk magnetization to completely invert it so that it is antiparallel to B_0. If the radiation is turned-off at exactly that point, the RF pulse is called a 180° pulse. RF pulses are quantified by the degree of this rotation, termed the flip angle (FA).

When the RF pulse ends, some antiparallel spins jump back to the parallel (low-energy) state. By this means, M_z eventually recovers back to M^0. Similarly, the spins contributing to M_{xy} gradually fall out of alignment, and M_{xy} will decay to 0.

Because M_{xy} rotates at the Larmor frequency in xy plane due to precession, the signal along the x-axis is sinusoidal. If a wire coil is placed sensitive to the xy plane, the magnetization change in the x direction will generate an alternating current in the coil. The magnitude and phase of the sinusoidal signal measured by the coil generate a complex NMR signal.

The time constants for M_z recovery and M_{xy} decay are named relaxation times. For M_z, the recovery time-constant is named the spin-lattice relaxation time, T1.

The equation for T1 recovery is given by Eq. 1.4:

$$\mathrm{M_z(t) = M_z(0)e^{-\frac{t}{T1}} + M^0\left(1 - e^{-\frac{t}{T1}}\right)} \qquad 1.4$$

Here, t is the time delay after the RF pulse ends and $\mathrm{M_z}(t)$ is the longitudinal magnetization at time t.

For M_{xy} decay, the time-constant is named spin-spin relaxation time (T2). Generally, T2 ≤ T1. The equation for T2 decay is given by Eq. 1.5:

$$\mathrm{M_{xy}}(t) = \mathrm{M_{xy}}(0)\mathrm{e}^{-\frac{t}{T2}} \qquad 1.5$$

However, in real experiments, M_{xy} usually decays faster than predicted by T2. Magnetic field inhomogeneity, susceptibility (internal magnetization of the spins), and chemical shift (different chemical environments of the spins) are three reasons for faster decay. This faster decay rate is usually referred to as T2* (≤ T2). The exponential decay pattern of T2* is usually treated the same as for T2 decay in Eq. 1.5, though it often varies from true exponential depending on the source of the additional dephasing.

1.2.2 Gradients, spatial encoding, and k-space

The signal obtained from NMR, as described above, is the bulk magnetization of the object being excited. That signal does not yet contain location information. For the purpose of imaging, Fourier encoding is the conventional method for obtaining multi-dimensional spatial information. The Fourier transform (FT) of an image is called ‘k-space.’ Fourier encoding of images in MRI is enabled by adding gradients to B_0. There are two Fourier encoding approaches in conventional MRI: frequency encoding and phase encoding.

In frequency encoding, a constant gradient is applied during data acquisition. As shown in Fig. 1.1, the spins at different spatial locations are exposed to a different B_0 field due to the gradient, resulting in different Larmor frequencies. $\nu(x)$, the Larmor frequency at location x, is linear with the location x:

$$\nu(x) = \bar{\gamma}(B_0 + Gx). \tag{1.6}$$

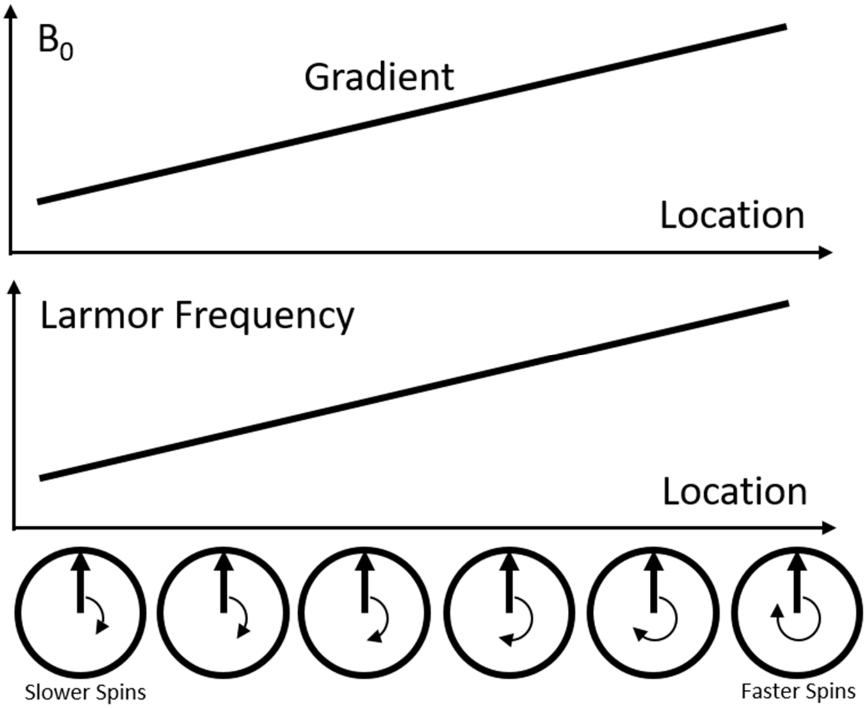

Figure 1.1: frequency encoding.

In phase encoding, a gradient is applied before data acquisition, resulting in a phase difference between the bulk magnetization of spins at different locations. This phase difference works as the phase modulation of the Fourier encoding. The phase difference accumulated from the gradient (Δφ) at location x is proportional to the gradient strength, G, gradient duration, τ, and location, x(Eq. 1.6).

$$\Delta\varphi = 2\pi\gamma G x\tau \qquad 1.7$$

As shown in Fig. 1.2, a phase difference is accumulated during the gradient, according to Eq. 1.7, proportional to the duration and amplitude of the gradient. Phase encoding is accomplished in multiple acquisitions in which the gradient strength is varied to provide different phase modulation for Fourier encoding.

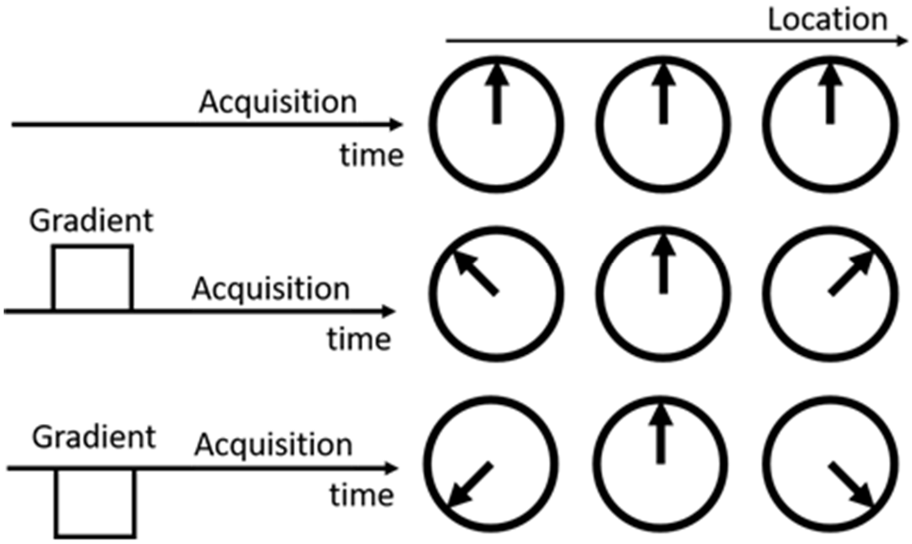

Figure 1.2: phase encoding.

Slice selection is another technique for localization. In this technique (Fig. 1.3), a gradient of B_0 is applied with the RF pulse, resulting in different Larmor frequencies at different location x. The applied RF pulse has a frequency of γB_0, and can only excite spins at a Larmor frequcney of γB_0, i.e. at the location of x=0. After that, a negative refocusing gradient lobe is applied to compensate for phase accumulation during slice selection.

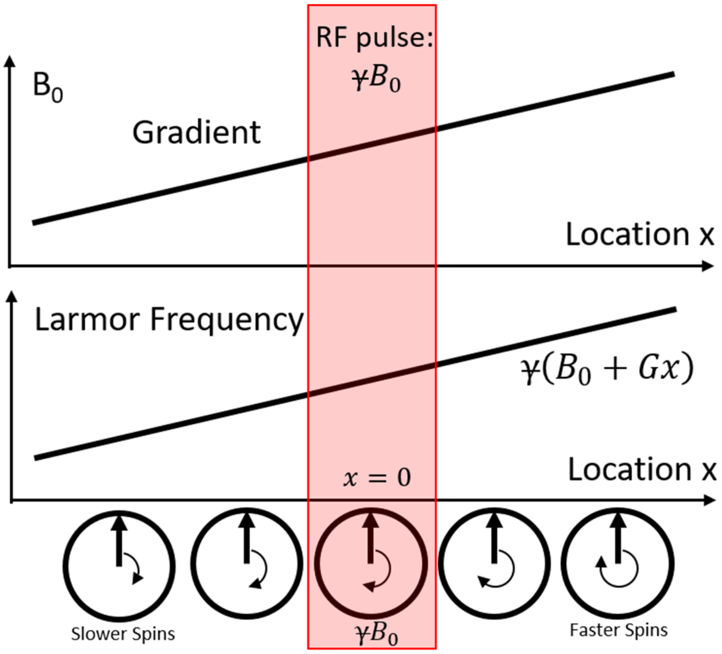

Figure 1.3: slice selection.

A typical two-dimensional (2D) image selects a slice in a first dimension then applies frequency encoding in one dimension within the plane of the slice and phase encoding in the other dimension. An example of this 2D encoding with Cartesian sampling is demonstrated in Fig. 1.4. An RF selective excitation pulse (RF_{ex}) is applied at the beginning of the sequence, rotating the magnetization into the xy plane. A gradient in z direction (G_{ss}) is applied during the period of the RF pulse for the slice selection, followed by the negative refocusing pulse. After the excitation pulse, a gradient in the y direction (G_{PE}) is applied to provide phase encoding. After the phase encoding gradient is applied, a gradient in the x direction (G_{FE}) is applied to enable frequency encoding during signal acquisition. A negative gradient pulse is applied in the x direction (G_{FEpre}) with half the area of the G_{FE} pulse before the acquisition, to offset the frequency encoding so that the spins will align (forming a gradient-induced echo) at the center of the acquisition window rather than at its beginning. The time delay of the echo after the excitation pulse is called the echo time (TE). One such sequence application with its acquisition window can fill one k-space line. Multiple acquisitions with different G_{PE} can be used to fill the whole k-space (blue lines in Fig. 1.4B). The time interval between two consecutive excitation pulses is called the repetition time (TR).

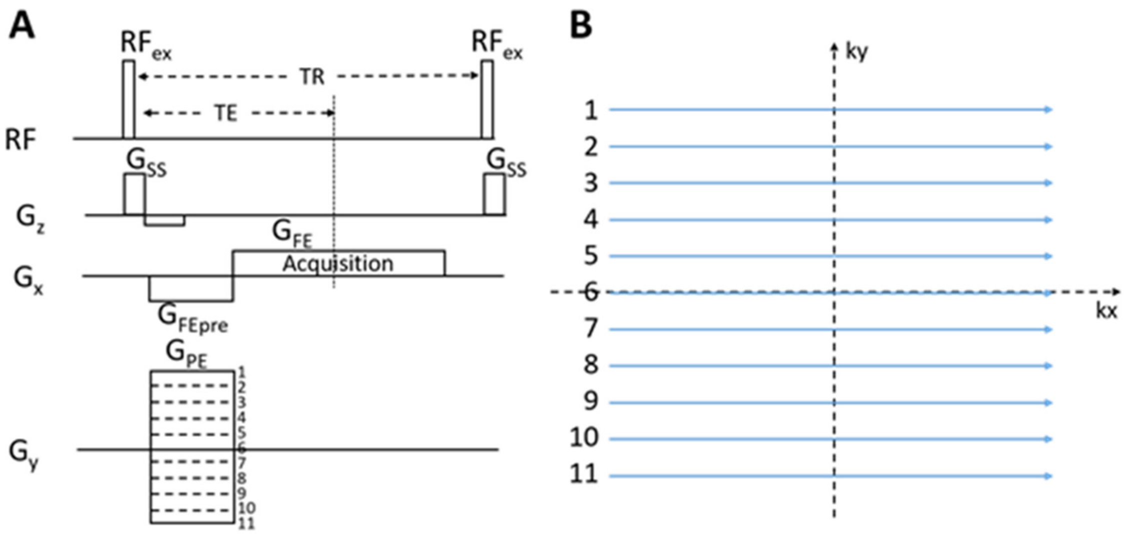

Figure 1.4: RF and gradients sequence (A) and corresponding k-space (B) of a 2-dimensional image with frequency encoding in x dimension and phase encoding in y dimension.

1.2.3 Gradient Echo (GRE) and Spin Echo (SE)

The G_{FEpre} gradient in Fig. 1.4A causes dephasing of the spins at different x locations, which are rephased at TE. The area of G_{FEpre} is the same as the area of the part of G_{FE} before the echo. The image sequence with this gradient-based rephasing is called gradient echo (GRE). The bulk M_{xy} signal decays during dephasing by the gradients.

An alternative sequence, as shown in Fig. 1.5, provides an additional RF pulse (RF_{echo}) after the excitation pulse (RF_{ex}), with FA = 180°, is applied to flip the spins whose phase is leading to a lagging phase and vice versa. Dephased spins during the first half of TE will rephase during the second half. The RF-pulse induced rephasing of the spins produces a refocused spin echo (SE) at time TE, and RF_{echo} is usually referred to as the refocusing pulse.

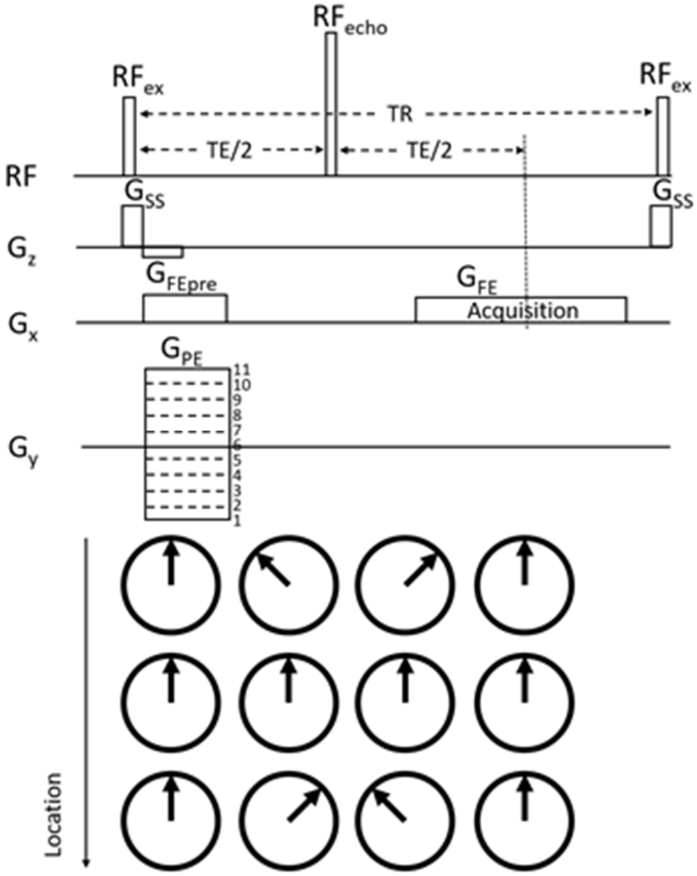

Figure 1.5: SE sequence of a 2-dimensional image.

Spins dephased by gradient, susceptibility, and chemical shift can all be refocused via SE, while GRE can only compensate for the effect of the applied dephasing gradients. Therefore, the M_{xy} signal at TE in SE follows a purely T2 decay compared to the signal after excitation. The M_{xy} signal at TE in GRE is still dephased by effects other than the dephasing gradients and follows the T2* decay.

T1, T2, and T2* relaxation times are tissue-specific, and differences between tissues provide contrast for structural MRI in addition to the proton density (PD). Although MRI shows a mixture of PD, T1, and T2 (for SE, or T2* for GRE) weighting, we are able to control the dominant weighting by tuning the acquisition parameters. For example, in a typical SE sequence. Short TR and TE generate~~s~~ T1-weighted (T1w) images, long TR and TE generate T2-weighted (T2w) images, and long TR but short TE generate PD-weighted (PDw) images.

1.3 Fast MRI techniques

Usually, it takes a relatively long time for M_z to recover and for M_{xy} to decay after each acquisition, leading to long TRs and total scan times. Standard SE or GRE sequences can take tens of minutes to obtain images of a target organ, limiting clinical applications of MRI. Therefore, many efforts have been made to accelerate MRI in the past decades.

1.3.1 Fast spin echo (FSE), spoiled gradient echo (SPGR), balanced steady-state-free-precession (bSSFP)

Fast spin echo (FSE), also known as turbo spin echo (TSE) or rapid acquisition with relaxation enhancement (RARE), is a SE sequence with multiple refocusing pulses (9). As shown in Fig. 1.6, multiple acquisitions of different k-space lines are performed in one TR to accelerate the scan.

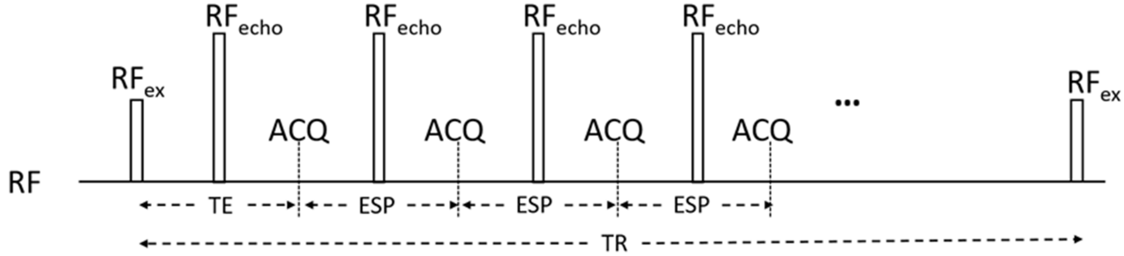

Figure 1.6: RF pulse trains of the FSE sequence. Abbreviations: ESP = echo spacing, ACQ = acquisition.

In a traditional FSE sequence, a 90° excitation pulse and 180° refocusing pulses (90°-180°-180°-) are used with an echo spacing time equal to TE. Some advanced FSE sequences use smaller flip angles to reduce RF power deposition in the body (as measured by the specific absorption rate, SAR), which can cause heating during scans. FSE sequence can cause image blurring due to T2 decay of the signal acquired between echoes. A variable flip angle (VFA) technique has been introduced (20) that can compensate for the blurring effect caused by T2 decay. This works by creating a signal plateau using refocusing pulse trains with gradually increasing FAs. Non-traditional FSE techniques are affected by stimulated echoes, which are also observed when the 180° refocusing pulses are not perfect. The stimulated echoes can be eliminated by applying crusher gradients (gradient pulses that dephase spins not contributing to the SE) before and after the refocusing pulses.

The spoiled gradient echo (SPGR) sequence, also known as the T1-weighted fast field echo (T1w FFE) or fast low angle shot (FLASH) sequence, is a GRE sequence that spoils the transverse magnetization M_{xy} after acquisition to enable the use of a short TR while avoiding spurious stimulated echo signals (10). Fig. 1.7 demonstrates a representative SPGR sequence. Compared to the traditional GRE sequence, there are two modifications to spoil the transverse magnetization: gradient spoiling and RF spoiling. For gradient spoiling, crusher gradients (G_{spoil_x} and G_{spoil_y}, also referred to as spoiling gradients) are applied after acquisition to dephase M_{xy} signal. For RF spoiling, a 117° phase-lag is added to consecutive excitation pulses.

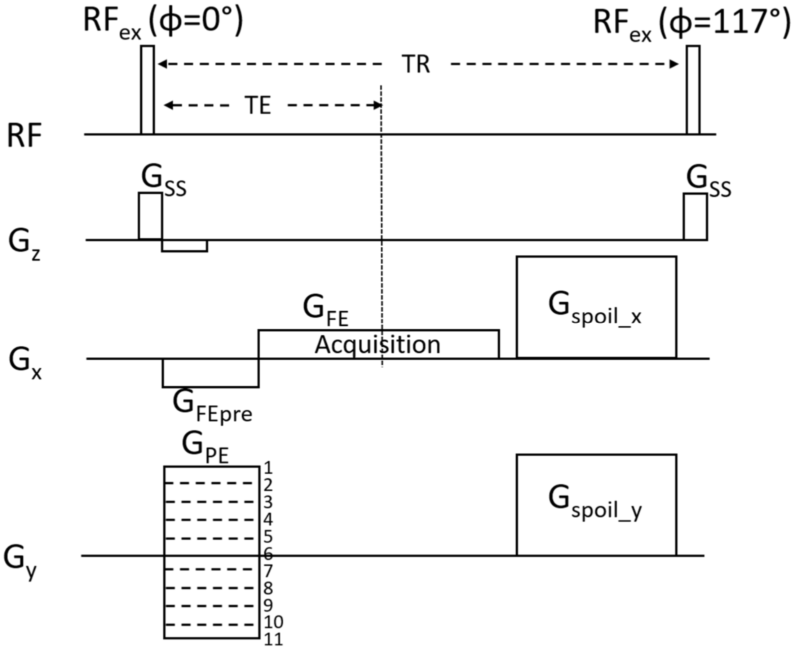

Figure 1.7: SPGR sequence.

Usually, the TR in SPGR is very short. As a result, the longitudinal signal M_z before the next excitation pulse does not recover to M^0. Instead, M_z in SPGR eventually reaches a steady-state, when the signal before two consecutive excitations is the same:

$$\mathrm{M_z^{SS}} = \mathrm{M_z^{SS}} \cos\theta\, \mathrm{e}^{-\frac{\mathrm{TR}}{\mathrm{T1}}} + \mathrm{M}^0 \left(1 - \mathrm{e}^{-\frac{\mathrm{TR}}{\mathrm{T1}}}\right) \qquad 1.8$$

Here θ is the flip angle of the excitation pulse. Eq. 1.8 is obtained by substituting $\mathrm{M_z}(0)$ with $\mathrm{M_z^{SS}} \cos\theta$ and substituting t with TR in Eq. 1.4. Therefore, the steady-state (longitudinal magnetization) M_z is given by Eq. 1.9 and the (transverse) M_{xy} signal which is acquired is given by Eq. 1.10:

$$\mathrm{M_z^{\mathit{SS}}} = \mathrm{M}^0 \frac{1-e^{-\frac{TR}{T1}}}{1-e^{-\frac{TR}{T1}}\cos\theta} \qquad 1.9$$

$$\mathrm{M_{xy}^{\mathit{SS}}} = \mathrm{M}^0 \frac{1-e^{-\frac{TR}{T1}}}{1-e^{-\frac{TR}{T1}}\cos\theta}\, e^{-\frac{TE}{T2^*}} \sin\theta \qquad 1.10$$

SPGR is typically dominated by T1 weighting. The steady-state signal $\mathrm{M_{xy}^{\mathit{SS}}}$ is much smaller than M^0 when TR<<T1.

According to Eq. 1.10, when TR and T1 are fixed, $\mathrm{M_{xy}^{\mathit{SS}}}$ can be maximized with a specific flip angle, called the Ernst angle. The Ernst angle θ_E as a function of TR and T1 is given by Eq. 1.11:

$$\theta_E = \arccos e^{-\frac{TR}{T1}} \qquad 1.11$$

For short TR, θ_E is usually small (around 10°). SPGR is stable with few artifacts but often has low SNR due to small $\mathrm{M_{xy}^{\mathit{SS}}}$ and T2* signal decay. It is also affected by B_0 inhomogeneity, which results in mild signal loss, distortion, and image blurring.

The balanced steady-state free precession (bSSFP) sequence, or TrueFISP

(Siemens Healthineers) or FIESTA (GE Healthcare), uses rewinder gradients rather than the spoiling gradients used in the SPGR sequence. Fig. 1.8 demonstrates a representative bSSFP sequence. The rewinder gradients ($G_{rewinder\_x}$ and $G_{rewinder\_y}$) compensate for the previous gradients in the x and y direction, and the phase difference between consecutive excitation pulses is 180°. For the best image quality with bSSFP sequence, TR =2TE. The bSSFP sequence rephases all the $\mathrm{M}_{\mathrm{xy}}^{SS}$ signal with rewinder gradients before excitation, so there is little signal lost compared to SPGR where M_{xy} is spoiled. As a result, bSSFP has higher SNR than SPGR. The most severe drawback of bSSFP is the banding artifacts caused by field inhomogeneity, which can be improved with shimming. On the other hand, bSSFP has better performance on systems with lower B_0 due to less B_0 off-resonance effects. Additionally, bSSFP is T2/T1 weighted, and lower B_0 benefits the steady-state signal with higher T2/T1 ratios.

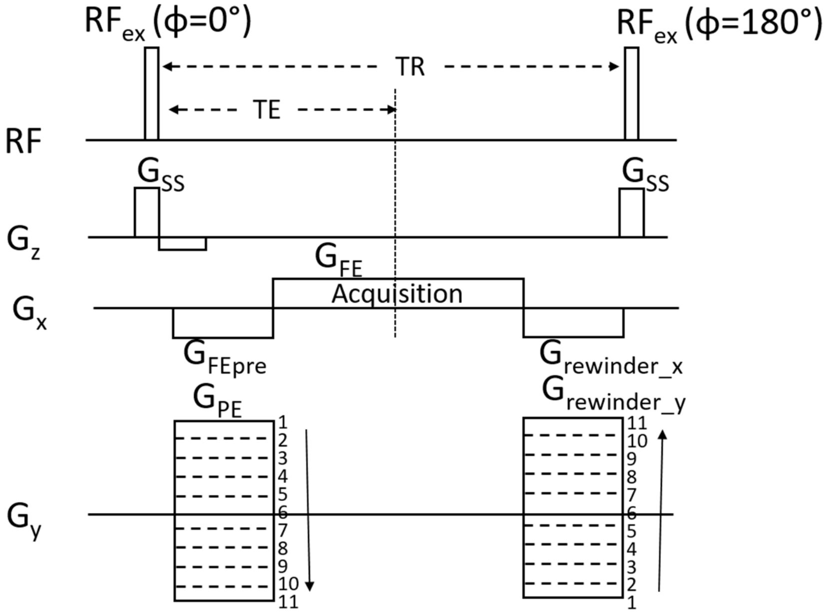

Figure 1.8: bSSFP sequence.

1.3.2 Echo-planer imaging (EPI) and Spiral acquisition

Section 1.3.1 introduced some fast imaging techniques that increase the number of acquisitions in limited total times. Techniques in this section accelerate MRI scanning by prolonging the acquisition window and obtaining more data within one acquisition.

Echo-planer imaging (EPI) covers the whole k-space in one acquisition, as demonstrated in Fig. 1.9. Because the whole k-space is acquired within one TR, EPI acquisition is very fast. Usually, it takes just a few seconds to acquire a 2D image slice.

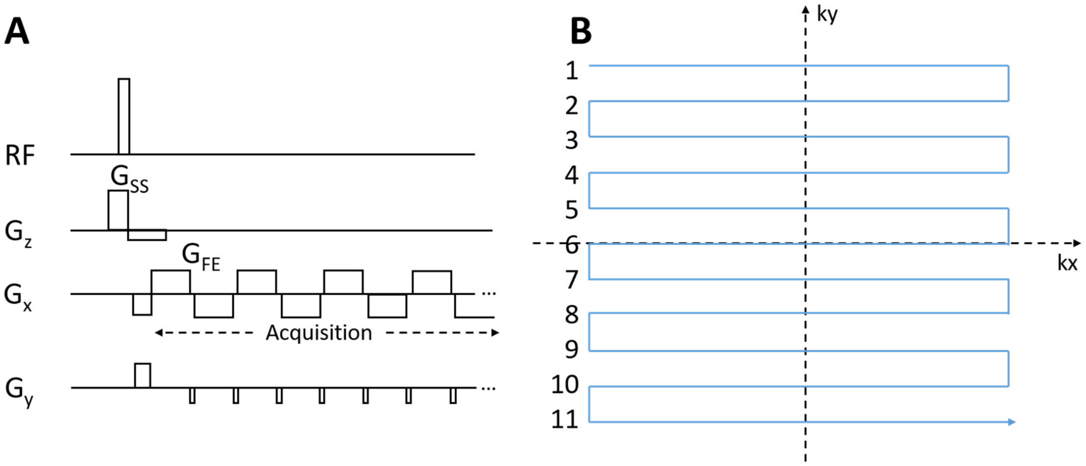

Figure 1.9: EPI Sequence (A) and k-space trajectory(B).

Despite the fast imaging speed, some drawbacks in EPI limit its application. The most common artifacts observed in EPI are the ghost artifacts (Fig. 1.10A). These artifacts are caused by the misalignment of the k-space lines acquired in different directions. Typically, the acquisition directions are flipped between odd and even lines, resulting in a Nyquist ghost, which is an aliasing artifact of an image shifted by half of the field-of-view (FOV). Therefore, this artifact is usually called a “1/2-ghost” (Fig. 1.9A). Another artifact that limits the application of EPI is the chemical shift artifact (Fig. 1.10B). Differences in the chemical environment of spins affect the local B_0 experienced by the MRI nucleon, causing small frequency differences called “chemical shifts” that result in a shift in the frequency-encoded image signal provided by the chemically-shifted species. This effect is mostly observed between water and fat due to their abundance in the body and their difference in chemical shift.

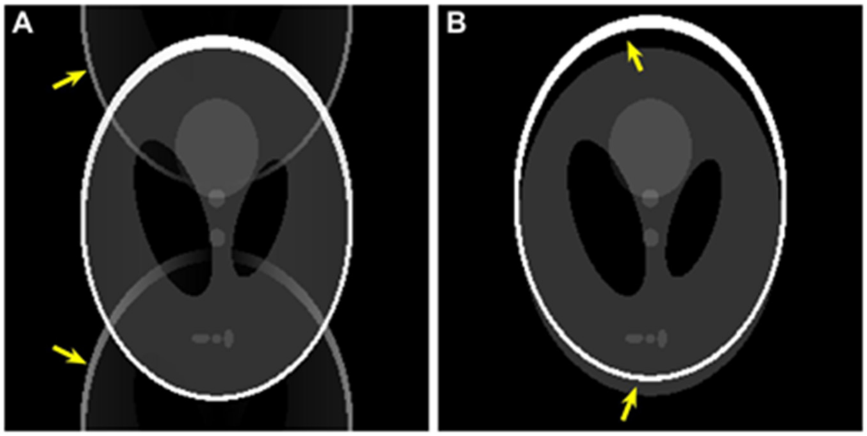

Figure 1.10: ghost artifacts (A) and fat-water chemical shift artifacts (B) of EPI sequence. Artifacts are pointed by yellow arrows.

Other effects such as distortion due to B_0 inhomogeneity, nonlinearity in the applied MRI gradients, and signal loss due to dephasing compared to traditional GRE image also limit the application of EPI. Recent studies demonstrate that improved image quality can be achieved with the EPI sequence by improving the field homogeneity (21), correcting ghost artifacts in post-processing (22), and by introducing multi-shot EPI wherein the whole of k-space is filled with several EPI acquisitions.

There are other trajectories that cover the whole k-space for image acquisition, for example, a spiral trajectory, as shown in Fig. 1.11.

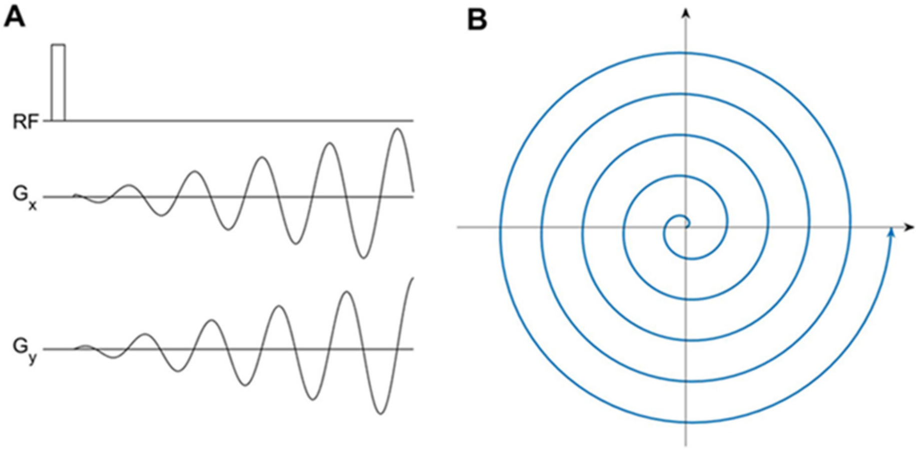

Figure 1.11: Sequence (A) and k-space trajectory (B) of a spiral sequence.

Spiral acquisitions are also efficient. Compared to the EPI sequence, there are some advantages of the spiral sequence. First, there is no ghost aliasing in spiral imaging. Second, chemical shift and B_0 inhomogeneity no longer cause artifacts. They do cause image blurring, which can be treated in post-processing. Third, the spiral trajectory starts at the center of the k-space, allowing very short TE and high SNR due to minor T2* effects. Finally, G_x and G_y gradients are smooth, so no extra time is wasted for gradient switching. Smooth gradients also enjoy mild eddy current effects.

The performance of the spiral trajectory depends highly on the accuracy and response time of the hardware. Non-Cartesian acquisition requires time-consuming non-uniform FT (NUFT) for image reconstruction. In recent years, the spiral acquisition has gained increasing interest as more powerful hardware and reconstruction workstations have become available.

1.3.3 Parallel Imaging (PI) and Compressed Sensing (CS) MRI

The previous two sections introduced techniques that increase acquisition efficiency. This section will talk about fast MRI methods that can further reduce the data required for image reconstruction.

Parallel imaging (PI) uses multi-channel receiver coils that can acquire multiple signals simultaneously (15). One strategy to reduce scan time is to acquire only a part of the k-space. This normally results in image aliasing artifacts that are intolerable. However, aliasing in images can be unfolded due to data redundancy when multiple channel acquisitions are available. The most commonly used PI methods used to unfold undersampling aliasings are sensitivity encoding (SENSE) (23) and generalized autocalibrating partial parallel acquisitions (GRAPPA) (24).

SENSE is an image-based PI reconstruction method where aliasing from the sub-Nyquist acquisition is removed based on the encoding provided from the coil sensitivities. Fig. 1.12 demonstrates a representative image of parallel imaging with a four-channel receiver coil. Images measured from different channels are modulated by their coil-specific sensitivity profiles. As a result, the image obtained from each coil is the original image (without sensitivity encoding) multiplied by a sensitivity map. When k-space is undersampled, aliasing artifacts are generally observed in multi-channel images. Traditionally, the k-space is undersampling uniformly. For example, in Fig. 1.12 with a Cartesian acquisition, even k-space lines are acquired, and odd lines are skipped, leading to a reduction factor of R = 2. In this case, an aliased image is superposed on top of an unaliased image, which is actually the same as the unaliased image shifted by half of the FOV. As a result, the top and bottom halves of the aliased images are identical and are equal to the superposition of the top and bottom halves of the unaliased image.

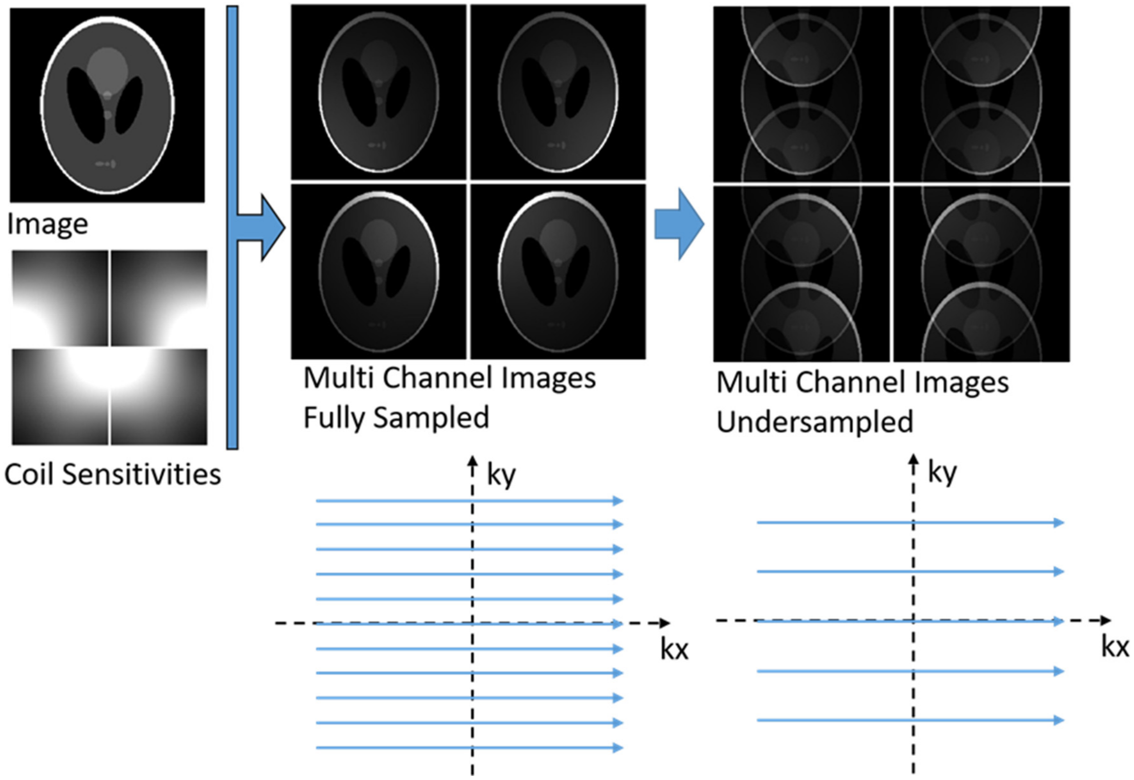

Figure 1.12: Imaging with multi-channel receiver coils.

With multi-channel data from different coil locations, the image recorded from different channels is intrinsically encoded with the sensitivity information, as shown in Fig. 1.13. With R = 2 equally-spaced undersampled k-space, pixel X and Y, with a distance of half the FOV, are aliased, resulting in pixels whose signal sum at X and Y, are weighted by the coil sensitivities. Though these are mixed in the undersampled images, the weights at X and Y vary between the different channels. As a result, 4 equations can be formed to solve X and Y in Fig. 1.13. In practice, the reduction factor R determines the number of unknowns. The number of channels, N_{ch} determines the maximum number of equations that can be solved. $R < N_{ch}$ is usually set to avoid under-determination of the equations. When overdetermined, X and Y can be calculated by a least-squares fit. Sensitivity maps are smooth and can be estimated from low-resolution images, which are calculated either from the fully sampled central k-space area or from an additional scan. Advanced SENSE techniques can also solve arbitrarily undersampled images or non-Cartesian sampled images using iterative reconstruction (25).

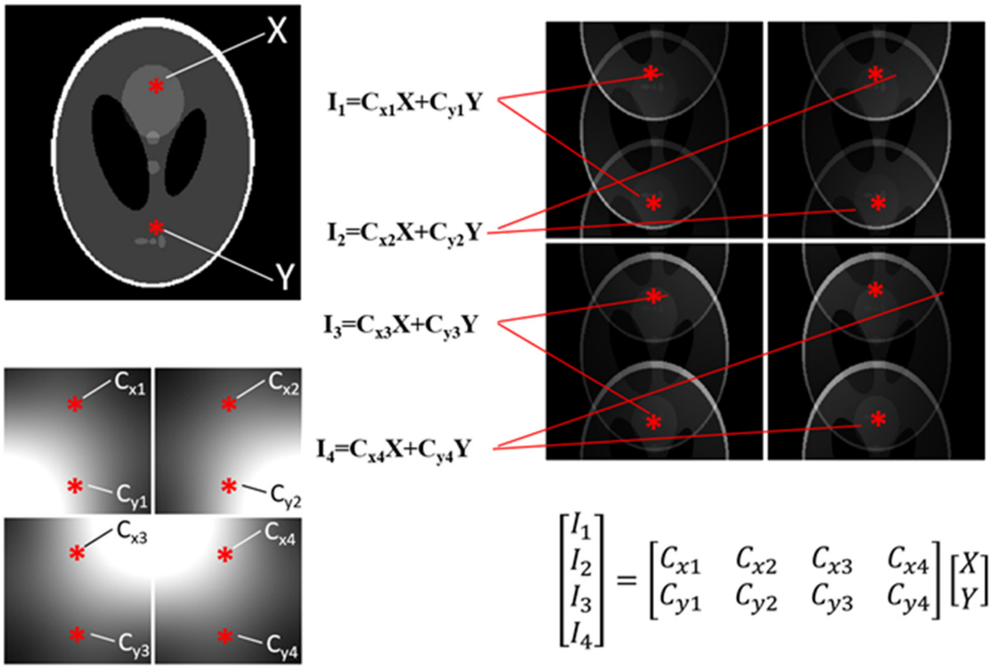

Figure 1.13: Sensitivity encoding of undersampled multiple channel images.

GRAPPA, on the other hand, is a k-space based reconstruction method. It is assumed that pixels in k-space can be expressed as a linear combination of neighboring k-space pixels, as shown in Fig. 1.14. Neighboring pixels of the same coil and from other coils are both included in the linear combination.

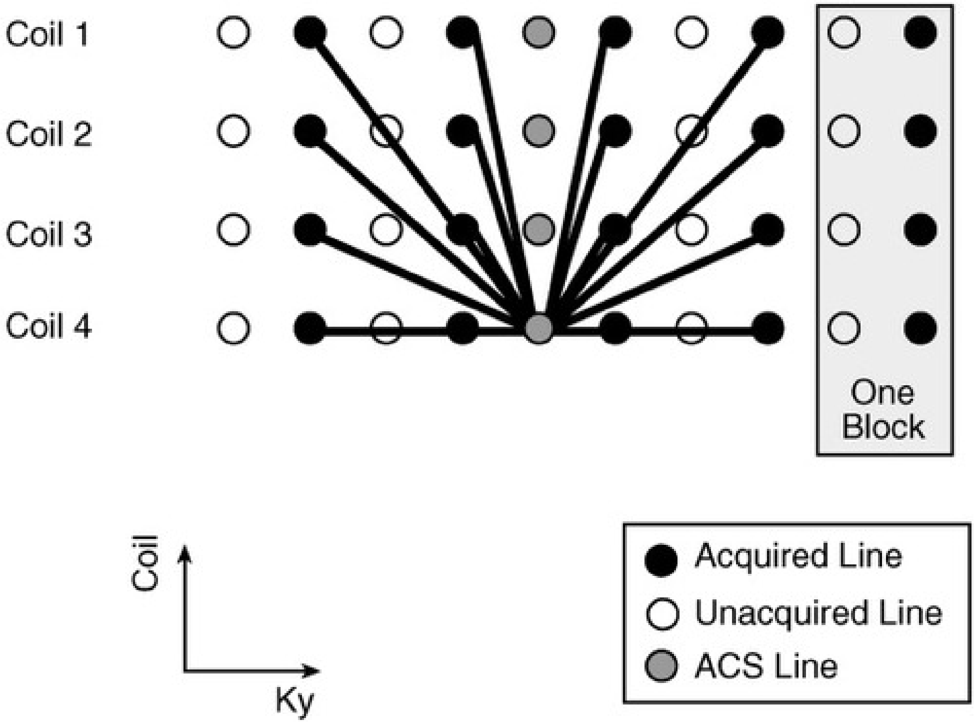

Figure 1.14: GRAAP (24).

For a given coil, the weights combining the neighboring k-space pixels are regarded invariant over all k-space. The weights are different for each coil. In GRAPPA, the MRI signal is undersampled in the outer k-space with a fully sampled central k-space area called the auto-calibration signal (ACS). The weights are fitted from the ACS region, and the missing data in outer k-space are calculated from the sampled k-space data using the fitted weights.

Another group of accelerated MRI reconstruction methods is based on compressed sensing (CS) (16). Generally, compressed sensing techniques require sparsity or transform sparsity of the data.

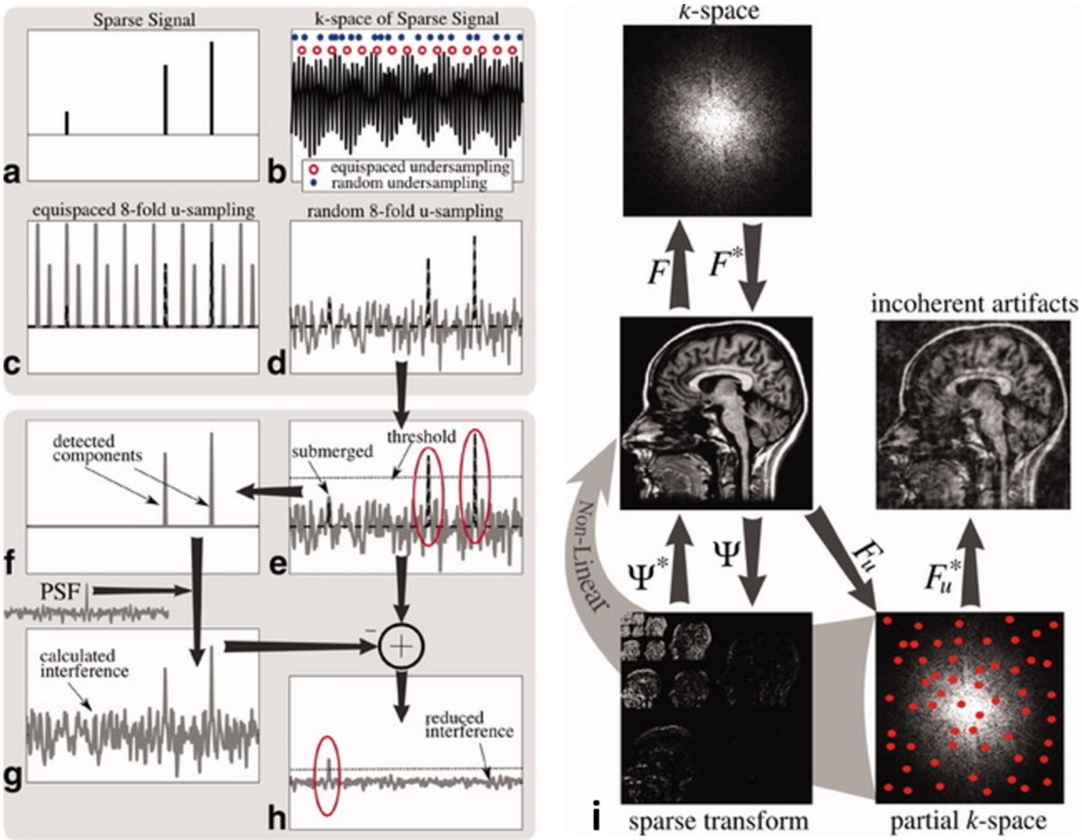

Figure 1.15: Basic idea of Compressed Sensing (16). Sparse signal with 3 non-zero elements (a) is the Fourier transform (FT) of a fully-sampled k-space data (b). If the k-space data in (b) is equally-spaced 8-fold undersampled (sample at red circles), the FT is aliased with 8 equally-spaced repeats of the 3 non-zero elements (c). The largest and smallest non-zero element in (a) are folded together in (c) and inseparable. If the k-space data in (b) is randomly 8-fold undersampled (sample at blue dots), the 3 non-zero elements are corrupted with incoherent noise-like aliasing (d). The two larger elements in d can be separated via thresholding (e, f). Corrupted signal of the two larger elements (g) are generated by undersampling the k-space of (f) at blue dots in (b). Signal with only the smallest element and its aliasing (h) can be obtained by subtracting (g) from (d). The smallest signal (h, red circle) can be separated from its aliasing with a threshold smaller than the threshold in (e). MRI image in (i) corrupted in random undersampling with incoherent artifacts can also be recovered with thresholding. The thresholding is applied in a sparse transform (Ψ) of the image. F and F^*: forward and inverse FT. F_u and F_u^*: forward and inverse FT with undersampling. Ψ and Ψ^* forward and inverse sparse transform.

Fig. 1.15 demonstrates the basic idea of CS reconstructions applied to sparse signal (parts a-h) and the transformed sparse image (part i). While equally-spaced undersampling is acceptable in PI, aliasing from equally-space undersampling cannot be eliminated by CS (part c, equally-spaced repeats of signals in part a). Instead, random undersampling is used in CS, leading to incoherent artifacts (part d, the noise-like signal other than the original sparse signal in part a), which can be separated from the original signal via thresholding (part e). At this stage, some small signals in (part a) are cut with aliasing. To restore these signals, a separation process with a smaller threshold is conducted on the subtracted signal (part h) with only the small signals and their aliasing (part h). This process can also be applied to MRI images (part i). Although the images themselves are not sparse, they can be sparse in certain transformed domains.

The transformations that sparsity MRI images are called sparsifying transforms, such as total variation (TV) (26) and wavelet transforms. In dynamic and parametric MRI, the sparsifying transforms can also be applied to temporal or parametric dimensions. For example, the FT applied to a temporal dimension is a sparsifying transform for dynamic MRI (27). Besides sparsity, incoherent aliasing is also key to CS reconstruction. As shown in Fig. 1.15d, random undersampling in Cartesian MRI generates incoherent aliasing artifacts. In non-Cartesian MRI such as radial and spiral, golden angle (GA) (28) rotation between consecutive acquisitions also generates incoherent aliasing artifacts (29). In this technique, the angle between consecutive radial spokes or spiral arms is 111.25° (Fig. 1.16) or 137.51°, respectively. CS reconstruction is a promising approach because there is no need for extra coils or calibration datasets. The limitation is a relatively long reconstruction time as compared to PI using nonlinear optimization and the difficulty in tuning the threshold to separate the sparse signal.

Nevertheless, the CS methods have been implemented clinically using high-speed graphics processing unit (GPU)-based reconstruction with data-driven parameter tuning methods (30).

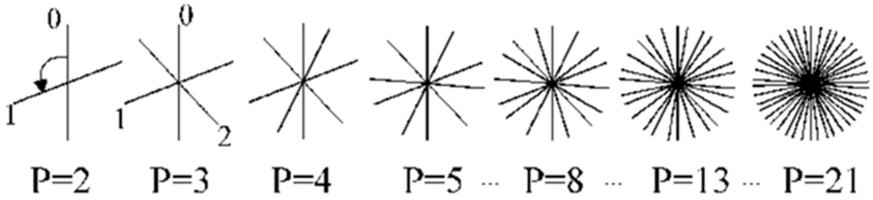

Figure 1.16: Golden angle (GA) radial sampling (28). P denotes the number of total projections (k-space lines) in radial sampling, which are sampled in the order labeled next to each projection. The angle between consecutively sampled projections is demonstrated by the arrow between projection 0 and 1 in the P=2 case.

Besides PI and CS, there are more techniques that can reduce the data needed for MRI reconstruction. For example, partial Fourier methods can acquire only 60% to 80% of the (full uniformly-sampled) k-space data for image reconstruction by taking advantage of symmetry in k-space (30). View-sharing techniques in dynamic MRI are another option that reuses the k-space lines in multiple dynamic frames to reduce the amount of data required. For the highest acceleration factors, the methods introduced in section 1.3 are usually combined.

1.4 Quantitative and functional MRI

The clinical advantage of MRI is the ability to obtain structural and functional images on a single modality with or without the usage of contrast agents. MRI can quantify various physiological parameters with its abundant controllable scan parameters and the additional phase information contained in the complex-valued images. This section will introduce some quantitative and functional MRI techniques explored in later chapters.

1.4.1 Relaxometry

Instead of relaxation-weighted images, techniques that can measure the absolute value of the MRI relaxation times (relaxometry) are playing an increasing role in quantifying clinical disease severity and monitoring therapeutic response.

The basic idea of T1 mapping is to measure repeat images with different T1-weighting after applying a global 180° or a repeated 90° RF pulse. The 180° (or repeated 90°) pulse, when applied at equilibrium, inverts (or partially saturates) M_z to $–M^0$ (or towards zero) and is usually referred to as an inversion (or partial saturation) pulse(s). After that, M_z will recover and generate contrast due to differences in T1 values among tissues. The signal recovery of the two sequences (called the inversion recovery (IR) and saturation recovery (SR) sequences), are shown in Fig. 1.17.

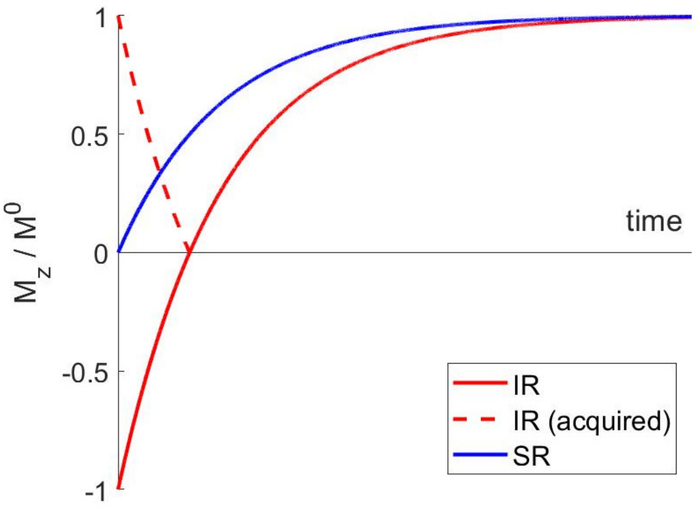

Figure 1.17: IR and SR curves (solid lines, Eq. 1.4 with Mz(0) = -M0 and Mz(0) =0, respectively). Usually, magnitudes of the image intensities are used for T1 mapping (dashed line).

Images are acquired after the inversion or saturation pulse. Each application of the inversion or saturation pulse is often referred to as a ‘shot.’ The time between the inversion pulse and image acquisition is called inversion time (TI). Typically, there is one acquisition in each shot. Images acquired at different TI results in different T1 weighting and are acquired in different shots. In the Look-Locker technique (31), images with different TI are sequentially acquired in one shot.

T1 maps are usually calculated with a pixel-wise exponential fitting of Eq. 1.4. In this model, three parameters, $M_z(0)$, M^0, and T1, are to be fitted. Empirically, due to imperfect RF pulses, a true $M_z(0)=-M^0$ or $M_z(0)=0$ condition is not always applicable. Instead, $M_z(0)$ is fitted with data. Other techniques such as modified Look-Locker inversion recovery (MOLLI) (32), saturation recovery single-shot acquisition (SASHA) (33) offer improved efficiency and accuracy, especially for more complicated heart T1 mapping, but are not used in this thesis work and are thus omitted.

T2 maps can be obtained using the FSE sequence. Instead of acquiring different k-space lines from each echo in an echo train, the same k-space line is acquired at different echo times. The whole k-space is filled by repeating the echo trains in multiple TRs. The exponential decay model of Eq. 1.5 is used for T2 fitting, with two unknowns, $M_{xy}(0)$ and T2. A similar technique can be used to fit T2* when the FSE sequence is replaced with the GRE sequence.

Another technique for T2 mapping is to add a T2 preparation pulse (Fig. 1.18) before the SPGR acquisition. This method is less sensitive to FSE-associated artifacts (2,34) at the expense of some SNR. Different T2 weighting is enabled by varying TE of the T2 preparation pulse. Usually, two refocusing pulses are used instead of one due to the imperfectness of 180° pulses.

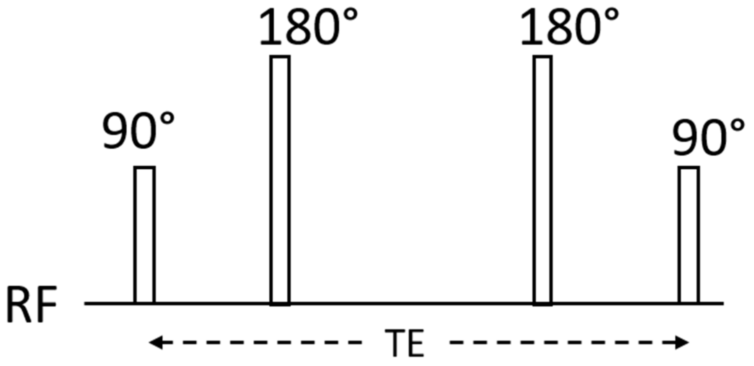

Figure 1.18: T2 preparation pulse.

For accurate relaxometry, the maximum IR or SR delay time and TE time are usually shorter than twice the relaxation times.

1.4.2 Velocity Mapping

MRI has the ability to measure velocity in arbitrary directions and thus enable the analysis of blood flow. This technique is based on the behavior of moving spins when they are exposed to velocity encoding (VE) gradients. Fig. 1.19 shows some typical VE and velocity compensated (VC) gradients. The phase accumulation of spins that are static in the gradient differs from those that move along the gradient direction. As a result, image pixels with moving spins and static spins have different phases when applying VE gradients. VC compensated gradients generate images with the same phase for moving and static spins. MRI techniques using the contrast of the phase to image flow are usually referred to as phase contrast (PC) MRI methods.

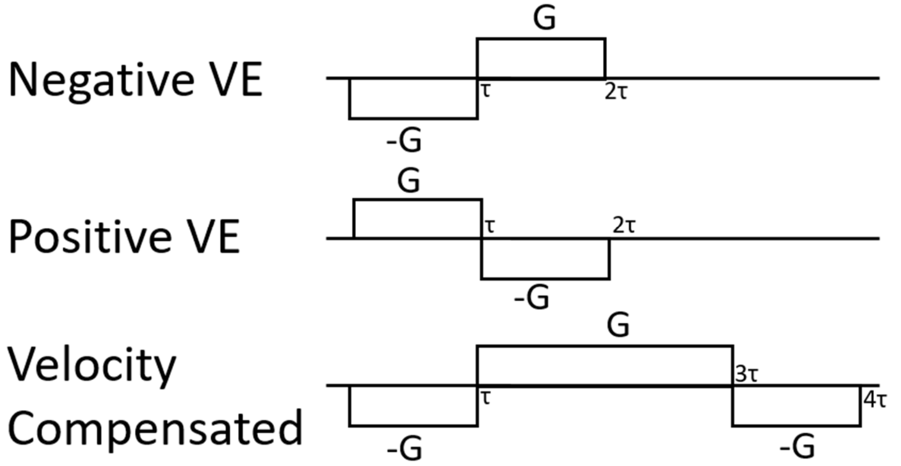

Figure 1.19: Velocity encoding and compensated gradients.

The effect of gradients on spin location, spin velocity, and acceleration on the phase of the signal depends on the high order symmetry properties of the applied VE gradients, which are characterized by their moments. Eq. 1.12 is an equation for the n^{th}-order moment. To encode velocity, n=1.

$$M_n = \int_t G t^n dt \qquad 1.12$$

For velocity encoding, $M_0 = 0$ and $M_1 \neq 0$ should be satisfied. For velocity compensated gradients, $M_0 = 0$ and $M_1 = 0$. The moments of positive VE gradients in Fig. 1.19 can be easily calculated: $\mathrm{M}_0 = 0, \mathrm{M}_1 = \mathrm{G}\tau^2$. Due to the symmetry of M_0 (Even) and M_1 (Odd), $\mathrm{M}_0 = 0, \mathrm{M}_1 = -\mathrm{G}\tau^2$ for negative VE gradient pulses. When VE gradients with both $M_0 = 0$ and $M_1 \neq 0$ are applied, no excess phase will be accumulated by static spins. Moving spins will accumulate phase proportional to M_1 and their speed v:

$$\Delta\Phi = 2\pi\gamma M_1 \mathrm{v} \qquad 1.13$$

Empirically, there is still a “background phase” that accumulates in static tissue, which will also add to moving spins. To calculate the absolute value of the velocity, the background phase has to be subtracted. This is realized by taking the difference in phase either between the positive and the negative VE data (two-sided) or between the positive VE and velocity compensated signal (one-sided).

Velocity mapping can be combined with dynamic MRI to observe velocity and flow changes within blood vessels during the cardiac cycle. In recent years, 4D flow has received increasing attention, with VE encoded in all 3 orthogonal spatial directions plus a time dimension.

1.4.3 Angiography and perfusion

Magnetic resonance angiography (MRA) and perfusion MRI can be contrast-enhanced (CE) with an exogenous contrast agent or non-contrast-enhanced (NCE) by adjusting MRI scan parameters alone. The basic idea to obtain MRA and perfusion images is similar, by changing the contrast between the flowing blood signal and the static background tissue. MRA is usually qualitative, while perfusion requires quantification. A lot of different quantitative metrics are provided in perfusion MRI, such as blood flow (BF), blood volume (BV), mean transit time (MTT), arterial input function (AIF), arterial transit time (ATT), and forward volumetric transfer constant (K^{trans}).

Gadolinium is a widely used MRI contrast agent that can significantly shorten T1 and boost blood signal in T1 weighted images, bringing enhanced blood contrast for CE-MRA and dynamic CE (DCE) perfusion studies. Exogenous gadolinium-based contrast agents can also shorten T2* by altering the local susceptibility. With intravascular administration, it lowers the blood signal thereby generating "dynamic susceptibility contrast (DSC) perfusion" images. With the DCE or DSC images, perfusion can be quantified by subtracting the image acquired before the ejection of the contrast agent. The usage of gadolinium-based contrast agents leads to safety concerns about gadolinium deposition. The use of some smaller particles such as Ferumoxides in CE MRA and perfusion has also been introduced in recent years.

NCE-MRA and NCE perfusion methods, on the other hand, are non-invasive and do not involve contrast agents, and therefore have received increasing technical and clinical interest these years.

Time-of-flight (TOF) is the most commonly used NCE-MRA technique. TOF is based on the SPGR sequence, which was introduced in section 1.3.1. Recall that the steady-state signal of SPGR is much lower than M^0. While the static tissue (background signal) reaches a low-level steady-state at reasonably high flip-angles (FAs), fresh blood flowing into the image volume is not in steady-state and may exhibit a much higher signal. Usually, the FA of a TOF sequence is larger than the Ernst angle (steady-state signal is maximized with the Ernst angle), so the background signal is suppressed, and the blood signal is enhanced. The TOF technique is usually implemented with a 3D image acquisition. Blood flowing into the image volume is unsaturated and shows a high signal but is gradually saturated by the SPGR sequence while passing. Therefore, the downstream blood in the image volume shows poor contrast, and the slab thickness of a TOF image is limited.

PC MRA makes use of the VE images introduced in section 1.4.2. While phase subtraction of two images with different VE provides velocity maps, the complex subtraction of the two images can be used for MRA. The complex subtraction of static tissue should ideally be zero because both the magnitude and phase are not sensitive to the VE gradient pulses. Flowing blood, in contrast, has a different phase and thus has a residual signal after subtraction. PC MRA shows promising results in many applications.

There are also some advanced techniques that are gaining interest such as: (i) ECG-gated 3D partial-Fourier FSE that subtracts systolic from diastolic images to evaluate the signal loss which is attributed to fast arterial blood flow (19); balanced SSFP that takes advantage of the intrinsic high T2/T1 contrast of arterial blood signal (35), and (iii) velocity-selective MRA that enhance blood contrast with velocity selection (36).

Arterial spin labeling (ASL) techniques are most widely used for NCE perfusion studies. The idea of these techniques is to invert the upstream arterial blood and quantify the amount of inverted blood as it perfuses downstream into the tissue. Saturation pulses are also used in some techniques but suffer from lower SNR. For quantification, both images with the inversion/saturation (label) and without inversion/saturation (control) upstream of flow are acquired from the downstream region in order to subtract out the background static tissue signal. An example of cerebral ASL is shown in Fig. 1.20. A labeling plane is placed on the neck to invert or saturate spins in the carotid arteries acquired in the inversion/saturation labeling scans. Brain images are acquired after a post-labeling delay (PLD), during which labeled blood spins perfuse into brain tissue.

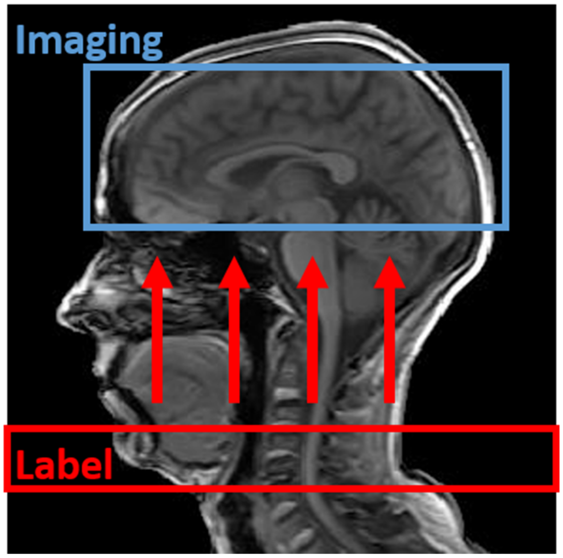

Figure 1.20: ASL labeling and imaging.

A drawback of the ASL technique is its low SNR compared to DCE and DSC. A compromise has to be made between a long PLD to allow more labeled blood (appearing as a bolus) to perfuse and a short PLD to mitigate the signal decrease due to T1 recovery. Empirically, multiple pairs of label and control scans are averaged to increase the SNR for ASL. Efforts have gone into increasing the SNR of ASL scans. Pulsed ASL (PASL) increases the labeled bolus by inverting a thick slab. Continuous ASL (CASL) and Pseudo-continuous ASL (PCASL) increase the labeling bolus by continuously or repeatedly inverting flowing spins in a period of time called the labeling duration (37,38). Velocity-selective ASL (VSASL) labels the blood spins directly within an organ rather than in large upstream vessels and requires shorter PLD for blood perfusion (39). More details about the implementation, quantification, and application of ASL scans can be found in the white paper providing consensus recommendations (40).

Chapter 2 Accelerating Whole-Heart 3D T2 Mapping: Impact of Undersampling Strategies and Reconstruction Techniques

2.1 Introduction

Recently, interest in parametric mapping of the relaxation times of myocardium has increased as techniques have improved and potential diagnostic value is uncovered and quantified (41–52). Most myocardial relaxometry techniques acquire multiple differentially-weighted images with varying contrast. Parametric maps are then reconstructed on a pixel-by-pixel basis, fitting data to two- or three-parameter models.

The acquisition of multiple images (in 2D) or image volumes (in 3D) for parametric mapping results in increased scan time. Clinical 2D single-shot imaging lacks k-space segmentation and utilizes relatively long diastolic acquisition windows which result in increased blurring due to motion as well as limited spatial resolution. Segmented 3D imaging (53–59) addresses these issues using shorter, narrower diastolic acquisition windows while providing much higher achievable spatial resolution. With these methods, image quality can be significantly improved although scan times are extended well beyond breath-holding and therefore require respiratory motion compensation. The increased scan time presents a barrier to the use of this approach in standard clinical workflows.

A typical 3D whole heart parametric mapping acquisition achieving an in-plane resolution of 1.5 mm and through-plane resolution of 5-10 mm (53–59) can span more than 10 min. With parallel imaging or sparsity driven reconstruction strategies, which take advantage of redundancies between individual coil images or across different contrasts, scan time can be significantly reduced, minimizing potential bulk motion artifacts or, conversely, increasing image resolution for a given scan duration. Clinically prevalent 2D single-shot imaging already uses parallel imaging to achieve high in-plane acceleration rates (typically ≥3) where each image must be acquired with accurate timing and within a single diastolic phase (42,44,47). Moreover, 3D imaging is amenable to higher acceleration rates due to two phase-encoding dimensions and a higher number of pixels contained in the 3D volume, in addition to the inherently increased signal-to-noise ratio (SNR) produced by slab selection. Hence, incorporating parallel imaging and sparsity-driven reconstruction into 3D parametric mapping presents a logical approach to reducing overall scan duration as is needed to facilitate the translation of 3D techniques into clinical practice.

There are many combinations of undersampling strategies and reconstruction techniques to accelerate image acquisition that integrate parallel imaging (60–62) or go beyond (60,61,63,64). The effects of these various approaches on the parametric maps are unclear. In this chapter, we explore the use of several likely candidate techniques for acceleration of multi-volume segmented 3D whole-heart T2 Mapping (65,61,62). We consider standard image-per-image reconstructions as well as joint reconstructions driven by either sparsity or a model describing the expected behavior of exponential decay. We focus both on their effects on the reconstructed images as well as on parametric maps, including the global distribution of T2 values throughout the whole heart and individual pixel-by-pixel changes in T2. The comparison amongst techniques is performed retrospectively on fully-sampled data acquired in naïve swine and normal human subjects. In addition, data from one swine with an acute myocardial infarction (MI) that demonstrated a significant elevation of T2, is studied to determine the effects of acceleration on T2-based segmentation of the injury.

2.2 Methods

Imaging studies were performed at 3T (Achieva TX, Philips Healthcare, Best, Netherlands) using a 32-channel phased array. Animal studies were approved by the institutional animal care and use committee, and the human studies were approved by the local institutional review board. Written informed consent was obtained from all subjects. Image reconstruction and processing, and statistical analyses were implemented in MATLAB (MathWorks, Natick, MA, USA).

2.2.1 Data Acquisition: Fully Sampled Whole Heart 3D T2 Mapping

The pulse sequence used for the acquisition of fully sampled 3D T2 maps is detailed by Ding et al. (53). The feasibility of this approach has been validated on phantoms, swine, and human subjects (53). Briefly, three or four saturation-prepared volumes with a variety of T2-weightings imparted by a T2-preparation (T2-prep) sequence (66) were acquired in an interleaved manner. The resulting image volumes are co-localized and suitable for pixel-by-pixel parametric fitting.

Whole-heart T2 mapping data were acquired using 3D Cartesian sampling with a 5/8 fractional readout segmented radiofrequency (RF)-spoiled gradient echo sequence. The following include typical imaging parameters: acquired resolution = 1.25×1.25×5.0mm^3, T2-prep echo times (TE) = 0, 25, 35, 45ms, repetition time/acquisition TE = 4.0/1.2ms, flip angle = 18°, 2.5 mm respiratory navigator acceptance window, ECG-triggered mid-diastolic acquisition, 12-18 readouts per heartbeat. Both volume localized B_{1+} and B_0 shimming (67,68) were performed to compensate for field inhomogeneities. Although fractional readouts were used, the datasets were regarded as fully-sampled because only undersampling in the phase-encoding directions was tested.

A total of 4 swine and 8 normal human subjects (1 male, 43±13 years old) were imaged. Three animals were imaged in a naïve state, and one was imaged 3 days after MI induced by a 2-hr balloon occlusion of the left anterior descending coronary artery. The infarction resulted in significant edema. For the swine with the infarction, the whole-heart T2 mapping data were acquired using the same methods as above but only 3 T2-prep TEs 0, 25, and 45ms.

2.2.2 Three Retrospective Undersampling Patterns

All raw data were retrospectively undersampled using three different patterns (Fig. 2.1). An auto-calibration signal (ACS) composed of the 16×16 central $k_y \times k_z$ lines was kept fully sampled and an elliptical k-space shutter was applied to all patterns. The remaining k-space was undersampled by an outer k-space reduction factor (ORF) varying from 2-8 (Fig. 2.1).

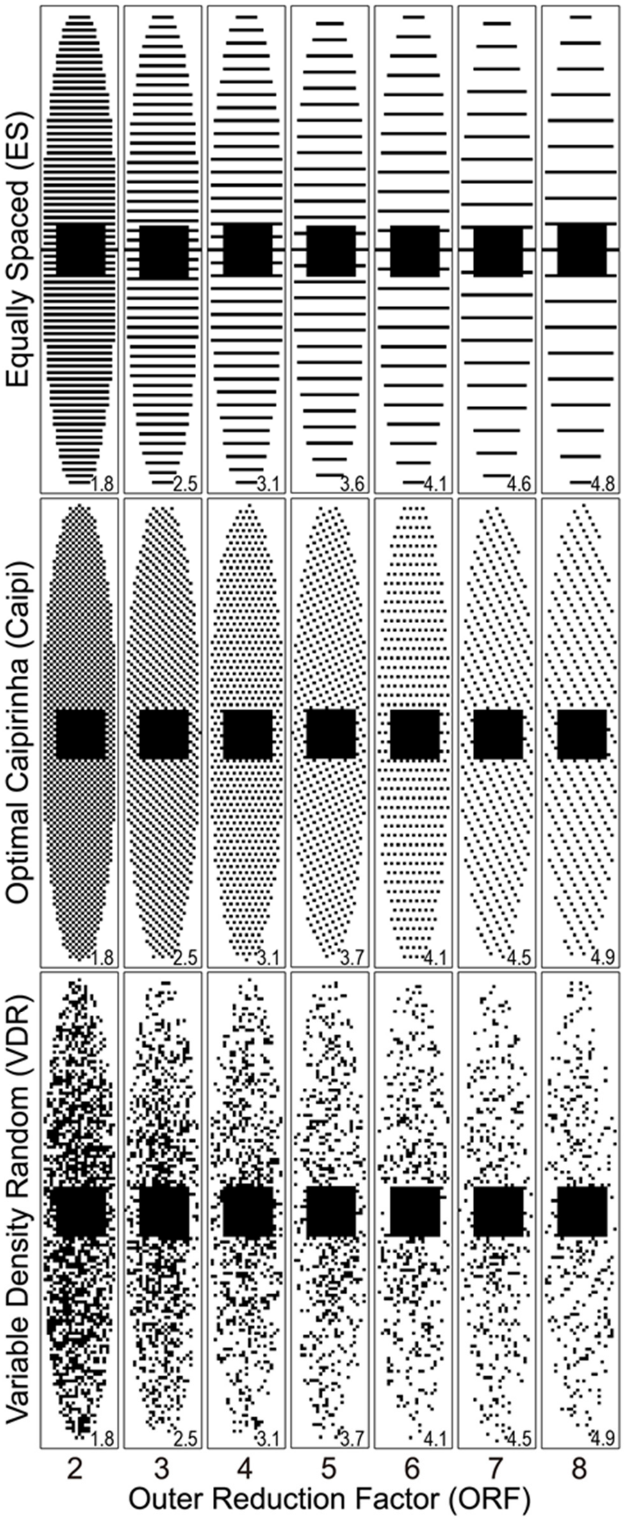

Figure 2.1: Sampling patterns in ky-kz plane used for the variety of reconstruction techniques tested. The net reduction rate (R_{net}), shown in the bottom corner of each panel, is reduced relative to the outer reduction factor (ORF) due to the complete sampling of the center of k-space. Six different VDR sampling patterns were tested (only one shown).

The net reduction factor (R_{net}) is defined as the ratio between the number of sampled k-space lines and the total number of k-space lines in the elliptical window. R_{net} is shown in the bottom right corner of each pattern in Fig. 2.1. The ACS not only preserves image contrast but also provides low resolution images for sensitivity map estimation (69). The sensitivity map was calculated by a root-of-the-sum-of-the-square approach (70). The size of the ACS was chosen empirically as a compromise between the quality of the calculated sensitivity maps and R_{net}.

Three different undersampling patterns were tested: equally spaced (ES) sampling, optimized 3D controlled aliasing in parallel imaging results in higher acceleration (Caipi) (71–73), and variable density random (VDR) sampling (63,74–76).

First, the ES sampling pattern (Fig. 2.1, top row) is typically utilized in Cartesian sensitivity encoding (SENSE) (70) and generalized autocalibrating partially parallel acquisitions (GRAPPA) (77) and is the pattern most widely used in the clinical setting. The same undersampling pattern was applied to all image volumes with different T2-prep TEs.

Second, the Caipi sampling pattern (Fig. 2.1. middle row) depends on the ORF (71) and carefully selects the sampling pattern to minimize undersampling-induced aliasing in both phase-encoding and parametric dimensions based on the point spread function (71–73). The optimal k-space temporal sampling patterns introduced in (71) were adopted. The sampling patterns for T2-prep images with larger TE were shifted by a pre-designed distance described in (71) compared to the image without T2-prep. This pre-designed distance is periodic in ORF so if the ORF was greater than the number of TEs, only the first 3 or 4 shifts were applied.

Finally, the VDR sampling pattern causes incoherent aliasing (78) and is suitable for compressed sensing or sparsity-driven reconstruction (63). In this work, 2D VDR sampling patterns were applied (76). K-space lines were chosen according to a Gaussian probability density function (mean=0, standard deviation = 0.5 × maximum k-space radius) with respect to the distance from the k-space center. N unrepeated k-space lines outside the fully sampled central ACS k-space were selected, where N is the number of acquired k-space lines in the Caipi pattern leading to the same ORF. Therefore, VDR patterns have identical R_{net} as Caipi patterns for each ORF. These patterns were repeated 6 times independently to better characterize the outcomes given the random nature of VDR. The same undersampling pattern was applied to all image volumes with different T2-prep TEs for VDR sampling.

2.2.3 Three Image Reconstruction Approaches

Three different reconstruction approaches were quantitatively compared in this work. All three utilize iterative reconstruction (65,79) and jointly reconstruct all volumes with different T2-prep weightings. The second and third approaches include regularization terms to reinforce similarity among volumes with different T2 weightings, based either on image structure or on exponential signal decay, and are expected to improve image quality (80).

The first approach, ‘multi-volume SENSE,’ uses conjugated gradient based iterative SENSE optimization (65), which is able to restore images from arbitrarily undersampled k-space. Compared to traditional iterative SENSE where each T2-prep weighted volume is reconstructed separately, here all volumes are combined and reconstructed jointly, which can be expressed as a minimization problem with a cost function of:

$$\hat{I}_{SENSE} = \underset{I}{\operatorname{argmin}}(\|DEI - k\|_2^2), \qquad 2.1$$

where I and $\hat{I}_{SENSE}$ are intermediate and final estimated multi-volume images, respectively, D is a diagonal undersampling operator, E is the encoding matrix, and k is the undersampled raw k-space data.

The second approach, ‘joint-sparsity SENSE’, incorporates joint total variation constraint (61) as a sparsity constraint for regularization that enforces similarity of the edges of the images with different T2-prep TEs to regularize the conjugate gradient optimization. As is the case with most parametric mapping, the differentially-weighted volumes share a large amount of structural information and differ primarily in contrast. Joint-sparsity SENSE should improve reconstruction performance by further reinforcing those common structural details. The cost function for joint-sparsity SENSE is:

$$\hat{I}_{JS-SENSE} = \underset{I}{\operatorname{argmin}}\left\{\|DEI - k\|_2^2 + \lambda\|I\|_{JTV}\right\}, \qquad 2.2$$

where the regularization parameter λ is a weight for the joint total variation across the parameter dimension (i.e. differentially-weighted image volumes), fixed at 0.1. We define joint total variation (62,81,82) as follows:

$$\|I\|_{JTV} = \sum_{\vec{r}} \sqrt{\sum_{p} \left(\left(\nabla_x I(\vec{r}, p) \right)^2 + \left(\nabla_y I(\vec{r}, p) \right)^2 + \left(\nabla_z I(\vec{r}, p) \right)^2 \right)} \qquad 2.3$$

where $\vec{r} = (x, y, z)$ is the location of the voxels, and *x*, *y*, and *z* are the pixel coordinate indexes in image space, $p \in \{1..\#\text{weighted images}\}$ indexes the parameter space, i.e., the differentially weighted images, and ∇_x, ∇_y and ∇_z correspond to the discrete first-order partial derivative in *x*, *y,* and *z*, respectively. Note that with this definition of a joint l_1 norm, the existence of large coefficients in one of the differentially-weighted images protects the coefficients in the rest of the images from being suppressed by the non-linear reconstruction (81).

The third approach, 'model-based SENSE,' applied a T2-decay fitting error as a regularization constraint (62). This fitting error is defined as the $l_{1,2}$ norm of the difference between reconstructed image intensities and a fitted exponential decay curve (I_{fit}) using the pixel-by-pixel natural log-transformed linear regression along the parametric dimension. This regularization enforces the T2 decay behavior of the T2-prepared images. I_{fit} were estimated from the parameters obtained from the intermediate image *I*. The cost function is expressed as:

$$\hat{I}_{MB-SENSE} = \underset{I}{\operatorname{argmin}}\left(\|DEI - k\|_2^2 + \lambda\left\|I - I_{fit}\right\|_{1,2}\right). \qquad 2.4$$

The $l_{1,2}$ norm of the parametric fitting error $\left\|I - I_{fit}\right\|_{1,2}$ is calculated as

$$\left\|I - I_{fit}\right\|_{1,2} = \sqrt{\Sigma_{\vec{r}}\left(\Sigma_p\left|I(\vec{r},p) - I_{fit}(\vec{r},p)\right|\right)^2}. \qquad 2.5$$

The projected gradients model consistency condition in robust (l_1) fashion algorithm described in (62), which is a Projection onto Convex Sets (POCS) (79) based iterative reconstruction algorithm, was implemented with an updated weight (λ) of 0.5 to balance SENSE and T2 fitting error. I_{fit} is synthesized form the log-transformed linear regression by:

$$I_{fit}(\vec{r},p) = \exp\left(\begin{bmatrix}1 & -TE_p\end{bmatrix}\begin{bmatrix}log\left(\overline{A_0}(\vec{r})\right)\\ \overline{R2}(\vec{r})\end{bmatrix}\right) \qquad 2.6$$

where A_0 is the image intensity without T2 weighting, and $R2 = 1/T2$ is the spin-spin relaxation rate. For any voxel $\vec{r}$, estimates $\overline{A_0}$ and $\overline{R2}$ are generated from linear regression of the image intensities as described in (53).

For comparison, two reference reconstructions were used: First, after pre-whitening and homodyne processing to compensate for partial echo sampling (83), the fully sampled data was reconstructed by direct inverse fast Fourier transform with a root-of-the-sum-of-the-squares coil combination to generate the ‘Reference’ reconstruction. Second, as an additional reference, standard SENSE reconstruction (70) using ES undersampling was applied separately to each T2-prep weighted image volume and referred to as ‘Traditional SENSE.’ The two references were used to determine the deterioration of the parametric maps with respect to reconstructions using original fully-sampled data as well as those obtained from undersampled data processed using a well-understood and readily available linear reconstruction approach.

2.2.4 Image Analysis

For each swine and human dataset, the left ventricular (LV) myocardium was manually segmented on the fully-sampled reference to generate a 3D region of interest (ROI) by an observer with >10 years' experience with cardiac MRI. Root-mean-square errors (RMSE) relative to the fully-sampled reference were calculated via pixel-wise comparison within the ROI. The RMSE was calculated for both reconstructed images and the T2 maps.

For naïve swine and human subject data, we assumed uniform T2 values in the LV and spatially averaged the T2 values in the ROI and calculated the corresponding standard deviation (SD) as a measure of precision. The bias in T2, the difference of the average T2 relative to that of the fully sampled reference data, was calculated to examine the potential loss of accuracy in T2.

For the swine with acute MI, an Otsu's threshold (84) was chosen to segment pixels into normal and edematous myocardium. The thresholds were separately computed from each reconstructed T2 map. The intersection-over-union index, i.e., the Jaccard index, was calculated as a measure of correspondence between normal T2 pixels and edematous T2 pixels ranging from 0 (no match) to 1 (all pixels in ROI match). This was used to examine the effects of acceleration rate on the accuracy of tissue characterization with parametric mapping.

While comparing T2 maps, voxels within the ROI with T2>100 or T2<15 were considered as unsuccessfully recovered from the reconstruction and excluded. These voxels were counted and the percentage relative to the total number of voxels in the ROI was determined for each individual.

To compare the most successful reconstructions, the Wilcoxson signed rank test was used for all 4 metrics as a function of ORF (significance at $p<0.0125$ after modified Bonferroni correction).

2.3 Results

The average scan time of fully-sampled data acquired from the 3 naïve swine and 8 normal human subjects were 6.6±1.8 min. R_{net} of the retrospectively undersampled data using ES, Caipi and VDR sampling patterns range from 1.8 to 4.9 when ORF was varied from 2 to 8 (Fig. 2.1). The net reduction factors further varied among subjects due to differences in the prescribed field-of-view and hence, matrix size.

Fig. 2.2 shows one slice of the reconstructed T2-weighted images (T2-prep TE=45ms) and the T2 maps of a representative normal human subject. All sampling patterns and reconstruction methods are demonstrated with the full range of ORF from 2-8 together with the fully sampled reference.

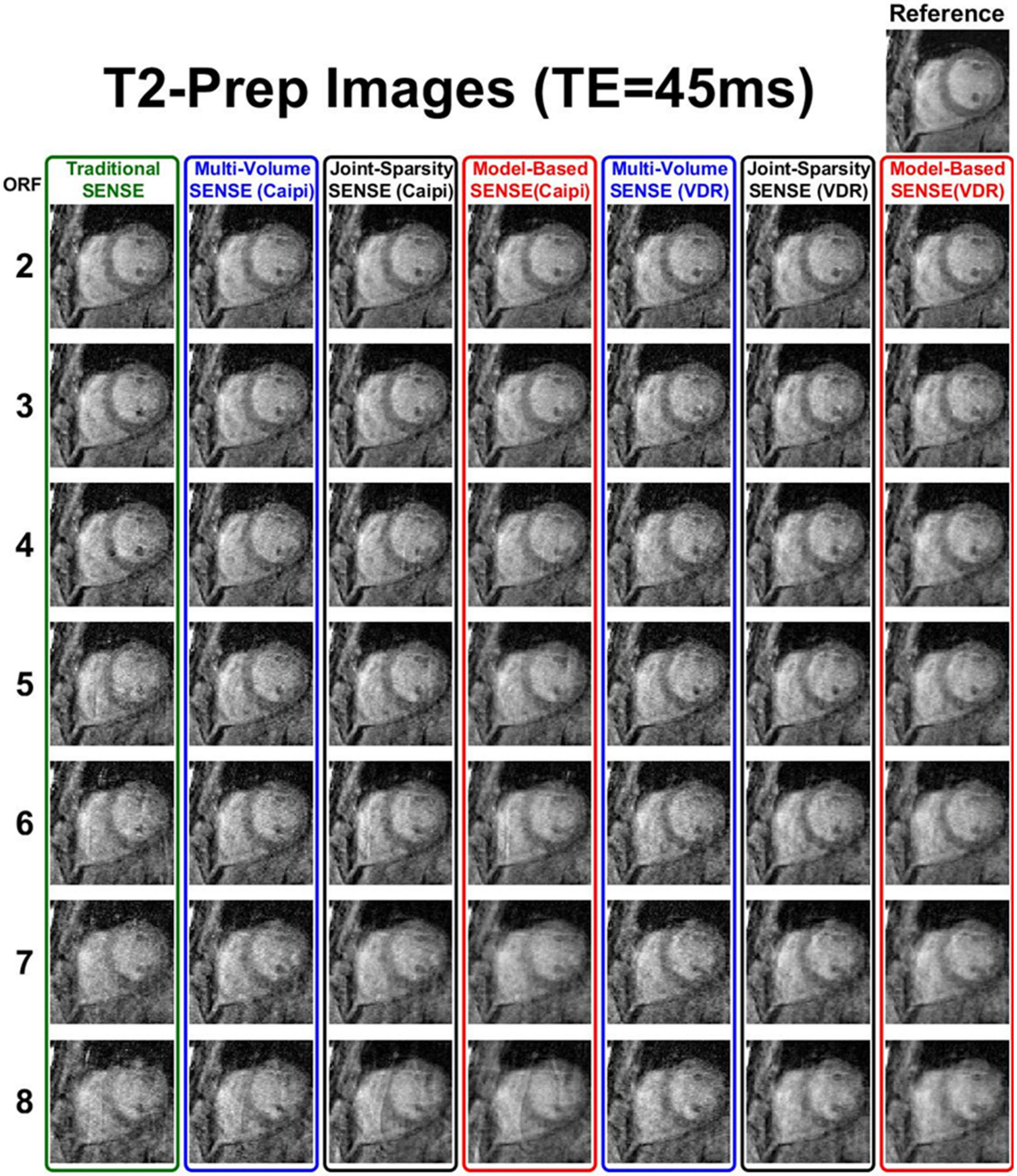

Continue on next page

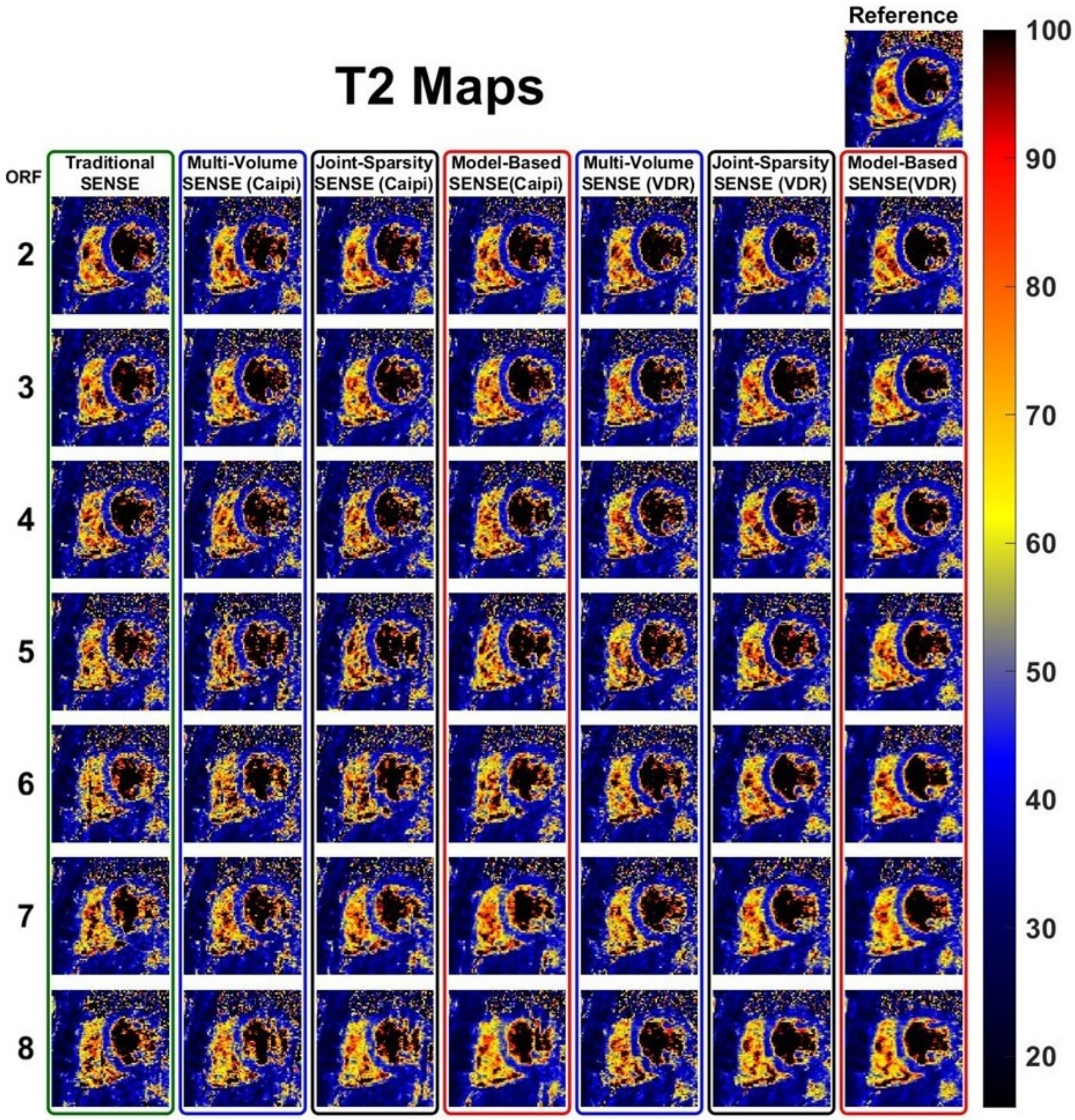

Figure 2.2: T2-weighted images and T2 maps of a normal human with ORF=2-8 and all reconstruction approaches. Comparison of images with T2-Prep TE of 45 ms (left, grayscale) and T2 maps (right, color map) obtained from a normal human subject for ORF=2-8 and all sampling and reconstruction approaches. As ORF increases (top to bottom), images from all approaches appear noisier and blurrier, and images from traditional SENSE and Caipi sampling patterns additionally suffer from ghosting artifacts.

At ORF=2 and 3, the reconstructed images and T2 maps are similar to the reference. As ORF increased to 4-6, some aliasing artifacts can be observed in the T2-weighted images with traditional SENSE and Caipi based reconstructions and some blurring can be observed in VDR based reconstructions. The T2 values of the inferior septal and posterior part of the LV wall using the joint-sparsity SENSE and the model-based SENSE with VDR sampling are better preserved than other methods. When ORF is high (7 and 8), both artifacts and blurring can be observed in the T2-weighted images of all methods and the artifacts and blurring in the T2-weighted images are much stronger. T2 maps using joint-sparsity SENSE and the model-based SENSE with VDR sampling are less corrupted than other methods although errors can be observed in septal and posterior part of the LV wall. The T2 maps with ORF>4 (R_{net} larger than 3) exhibit significant artifacts compared to the fully sampled reference, therefore, the following results focus on ORF=2, 3, and 4.

Fig. 2.3 demonstrates one image of the T2-prepared volume with the longest T2-Prep TE=45 ms (Figs. 2.3A,C,E) and, hence, the lowest SNR of the differentially-weighted volumes, and the corresponding T2 maps of a naïve swine dataset (Figs. 2.3B,D,F). At ORF=2 (Figs. 2.3A,B), all T2-weighted images are well preserved. The error maps of traditional SENSE and all other reconstruction methods sampled with the VDR pattern are slightly higher in intensity (larger error) compared to those obtained with Caipi undersampling. Model-based SENSE reconstruction with Caipi undersampling shows the lowest error intensity. The T2 errors are slightly larger in the posterior wall of the LV in all sampling patterns and reconstruction methods. Model-based SENSE has the lowest error in T2 for both Caipi and VDR sampling. At ORF=3 (Figs. 2.3C,D), the reconstructions are similar to ORF=2 though with a slight increase in errors in both images and maps.

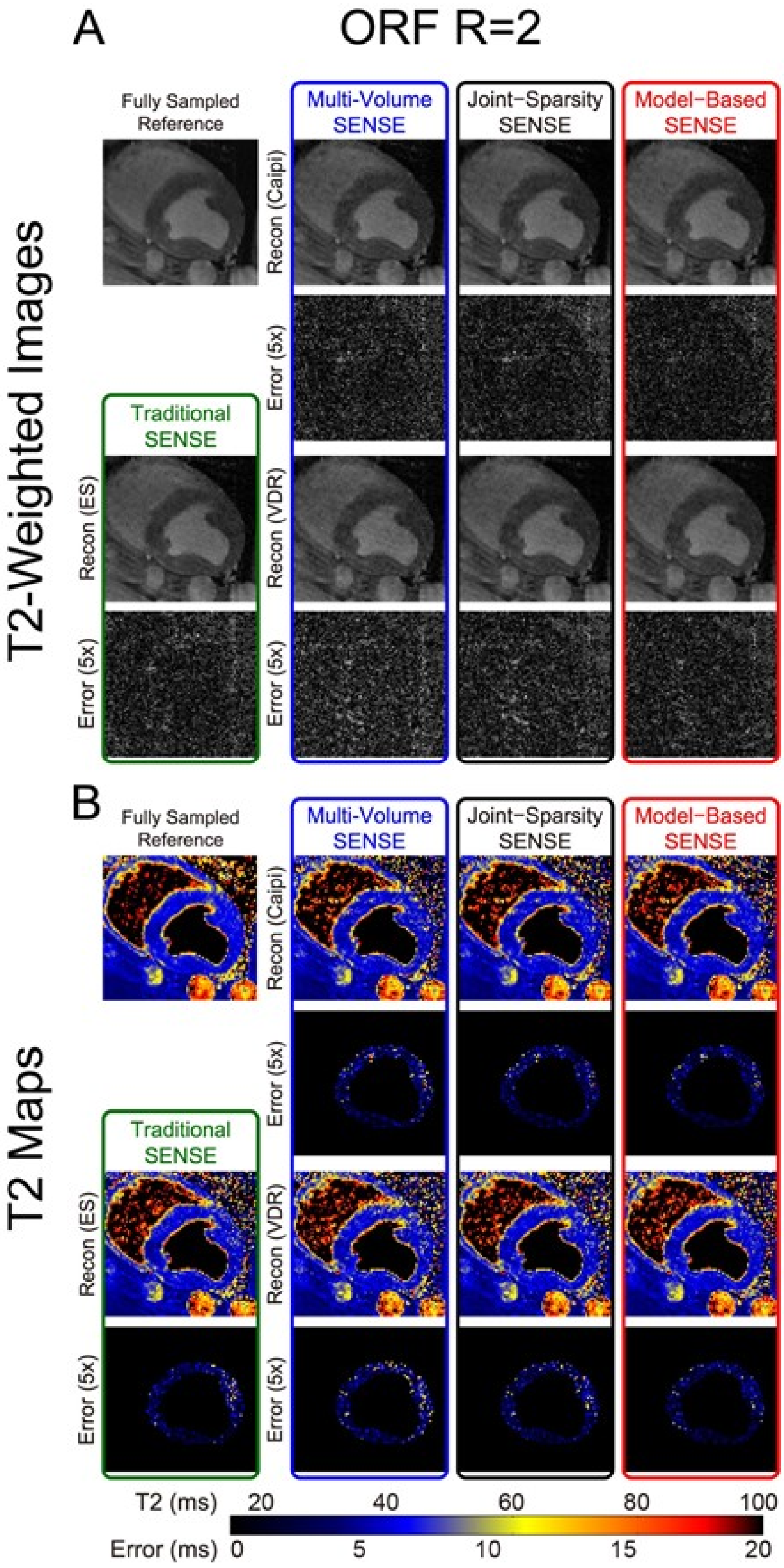

Continue on the next page

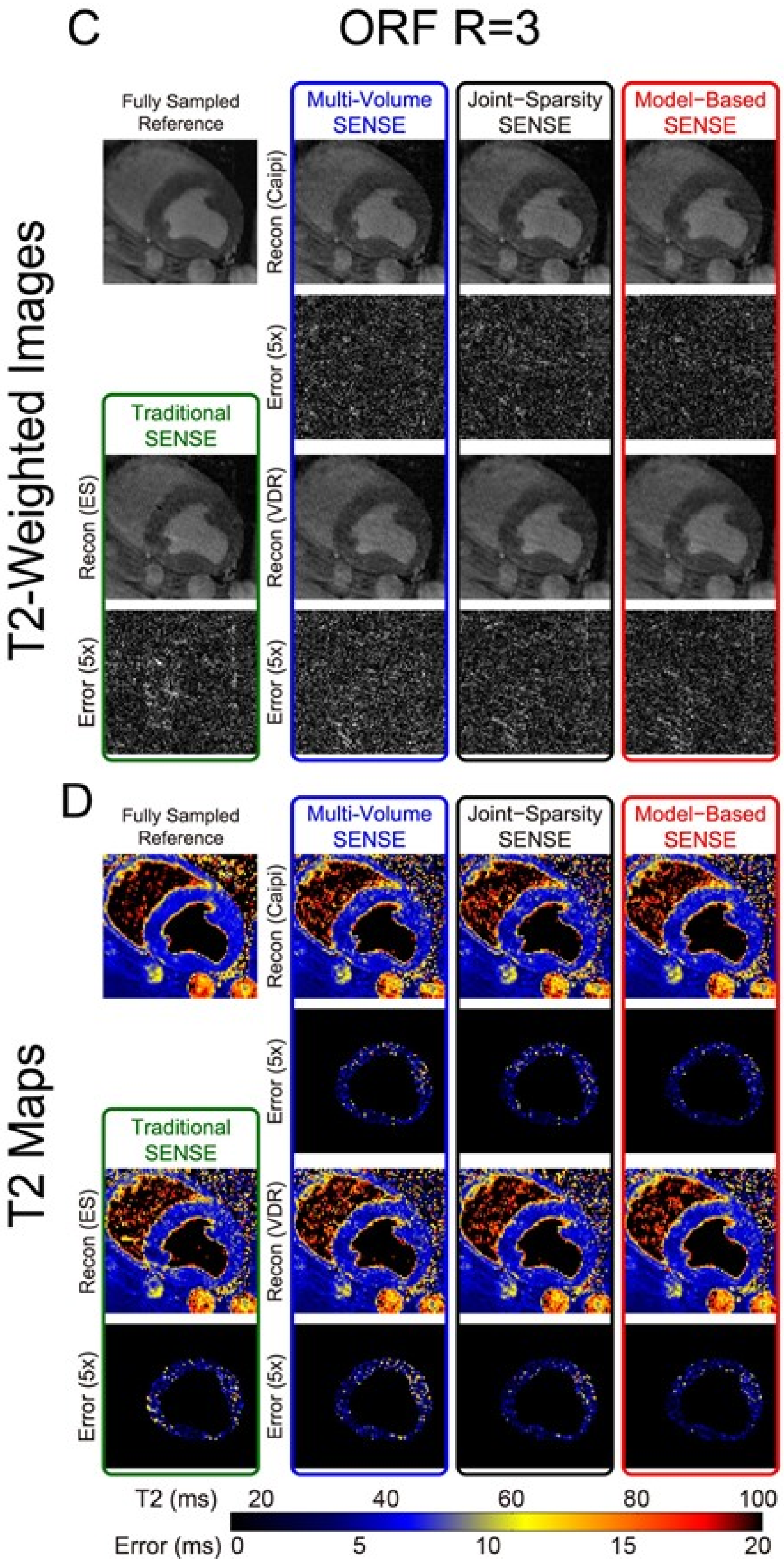

Continue on the next page

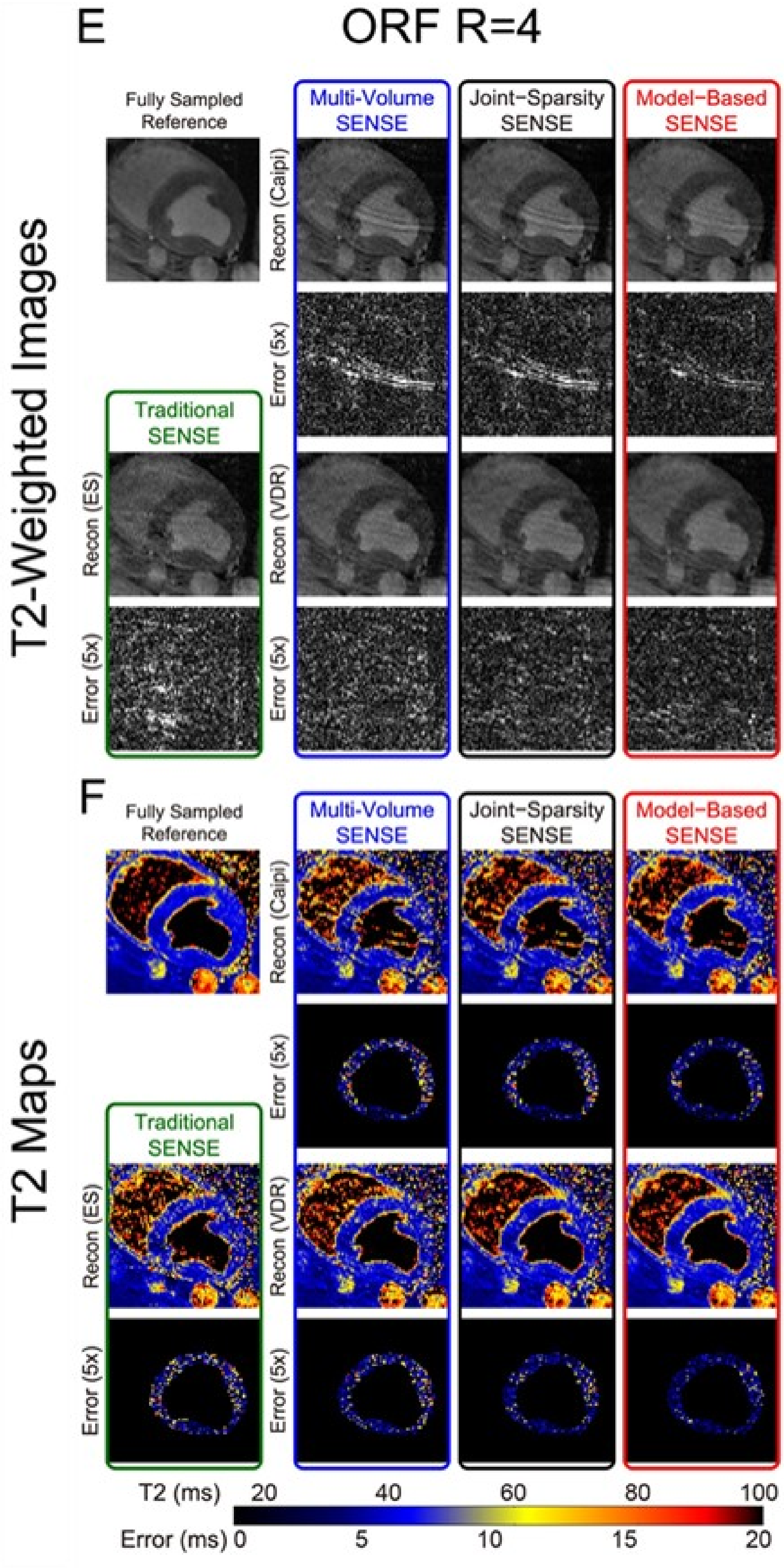

Figure 2.3: T2-weighted images and T2 maps of a normal swine with ORF=2-4 and all reconstruction approaches. Comparison of images with T2-Prep TE of 45 ms (A, C, and E) and T2 maps (B, D, and F) obtained from normal swine using ORF= 2 (A,B), 3 (C,D), and 4 (E,F) for all sampling and reconstruction approaches. Errors maps are multiplied by 5 for increased visibility, and T2 map error maps are masked with the segmented left ventricular ROI. As ORF increases (left to right), traditional volume-by-volume SENSE reconstruction begins to fail. At ORF=4, images based on the Caipi sampling pattern suffer from significant ghosting artifacts, which are reduced with VDR sampling (E), and T2 maps based on VDR sampling show lower T2 error (F).

For ORF=4 (Figs. 2.3E,F), strong aliasing artifacts in images sampled with the Caipi pattern appear with concordant errors reflected in the T2 maps. VDR sampling does not exhibit these aliasing artifacts. At ORF=4, images from ES sampling reconstructed with the traditional SENSE method also have increased errors and g-factor map based noise. Fig. 2.3F shows that T2 maps based on VDR sampling pattern combined with model-based SENSE have the lowest errors in the LV, especially in septal and posterior wall areas.

Fig. 2.4 plots the mean and SD (error bars) of T2 for the entire LV corresponding to the swine data shown in Fig. 2.3. The black and green lines indicate the mean and SD of the two reference methods. The bias remains low (<1.1 ms) for all methods and ORF=2-4. The SD of traditional SENSE acquired with ES pattern (shown in green) increases by 52% from 5.2 ms to 7.9 ms for ORF 2 to 4, respectively, as compared to 3.6 ms of the fully sampled reference. The SD of multi-volume SENSE is similar to that of traditional SENSE for both Caipi and VDR sampling patterns. The SD is reduced for Caipi sampling and further improved for VDR sampling for both joint-sparsity and model-based SENSE. The lowest SD and the highest precision are achieved by combining VDR sampling and model-based SENSE reconstruction for all 3 acceleration factors.

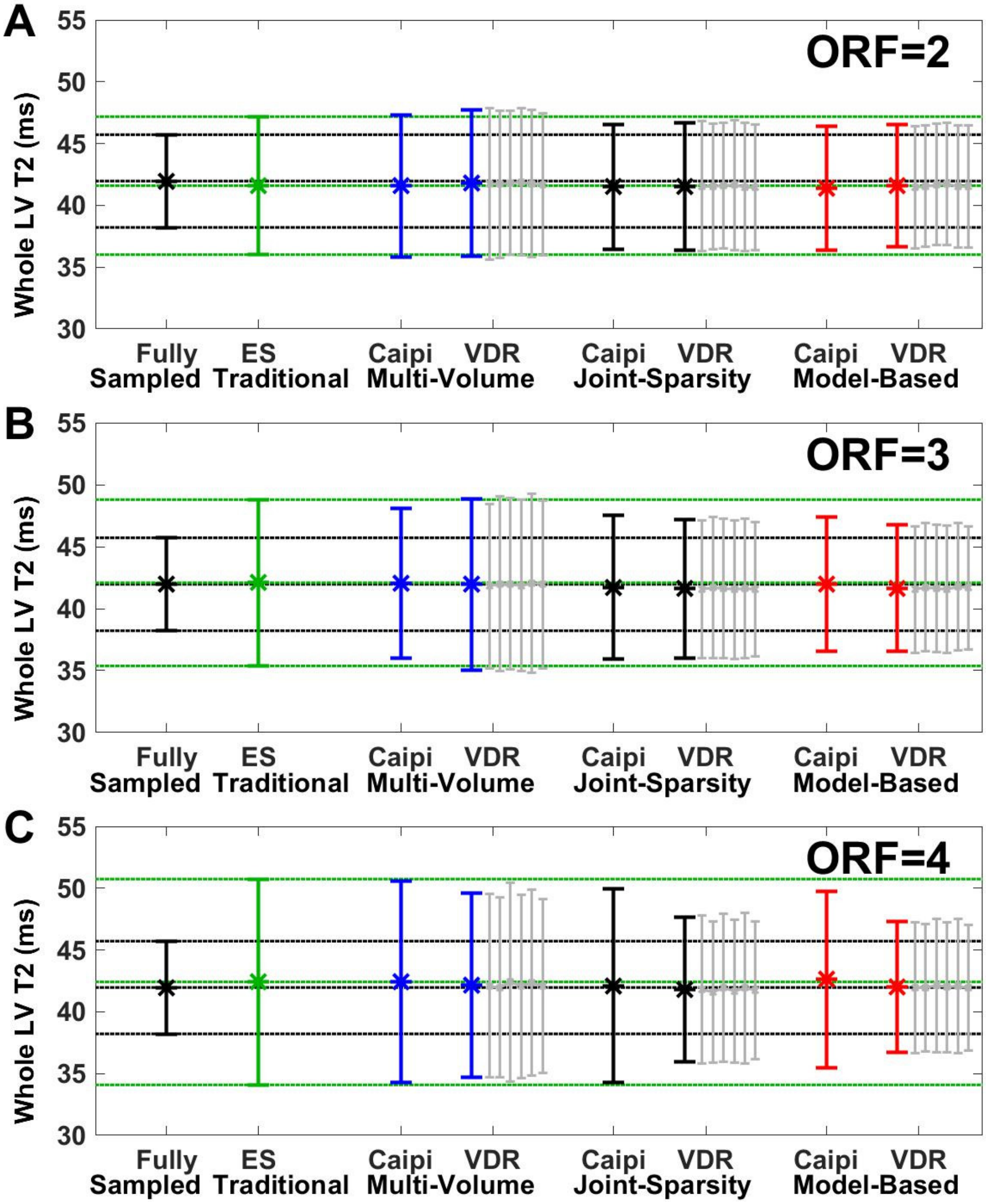

Figure 2.4: T2 error bars of different reconstruction approaches compared to references in whole-heart LV with ORF=2-4. Comparison of the effects of sampling patterns and reconstruction approaches on whole-heart LV T2 mean and SD (error bars) of the swine shown in Fig. 2.3 with ORF=2 (A), 3 (B), and 4 (C). Reconstruction of fully sampled data (black) is used as the reference, with mean and standard deviation extended throughout the plots (black dotted lines). Traditional SENSE (green) represents a secondary reference with independent volume-by-volume processing, which demonstrates the results of acceleration as readily available online on scanners, with mean and SD extended throughout the plots (green dotted lines). Variable density random (VDR) sampling was repeated six times (gray lines) for each method and results were averaged. Deviation from the mean T2 of the fully sampled reference represents bias and SD represents precision.

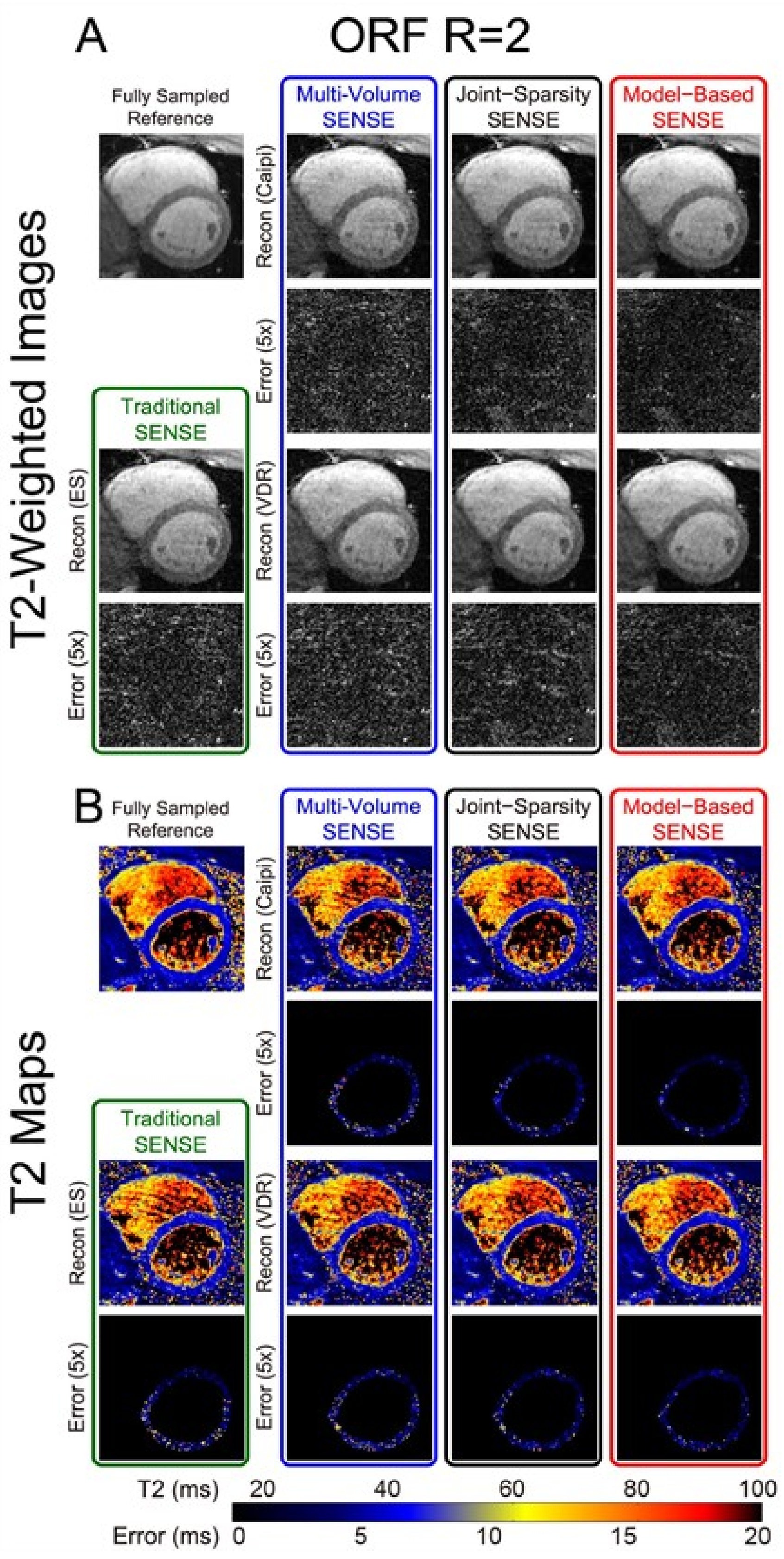

Continue on the next page

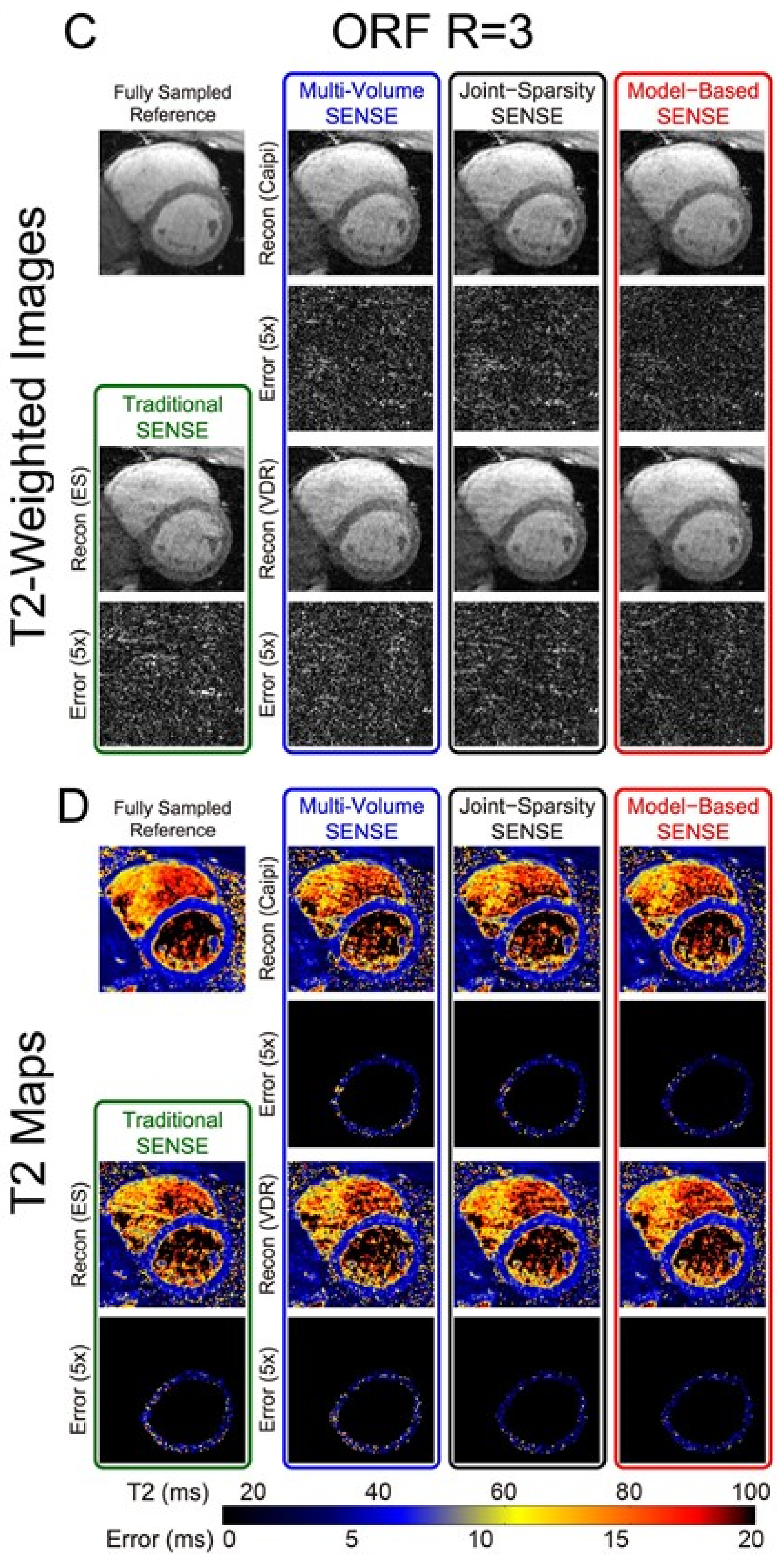

Continue on the next page

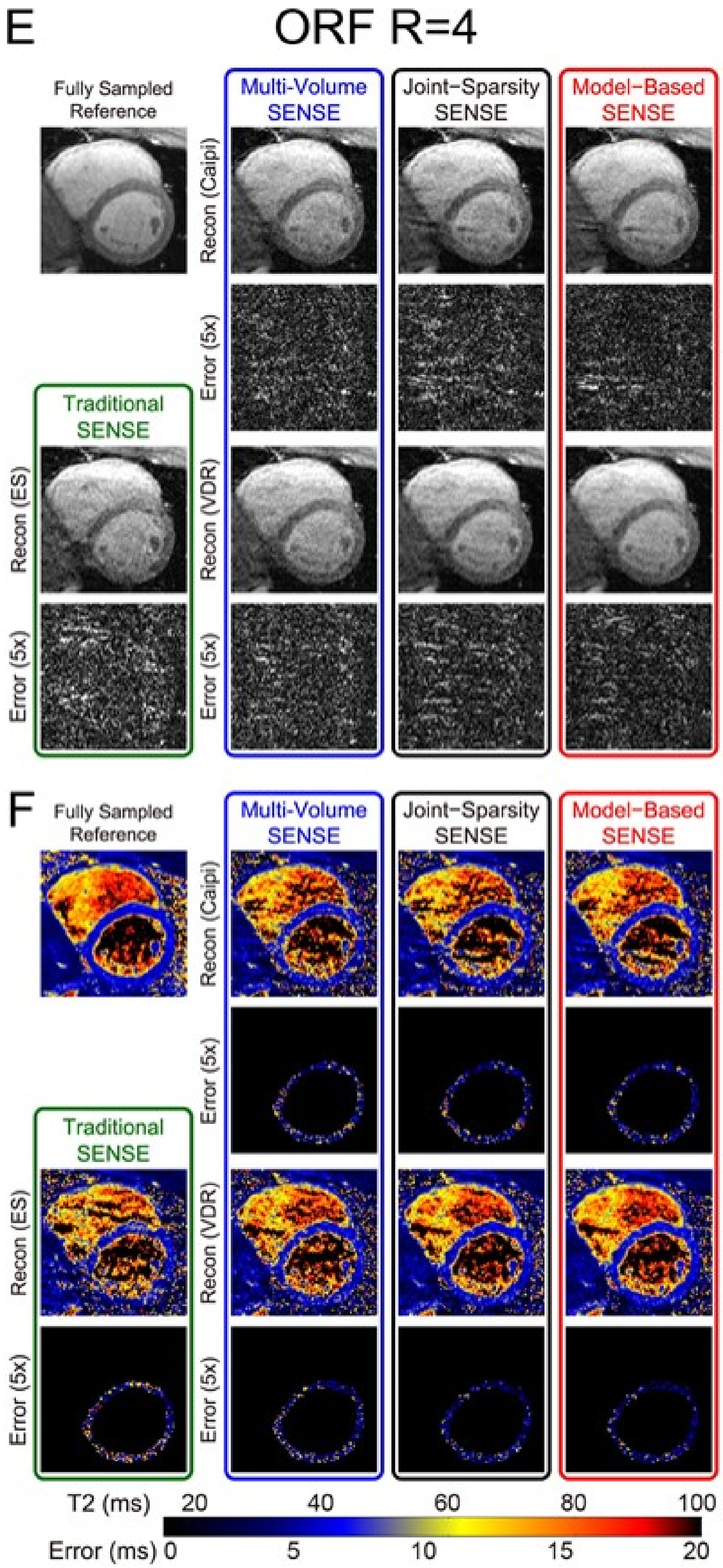

Figure 2.5: T2-weighted images and T2 maps of a normal human with ORF=2-4 and all reconstruction approaches. Comparison of images with T2-Prep TE of 45 ms (A,C and E) and T2 maps (B, D and F) obtained from normal human subject (different from the case in Fig. 2.2) using ORF= 2(A,B) ,3(C,D) and 4(E,F) for all sampling and reconstruction approaches. Error maps are multiplied by 5 for increased visibility, and T2 map error maps are masked with the segmented left ventricular ROI. As ORF increases (left to right), artifacts become apparent for all methods, most severely for traditional SENSE and least for VDR sampling.

Fig. 2.5 shows one image of the volume with T2-Prep TE=45 ms and the corresponding T2 maps of a human subject dataset (different from that in Fig. 2.2). With ORF=2, all approaches obtained good image quality. Similar to the results shown in Fig. 2.3, the error of T2-weighted images sampled with the VDR pattern is slightly higher compared to those sampled with the Caipi pattern. T2 maps shown in Fig. 2.5B have comparable error levels. The behavior of images and T2 maps at ORF=3 (Figs. 2.5C and 2.5D) is similar to ORF=2 except for a minor increase in errors. For ORF=4, aliasing artifacts can be observed in images (Fig. 2.5E) undersampled with Caipi pattern and less so with VDR pattern. Similar to Fig. 2.3, the combination of VDR and joint-sparsity or model-based SENSE reconstruction shows the lowest errors in T2 maps (Fig. 2.5F).

Fig 2.6 demonstrates the mean and SD (error bars) of T2 values of the entire LV corresponding to the data of the human subject shown in Fig 2.5. Again, results from human data are consistent with those from swine. The bias is <1.7 ms for all methods and ORF=2-4. The SD of traditional SENSE acquired with ES pattern (shown in green) increases by 51% (6.3 ms to 9.5 ms) for ORF 2 to 4, respectively, compared to 3.3 ms of the fully sampled reference. The SD of multi-volume SENSE is similar to that of traditional SENSE for both Caipi and VD sampling patterns for ORF 2 and 3. At ORF=4, the SD of multi-volume SENSE (8.1 ms) is lower by 15% than the SD of traditional SENSE (9.5 ms). The SD of the T2 values estimated from the combination of VDR sampling patterns and model-based SENSE reconstruction (4.6 ms, 4.8 ms, and 5.1 ms for ORF=2, 3, and 4, respectively) are smallest, followed by the combination of VDR sampling patterns and joint-sparsity SENSE reconstruction (5.0 ms, 5.4 ms, and 5.8 ms for ORF=2,3, and 4, respectively).

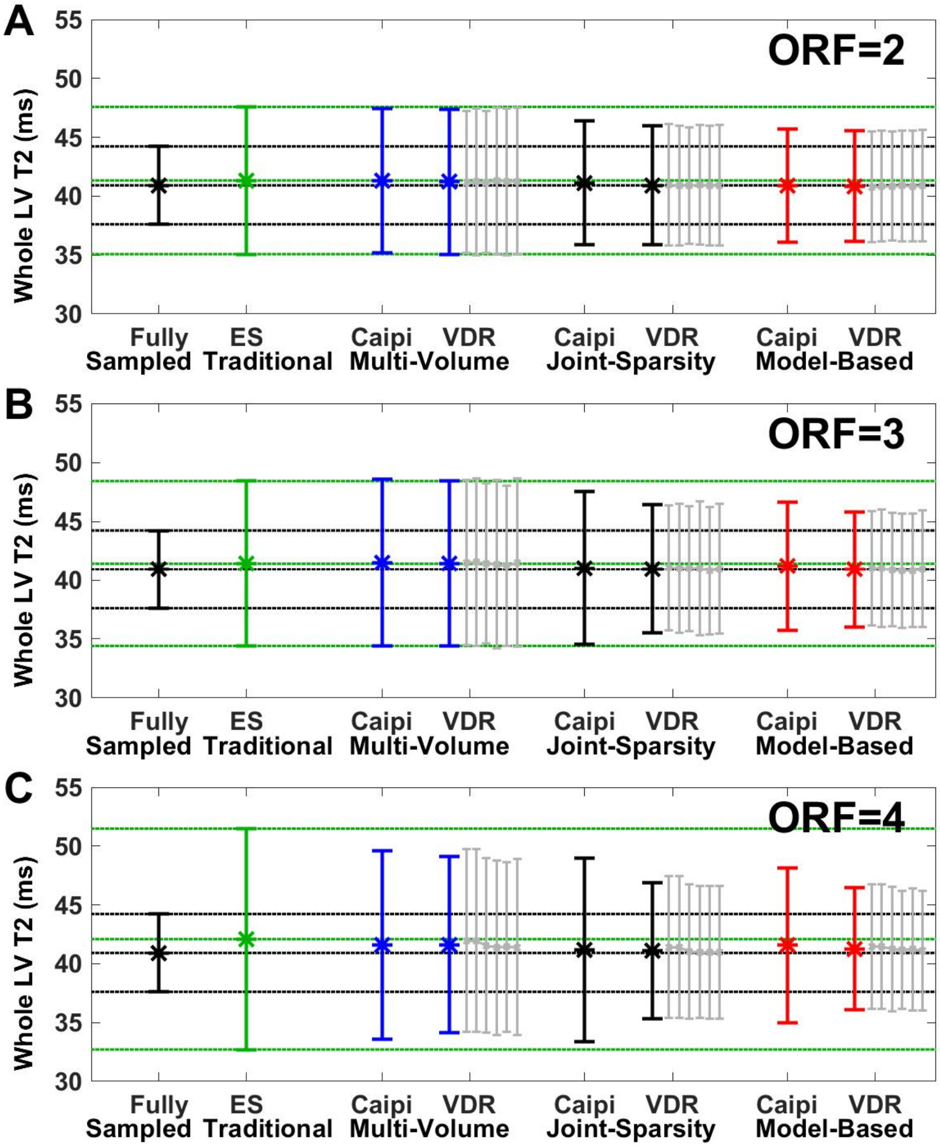

Figure 2.6: T2 error bars of different reconstruction approaches compared to references in whole-heart LV with ORF=2-4. Comparison of the effects of the reconstruction approach on whole-heart LV T2 mean and standard deviation of the human subject shown in Fig. 2.5 with ORF=2 (A), 3 (B), and 4 (C). Reconstruction of fully-sampled data (black) is used as the reference, with mean and SD extended throughout the plots (black dotted lines). Traditional SENSE (green) represents a secondary reference with independent volume-by-volume processing, which demonstrates the results of acceleration as readily available online on scanners, with mean and SD extended throughout the plots (green dotted lines). Variable density random (VDR) sampling was repeated six times (gray lines) for each method and results were averaged. The VDR approach smaller error bars than Caipi undersampling at all ORF values tested.

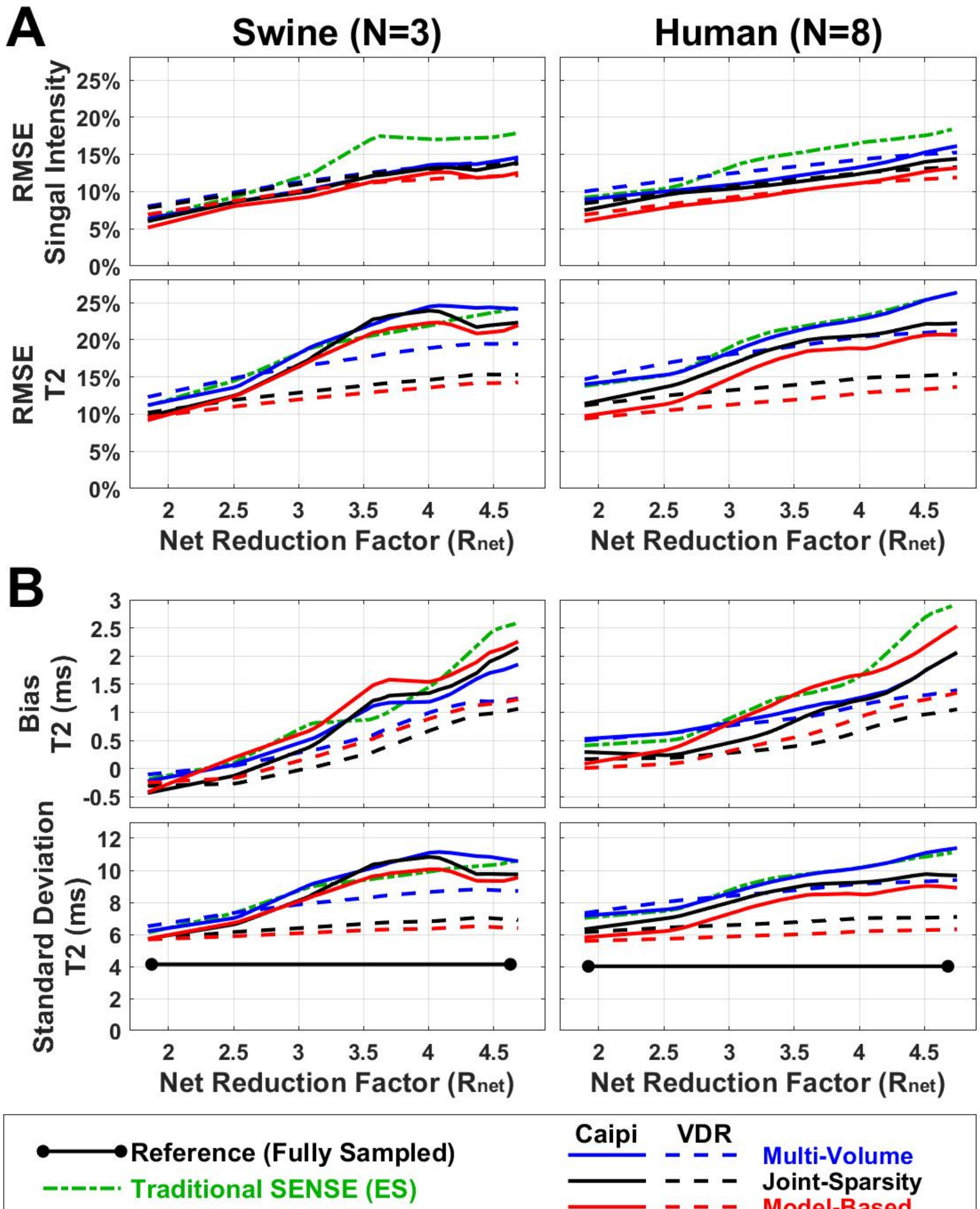

Figure 2.7: Average effects of the 4 metrics on different undersampled reconstruction approaches. The RMSE of both image data and T2 (A); and the accuracy (bias) and precision (SD) of T2 (B) are plotted as a function of increasing acceleration rate. The bias in T2 represents the difference between mean T2 and the reference mean T2. The results in naïve animals (left) and normal human subjects (right) follow very similar patterns. The VDR undersampling pattern outperforms the Caipi pattern (minimum err and bias) as acceleration factors increase.

Fig. 2.7A shows the effects of acceleration on RMSEs in the LV ROI averaged over 3 naïve swine (left) and 8 normal human subjects (right). There is good consistency between results from swine and humans. In general, the RMSE of T2 (9.2%-24.6%) is higher for a given R_{net} than the RMSE of signal intensity (5.2%-18.4%). As expected, RMSEs of both signal intensity and T2 increase with R_{net}. The RMSE of the signal intensity (top row) of the traditional SENSE method is highest when $R_{net}>3$. Model-based SENSE with either Caipi or VDR sampling produces RMSEs that are consistently, albeit slightly lower than, all other methods. For T2, the RMSEs of most approaches are comparable for $R_{net}<2.5$ (9.2%-16.8%). For $R_{net}>2.5$, the T2 RMSE of joint-sparsity SENSE and model-based SENSE reconstructions with VDR sampling (10.5%-15.4%) is lower than those of other methods (11.3%-26.3%). Finally, model-based SENSE with VDR sampling has consistently lower T2 RMSE than that of the joint-sparsity SENSE reconstruction with VDR sampling (p=0.0156, not significant, Wilcoxson signed rank test with modified Bonferroni correction).

Fig. 2.7B shows the effects of acceleration of T2 bias (top) and SD (bottom). Bias in T2 is <1 ms for $R_{net}<3$ in both swine and human data. As acceleration increases ($R_{net}>3$), the bias of VDR-based methods (0.0-1.4 ms) is lower than traditional SENSE and the corresponding Caipi-based (0.3-2.9ms) and VDR sampling methods, with joint-sparsity SENSE showing the least bias (0.0-1.1ms). The shape of T2 SD curves (Fig. 7B, bottom) is very similar to the T2 RMSE curves (Fig. 7A, bottom). The reference SD from fully-sampled data (3.9 ms for swine, 3.7 ms for humans) is shown as a lower bound. The increase in the SD of

T2 with the most undersampling is comparable when $R_{net}<2.5$ (+1.6-4.0 ms), wherein the SD of T2 increases by 39.4-99.8%. When $R_{net}>2.5$, the SDs of T2 with joint-sparsity SENSE and with model-based SENSE and VDR sampling (+1.8-2.9 ms) are lower than the other methods (+2.5-7.0 ms). The combination of VDR sampling with model-based SENSE produced SDs lower than that of VDR sampling with joint-sparsity SENSE for all R_{net} tested ($p=0.016$, not significant by Wilcoxson signed rank test with modified Bonferroni correction).

Fig. 2.8A displays representative T2-weighted images (T2-Prep TE=45 ms) and T2 maps of the swine with acute MI with ORF=3. Edema in the anterior LV wall and septum shows elevated T2 (60.2±6.8 ms) compared to normal LV tissue (44.4±4.4 ms) in the T2 map. The RMSEs in T2-weighted signal intensity and T2 increase monotonically with acceleration (Fig. 2.8B). The combination of ES sampling and traditional SENSE leads to larger errors compared to VDR sampling combined with joint-sparsity SENSE or model-based SENSE.

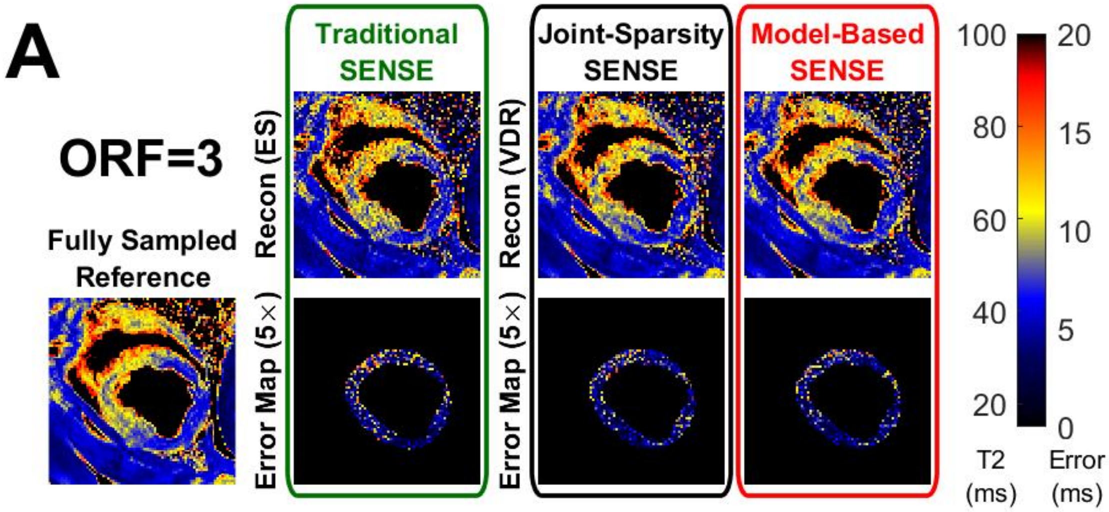

Continue on the next page

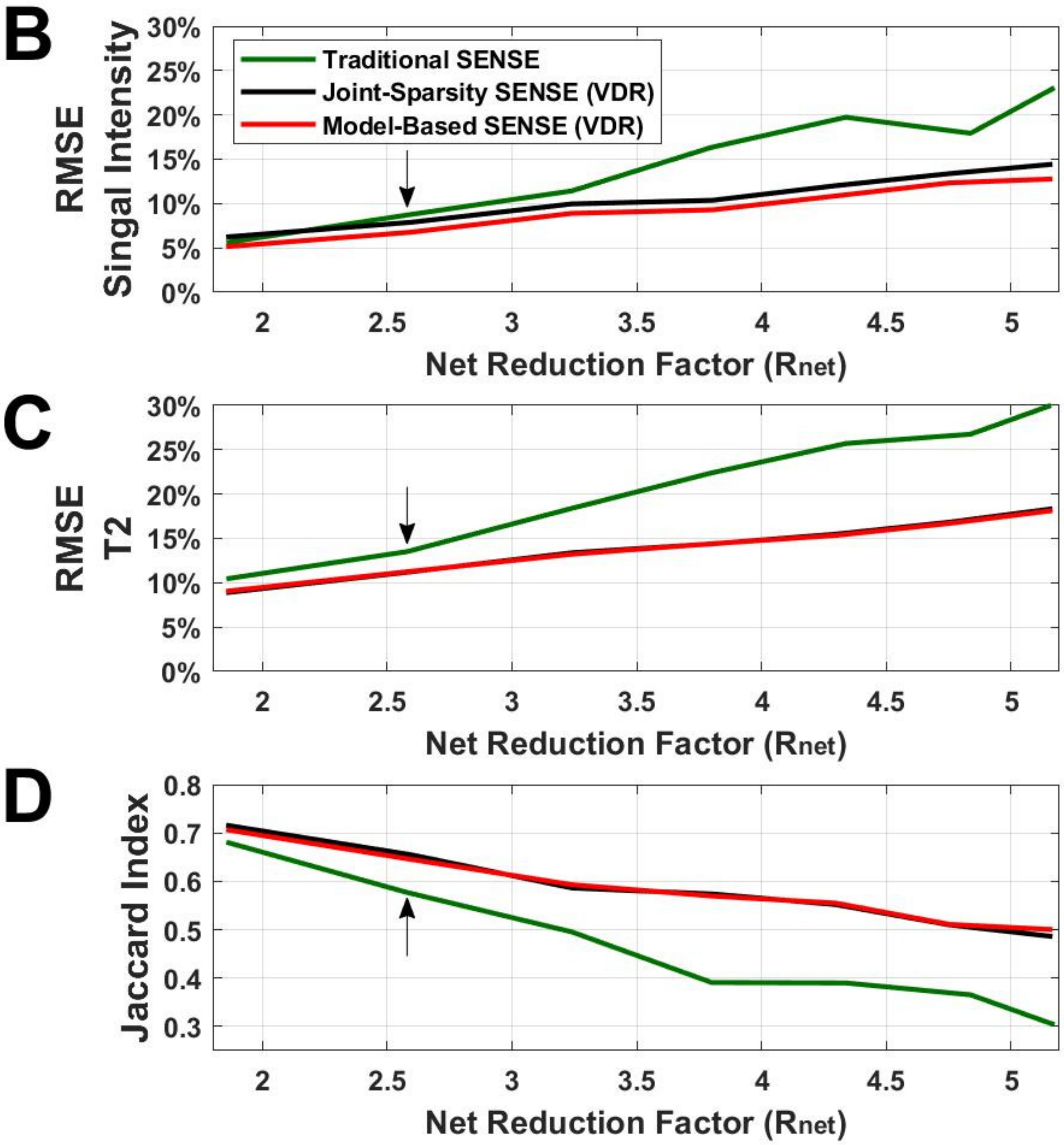

Figure 2.8: Results from the swine with acute MI displaying significant edema in the anterior LV wall and septum. (A) Comparison of images with T2-Prep TE 45 ms and T2 maps generated with fully sampled reference, ES sampling pattern with widely available traditional SENSE reconstruction and the two best-performing methods tested here: variable density random (VDR) sampling reconstructed with both joint-sparsity SENSE and model-based SENSE. (B) RMSE of T2 prepared images and (C) RMSE of T2 maps in LV increase as R_{net} increase. Arrow corresponds to images shown in (A) using ORF=3. These results show that though the images can support acceleration rates ORF>3, parametric maps quickly degrade, resulting in differences in the sensitivity to changes in T2. (D) Jaccard index, a measure of pixel-by-pixel correspondence of the segmented area with enhanced T2, decreases as the acceleration rate increases. Both joint-sparsity SENSE and model-based SENSE with VDR produce similar results and outperform traditional SENSE.

While T2-W signal intensity RMSE increased by 0.4%, 1.9%, and 2.5% (Fig. 2.8B), T2 RMSE of traditional SENSE increased by 1.4%, 2.2%, and 5.2% (Fig. 2.8C), respectively, compared to VDR sampling combined model-based SENSE, for ORF=2-4 (R_{net}=1.9, 2.6, and 3.2), respectively. The increase in T2 RMSE affected tissue characterization (Fig. 2.8D). As R_{net} increased, the Jaccard index, a measure of the accuracy of the area-at-risk segmentation where 1 indicates a complete pixel-to-pixel match, decreased. For ES undersampling with traditional SENSE reconstruction, the Jaccard index dropped from 0.68 to 0.30 (44.6%) as R_{net} increases from 1.9 to 5.2. Conversely, for VDR undersampling with model-based SENSE reconstruction, the Jaccard index decreases by 31% to 0.50. The Jaccard indices of joint-sparsity SENSE and model-based SENSE applied to VDR undersampled data were equivalent.

Fig. 2.9 demonstrates the percentage of unsuccessfully recovered pixels (defined as having T2<15ms or T2>100ms) within the LV ROI in swine (left) and human subjects (right). These percentages, which indicate the number of pixels in which a credible pixel intensity or T2 was unobtainable through reconstruction, were ≤1.61% for all methods when R_{net}≤2.5. In swine data, both the joint-sparsity SENSE and the model-based SENSE reconstruction undersampled by VDR patterns show ~0% unsuccessfully recovered pixels from reconstruction. In human data, only the model-based SENSE with VDR sampling achieves this level of pixel recovery, though joint-sparsity SENSE achieved good performance as well. Caipi-based methods displayed rapid growth with increasing R_{net}, as did traditional SENSE.

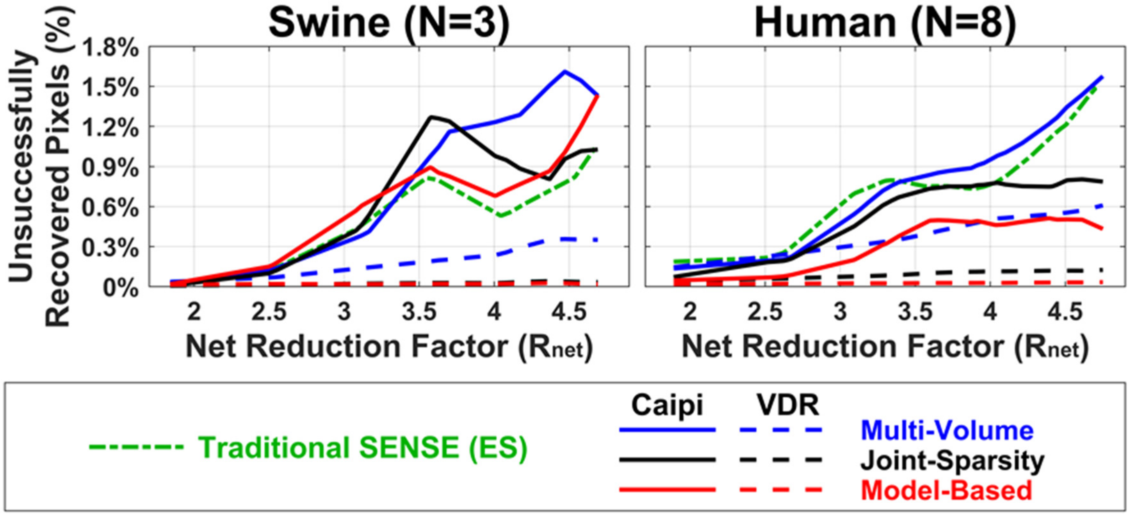

Figure 2.9: Average percentage of unsuccessfully recovered pixels. Average percentage of pixels with T2 beyond 15 ms and 100 ms in LV ROI of T2 maps from naïve animals (left) and normal human subjects (right) in response to increases in acceleration rate. VDR sampling with either joint-sparsity SENSE and model-based SENSE reconstruction yields a high degree of pixel recovery, maintaining very low percentages of unrecovered pixels for all R_{net}.

2.4 Discussion

In this chapter, we studied the impact of different undersampling strategies and on 3D cardiac T2 reconstruction approaches parametric maps. Fully-sampled acquisitions were retrospectively undersampled with ES, Caipi, and VDR patterns with ORF ranging from 2-8 leading to net reduction factors R_{net} from 1.8-4.9. Images were reconstructed with traditional SENSE, multi-volume SENSE, joint-sparsity SENSE, and model-based SENSE. The performance of the different sampling patterns and reconstruction methods were comparable for lower acceleration rates, $R_{net}<3$. For $R_{net}\geq3$, the VDR sampling pattern in combination with either joint-sparsity SENSE or model-based SENSE outperformed the other methods. VDR with joint-sparsity SENSE had the lowest T2 bias, while the VDR with model-based SENSE showed the lowest RMSE and

SD in T2. Acceleration resulted in increased SD but with a very small bias, trading some precision for a shorter scan time.

A central finding in this work was that the error in T2 was larger and the anatomy in T2 maps was degraded more vs. the source images with increasing acceleration. Although errors in T2 measurements may be reduced due to the fitting of data from multiple T2-weighted image volumes, it is clear that small errors in image intensity can result in more pronounced errors in T2, including the proportion of unsuccessfully reconstructed pixels (Fig. 2.9). Further work is needed to explore the tradeoff between the number of T2-weighted volumes and acceleration (with constant scan time).

In both swine and human subjects, all tested methods of acceleration resulted in degradation of the parametric maps as expected. Given the pervasive use of parallel imaging with high undersampling factors in 2D single-shot mapping, it is important to evaluate whether its deleterious effects on image fidelity can be ameliorated by appropriate selection of the undersampling approach. Case and point, for the swine with acute MI, the use of the higher performance acquisition/reconstruction combinations studied permitted more accurate segmentation of the area-at-risk despite significant acceleration. Considering the compromise between the quality of T2 maps and R_{net}, the choice of undersampling patterns and reconstruction methods, could be made based on the metrics discussed herein. Furthermore, from this work, it is clear that to accurately test a 3D parametric mapping technique, metrics beyond the mean value of the fit parameter relative to that of a reference need to be considered:

bias and standard deviation, as well as the preservation of potential segmentations, must be included to truly assess the feasibility of an approach.

2.4.1 Undersampling Patterns

The Caipi patterns outperformed the traditional ES patterns with respect to the RMSE of T2-weighted images, but there was little improvement in all metrics with regard to the T2 maps. Instead, VDR undersampling, which achieved results comparable to Caipi in terms of the RMSE of T2-weighted images, showed improvements in all other metrics measured from the T2 maps. As expected, VDR undersampling whose artifacts are incoherent across differentially-weighted volumes, supported higher undersampling rates when combined with sparsity-driven reconstructions, whether sparsity is enforced in the image (as in joint-sparsity SENSE) or in the parameter space (as in model-based SENSE).

2.4.2 Reconstruction Algorithms

Multi-volume SENSE reconstruction differs from traditional SENSE by jointly reconstructing all weighted image volumes. This approach maintains individual image contrast (80), and represents an achievable extension for manufacturers to incorporate into online reconstructions, as it makes no assumptions about the jointly-reconstructed data and therefore requires no tuning (e.g., Lagrange multipliers). Images and parametric maps obtained with multi-volume SENSE was equivalent to traditional SENSE for lower R_{net}, and outperformed traditional SENSE at higher R_{net} (Figs. 4,6). These maps were more consistent with those from joint-sparsity SENSE and model-based SENSE (Figs. 3,5).

For $R_{net}<2.5$, all tested methods provide similar T2 RMSE, T2 bias, and T2 SD. The percentage of recovered pixels in the LV ROI is also high (≥99.8%) for all methods. Relative to traditional SENSE, joint-sparsity SENSE or model-based SENSE with VDR sampling offered a lower bias (higher accuracy), a lower SD (higher precision), a higher percentage of recovered pixels, and a more accurate segmentation of edematous tissue. Nevertheless, traditional SENSE provides a reasonable alternative which is fast and, with online reconstruction on MR scanners, is easily achieved with only a small cost in image quality.

For $R_{net}>2.5$, compared to the other methods, joint-sparsity SENSE and model-based SENSE with VDR sampling had a lower impact on the RMSE, bias, SD, percentage of recovered pixels, and Jaccard index in T2 images. Comparing just these two methods, joint-sparsity SENSE resulted in the lowest bias in mean T2 values while model-based SENSE resulted in the lowest SD. Lower SD can be beneficial in the separation of bimodal distributions. Hence it is not surprising that model-based SENSE reconstruction resulted in accurate segmentation of the area-at-risk, as corroborated by the highest Jaccard indices for the majority of tested R_{net} values (Fig. 2.8B).

Note that the methods tested here are limited to a sampling of the better-understood image reconstruction techniques, but other approaches exist. Nevertheless, the images and maps utilized here are not significantly different in SNR from other approaches, indicating that the results from this work are likely applicable to other scenarios. Similarly, we exemplify applications to 3D T2 mapping, but the mapping of many other parameters will be of interest and extrapolation of the current results to other scenarios would require further work and testing.

2.4.3 Choice of R_{net}

The choice of the undersampling factor for 3D parametric mapping must consider the balance between the fidelity of the target measurements and the total scan duration. In this work, $R_{net} \leq 3$ (ORF~2-4) yielded reasonable results. At this acceleration factor ($R_{net}=3$), scan time is reduced to approximately 3 min. Joint-sparsity SENSE with VDR sampling resulted in mean T2 bias of -0.03±0.26 ms and 0.28±0.24 ms, T2 standard deviation of 6.39±0.87 ms and 6.58±0.87 ms, in swine and humans respectively. The increase in T2 SD was 54.6%±0.8% and 64.5%±10.1%. Similarly, model-based SENSE with VDR sampling resulted in a mean T2 bias of 0.14±0.23 ms and 0.31±0.14 ms, a T2 SD of 6.07±0.98 ms and 5.86±0.59 ms, in swine and humans respectively. The increases in SD was 46.7%±6.3% and 46.9%±7.2%, though large in magnitude, still resulted in accurate segmentation of an edematous heart. The Jaccard index of segmentations from reconstructions with joint-sparsity SENSE or model-based SENSE with VDR undersampling was maintained at 0.59 vs. a 0.50 for traditional SENSE, which suffered an additional 16.5% drop. Further increase in R_{net} requires a more aggressive increase in ORF due to the overhead cost in scan-time of fully-sampling the center of k-space which is needed for coil sensitivity autocalibration (ACS). More work is needed to determine the optimal size of the ACS region in the context of parametric mapping where preserving image contrast is critical for accurate fitting.

2.4.4 Limitations

This study does not include many of the optimizations that are currently available for the different reconstructions approaches as these are continuously evolving and improving. Nevertheless, the impact of reconstruction on the parametric maps requires direct quantification and study. The results obtained on the animal with acute MI represent anecdotal findings (N=1) and more studies should be performed to demonstrate the effects of reconstruction on the segmentation of parametric maps, and compare the accuracy of areas of elevated T2 measured in parametric maps with areas of MI measured by post-mortem histology. No statistical comparisons are made in the MI case between quantitative metrics as the number of samples is likely too small to generate valid statistically significant results.

This study utilized the retrospective undersampling of fully sampled data, which resulted in long acquisition times. Though prospective acquisition could yield more accurate results since protracted scans are more susceptible to motion artifacts, adding prospective scans to the full-sampled acquisition protocol would have resulted in a prohibitive scan duration given the large number of permutations tested herein.

Chapter 3 Quantitative T2 Mapping using Accelerated 3D Stack-of-Spiral Gradient Echo Readout

3.1 Introduction

Quantitative relaxometry is a desired MRI tool for longitudinal or cross-sectional characterization of lesion structures (85,86). Conventional T2 mapping methods generate and reconstruct T2-weighted images frame-by-frame followed by a voxel-wise fitting. The associated long acquisition time hinders its practical utility, especially for applications that require 3D high spatial resolution and broad volume coverage.

Various rapid imaging techniques have been adapted to T2 mapping experiments. Parallel imaging exploits the data redundancy generated by multiple receiver coils to recover missing k-space samples (87,88). With the development of compressed sensing (CS) (89), several constrained reconstruction methods have been developed for acceleration and applied to parameter mapping (90–98). Block et al. proposed iterative reconstruction using a total variation (TV) constraint on radial acquisition (90); Lustig et al. applied a sparsifying transform to images acquired with incoherent sampling to achieve acceleration (91). In addition to the undersampling of spatial characteristics, redundancy in the temporal (92) or parametric (93–96) dimensions of image series has been explored as well. Some methods combined the aforementioned constraints (97,98). Another promising strategy for fast parameter mapping is the model-based reconstruction, which incorporates the underlying signal model as prior knowledge in an iterative reconstruction to estimate parameter maps directly from the k-space data (99–105). Advanced reconstruction imposing subspace constraints has also been demonstrated for parameter mapping (106–108).

The majority of these studies applied 2D multi-slice acquisition with Cartesian trajectories (93,94,97,99,102) to achieve up to 5-fold acceleration. 3D acquisitions typically use smaller slice thicknesses without gaps and even isotropic resolution. This allows the visualization of small lesions in any reformatted orientation. The 3D radial trajectory has been adopted for T1 and/or T2 estimation with undersampling (109,110). The spiral trajectory offers great advantages in high acquisition efficiency (111), accelerated reconstruction (112), and robustness to motion artifacts (113). 3D T2 mapping has been performed using pulse sequences based on gradient-echo (GRE) steady-state conditions (114), multi-echo fast spin-echo (FSE) (109), and T2 magnetization preparation followed by GRE (110,115–121) or FSE (122,123).

During the last decade or so, brain T2 mapping has largely been applied with advanced 2D acquisitions (93,96–100,102,107,124,125) and a few with 3D methods (109,114,121). In the clinical setting, multi-parametric MRI straightforward for coregistration when different magnetization preparation modules are appended to the same acquisition readout. In the present work, we chose a T2-prepared GRE sequence combined with a 3D stack-of-spiral acquisition to provide T2 mapping with whole-brain coverage and high spatial resolution. Different fitting models, k-space sampling strategies, and reconstruction techniques were evaluated in both numerical simulation and experimental brain scans to optimize performance. The effect of suppressing cerebrospinal fluid (CSF) signal in order to reduce its partial volume effect, was also tested for brain T2 quantification.

3.2 Methods

3.2.1 Simulation of T2 Fitting

All numerical simulations were implemented in MATLAB 2019B (Mathworks, Natick, MA, USA). In order to investigate the effects of various B_1 offsets on the 90°/-90° hard pulses used at the beginning and end of the T2 preparation module (see Appendix) as well as different noise levels, numerical simulations were conducted to study the performance of three non-linear T2-fitting models: 1) classic 2-parameter fitting to a mono-exponential decay; 2) 2-parameter-weighted fitting with the signal intensity of the T2-weighted images as the weighting; and 3) 3-parameter fitting with an additional constant to account for the effect of inhomogeneous B_1 setting.

Typically, the longitudinal magnetization after a T2 preparation module follows an exponential decay with respect to its duration ($\mathrm{TE_{prep}}$):

$$\mathrm{y} = A_0 e^{-\mathrm{TE_{prep}}/T2}, \tag{3.1}$$

where A_0 is the longitudinal magnetization prior to the T2 preparation. This is a 2-parameter model where only two parameters, A_0 and $T2$ are fitted, with several fixed $\mathrm{TE}_{\mathrm{prep}}$ values defined as a vector $\overline{\mathrm{TE}}_{prep}$, and a corresponding signal acquired as a vector $\bar{\mathrm{y}}$. The first classic 2-parameter fitting model makes use of least-squares-fitting with a cost function of:

$$\min_{A_0,T_2}\left\|\bar{\mathrm{y}} - A_0 e^{-\overline{\mathrm{TE}}_{prep}/T_2}\right\|_2^2 \qquad 3.2$$

Alternatively, in the second model, the 2-parameter-weighted fitting method weights the least-square-fitting with signal intensity for different $\mathrm{TE}_{\mathrm{prep}}$ values, resulting in a modified cost function:

$$\min_{A_0,T_2}\left\|\mathrm{diag}(\bar{\mathrm{y}})\left(\bar{\mathrm{y}} - A_0 e^{-\overline{\mathrm{TE}}_{prep}/T_2}\right)\right\|_2^2 \qquad 3.3$$

where $\mathrm{diag}(\bar{\mathrm{y}})$ reshapes the vector $\bar{\mathrm{y}}$ to a diagonal matrix.

In the third model which considers B_1 inhomogeneity, a constant ε is added to the exponential decay to make up a 3-parameter model:

$$\mathrm{y} = A_0 e^{-\overline{\mathrm{TE}}_{prep}/T_2} + \varepsilon \qquad 3.4$$

Therefore, the cost functions for the 3-parameter fitting model can be formulated as:

$$\min_{A_0,T_2}\left\|\bar{\mathrm{y}} - \left(A_0\left(e^{-\overline{\mathrm{TE}}_{prep}/T_2} + \varepsilon\right)\right)\right\|_2^2 \qquad 3.5$$

For all three models, the Levenberg–Marquardt algorithm (126) was used to solve the non-linear least-squares fitting. The voxel-wise fitting iterations were calculated in a matrix form that is much faster than a sequential pixel by pixel fitting. T2 values were set from 40 ms to 200 ms in intervals of 10 ms, and the T1 value was set as 1000 ms. Their signal intensities at the end of different TE_{prep}, [20, 40, 80, 120, 160] ms, with B_{1+} = 1.0 and 0.8, were calculated based on Eq. A.3 in the Appendix. With a signal-to-noise ratio (SNR) of the data at TE_{prep} = 20 ms increasing from 10 to 50 in intervals of 5, random noise with a normal distribution was added to signals acquired with different T2 weighting. For each noise level, data generation was repeated 10000 times in a Monte Carlo simulation in order to compute the mean and standard deviation (SD) of the estimated T2. The mean values of the percentage errors in the fitted parameters relative to the input values were analyzed as an indicator of the accuracy of each fitting approach. The corresponding coefficient of variations (CoV = SD/mean) was measured as an indicator of precision.

3.2.2 Simulation of k-space Sampling and Reconstruction

To evaluate the performance of different k-space sampling and reconstruction methods used in the in vivo experiments, a 2D digital phantom (192×192) with four T2 values, [80, 100,150, 200] ms, and a uniform T1 value (1000 ms) was used and five T2 weighted images were attained with echo times (TEs) = [20, 40, 80, 120, 160] ms, respectively.

3.2.3 k-Space Sampling

A 2D variable-density spiral trajectory (113,127) was applied to generate k-space data based on a Bloch equation simulation (Fig. 3.1).

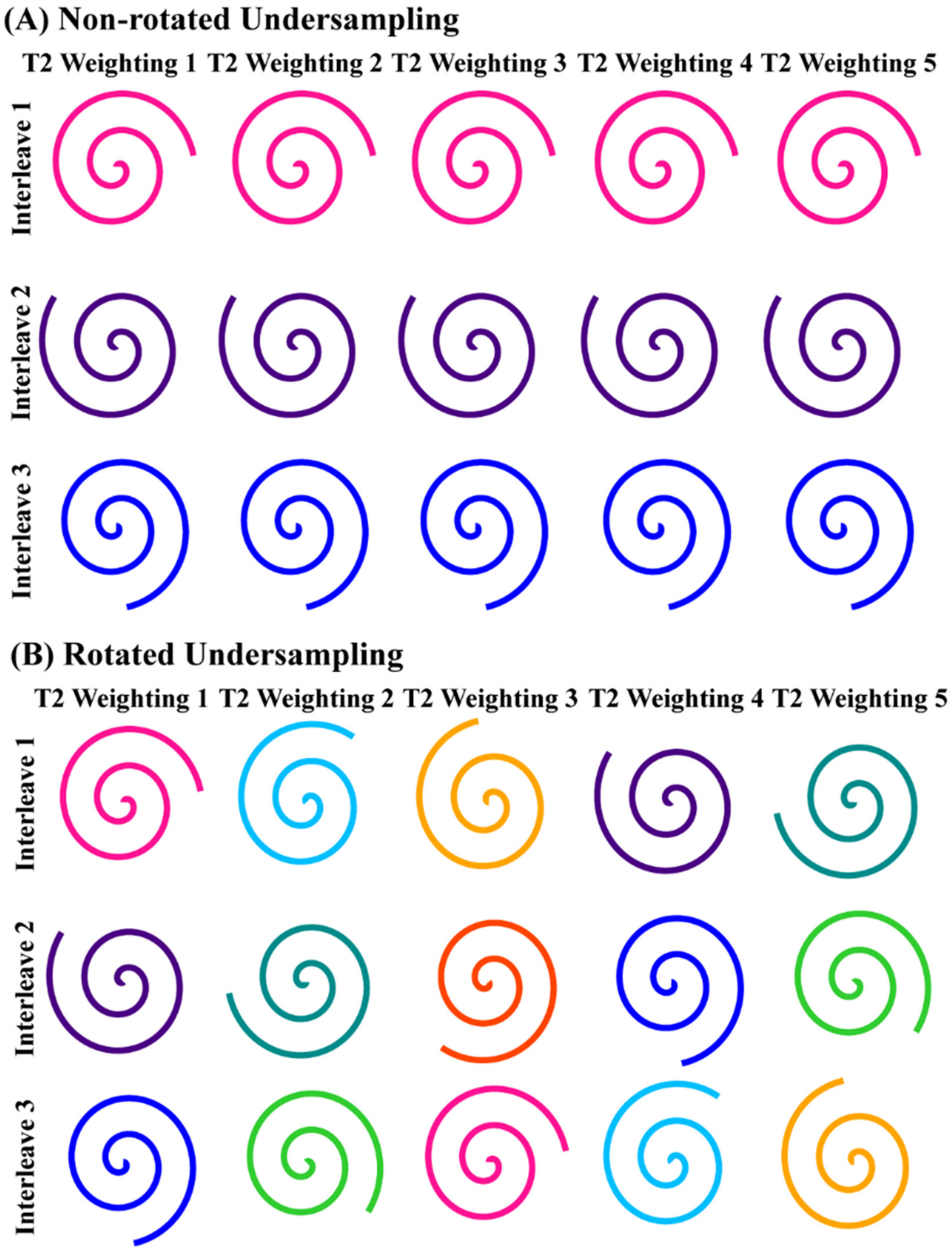

Figure 3.1: Spiral interleaves in kx-ky plane. (A) Non-rotated retrospective undersampling scheme: the same interleaves selected for each T2 preparation; (B) Rotated retrospective undersampling scheme: different interleaves selected for each T2 preparation.

Specific parameters for the sampling include: the central 15% k-space was fully sampled; the peripheral 15% k-space was sampled with an acceleration factor of

3; the sampling density reduced linearly between those central and peripheral k-space areas; the readout duration of the spiral trajectory for each phase-encoding interleave was kept to 10 ms to mitigate blurring due to off-resonance effects (128) and the T2* decay (129) during the k-space sampling and the dwell time of the readout sampling was 4.3 μs; the number of interleaves was 8 with an acceleration factor of 2; and 8 simulated coils were uniformly distributed around the digital phantom. Retrospective undersampling was performed for each TE by selecting a subset of three equally-spaced interleaves (total acceleration factor of 5). For k-space sampled with different $\mathrm{TE_{prep}}$, both non-rotated and rotated undersampling schemes were tested, with the sampled spiral interleaves identical or rotated with a fixed angle between adjacent interleaves (360°/8 = 45°) (Fig. 3.1).

3.2.4 Reconstruction

For T2 estimation, a model-based reconstruction method incorporating CS in the spatial domain was applied, which can be formulated as:

$$\underset{\hat{I}}{\text{minimize}} \left\|E\hat{I} - k\right\|_2^2 + \lambda \left\|S\left(\tilde{S}(\hat{I})\right) - \hat{I}\right\|_1 + \alpha \mathrm{TV}(\hat{I}) \qquad 3.6$$

where *E* is the encoding matrix including the non-uniform Fourier transform and the complex coil sensitivity; $\hat{I}$ is the image series; *k* is the k-space data; *S* is the 2-parameter T2 decay model (Eq. 3.1); $\tilde{S}$ is the adjoint operator which maps the image series to T2 maps via the 2-parameter-weighted fitting model (Eq. 3.3); and TV is the in-plane spatial total variation (90). The $\|\cdot\|_2$ stands for the spatial

l_2-norm. The $\|\cdot\|_1$ denotes the l_1-norm along parameter dimension, which was implemented to eliminate outliers in the T2 fitting process (101). The parameter λ balances the data and model consistency. Parameter α trades sparsity with data consistency: specifically, if $\alpha = 0$, the objective function degenerates to model-based reconstruction (101). A fully-sampled central k-space was used to obtain a low-resolution coil sensitivity map. The algorithm was implemented using a projected-gradient approach (130), with a projection designed to apply the model-consistency condition (101). Data consistency, model consistency, and the spatial sparsity constraint were combined into a joint constrained problem and iteratively optimized with a maximum iteration number set to 60, which was empirically determined to ensure full convergence. The proposed method was compared with regular SENSE (131), CS SENSE (132), and model-based methods without a CS constraint (101). SENSE and CS SENSE were implemented using a non-linear conjugate gradient algorithm (91) and the model-based methods were implemented using the projected-gradient approach described above. All reconstruction and fitting processes were implemented in MATLAB 2019B (Mathworks, Natick, MA, USA).

3.2.5 In vivo Experiments

Experiments were performed on a 3T Philips Ingenia scanner (Philips Medical Systems, Best, The Netherlands) with a 32-channel head-only coil for signal reception. Four healthy volunteers (3 females and 1 male, 44-59 years old) were enrolled after providing informed consent in accordance with the Institutional Review Board guidelines.

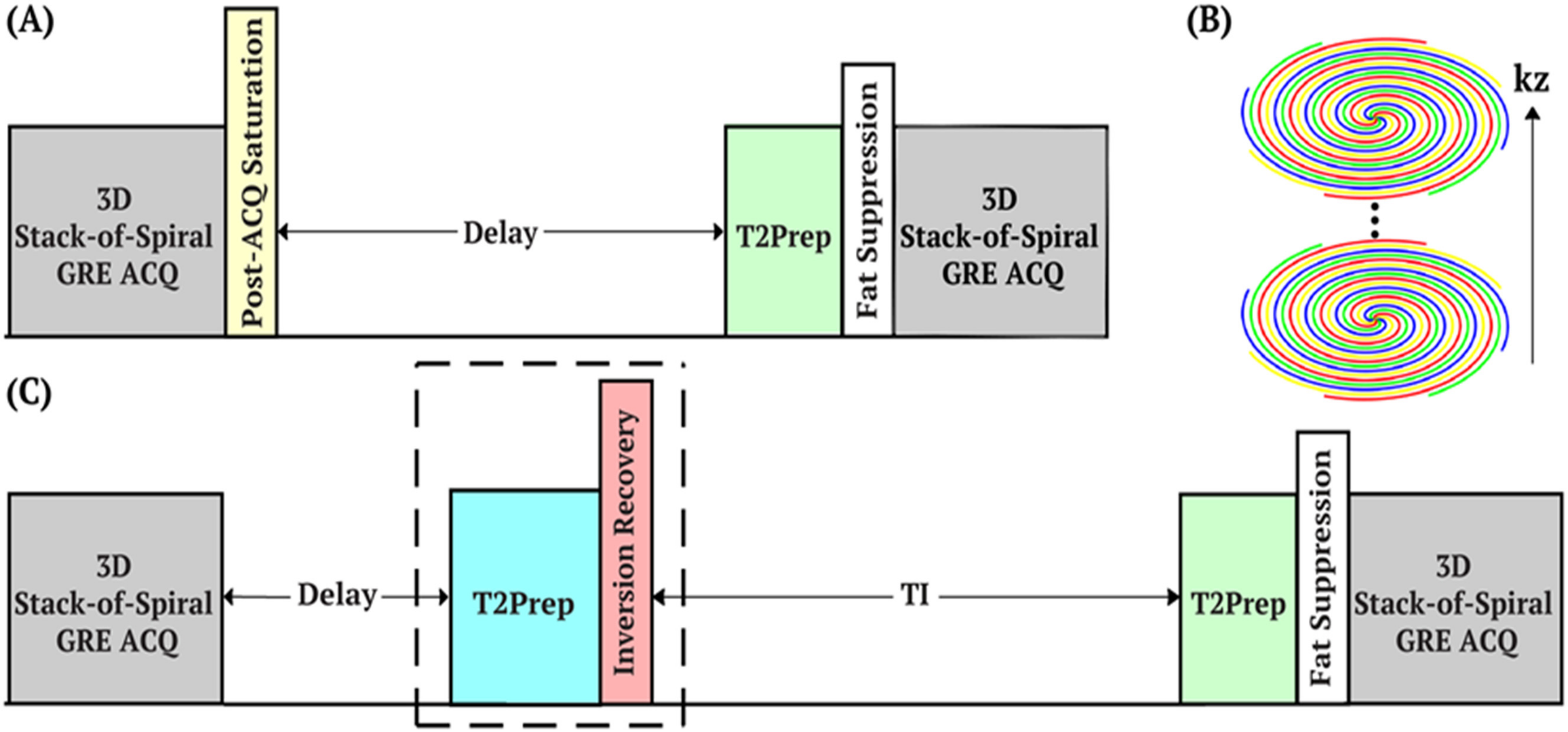

Figure 3.2: (A) Diagram of the pulse sequence with T2-prepared gradient echo (GRE) readout for each T2 weighting. (B) 3D stack-of-spiral trajectory with turbo direction applied along slice direction. (C) Diagram of the pulse sequence with a CSF nulling module (the dashed box) to remove the CSF partial volume effect. Abbreviations: acquisition (ACQ), T2 preparation (T2Prep).

The pulse sequence diagram for T2 mapping is shown in Fig. 3.2A. A post-acquisition spatially-selective saturation pulse train was applied with a fixed delay (1500 ms) to ensure the same longitudinal magnetization before each T2 preparation module. The non-selective T2 preparation pulse train starts with a hard pulse excitation ($90°_x$), followed by a series of composite refocusing pulses ($90°_x180°_y90°_x$) with an MLEV phase-cycling pattern (133) and then a flip-back pulse ($90°_{-x}$). In order to successively generate different T2 contrasts with TE_{prep} = [20, 40, 80, 120, 160] ms, the number of refocusing pulses was chosen to be [2, 4, 8, 12, 16], respectively, with a constant inter-echo spacing of τ_{CPMG} = 10 ms (134). Immediately following the T2 preparation, a frequency-selective fat-suppression module was inserted before data acquisition.

A GRE sequence, using turbo-field-echo (TFE) and with a train of low-flip-angle excitation pulses, was applied with a 3D segmented stack-of-spiral trajectory (Fig. 3.2B) in the axial orientation. In addition to the variable-density spiral trajectory described in the simulation section (acceleration factor of 2), a fully sampled readout with a uniform density spiral trajectory (no acceleration) was acquired for reference. Readout duration of the fully sampled uniform density acquisition was identical to the variable-density case (10 ms) and 16 phase encoding interleaves were required to fill the k-space, indicating a net prospective acceleration factor of 2 (16/8 interleaves) using variable-density spiral trajectory and a net acceleration factor of 5.3 (16/3 interleaves) after retrospective undersampling (approximately 5-fold). Acquisition parameters: TR/TE/flip angle = 15 ms/1.2 ms/12°; the acquisition resolution was 1.2 mm isotropic and the reconstructed voxel size was 0.6 mm isotropic; field of view (FOV) = 220×220×96 mm^3, slice oversampling = 1.25, number of acquired slices = 100; low-high profile order with TFE factor = 25 along the slice direction. Thus, each spiral interleave required four shots for a full encoding of the slice direction, and for the variable-density undersampled and uniform density fully-sampled spiral trajectories, 8 and 16 spiral interleaves for in-plane encoding or 32 and 64 shots needed to be interleaved, respectively. With a 2000 ms shot interval and five separate T2 preparations, the total scan duration was 5.5 min and 11 min for the two datasets. Note that the undersampled acquisition with an acceleration factor of 5 would only take 2.2 min. The reference T2 map was fitted by the non-linear 2-parameter-weighted T2 decay model using fully-sampled data voxel by voxel. Singular value decomposition (SVD) was used to compress 32 channels to 8 virtual channels to mitigate the computational burden in the reconstruction. Retrospective undersampling and reconstruction methods were the same as used in the simulations, and the 2-parameter-weighted fitting model was applied.

When CSF suppression is desired, an SNR-improved inversion recovery method can be implemented (135). This CSF-suppression module (the dashed box in Fig. 3.2C) utilized a T2 preparation module (TE_{prep} = 300 ms) with double-refocused hyperbolic tangent pulses (5.0 ms, tanh/tan, maximum amplitude of 575 Hz and a frequency sweep of 9 kHz(136)). Since the CSF has a long T2 value (~1500 ms (137)), its signal would be less affected by the prior T2 preparation and inverted and nulled by the following inversion pulse with a delay TI = 1100 ms. The brain tissue with relatively short T2 values was largely saturated by T2 preparation and thus recovered with a higher longitudinal magnetization than experiencing inversion alone. Only the variable-density spiral trajectory was used in the CSF-nulled sequence. With a 3000 ms TFE shot-interval, total scan time was 8 min with 2-fold prospective undersampling using the variable-density spiral acquisition, as compared to 3.2 min with an undersampled acquisition at a total acceleration factor of 5.

3.2.6 Data Analysis

Quantitative evaluation was performed by simulation and by in vivo experiments. To compare the performance of different reconstruction methods and retrospective undersampling schemes, the relative difference of T2 maps compared to the reference values were computed in each voxel. Normalized root-mean-square-error (nRMSE) was calculated over the entire digital phantom in simulations:

$$\mathrm{nRMSE} = \frac{\left\|\hat{I} - I\right\|_2}{\|I\|_2} \tag{3.7}$$

Here $\hat{I}$ is the image series reconstructed from the undersampled dataset and I is the fully-sampled reference.

For in vivo experiments, the signal from CSF and nearby tissue were thresholded by masking areas with T2 values longer than 200 ms. In the CSF nulling studies, the mask was created by thresholding the intensity of the images acquired when TE_{prep} = 20 ms. The mask was eroded by one pixel to ensure exclusion of CSF. The nRMSE values were estimated from the segmented brain tissue as well as manually selected regions of interest (ROIs) of white matter and gray matter. To compare the pulse sequences with and without the CSF nulling module, estimated T2 values and corresponding differences were reported in ROIs of frontal gray matter (FGM), frontal white matter (FWM), globus pallidus (GPA), occipital gray matter (OGM), occipital white matter (OWM), the splenium, and the thalamus.

3.3 Results

3.3.1 Simulation of T2 Fitting

Fig. 3.3 shows the mean of relative errors of estimated T2 and the corresponding CoV (SD/mean) using the prescribed T2 preparation modules under different noise levels with the three T2 fitting approaches. For each fitting, higher SNR almost invariably delivered more accurate and precise estimates as expected. When the B_1 scale was ideal ($B_{1+} = 1.0$), for the same SNR levels the 2-parameter or 2-parameter-weighted fitting was more robust than fitting with the 3-parameter model. The relative T2 errors and CoV of the 2-parameter-weighted fitting were slightly higher than the results from the 2-parameter fitting, being under 5% and 10%, respectively, for most cases. 3-parameter fitting was much more sensitive to noise with higher T2 errors and CoV in most cases.

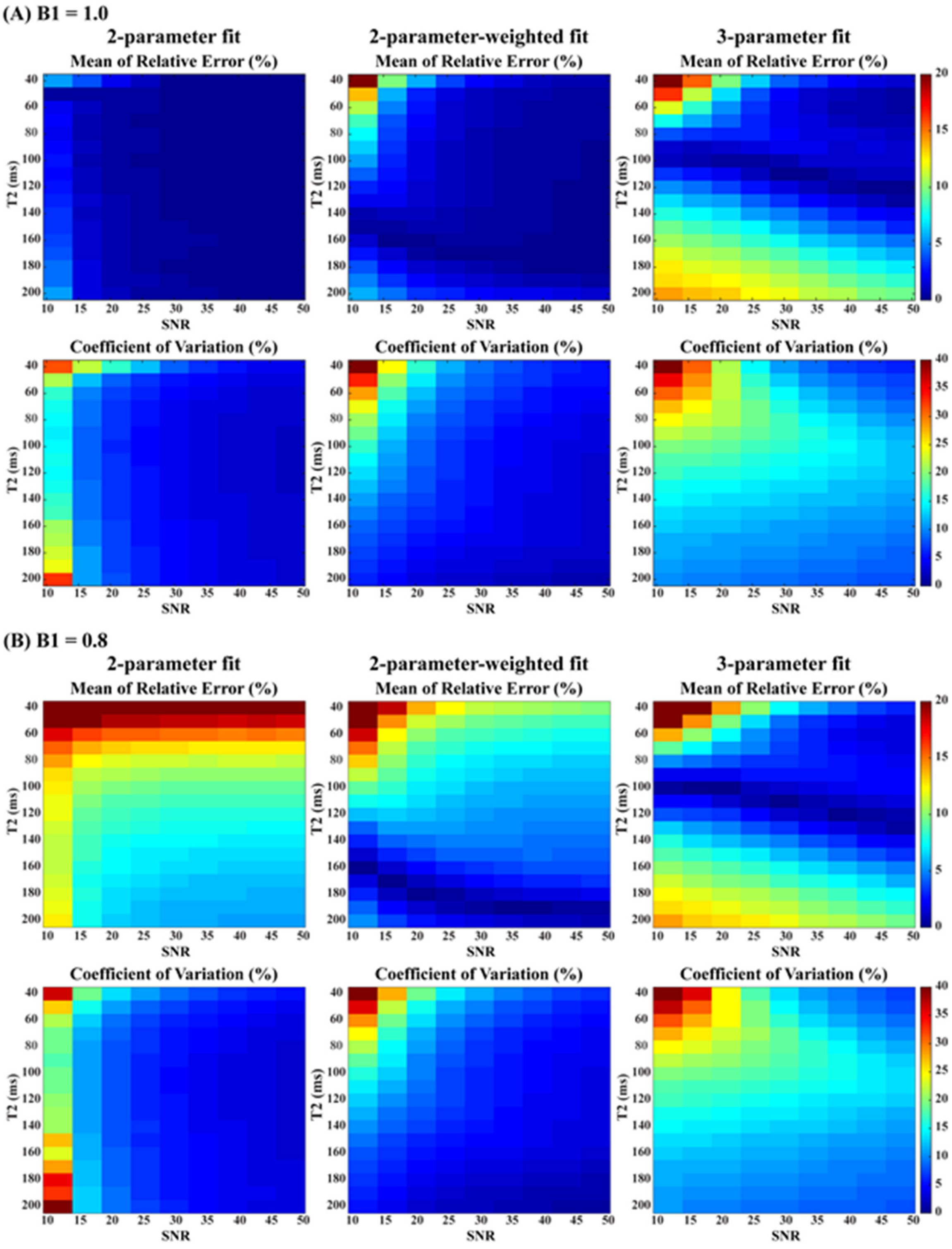

Figure 3.3: Simulation results of T2 estimation using 2-parameter, 2-parameter-weighted, and 3-parameter fitting models: the mean of relative errors (indicating accuracy) and coefficient of variation (indicating precision) of 10000 repetitions as a function of SNR using Monte Carlo simulation with (A) B_{1+} = 1.0 and (B) B_{1+} = 0.8. Compared to the other two fitting approaches, the 2-parameter-weighted fitting demonstrated balanced robustness to different B1 scales and noise levels.

When the B_1 scale was with offset (B_1+ = 0.8), 2-parameter fitting overestimated the shorter T2 values (40-80 ms) by 15-20%, indicating that 2-parameter fitting was more sensitive to B_1 inhomogeneities. In contrast, 2-parameter-weighted fitting reduced these relative errors largely to under 15%. The 3-parameter fitting yielded minimal sensitivity to B_1 inhomogeneities, with relative errors less than 5% when SNR was high, but this fitting was much more sensitive to noise. The 2-parameter-weighted fitting was thus chosen for its overall stable performance with these noise levels and B_1 variations in this range.

3.3.2 Simulation of k-space Sampling and Reconstruction

Fig. 3.4A shows the simulation results of T2 maps obtained by different undersampling schemes and reconstruction methods with 5-fold acceleration. CS SENSE reduced the aliasing artifacts which were apparent in the T2 maps obtained using SENSE alone. Model-based methods with joint reconstruction provided more accurate T2 estimation with less artifacts and noise than applying the individual reconstruction followed by 2-parameter-weighted voxel-by-voxel fitting (Fig. 3.4B). Incorporating CS further improved the performance of the model-based approach with reduced T2 SD by reducing the artifacts manifesting as stripes. Results show slight improvements when rotating the spiral interleaves with different T2 weighting (bottom panel) than the corresponding ones from the non-rotating methods (top panel). These qualitative observations were confirmed by the absolute normalized errors of the estimated T2 values across the pixels within the digital phantom, as shown in Fig. 3.4B.

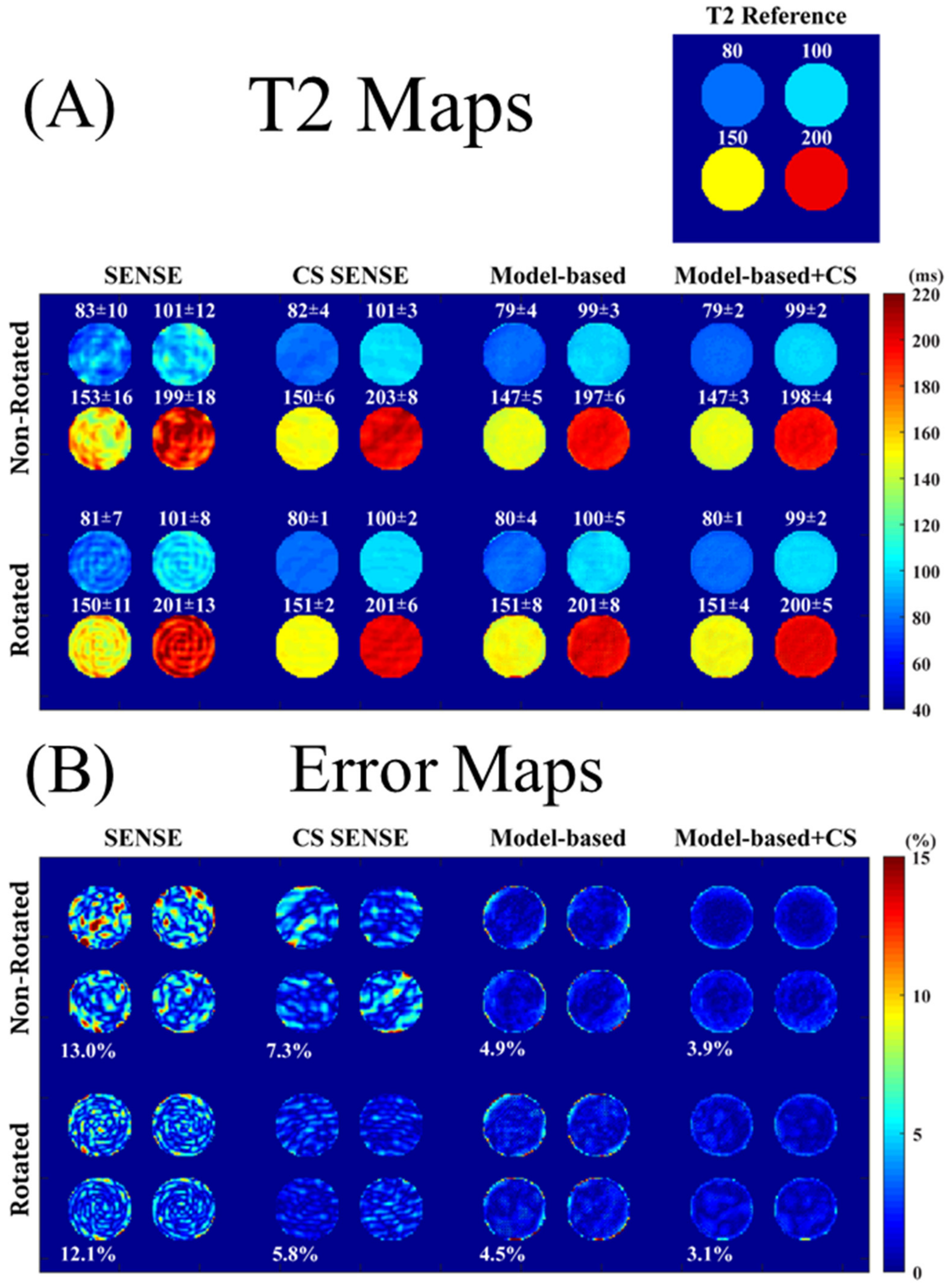

Figure 3.4: Simulation results of (A) T2 maps: (left) T2 reference map composed of four regions with values of 80 ms, 100 ms. 150 ms and 200 ms, respectively; (right) T2 maps estimated by different undersampling schemes (non-rotated and rotated trajectories along T2 weighting dimension) and different reconstruction methods (SENSE, CS SENSE, model-based, and model-based CS-incorporated) with an in-plane acceleration factor of 5. Corresponding mean and SD of the T2 values of each region are labeled above the region. (B) The absolute normalized error maps in percentage of different undersampling schemes and different reconstruction methods. The corresponding nRMSE of the T2 estimation of the entire digital phantom is labeled on the left bottom corner of each cell.

The nRMSE of SENSE, CS SENSE, model-based, and model-based CS-incorporated were 13.0%, 7.3%, 4.9%, and 3.9% using non-rotated spiral trajectories, slightly higher than 12.1%, 6.8%, 4.1%, and 3.1% using rotated spiral trajectories (*P* < 0.05 on the corresponding error maps, two-tailed student's t-test). The nRMSEs of the model-based methods were all less than 5% with the model-based CS-incorporated delivering minimum errors. The computation speed to fit a 192×192 T2 map from 5 T2-preparation TEs was around 0.07 s and 0.10 s on a 2.3 GHz 4-core CPU with 8 GB memory for 2-parameter and 3-parameter models, respectively.

3.3.3 In vivo Experiments

The T2 maps and corresponding error maps obtained by different sampling and reconstruction methods of one slice from one volunteer are displayed in Fig. 3.5. Similar to the simulation results from the digital phantom (Fig. 3.4), aliasing artifacts and noise were most notable when using SENSE, and were minimized when applying the model-based CS-incorporated method, for both non-rotated or rotated spiral trajectories. The nRMSE of SENSE, CS SENSE, model-based, and model-based CS-incorporated of brain tissue without CSF partial volume averaged from four volunteers were 16.9%, 11.4%,10.0%, and 8.9% using non-rotated trajectories, vs. 15.9%, 11.2%, 9.6%, and 8.2% using rotated trajectories. The model-based CS-incorporated method generated 47%, 22%, 11% and 48%, 27%, 15% less nRMSE using non-rotated and rotated trajectories than the other three reconstruction approaches, respectively (P < 0.05 on the corresponding error maps, two-tailed student's t-test). Compared to non-rotated trajectories, rotated spiral trajectories returned slightly improved accuracy, similar to that found with the simulations.

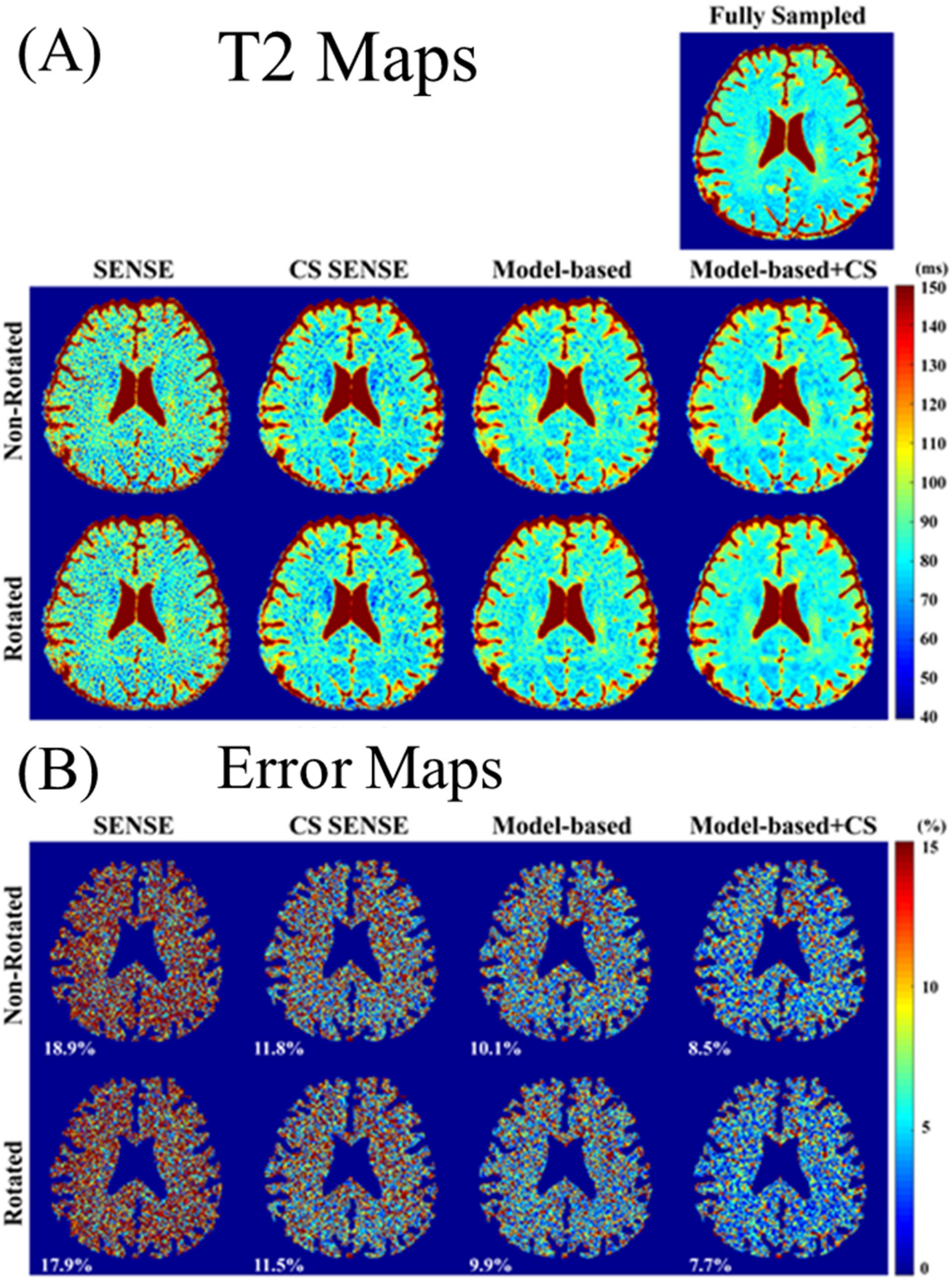

Figure 3.5: In vivo experiment results of a 44-year-old male: (A) T2 maps and (B) corresponding normalized error maps estimated by different undersampling and reconstruction methods with an in-plane 5-fold acceleration. Error maps were masked by an eroded mask of T2 maps to exclude CSF. The corresponding nRMSEs of the masked maps were labeled in the left bottom corner of each cell in the error maps.

The CSF-nulling sequence (Fig. 3.2C) yielded similar results among different reconstruction techniques (data not shown). The whole-brain T2 maps with and without the CSF nulling module, as estimated by the Model-based CS-incorporated method using rotated spiral trajectories, are exhibited for three healthy volunteers (Fig. 3.6) for comparison, showing largely in agreement. The corresponding whole-brain T2-weighted images at TE_{prep} = 80 ms are shown in Fig. 3.7, where the CSF was mostly suppressed with the sequence with the CSF nulling module. The averaged T2 values of several brain tissues (See Fig. 3.8 for ROI selections) are listed in Table 3.1. The absolute T2 values were close to other literature values (103,138,139), with white matter in the range from 70 to 80 ms, and gray matter in the range from 90 to 110 ms. For all ROIs, the estimated T2 values were found to be slightly shorter by the sequence with CSF nulling.

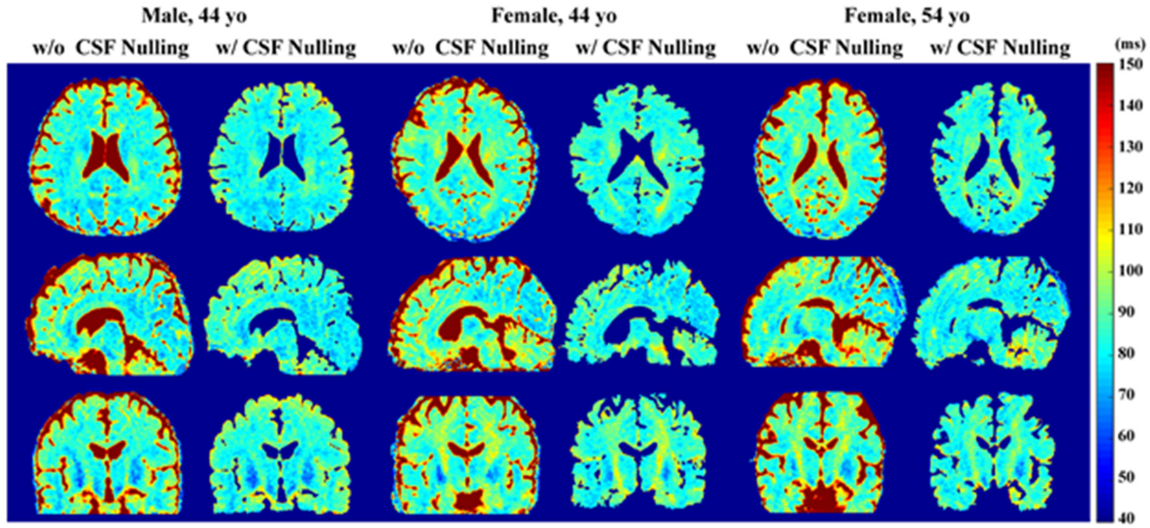

Figure 3.6: Whole-brain cross-sectional T2 maps in axial, sagittal, and coronal views of three healthy volunteers estimated by pulse sequences with and without CSF nulling, using the rotated spiral trajectories and the model-based CS-incorporated reconstruction method with an in-plane 5-fold acceleration.

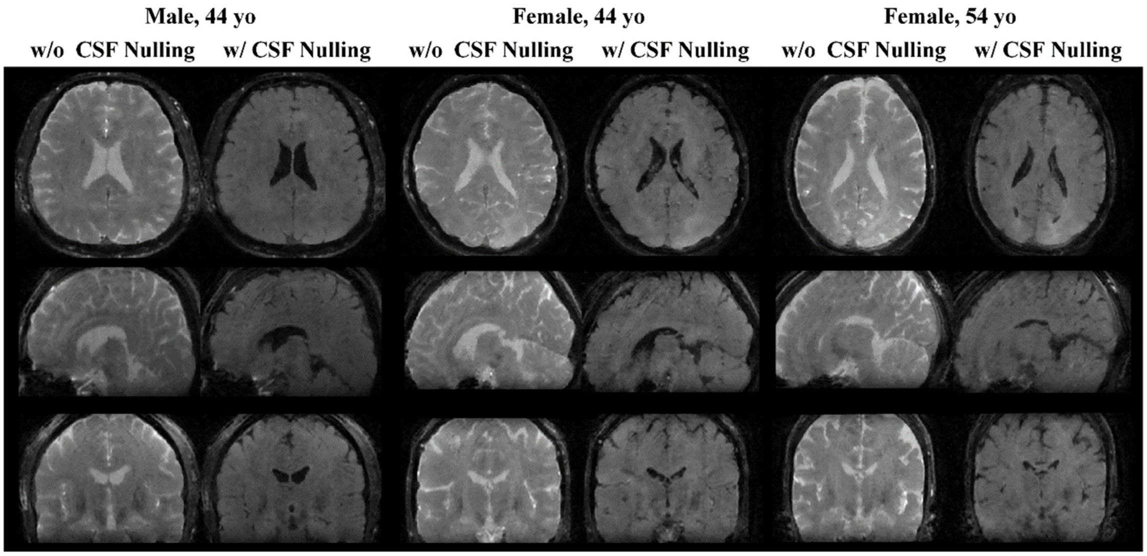

Figure 3.7: Whole-brain cross-sectional T2-weighted images (TEprep = 80 ms) in axial, sagittal, and coronal views of three healthy volunteers estimated by pulse sequences with and without CSF nulling, using the rotated spiral trajectories and the model-based CS-incorporated reconstruction method with an in-plane 5-fold acceleration.

	without CSF nulling	with CSF nulling
FGM	92±5	90±4
FWM	80±2	75±2
GPA	68±7	64±4
OGM	81±3	76±4
OWM	78±3	74±3
Splenium	85±3	81±2
Thalamus	75±3	70±4

Table 3.1: The averaged T2 values (ms, mean±SD) within ROIs of typical structures, estimated by pulse sequences with and without CSF nulling, using the rotated spiral trajectories and the model-based CS SENSE incorporated reconstruction method. ROI: FWM = frontal white matter; FGM = frontal gray matter; GPA = globus pallidus; OWM = occipital white matter; OGM = occipital gray matter.

Note that the SNR (mean/SD) within these ROIs of the T2-weighted images at TE_{prep} = 20 ms were around 10–50 (data not shown) with 5-fold reconstruction, which meets the setting in simulation.

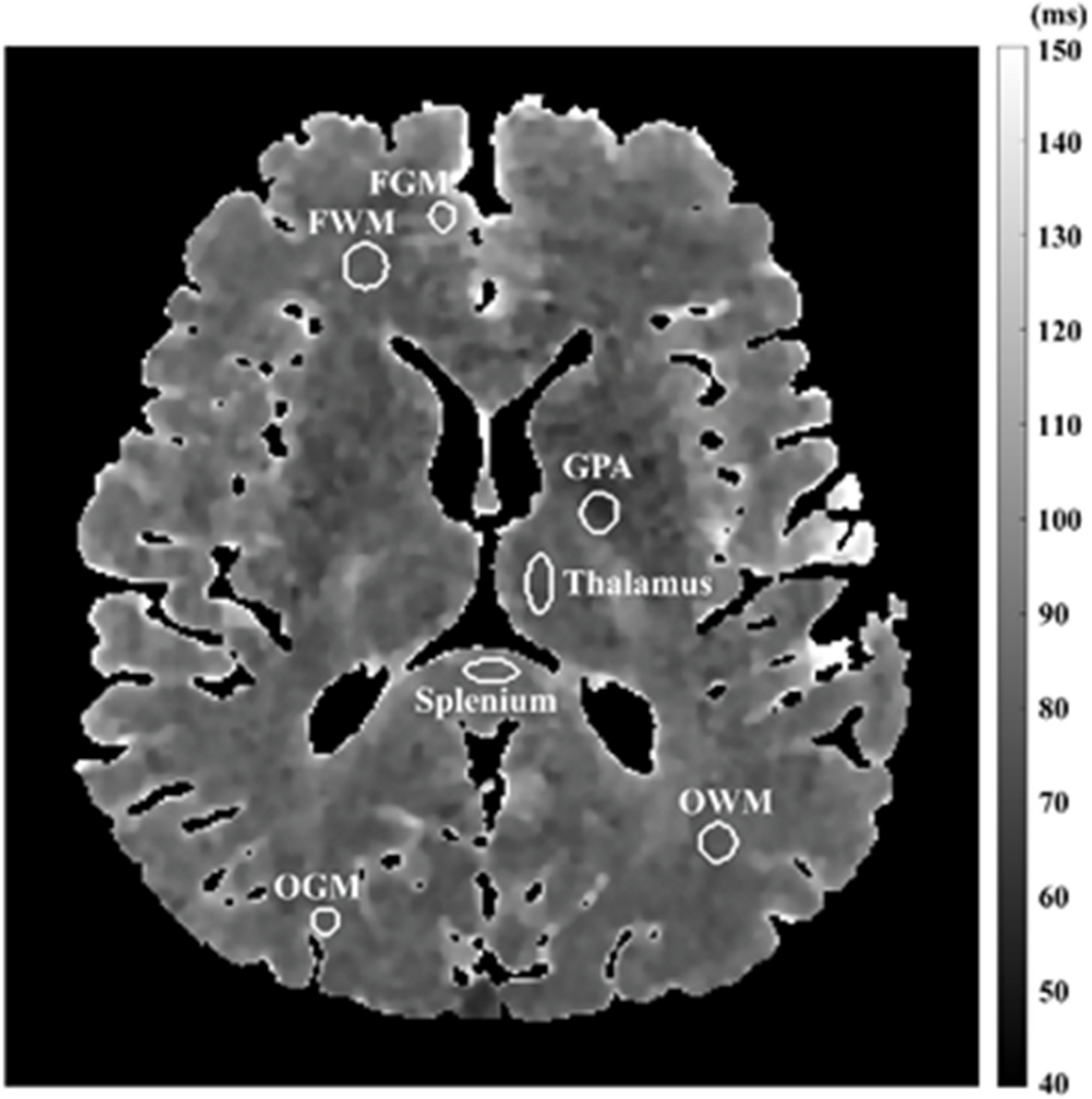

Figure 3.8: A T2 map with manually drawn ROIs of frontal gray matter (FGM), frontal white matter (FWM), globus pallidus (GPA), occipital gray matter (OGM), occipital white matter (OWM), splenium, and thalamus.

3.4 Discussion

This work demonstrated the feasibility of a rapid (2-3 min with 5-fold in-plane acceleration) T2 quantification technique with 3D high-resolution (1.2 mm isotropic) and whole-brain coverage. The method utilized a T2-prepared GRE sequence and the model-based CS-incorporated joint reconstruction. The reliability of its T2 estimation across the brain was achieved with around 8% normalized errors compared to reference scans using fully-sampled data.

This work only explored 3D stack-of-spiral trajectory with in-plane variable-density. The acceleration could be further improved with undersampling along the slice direction or using alternative 3D non-Cartesian trajectories (140,141). The combination of model-based and CS reconstructions in this study delivered 11-28% less error than applying them separately. This might be expected from the improved performance of the reconstruction provided by the joint spatial and parametric constraints.

The non-rotated and rotated undersampling schemes in the spiral trajectories along the T2 weighting (TE) dimension implemented here, are similar to the shifting Cartesian (102,142) and golden-angle radial trajectories (92,110) published elsewhere. Presumably, different undersampling trajectories introduce different artifacts that might be compensated and reduced by reconstructing the k-space data along the parametric dimension jointly. However, the improvements achieved with the rotated spiral trajectory was small. One possible reason was that we used a fixed 45° angle between successive interleaves within one T2 preparation or rotation between T2 preparations in the acquired spiral trajectories instead of the golden angle (143), which might afford a lesser degree of incoherence for compressed sensing. Further improvements might be achieved with golden-angle rotations of interleaves along the parametric (TE) dimension or exploring other trajectories designed to optimize incoherent sampling.

In the current implementation, the iterative reconstruction was implemented slice-by-slice, through 2D nonuniform Fast Fourier transform (NUFFT) (144) performed on an external CPU using projected-gradient constraint optimization. An improved implementation would be to conduct the iteration and 3D NUFFT on a Graphics Processing Unit (GPU) directly connected to the scanner. The projected-gradient algorithm converges quickly to obtain a local optimal solution, but there is no guarantee on the convergence of the non-convex problem to a global minimum (100). Magnetic resonance fingerprinting (MRF) (145–147) and other techniques (93,116,148,149) have circumvented this problem using dictionary matching reconstruction methods by generating data with varying both sequence parameters and sampling trajectories together.

An essential module of the proposed pulse sequence is T2 preparation, which is commonly adopted for T2 weighting with a 3D readout. The effect of imperfect B_1 on the prescribed 90° flip-down and flip-up hard pulses appends the desired pure T2 weighting with a complexed T1 component (Eq. A.3 in the Appendix). The resultant deviation from a simple mono-exponential decay model can cause fitting bias for T2 prepared approaches, which has been largely overlooked to date. Although more exact fitting with a 3-parameter model could avert this issue, we found that its accuracy and precision were rather poor at moderate SNR levels (Fig. 3.3). Our simulation results indicated that the 2-parameter-weighted fitting was robust over a wide range of B_1 scales and noise (SNR) levels. The simulation was performed for T1 = 1000 ms. According to Eq. A.3 in the Appendix, longer T1 values, such as in gray matter or at higher fields (B_0), would induce more bias to the 2-parameter fitting model with an approximate $\cos^2(B_{1+} \times 90°)$ dependence

in the presented work, the previous T2-weighting history before each T2 preparation module was removed using a post-acquisition saturation pulse applied with a fixed delay. Another strategy is to add a sufficient number of dummy pulses after the GRE readout to ensure the same steady-state conditions are reached with each T2 weighting (118). This could potentially enhance the available signal as it leads to higher longitudinal magnetization before the T2 preparation.

Routine T2-weighted FLAIR imaging enhances the conspicuity of brain lesions with long T2 by suppressing the CSF signal. Similarly, brain T2 mapping would be more readily translated to the clinic if the fluid signal were removed. In this study, a CSF nulling module (Fig. 3.2C) was applied to mitigate the CSF partial volume effect. This method was shown to be effective for T2 estimation of typical structures in the brain, which, however, only provided small differences with the results obtained by the sequence without CSF nulling (Fig. 3.6, Table 3.1). This method also suffered some loss in SNR due to the longer recovery time per acquisition, a challenge also faced by the 3D FLAIR sequence (150). Alternatively, CSF partial volume effects could be accounted for with additional sampling of the relaxation curves and fitted by a two-compartment (three- or even four-parameter) model, which however, would be more SNR-demanding and computationally complex.

The proposed protocol was compared to the same T2-prepared spiral GRE protocol using fully-sampled data. A fully-sampled Cartesian spin-echo acquisition would be desirable for a more rigorous validation. However, the gold-standard single-echo spin-echo sequence is quite time-consuming even for a 2D scan (116,149) and generally not practical for 3D high-resolution human experiments. A multi-spin-echo sequence would be more efficient but its signal is not a pure mono-exponential decay, as stimulated echoes could be generated from imperfect echo refocusing (148,151). The accuracy, precision, and reproducibility of our method could be evaluated using system phantoms with known relaxation properties (152,153). Note that if the spatial resolution is coarser than the 1.2 mm isotropic chosen for this study, acquisition time would be faster than 2-3 min, and the SNR would also be higher due to the larger voxel size, at the cost of more partial volume effects mixing gray matter and white matter, and normal tissue and lesion. Further studies of patients with central nervous system disease are needed to explore the clinical value of the proposed technique.

Chapter 4 Phase contrast coronary blood velocity mapping with both high temporal and spatial resolution using triggered Golden Angle Spiral k-t Sparse Parallel imaging (GASSP) and shifted binning

4.1 Introduction

Phase contrast (PC) velocity-encoded MRI (154) enables blood velocity and flow measurements of the coronary arteries (155,156). Coronary blood flow measurements are of clinical interest, because they enable the assessment of vascular physiology, to complement conventional anatomic lumen imaging. Among others, coronary PC MRI has been applied to assess coronary flow reserve (157–160), local coronary endothelial dysfunction (161–163), and more recently, to measure the pressure gradients across a coronary artery stenosis (164).

Coronary PC MRI is challenging because the coronary arteries are small in diameter (<3-4 mm) and move due to cardiac contraction and respiration. High spatial resolution $\Delta x \leq 1$mm is needed for accurate assessment of the mean flow (165), including the determination of cross-sectional areas that may benefit from even smaller voxel sizes (166). Furthermore, high temporal resolution is needed due to fast cardiac motion and to resolve temporal detail, especially for the right coronary artery (RCA), which is twice as mobile as the left anterior descending artery (LAD) (167). According to Marcus et al., the temporal resolution τ should be ≤58ms and ≤23ms for LAD and RCA, respectively (168). Additionally, PC MRI requires two acquisitions with identical parameters except for the strength of the velocity encoding (VE) gradients to subtract out any background phase (154). As a result, PC MRI is twice as time-consuming as anatomical cine scans, which is especially challenging when using breath-holding to suppress respiratory motion.

Initial coronary PC MRI utilized single breath-held Cartesian segmented spoiled gradient echo techniques enabling acquisitions with Δx of 1.4-1.6mm and a τ of 120-160ms (155,156). Keegan et al. pioneered the use of highly efficient spiral readouts to improve the temporal resolution of breath-held cine PC MRI (169–171). More recently, 3T-scanners have been applied to take advantage of the increased signal-to-noise ratio (SNR), enabling higher spatial resolution as well (161,171,172). Nevertheless, state-of-the-art breath-held spiral techniques at 3 T focus on either high spatial resolution (161,172) or high temporal resolution (171). Brandts et al. use Δx = 0.8mm and show accurate and reproducible measurements of RCA peak velocity and flow volumes (172). To achieve such a small voxel size, they used a long, 26-ms spiral readout window, leading to a temporal resolution of 33ms and, potentially susceptible to motion blurring. Moreover, the long spiral readouts may lead to off-resonance induced image blurring (173). Keegan et al. trade spatial resolution for high temporal resolution (τ = 20ms) to assess temporal patterns of coronary blood flow throughout the cardiac cycle (171). To achieve such a high temporal resolution, they shorten the spiral readout to 12 ms, forcing a rather large voxel size Δx of 1.4mm.

To achieve both high temporal and high spatial resolution in a single breath-hold, the data acquisition needs to be accelerated. Acquisitions with non-Cartesian trajectories can be accelerated with parallel imaging (PI) (174,175) and additionally with compressed sensing (CS) (176), which allows acceleration using data redundancy due to sparsity in any actual or transformed domain. In cine MRI, the temporal domain is transform-sparse and suitable for CS reconstruction (177,178). Besides sparsity, incoherent undersampling artifacts are also essential for successful CS reconstructions (176). Incoherence in the temporal domain can be achieved using a golden angle (GA) rotation of radial or spiral readouts (179,180). K-t sparse SENSE combines PI and CS in the temporal dimension with acceleration factors of 8 for structural cine (181) or 6 for phase-contrast cine (182) using Cartesian sampling. The combination of k-t sparse SENSE and GA rotation of either radial or spiral sampling is feasible in cine MRI as well (183–185).

However, while the acquisition of consecutively GA-rotated radial spokes or spiral arms offers flexibility in terms of temporal resolution versus spatial resolution in dynamic imaging with uniform coverage of k-space (179), when binning data into non-consecutively acquired cardiac frames, the k-space coverage may not be uniform (186–189). This non-uniformity creates gaps in azimuthal distribution and strongly depends on the number of cardiac frames and the heart rate (HR), which is unpredictable especially for stress studies. To achieve higher k-space uniformity in cine MRI, Han et al. proposed the use of a segmented golden ratio approach, where k-space is divided into smaller segments for each heartbeat during the acquisition. Spokes are then distributed by the golden ratio within each segment, which enables retrospective selection of the temporal window with reduced k-space gaps (189) but requires prospective triggering and prevents retrospective data rejection due to motion or arrhythmias.

In this chapter, we combine k-t sparse SENSE with GA rotated spiral readouts to achieve single breath-held coronary PC MRI with both high spatial (0.8mm) and high temporal (~ 21ms) resolutions. GA Spiral k-t Sparse Parallel imaging (GASSP) (190) is combined with interleaved two-sided VE (191) and electrocardiogram (ECG) based retrospective cardiac gating (192). To reduce k-space gaps of binned cine data, two new methods are tested (193). First, the binning window is shifted by up to the duration of one cardiac frame, and the shift leading to the smallest k-space gap is picked for image reconstruction. Second, a triggered GA scheme is introduced that applies a new rotation angle to consecutive arms and the standard GA at the beginning of each heartbeat using prospective ECG-triggering. Compared to the segmented golden ratio approach (189), this triggered GA scheme is suitable for retrospective rejection of data that is corrupted by motion or for other reasons. Monte-Carlo numerical simulations are performed to determine the optimal rotation angles in the triggered GA scheme, and to quantitatively evaluate the performance of the proposed methods to reduce k-space gaps. The proposed methods are tested at 3 T in healthy human subjects, validated against published methods (171,172), and intra-scan, inter-scan, and intra-observer reproducibility are determined.

4.2 Methods

4.2.1 Coronary PC MRI with Standard GA Scheme

Coronary PC cine with both high temporal and high spatial resolution was implemented by combining GASSP with interleaved two-sided VE (192), referred to here as the standard GA scheme. Spiral arms were acquired in pairs of positive and negative VE with the same azimuthal angle, and then rotated by GA for the next pair (top row of Fig. 4.1a). The GA was 137.508° (179,182). Spiral arm pairs were continuously acquired while the ECG signal was recorded for retrospective data binning.

To achieve high temporal resolution and to mitigate blurring effects due to B0 inhomogeneity, the spiral readout window was set to ~14 ms leading to a repetition time (TR) and minimal τ of <21 ms. The spatial resolution was set to 0.8 mm for a 350×350 mm^2 field-of-view (FOV). This would normally require 34 spiral arms to obtain a fully sampled k-space, i.e., 68 heartbeats to acquire both VE datasets, which is too long for a single breath-hold scan. Therefore, the spiral trajectory was undersampled with a variable density pattern (194,195). The spiral trajectory was designed (196) so that the central 15% of k-space were fully sampled with 10 arms. The outer 70% of k-space were uniformly undersampled by a factor of 4.6, and the undersampling factor was linearly increased in between. 500 spiral arm pairs (1000 arms) were acquired in total, leading to a scan time of ~21 s. The maximum encoded velocity (V_{enc}) was set to ±35cm/s. Other parameters of the two-dimensional (2D) gradient echo sequence were an echo time (TE) = 3.3 - 3.5ms; a 1-2-1 binomial spectral-spatial water excitation to suppress fat; a flip angle (FA) = 20°; and a slice thickness (ST) = 8 mm.

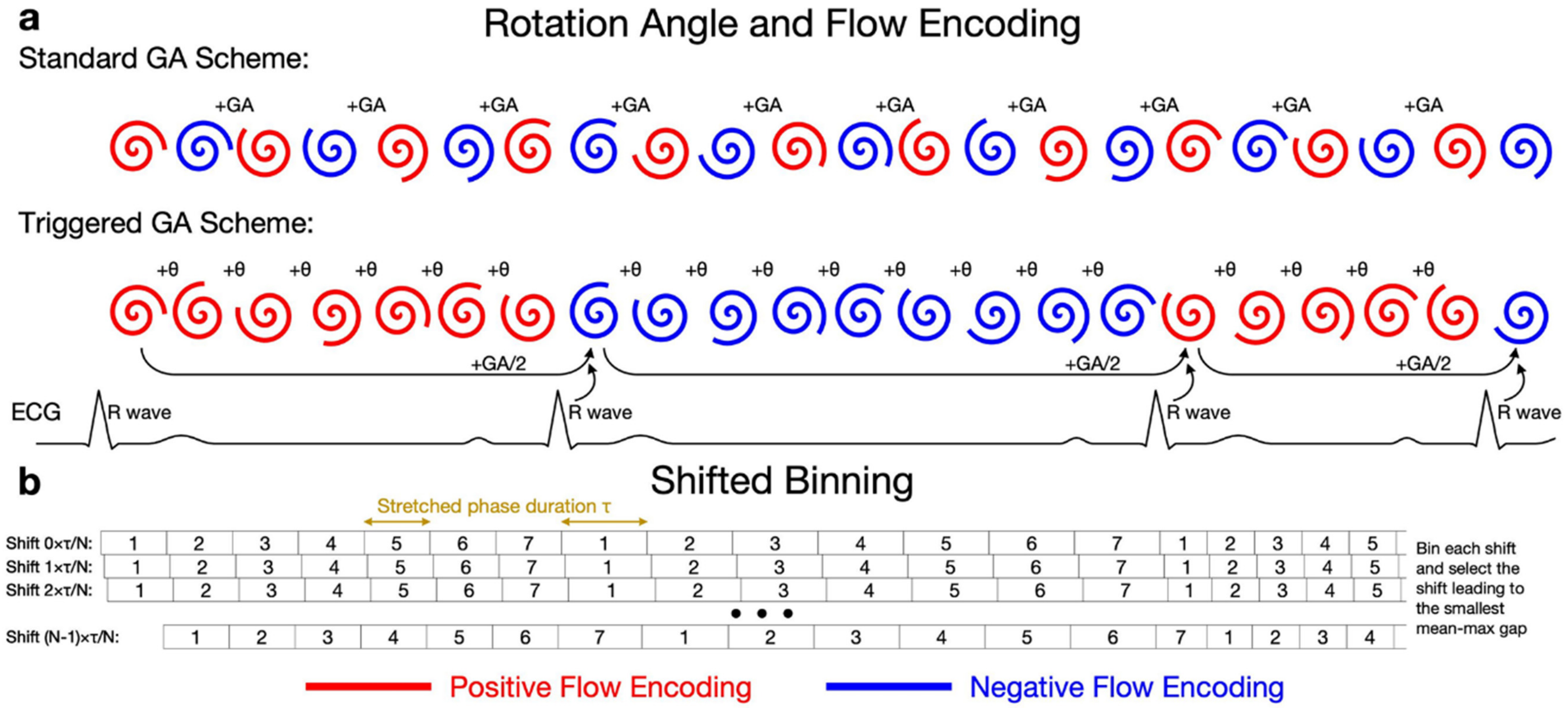

Figure 4.1: Rotation angle and velocity encoding (VE) directions of the triggered GA scheme compared to the standard GA scheme (a) and shifted binning process (b). The VE direction in the standard GA scheme is toggled each TR while it is toggled every heartbeat in the triggered GA scheme. The rotation angle in the standard GA scheme is GA = 137.508° throughout, whereas in the triggered GA scheme it is θ = 83.8° except at the beginning of each heartbeat, when the rotation is set to GA/2 = 68.754° relative to the first spiral arm of the previous heartbeat (a). Both schemes are subject to the shifted binning process (b). Bins were shifted N times by temporal resolution τ divided by N (N=20), and for each shift the mean-max-gap was determined. The shift that resulted in the smallest mean-max-gap was selected for image reconstruction.

4.2.2 Retrospective Gating with Shifted Binning

The continuously acquired spiral data were binned into cardiac frames based on the ECG signal using non-linear stretching (197). Positive and negative VE data were binned separately. The number of cardiac frames was determined by dividing the acquisition's average RR-interval, the time between two consecutive R-waves, by the required temporal resolution τ (= TR <21 ms), and was, therefore, subject-specific. As a result, subjects with lower HR had more cardiac frames and less data assigned to each cardiac frame (i.e. higher undersampling factor). Relative to a uniformly sampled k-space, the undersampling factor was around 3.0 for HR = 80, but increased to 3.9 and 4.7 for HR = 60 and 50, respectively, but was higher in practice because binning leads to non-uniform undersampling, and hence, gaps in k-space (186–189).

In this work, we tested two methods to reduce the largest k-space gaps to improve image quality. The first method, referred to as shifted binning, shifted the binning windows by up to the duration of τ, by trying N = 20 equally spaced shifts and selecting the shift that minimized the largest gaps (Fig. 4.1b). For this, the k-space gaps after binning were quantitatively evaluated by determining first the maximal angular spacing between the sorted spiral arms (max-gap) in each bin (for each cardiac frame and VE direction); and second, the average of the max-gaps (mean-max-gap) over all of the cardiac frames and both VE directions. This was repeated N times, each time shifting the binning windows by τ/N, leading to N different mean-max-gaps (Fig. 4.1b). The shift resulting in the lowest mean-max-gap was eventually chosen to bin the data, and the resulting images were labeled with ‘best shift.’ For comparison, the shift associated with the largest mean-max-gap was applied as well, and labeled as ‘worst shift.’

4.2.3 Coronary PC MRI with triggered GA scheme

In addition to shifted binning, a triggered GA scheme was implemented as the second method to improve k-space uniformity. The triggered GA scheme uses two different rotation angles and prospective ECG-triggering to reset the rotation angle and to toggle the VE direction at the beginning of each heartbeat. As shown in the bottom row of Fig. 4.1a, spiral arms with the same VE direction, either positive or negative, were continuously acquired within one heartbeat. The rotation angle between consecutive arms within a heartbeat was modified to $\theta = 83.8°$, which was selected based on the numerical simulations below. When an R-wave was detected, the rotation angle was reset so that the first spiral arm in a new heartbeat was rotated by half the GA (68.754°) as compared to the first spiral arm of the previous heartbeat. The subsequent arms were rotated again by θ. Concurrently with the angle being reset, the VE direction was inverted to toggle its direction after every heartbeat. Hence, the first spiral arms of heartbeats with the same VE direction were rotated by the GA.

1000 spiral arms were acquired in total for the triggered GA scheme, but due to varying RR-intervals, the total number of spiral arms in each VE direction was usually slightly different than 500. All other acquisition parameters of the triggered GA scheme were identical to the standard GA scheme including the shifted binning gating process.

4.2.4 Simulation of k-space gap after binning

A Monte-Carlo numerical simulation was performed to determine the optimal rotation angle θ in the triggered GA scheme, and to quantitatively evaluate the performance of the shifted binning method and the triggered GA scheme. To quantify k-space uniformity, both the mean-max-gap and the largest max-gap (max-max-gap) were determined and called ‘1-frame mean-max-gap’ and ‘1-frame max-max-gap’, respectively. Additionally, because the reconstruction applies temporal sparsity constraints, k-space gaps in one cardiac frame can be compensated for during the reconstruction using spiral arms from neighboring frames. For this, spiral arms from consecutive frames should be located at the center of the largest gap, which can be achieved if θ ≈ max-max-gap / 2. Therefore, θ was chosen to minimize the absolute of (max-max-gap / 2) - θ. To test if the triggered GA scheme indeed reduces gaps that overlap in consecutive cardiac frames, the mean-max-gap and max-max-gap were also calculated after combining the arms of three consecutive frames, and called ‘3-frame mean-max-gap’ and ‘3-frame max-max-gap’, respectively.

The simulation covers a wide range of HR from 40 to 100 beats per minute with a step size of 1 beat per minute. TR = 20.65 ms was used, leading to a duration of 20.65 s for 1000 spiral arms. For each HR, a series of RR-intervals were simulated to cover the 20.65 s duration using a normal distribution with a mean value of the given RR-interval and a standard deviation (SD) of 50 ms (198). A series of spiral rotation angles were generated using the standard or a triggered GA scheme. These angles were then binned with shifted binning, and mean-max-gap and max-max-gap determined. The simulation was repeated 200 times for each HR and the corresponding values averaged. For the triggered GA scheme, these simulations were repeated for θ ranging from 1° - 160° in steps of 3.6°. For the chosen θ (83.8°), the best shift was compared to the worst shift, and the triggered GA scheme to the standard GA scheme.

4.2.5 In vivo experiments and reference acquisitions

All human studies were approved by the Johns Hopkins School of Medicine Institutional Review Board and informed, written consent was obtained from all study subjects. In vivo studies were conducted on 8 healthy human subjects with no history of heart disease (37±7 years old, 1 female). MR studies were carried out on a 3T scanner (Achieva, Philips Healthcare, Best, The Netherlands) using a 32-channel cardiac receive coil and subject-specific shimming of the excitation radiofrequency field (199).

All 2D coronary PC scans were acquired within a single end-expiratory breath-hold and were planned orthogonally to intersect either proximal or mid segments of the coronary arteries that were straight for at least 20 mm. To facilitate careful planning of the image orientations, targeted 3D DIXON scans were performed to provide water and fat images of both RCA and LAD in 3D double oblique views (200,201) with TR/TE1/TE2 = 5.6-6.1/1.9-2.2/3.6-3.9 ms, FOV = 200×200×32 mm^3, acquired voxel size = 1×0.85×3 mm^3, and scan duration of ~1.5-6 min depending on the efficiency of the respiratory navigator system. These targeted views were defined using the three-point planning tool on the target vessel of a whole heart coronary angiography scan with intermediate resolution acquired in ~1 minute. All scans for image planning were gated by respiratory navigator-echo and were ECG-triggered to mid-diastole.

The standard and triggered GA scheme were compared to existing methods with either high spatial but low temporal resolution (161,172) (the 'high-spatial' sequence), or high temporal but low spatial resolution (171) (the 'high-temporal' sequence).

The high-spatial sequence was ECG-triggered and acquired a fixed (depending on the patient's HR) number of arms with the same spiral rotation angle in each heartbeat. The VE direction was inverted at every heartbeat, and 10 spiral arms were acquired for each VE, leading to a total scan time of 20 heartbeats. A high in-plane spatial resolution of 0.8mm led to long spiral readouts of ~33 ms and a long TR of ~40 ms. Other acquisition parameters were identical to the standard GA sequence except for the FOV = 250×250 mm^2. Because of the ECG-triggering, the last end-diastolic cardiac frames were missed as the sequence was interrupted to wait for and detect the next R-wave. Images and velocity maps were generated on the vendor-provided platform.

In the high-temporal sequence, VE direction was also inverted every heartbeat, with positive and negative arms acquired in 13 heartbeats each. With a high temporal resolution of TR = ~20 ms (spiral readout = ~13 ms), the spatial resolution was relaxed to 1.4 mm to fully cover the k-space with 13 arms. Retrospective ECG-gating was used to bin the data into cardiac frames. Other acquisition parameters were identical to the standard GA sequence. Images were reconstructed off-line.

To determine inter-scan reproducibility of the triggered GA sequence, the subjects were removed from the scanner and given a 10-minutes break, before repeating the examination. For 4 of the subjects, the triggered GA sequences were also repeated immediately without repositioning to evaluate the intra-scan reproducibility.

4.2.6 Image reconstruction and Flow analysis

Image reconstruction and off-resonance deblurring (except for the high-spatial sequence) were implemented in the graphical programming interface (202), and code is available at https://github.com/jhu-cardiac-mri/triggeredGASSP/ (SHA-1: 86fee6aa3d7baf885c33dae6ad27ffcde0700750) including a subject-approved, anonymized dataset. Retrospective binning of k-space was performed with shifted binning and data were reconstructed by GASSP (190), minimizing parallel imaging data consistency and temporal total variation (TV) sparsity constraints (183). In this work, the original GASSP reconstruction for structural CINE images was adapted for PC by joint reconstruction of both VE steps with an additional TV sparsity constraint along the flow dimension. The flow sparsity constraint was only applied to the magnitude of the signal to preserve the phase information of each VE direction. The weight was set to 0.03 for the temporal sparsity constraint, and 0.015 for the additional flow sparsity constraint.

Flow-compensated images were generated by geometric mean, by which positive and negative VE phases were canceled by complex multiplication. Flow-compensated images were utilized to determine the deblurring frequency at the location of the coronary artery (203), which was subsequently used to deblur the original two VE images I_+ and I_-. The deblurred VE images were used to compute deblurred flow-compensated images for vessel segmentation and deblurred velocity maps for velocity quantification. The velocity maps were computed by phase-difference with pixel-wise conjugated multiplication (173)

$$V = \frac{V_{enc}}{\pi} \arg(I_+ I_-^*). \qquad 4.1$$

Here V is the velocity and arg is the argument of the complex values.

A semi-automatic flow analysis software was implemented in MATLAB (Mathworks, Natick, MA, USA) that included vessel segmentation and background phase correction. All images were Fourier-interpolated to 0.1 mm spatial resolution for more precise segmentation (166). First, the vessel area A_v was semi-automatically computed from three consecutive end-diastolic frames by full-width-half-maximum thresholding. Second, the vessel in each cardiac frame was segmented with a circular region of interest (ROI) with the same area A_v, by clicking the center of the interpolated vessel. Another circular ROI, the myocardial ROI with the same area A_v, was manually selected on surrounding myocardial tissue for background phase correction. Background phase correction was achieved by subtracting the mean velocity in myocardial ROI from the velocity in the vessel ROI.

Eleven metrics were determined. The vessel area A_v was determined in the first step of the segmentation. Eight velocity metrics were measured: peak systolic and diastolic velocity (PSV, PDV) together with the trigger delays to those peaks (TSV, TDV); and those velocity metrics were determined in two ways, that is, as the spatial mean (mean) and maximum (max) velocity within the vessel ROI. And two flow metrics were measured: product of mean velocity and A_v integrated over all cardiac frames as flow volume either per cardiac cycle or per minute.

To limit the number of statistical tests, only four of the metrics (mean PSV, mean PDV, flow per minute, and A_v) acquired with the proposed triggered GA scheme were compared to the high-spatial and the high-temporal sequences using paired Student’s t-test with a modified Bonferroni correction to account for the eight tests. Additionally, Bland-Altman analysis was performed for the same four metrics.

The intra-scan, inter-scan, and intra-observer reproducibility were determined by the intra-class correlation coefficient (ICC) for absolute agreement. For intra-scan reproducibility, Bland-Altman analysis was performed as well. To test the intra-observer agreement, the same observer repeated the flow analysis at least one month after the first observation, whereas the two analyses of the intra-scan and inter-scan reproducibility were performed on the same day. A *P*-value smaller than 0.05 was considered significant for all tests.

4.3 Results

The simulation results demonstrate the dependencies between the rotation angle θ of the triggered GA scheme, the RR-interval, and the mean-max-gap and max-max-gap, respectively (Fig. 4.2).

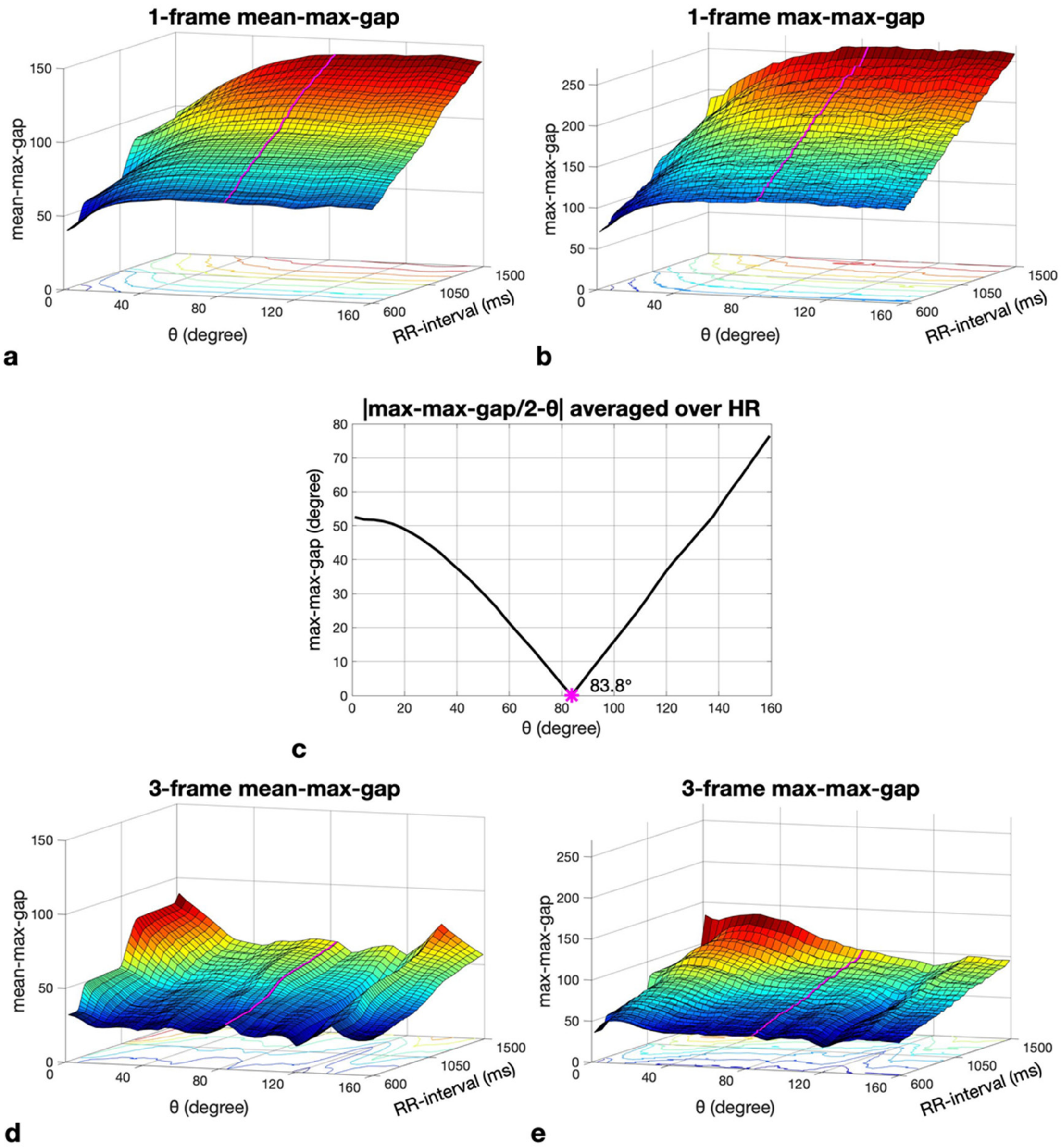

Figure 4.2: Surface plots of the mean-max-gap (a, d) and the max-max-gap (b, e) of the proposed triggered GA scheme with best binning shift were determined for a range of RR-intervals and rotation angles θ using Monte-Carlo simulations. The gaps were determined for a single cardiac frame (a, b) or for three consecutive frames (d, e). In (c), the minimum of |max-max-gaps/2-θ| averaged over all heartrates (HR) is used to determine the rotation angle θ = 83.8° that ensures that neighboring cardiac frames have k-space data in the center of the largest gap, which is beneficial for reconstruction with temporal sparsity constraints. The purple line in the surface plots indicates the chosen θ.

The 1-frame mean-max-gap increases as functions of both the RR-interval and θ (Fig. 4.2a). A similar behavior but with larger gaps is seen for 1-frame max-max-gap (Fig. 4.2b). The |1-frame max-max-gap / 2 – θ| averaged over the range of simulated HR in Fig. 4.2c is minimized for θ = 83.8°. Therefore, the rotation angle θ in the triggered GA scheme was chosen to be 83.8° as noted in section 4.2.4. The 3-frame mean-max-gap and 3-frame max-max-gap at θ = 83.8° are smaller than even the best 1-frame gaps, and are also smaller than the 3-frame gaps for smaller θ (Figs. 4.2d and 4.2e).

Figs. 4.3a and 4.3b illustrate the simulated 1-frame and 3-frame mean-max-gaps, respectively, as a function of the mean RR-interval of both the standard and triggered GA schemes with both best and worst shift. As the RR-intervals increase, larger gaps are observed. By using shifted binning, the 1-frame mean-max-gaps of the best shift drop about 14°-22° for triggered GA and 14°-27° for standard GA scheme (Fig. 4.3a). The 1-frame and 3-frame mean-max-gaps of the triggered GA scheme increase approximately linearly with the mean RR-interval (608-1503ms), whereas those of the standard GA scheme exhibit an additional modulation pattern. The shifted binning has little effect on the 3-frame mean-max-gaps (Fig. 4.3b). The 3-frame mean-max-gaps of the standard GA scheme are larger than those of the triggered GA scheme for most RR-intervals and the modulation pattern is even stronger than the 1-frame mean-max-gaps.

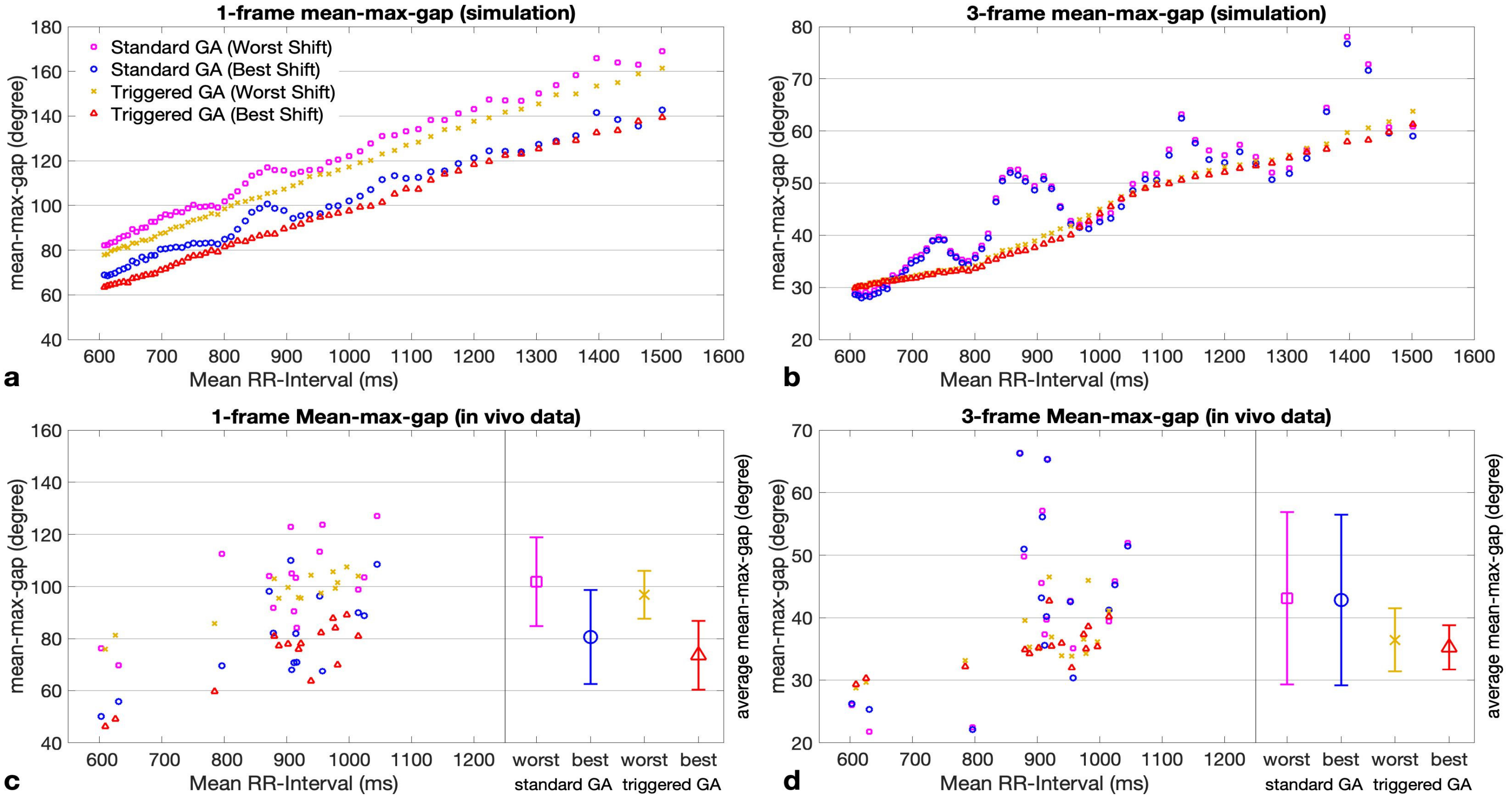

Figure 4.3: 1-frame mean-max-gap (a, c) and 3-frame mean-max-gap (b, d) as a function of RR-interval of simulated datasets (a, b) and in-vivo datasets(c, d) for both standard GA and triggered GA schemes with both the best and the worst binning shift. Each marker in (a) and (b) is an average of 200 repeated simulations. In (c) and (d), each data point of the standard GA scan (purple rectangles and blue circles) is from a single scan, while the points of the triggered GA data (yellow crosses and red triangles) are averages of either 2 (inter-scan) or 3 (intra- and inter-scan) repetitions. In the simulations, the 1-frame and 3-frame mean-max-gaps of the triggered GA scheme are approximately linear, whereas the ones of the standard GA scheme exhibit an additional modulation which is magnified in the 3-frame case. The mean and standard deviation (error bars) of in-vivo experiments (c, d) are demonstrated to the right of their respective graphs. T-tests show a significant reduction of the gaps for triggered GA scheme with best binning shift compared to the standard GA scheme with best binning shift.

Complete datasets with both the RCA and the LAD were obtained from all 8 subjects. However, the RCA of one subject was too small and hence was excluded from analysis, leading to a total of n = 15 analyzed vessels.

Figs. 4.3c and 4.3d illustrate the 1-frame and 3-frame mean-max-gaps, respectively, measured in human subjects. In Fig. 4.3c, the 1-frame mean-max-gaps with the best shift are smaller compared to those with the worst shift. The mean-max-gaps averaged among all cases using the triggered GA scheme (73.6°±13.3°, best shift) are significantly smaller (t-test *P*=0.03) than those of the standard GA scheme (80.6°±18.0°, best shift). When combining 3 consecutive frames (Fig. 4.3d), some large gaps were observed in the scatter plot of the standard GA scheme at RR-interval of around 872 ms and 916 ms, which is consistent with the simulation results in Fig. 4.3b. As a result, the 3-frame average mean-max-gaps of the standard GA scheme (42.8°±13.7°, best shift) is significantly larger (t-test *P*=0.04) than that of the triggered GA scheme

Fig. 4.4 shows an example dataset acquired with both GA schemes and worst and best shifts. By using the best shift, the mean-max-gaps were reduced by 21° and 19° for standard and triggered GA scheme, respectively. With the best shift, the triggered GA scheme has lower mean-max-gaps (-5.5°) as compared to the standard GA scheme. Swirling artifacts were observed in the right ventricle (RV) and the left ventricular (LV) wall (yellow arrows) in the standard GA images, for both VE and flow-compensated magnitudes, but not in the triggered GA scheme.

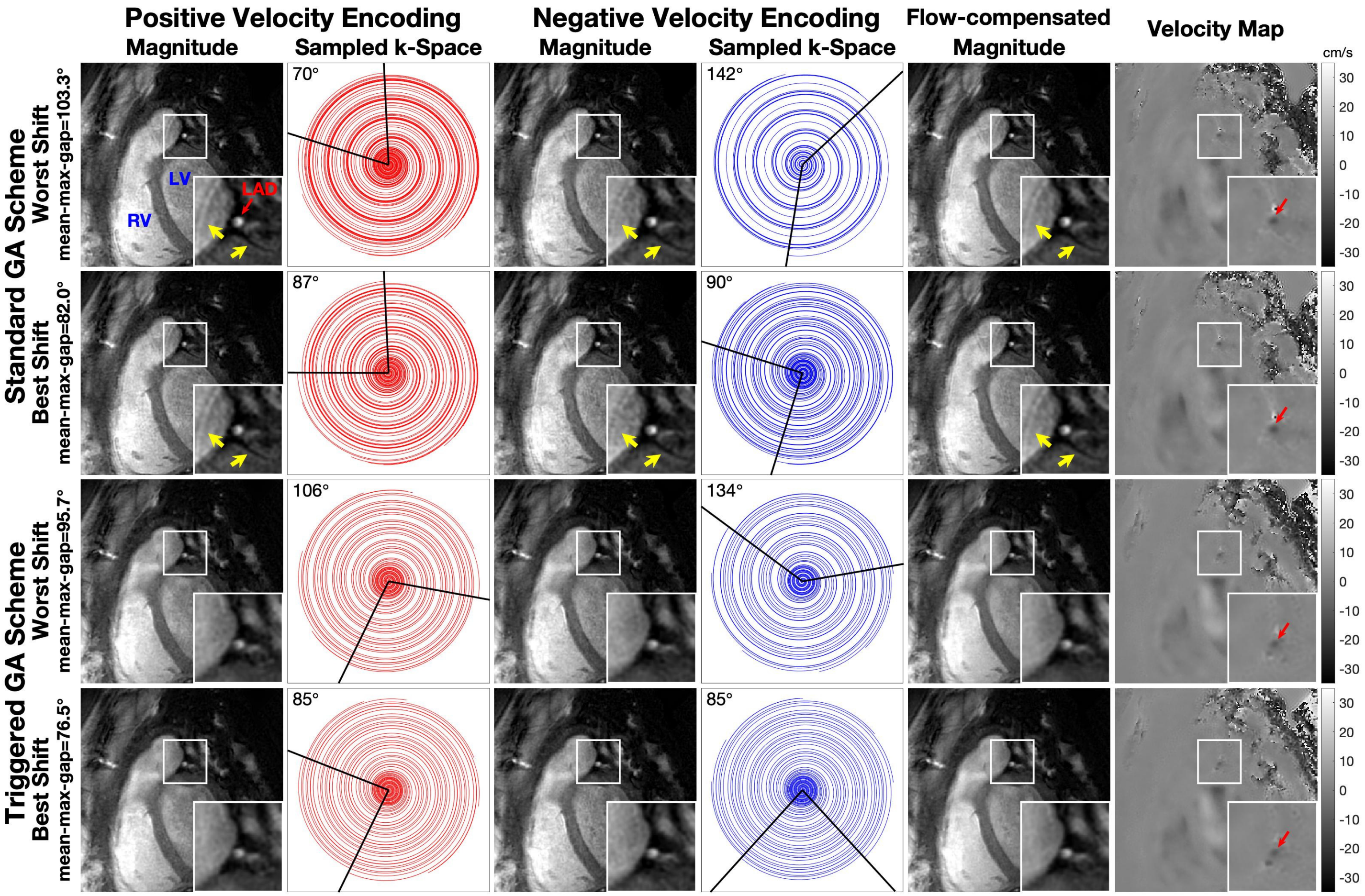

Figure 4.4: Representative LAD PC images of a 39-year-old male showing gap angle and image artifact reduction by applying triggered GA scheme and shifted binning. The max-gaps of the spiral arms are visualized by two black arms from the origin to the end of the corresponding spiral arms, with the angle labeled in degrees at the left top corner of each k-space. The LAD (red arrow) is visualized in cross-sectional view above the left ventricle. Zoomed insets of the LAD are shown at the right-bottom corner in each image. Artifacts in the right ventricle (RV) and left ventricular (LV) wall (yellow arrows) in the images acquired with the standard GA scheme disappear in the proposed triggered GA scheme.

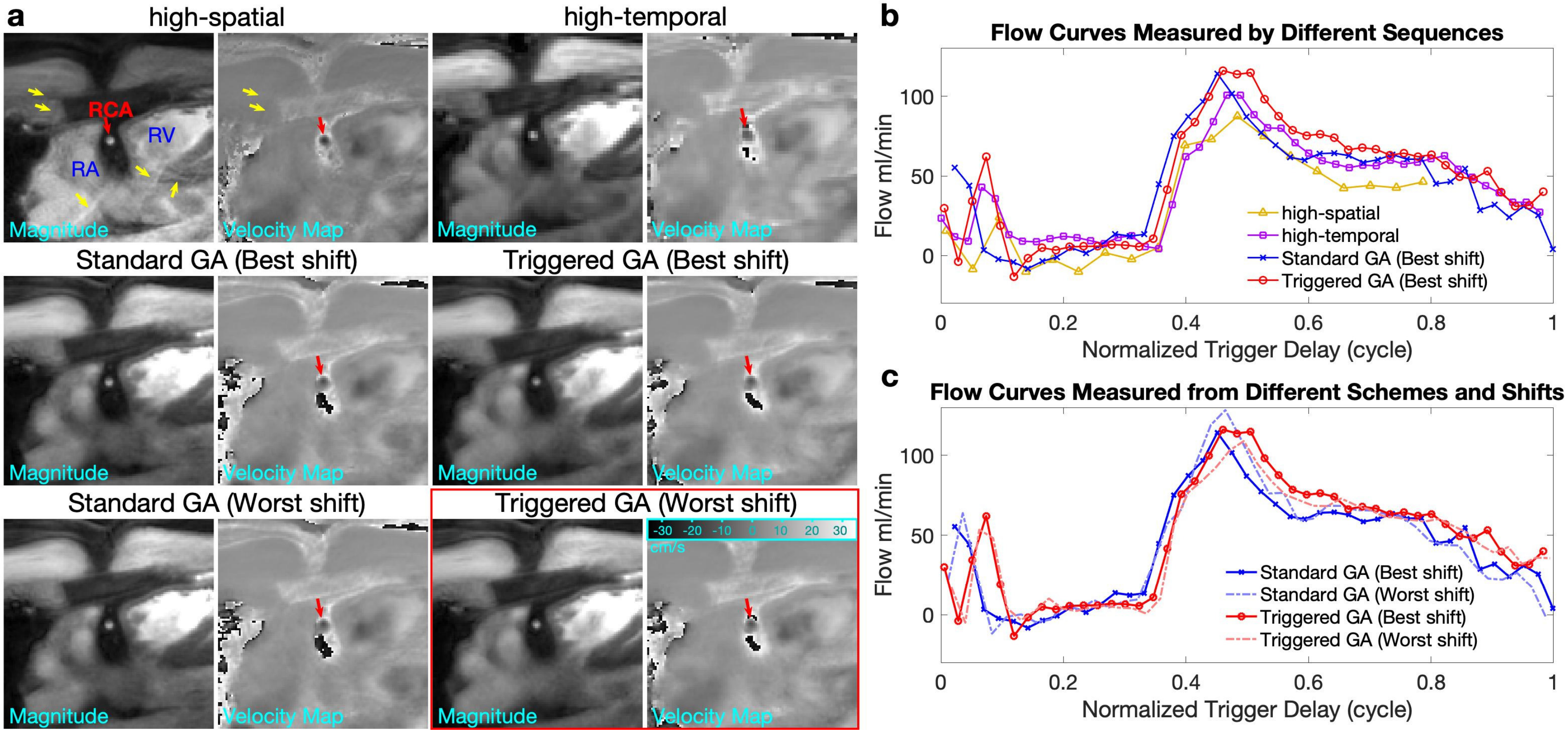

Figure 4.5: Examples of PC data of the RCA (red arrow) from a 20-year old male acquired and reconstructed with all of the different techniques applied in this work. The magnitude of the flow-compensated images and velocity maps of a mid-diastolic cardiac frame are shown in (a) and flow curves in (b-d). Aliasing artifacts (yellow arrow) are seen in the magnitude images of the high-spatial sequence. Images acquired with the proposed triggered GA method with the best binning shift and combined GASSP reconstruction are highlighted with a red frame. The flow curves from the four different acquisition sequences (b) and using best and worst binning shift (c), generally agree well with each other. Abbreviations: RA = right atrium and RV = right ventricle.

Fig. 4.5 shows an exemplary dataset of a mid-diastolic frame acquired and reconstructed with all of the different techniques. The flow compensated image of the high-spatial sequence demonstrated in Fig. 4.5a suffers from aliasing artifacts (yellow arrow). The high-temporal sequence, on the other hand, shows a pixelated pattern on the RCA due to the low spatial resolution. The velocity map of the triggered GA method with the best binning shift (red frame) has excellent quality across the heart and appears to have less noise and artifacts compared to other methods, although the differences are only subtle. Flow curves in Figs. 4.5b and 4.5c agree well across sequences and shifts. Of note, the high-spatial sequence underestimates PSV by about half because of its lower temporal resolution.

Fig. 4.6 demonstrates the agreement of flow curves of the repeated scans using the triggered GA scheme with best binning shift of all 15 coronary arteries. The 8 intra-scan repeats all show excellent agreement with the initial scan. The inter-scan repeats still agreed well in most cases. The velocity and flow metrics for all 4 techniques are shown in Table 4.1, separately averaged among 7 RCA and 8 LAD scans.

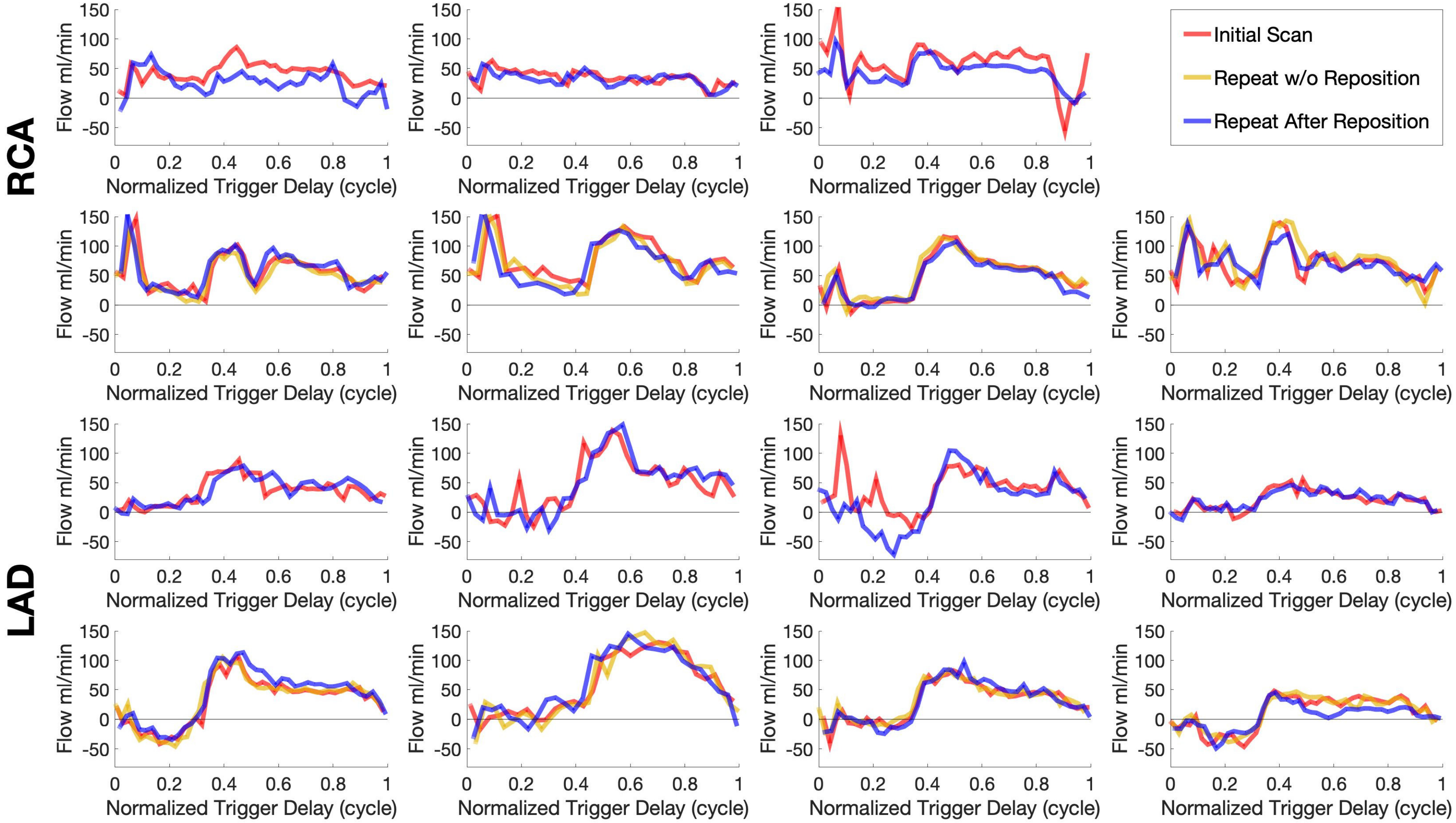

Figure 4.6: Flow curves of the repeated scans acquired with the triggered GA scheme and reconstructed with the best binning shift and combined reconstruction of the 7 RCA and the 8 LAD cases. All 15 cases were repeated after repositioning while 4 RCA and 4 LAD cases were repeated without repositioning.

RCA (n=7)	High-spatial	High-temporal	Standard GA	Triggered GA
PSV max (cm/s)	21.2 ± 5.4	18.8 ± 4.7	18.9 ± 4.2	19.3 ± 3.8
TSV max (cm/s)	87.9 ± 40.0	65.9 ± 9.7	51.2 ± 20.6	69.8 ± 9.3
PDV max (cm/s)	23.7 ± 5.1	20.5 ± 4.5	19.8 ± 5.8	19.0 ± 5.9
TDV max (cm/s)	400.1 ± 35.5	398.1 ± 42.0	386.8 ± 29.0	394.5 ± 33.4
PSV mean (cm/s)	15.7 ± 5.4	15.8 ± 3.8	14.5 ± 4.0	14.4 ± 3.4
TSV mean (cm/s)	76.4 ± 19.4	74.4 ± 29.9	51.2 ± 20.6	69.8 ± 9.3
PDV mean (cm/s)	15.8 ± 4.8	17.8 ± 4.1	14.6 ± 5.4	14.3 ± 5.2
TDV mean (cm/s)	416.9 ± 57.0	395.2 ± 35.3	381.0 ± 41.7	391.5 ± 34.0
flow (ml/cycle)	0.69 ± 0.18*	0.76 ± 0.13	0.75 ± 0.26	0.82 ± 0.18
flow (ml/min)	48.8 ± 16.4*	52.8 ± 12.7	52.5 ± 19.3	55.7 ± 15.4
area (mm^2)	9.1 ± 3.0	9.1 ± 1.9	11.6 ± 4.3	12.4 ± 3.7

LAD (n=8)	High-spatial	High-temporal	Standard GA	Triggered GA
PSV max (cm/s)	6.3 ± 4.1	5.0 ± 5.4	9.1 ± 3.6	7.8 ± 6.8
TSV max (cm/s)	137.8 ± 72.9	130.1 ± 65.9	118.5 ± 59.5	106.6 ± 84.4
PDV max (cm/s)	27.1 ± 8.1	22.5 ± 5.4	23.2 ± 6.4	21.4 ± 5.5
TDV max (cm/s)	451.4 ± 57.9	435.2 ± 56.3	432.5 ± 55.4	428.4 ± 51.5
PSV mean (cm/s)	2.5 ± 2.2	3.9 ± 2.7	3.8 ± 1.6	5.0 ± 4.1
TSV mean (cm/s)	142.8 ± 42.0	105.1 ± 49.9	115.8 ± 66.9	96.2 ± 69.9
PDV mean (cm/s)	16.7 ± 6.1	17.4 ± 4.4	15.4 ± 4.6	14.0 ± 3.7
TDV mean (cm/s)	436.4 ± 41.0	437.7 ± 47.2	440.4 ± 28.7	438.7 ± 45.2
flow (ml/cycle)	0.41 ± 0.16*	0.44 ± 0.15	0.44 ± 0.12	0.48 ± 0.16
flow (ml/min)	28.3 ± 12.0*	31.1 ± 14.4	29.9 ± 9.7	33.8 ± 14.3
area (mm^2)	8.4 ± 2.3	9.1 ± 2.5	10.1 ± 2.2	11.1 ± 3.5

Flow velocity metrics are mean ± SD.
Abbreviations: PSV = peak systolic velocity, TSV = time to PSV, PDV = peak diastolic velocity, TDV=time to PDV, max = maximum velocity in vessel ROI, mean = average velocity in vessel ROI.
*Due to prospective triggering used in high-spatial sequences, flow data was calculated based on incomplete cardiac cycle.
Both standard GA and triggered GA use the best binning shift.

Table 4.1: Coronary flow velocity metrics acquired with reference and proposed methods.

After combining all 15 vessels, Fig. 4.7 shows Bland-Altman analysis of the mean PSV, the mean PDV, the flow per minute, and A_v comparing the proposed triggered GA scheme with the high-spatial and high-temporal reference methods. There is a high agreement for velocity and flow metrics, validating the new technique. Bonferroni corrected t-tests show that the area measured with triggered GA scheme is significantly larger than with both high-spatial and high-temporal sequences, and PDV is significantly lower compared to high-temporal sequence.

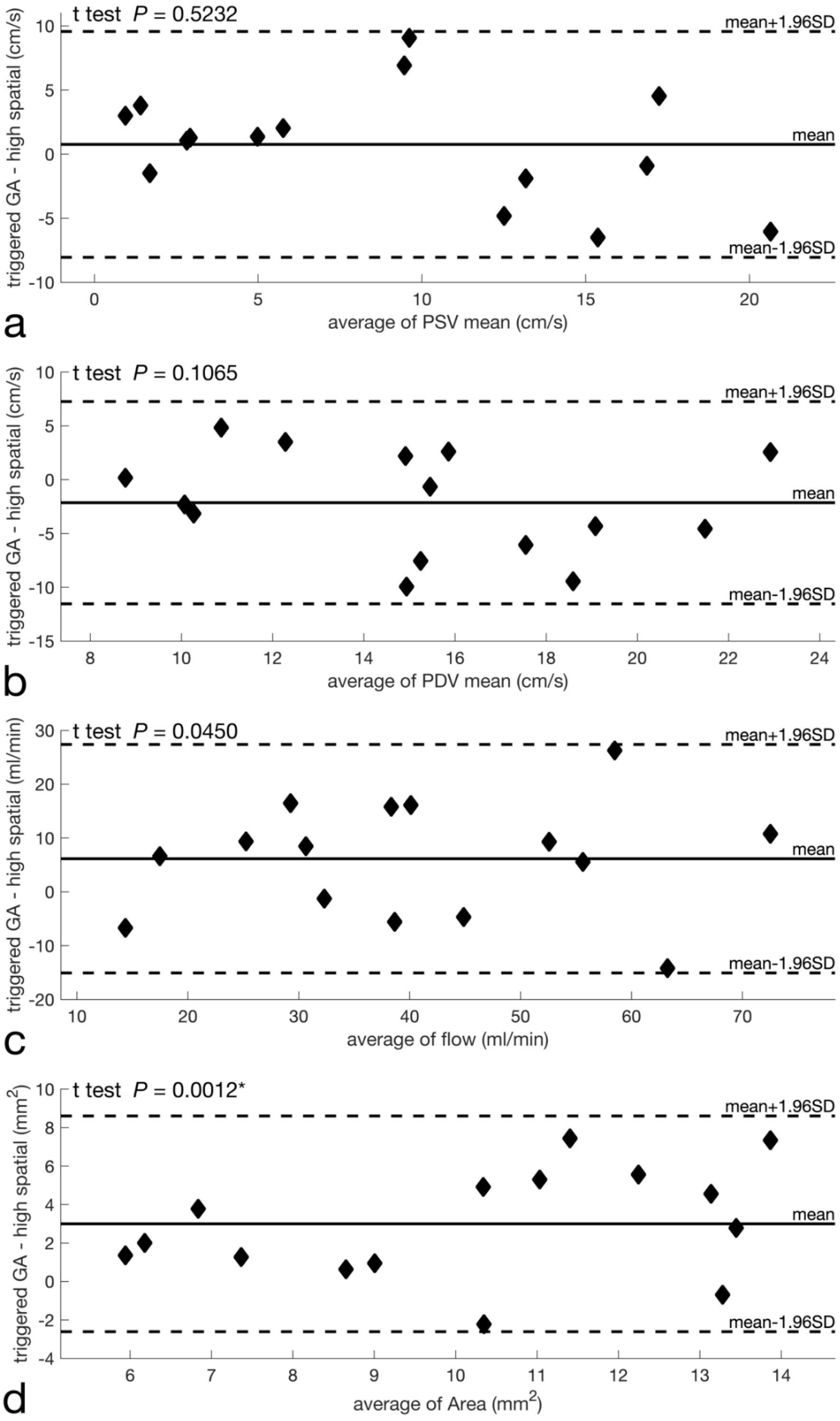

Continue on the next page

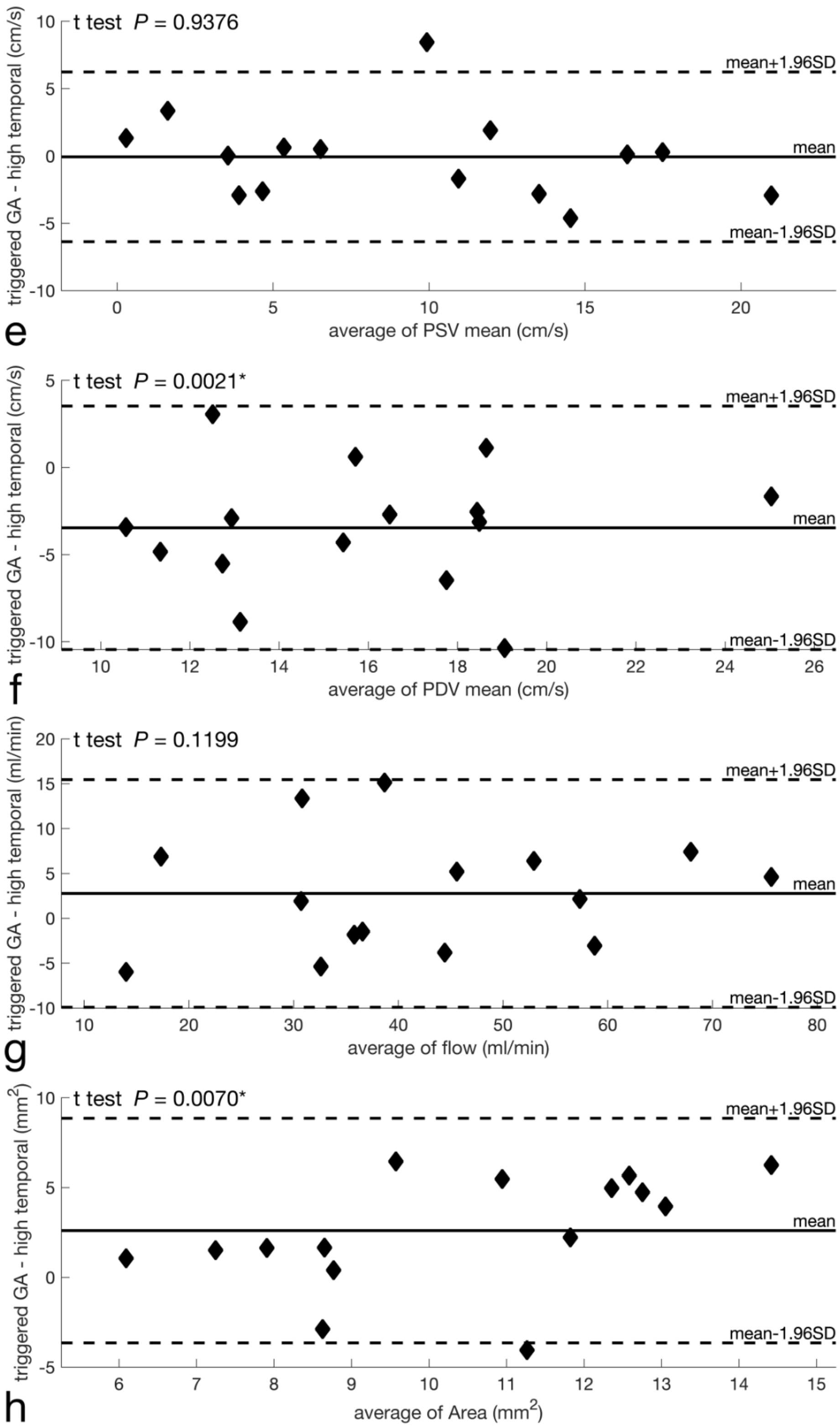

Figure 4.7: Bland-Altman analysis of the proposed triggered GA scheme with the best binning shift plotted for the high-spatial (a-d) and the high-temporal (e-h) sequence measurements of PSV (a, e), PDV (b, f), coronary blood volume (c, g), and cross-sectional vessel area (d, h).

Table 4.2 demonstrates the results of intra-scan and inter-scan reproducibility. The spatial max PDV, spatial mean PSV and PDV, the flow and area are highly correlated (ICC≥0.97, *P*<0.01) with intra-scan repeats. Spatial max PSV is also significantly correlated (ICC=0.92, *P*<0.01) with intra-scan repeats. TSV and TDV are not correlated (-0.12≤ICC≤0.35, 0.16<*P*<0.62) with intra-scan repeats.

	Intra-Scan Reproducibility (n=8)				Inter-Scan Reproducibility (n=15)			
	First Scan	Repeat	ICC	*P*	First Scan	Repeat	ICC	*P*
PSV max (cm/s)	11.8 ± 9.8	13.6 ± 7.7	0.92	<0.01	13.1 ± 8.0	12.6 ± 8.0	0.88	<0.01
TSV max (cm/s)	79.7 ± 76.9	53.0 ± 10.8	-0.11	0.609	89.4 ± 62.9	89.6 ± 65.8	0.52	0.018
PDV max (cm/s)	22.3 ± 5.7	21.6 ± 5.4	0.98	<0.01	20.3 ± 5.6	20.9 ± 5.8	0.81	<0.01
TDV max (cm/s)	394.8 ± 35.7	398.6 ± 29.5	0.35	0.164	412.6 ± 45.9	437.7 ± 98.5	0.41	0.054
PSV mean (cm/s)	8.9 ± 7.2	9.5 ± 7.2	0.99	<0.01	9.4 ± 6.1	8.5 ± 6.8	0.84	<0.01
TSV mean (cm/s)	84.7 ± 66.5	53.0 ± 10.8	-0.12	0.619	83.9 ± 51.6	77.5 ± 43.8	0.66	<0.01
PDV mean (cm/s)	15.3 ± 4.8	15.2 ± 4.7	0.99	<0.01	14.2 ± 4.3	14.4 ± 4.5	0.78	<0.01
TDV mean (cm/s)	400.0 ± 35.0	393.5 ± 25.0	0.33	0.176	416.7 ± 45.9	440.4 ± 95.2	0.36	0.079
flow (ml/cycle)	0.65 ± 0.29	0.65 ± 0.29	0.98	<0.01	0.64 ± 0.24	0.58 ± 0.24	0.86	<0.01
flow (ml/min)	48.0 ± 22.6	48.2 ± 21.5	0.99	<0.01	44.0 ± 18.2	40.6 ± 18.8	0.91	<0.01
area (mm^2)	12.2 ± 3.7	12.2 ± 4.1	0.97	<0.01	11.7 ± 3.5	11.1 ± 3.1	0.85	<0.01

Flow velocity metrics are mean ± SD.
Abbreviations: PSV = peak systolic velocity, TSV = time to PSV, PDV = peak diastolic velocity, TDV=time to PDV, max = maximum velocity in the vessel ROI, mean = average velocity in the vessel ROI, ICC = intra-class correlation coefficients of absolute agreement

Table 4.2: Intra- and inter-scan reproducibility of coronary flow velocity metrics using proposed triggered GA scheme with shifted binning.

Fig. 4.8 demonstrates the high intra-scan reproducibility of mean PSV, mean PDV, flow, and A_v metrics using Bland-Altman analyses. For inter-scan reproducibility, the correlation of flow, area, PSV, and PDV were still high and statistically significant (0.78≤ICC≤0.91, *P*<0.01) with inter-scan repeats.

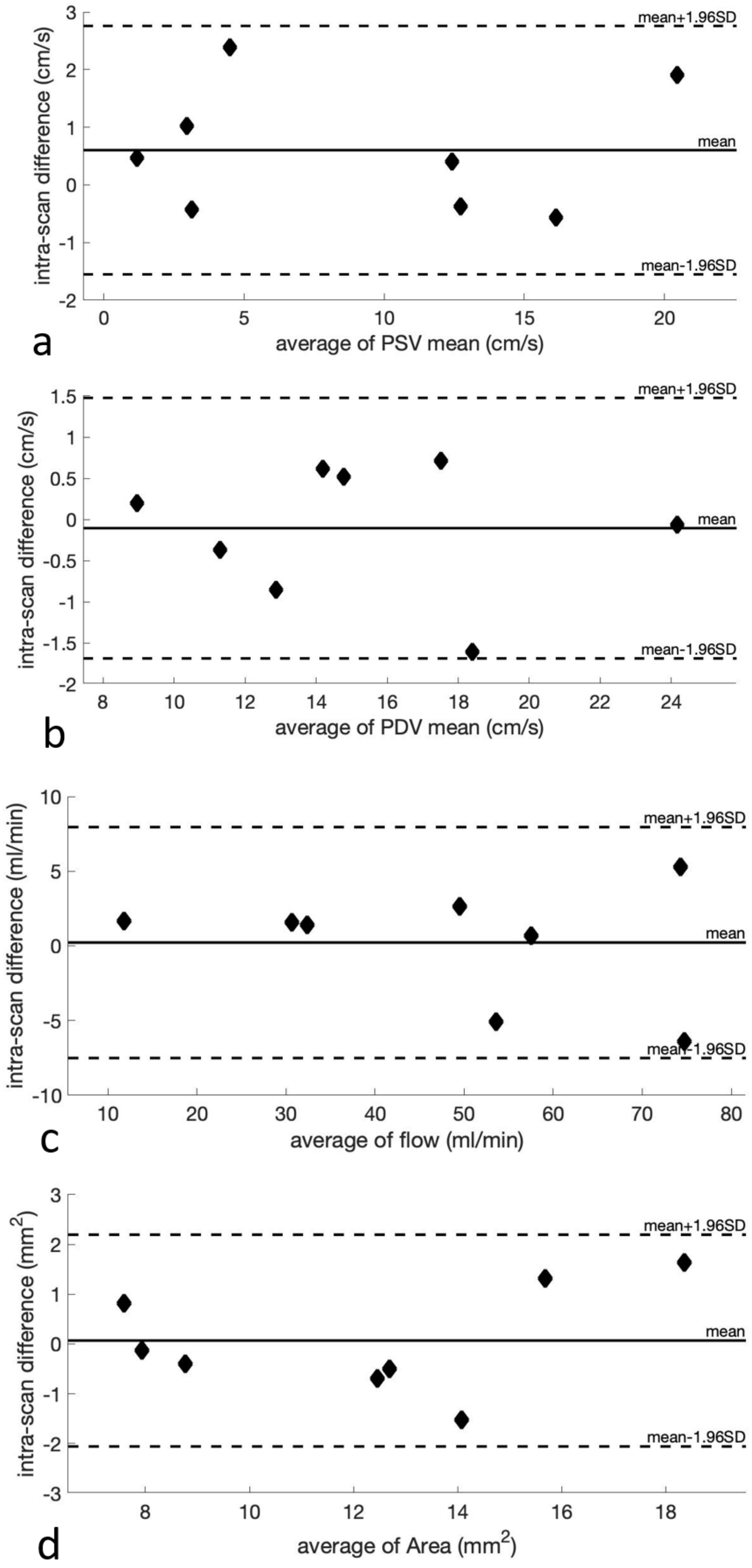

Figure 4.8: Bland-Altman analysis of the intra-scan reproducibility for PSV (a), PDV (b), coronary blood volume (c), and cross-sectional vessel area (d).

The intra-observer reproducibility is demonstrated in Table 4.3. Area analysis correlation (ICC=0.98, *P*<0.01) is very high with repeated observation. Also the flow per cycle (ICC=0.91, *P*<0.01), flow per minute (ICC=0.94, *P*<0.01), and PSV and PDV (ICC≥0.94, *P*<0.01) correlate very well with repeated observation. The correlations of TDV and TSV with repeated observation are lower, especially for TSV, but are still significant *P*≤0.01.

	Intra-Observer Reproducibility (*n=38,18 RCA and 20 LAD)			
	First Observation	Second Observation	ICC	*P*
PSV max (cm/s)	13.0 ± 7.7	13.2 ± 9.0	0.94	<0.01
TSV max (cm/s)	81.8 ± 58.2	95.8 ± 79.0	0.38	<0.01
PDV max (cm/s)	20.8 ± 5.5	21.1 ± 5.4	0.98	<0.01
TDV max (cm/s)	419.6 ± 69.8	414.2 ± 71.9	0.92	<0.01
PSV mean (cm/s)	9.1 ± 6.4	9.4 ± 7.1	0.96	<0.01
TSV mean (cm/s)	74.9 ± 43.5	90.8 ± 72.9	0.37	=0.01
PDV mean (cm/s)	14.5 ± 4.4	14.7 ± 4.1	0.96	<0.01
TDV mean (cm/s)	421.2 ± 68.3	414.2 ± 72.4	0.88	<0.01
flow (ml/cycle)	0.62 ± 0.25	0.64 ± 0.31	0.91	<0.01
flow (ml/min)	43.5 ± 18.9	44.6 ± 21.4	0.94	<0.01
area (mm^2)	11.6 ± 3.4	11.3 ± 3.3	0.98	<0.01

Flow velocity metrics are mean ± SD.
Abbreviations: PSV = peak systolic velocity, TSV = time to PSV, PDV = peak diastolic velocity, TDV = time to PDV, max = maximum velocity in the vessel ROI, mean = average velocity in the vessel ROI, ICC = intra-class correlation coefficients for absolute agreement
*18 RCA scans include 7 first scans, 4 intra-scan repeats without repositioning, and 7 inter-scan repeats after repositioning. 20 LAD scans include 8 first scans, 4 intra-scan repeats without repositioning, and 8 inter-scan repeats after repositioning

Table 4.3: Intra-observer reproducibility of coronary flow velocity metrics using proposed triggered GA scheme with shifted binning.

4.4 Discussion

The proposed triggered GA method combines GASSP and shifted binning to enable single breath-held coronary PC MRI with both high spatial (0.8mm) and high temporal (<21ms) resolutions. The feasibility of the technique has been demonstrated in 8 healthy subjects leading to high image quality and highly reproducible quantitative coronary flow measures. The method was validated against two previously published methods with either high spatial or high temporal resolution with the flow per minute and PSV agreeing well.

However, the vessel areas were measured to be larger with the proposed method than either of the other two, and PDV was measured to be lower than the high-temporal sequence. With regards to the area, it has been shown that a larger voxel size, such as in the high-temporal sequence, in combination with Fourier interpolation (used to improve precision) leads to area measurement underestimation (166). Therefore, a larger area compared to the high-temporal sequence was, perhaps, to be expected. The similarly small area measured with the high-spatial sequence was not expected, and this may be due to remaining image blurring as it was not possible to deblur images reconstructed and processed on the vendor’s platform. A lower PDV compared to the high-temporal sequence may be due to the aforementioned area underestimation of the high-temporal sequence. This is supported by agreement in the flow metric wherein both vessel area and measured velocities are combined. Additionally, the values reported here agree well with those in the original publications of the reference methods (171,172).

Intra-scan, inter-scan, and intra-observer reproducibility were also determined (Tables 1-3). Intra-scan reproducibility of coronary flow volume per minute, peak systolic velocity (PSV) and peak diastolic velocity (PDV, both using spatial mean) were the highest with ICC = 0.99. Intra-scan reproducibility is important when coronary flow and velocity are measured before and during an intervention such as when assessing coronary flow reserve or endothelial function. Inter-scan reproducibility was determined after the participant was given a 10-minute break outside of the scanner, and coronary flow volume per minute had the highest ICC (ICC = 0.91), while PSV and PDV correlated well with an ICC of 0.78 to 0.88. Intra-observer reproducibility was also very high with ICC ≥ 0.94 for cross-sectional area, PSV and PDV, as well as coronary flow volume per minute. Interestingly, intra-scan reproducibility was higher than intra-observer reproducibility. This is likely because the intra-scan analysis was conducted on the same day allowing the operator to remember what cardiac frames were selected to determine the area, while the intra-observer analysis was conducted after at least 30 days.

Binning of GA-rotated data into cardiac frames may cause large gaps in k-space, and two methods to reduce those were tested here. First, shifted binning reduced the 1-frame mean-max-gap by about 20° in agreement with numerical simulations. Second, the triggered GA scheme reduced the 3-frame mean-max-gap compared to the standard GA scheme from 42.8°±13.7° to 35.3°±3.6° and hence reduced the overlap of k-space gaps across adjacent cardiac frames. For this, the rotation angle $\theta = 83.8°$ was chosen based on numerical simulations in order to compensate for missing data in k-space with data from neighboring cardiac frames acquired at the same k-space position. Simulations show that the 3-frame mean-max-gap and max-max-gap (Figs. 4.2d and 4.2e) increase if θ is chosen smaller even though the 1-frame mean-max-gap and max-max-gap could be reduced with smaller θ, especially for θ < 40°.

To keep a fixed temporal resolution of about 21ms as well as to cover the entire cardiac cycle, the total number of cardiac frames is proportional to the mean RR interval. Due to the fixed number of acquired arms, acquisitions in subjects with lower HR (longer RR-intervals) had higher undersampling and, hence, larger gaps in k-space (Fig. 4.3), potentially leading to reduced image quality in subjects with very low HR compared to those with high HR.

While shifted binning reduces the k-space gaps, it may also shift the temporal sampling by up to τ from one scan to another. Some shifts might better capture the temporal flow peak than others but that shift may not be the best shift considered by the shifted binning algorithm. This effect is kept minimal by the high temporal resolution.

Chapter 5 Non-Contrast-Enhanced Abdominal MRA at 3.0 T using Velocity-Selective Pulse Trains

5.1 Introduction

Abdominal magnetic resonance angiography (MRA) is an ionizing-radiation-free imaging technique that can play a significant clinical role in the setting of aortoiliac and visceral vascular pathology, including steno-occlusion, aneurysm, and dissection (204). MRA provides both contrast-enhanced (CE) and non-contrast-enhanced (NCE) approaches (205).

Allowing large spatial coverage and rapid acquisition, gadolinium (Gd)-based CE MRA is established for examining the abdominal aorta and its major branches (206–208). However, the use of traditional Gd-based contrast agents (GBCAs) is restricted for patients with severe renal impairment, due to the risk of developing nephrogenic systemic fibrosis (NSF) which can be life-threatening (209,210). There is also a growing concern for Gd deposition within the body and deep brain even when no kidney disease is present (211). This is particularly significant for patients with vascular pathology, as they often undergo serial surveillance exams, resulting in larger cumulative doses of gadolinium contrast (212). While the clinical implications of gadolinium deposition remain largely unknown, current FDA guidelines recommend health care professionals “minimize repeated GBCA imaging studies when possible, particularly for closely spaced MRI studies” (213). Given these concerns, alternative blood-pool contrast agents such as

Ferumoxytol have been utilized for cardiovascular MRI (214,215). Nonetheless, other disadvantages of CE-MRA persist, including the need for intravenous injection and the potential for an anaphylactic reaction to contrast materials (216), as well as the additional scan costs.

NCE-MRA does not require exogenous contrast agents and thus is ideal for first-line screening or frequent monitoring in follow-up exams, especially for patients with renal impairment (217). Several NCE-MRA techniques have been applied for depicting vasculatures of the abdomen (218). 3D half-Fourier fast spin-echo (FSE) acquisitions with electrocardiographic (ECG) gating provides arteriography by subtracting two images acquired at systolic and diastolic phases based on the dephasing of fast arterial flow during systole (219,220). 3D balanced steady-state-free-precession (bSSFP) acquisition has been combined with ECG-triggering, respiratory-gating with and without aortic labeling pulses, to image renal arteries through subtraction (221).

Since bSSFP offers high blood signal due to both its intrinsic T2/T1 contrast and its inherent flow-compensation in all three spatial coordinates (222), it is a popular choice for NCE-MRA (217,218,223), especially at low MRI field strengths. Renal arteriography with bSSFP under breath-holding has been demonstrated by applying three spatially-selective saturation pulses prior to the acquisition module for venous suppression: one slab covering each kidney for saturating signal from the renal veins, and the third one positioned below the two kidneys for mitigating signal from the inferior vena cava (224–227). This method was applied to detect renal artery stenosis at the main renal arteries before branching to segmental and intrarenal arteries. However, its maximum-intensity-projection (MIP) images often have insufficient quality, as the blood signal overlaps hyperintense fluid and fat in surrounding tissue with high T2/T1 ratios (224). Nevertheless, this technique does not need paired acquisitions for subtraction, thus reducing both the time required and the sensitivity to motion-induced misregistration.

To suppress both the renal parenchyma and veins, non-subtraction based ECG-triggered and respiratory-gated 3D bSSFP sequence for renal arteriography was further developed using a spatially-selective inversion (SSI) pulse followed by a delay, during which fresh upstream arterial blood above the inversion volume flows into the imaging slab (35). Variants of this technique were applied with respiratory triggering for depicting renal arteries (228–230), hepatic arteries (231), hepatic veins (232), and portal veins (233). One such SSI sequence known as ‘bTrance’ is provided by Philips healthcare for depicting renal arteries. For this method, better visibility of distal arterial blood with longer inflow time is restricted by the suboptimal background suppression due to partial recovery of the static tissue signal. Thus in practice, an inflow time of 0.8-1.4 s was often used for a 100-120 mm slab coverage in the axial plane. To extend the superior-inferior field of view (FOV) to the entire abdominal and pelvic arteries, another method performed coronal imaging and applied a sagittally-prescribed SSI pulse immediately following a non-selective inversion (NSI) pulse to reinvert the spins within the abdominal aorta above the aortic bifurcation (234). However, this demanded careful manual placement of the SSI pulse, which also adversely caused a bright background sagittal band.

Alternatively, a velocity-selective inversion (VSI) pulse triggered by respiratory bellows and ECG signals sequentially was proposed for imaging abdominopelvic arteries with 3D bSSFP in coronal orientation at 1.5T (235). The VSI pulse was aimed to invert the stationary tissue and venous blood and null these signals at the end of the inversion delay, while preserving arterial blood in the abdominal aorta and in the iliac arteries within the FOV. The original scheme of the velocity-selective pulse train (236), which did not include any refocusing pulses in the velocity-encoding segments, is known to be sensitive to off-resonance-induced phase modulation.

The emerging velocity-selective (VS) MRA (VS-MRA) method has also been developed for other parts of the body (237–239), in which velocity-selective saturation (VSS) pulse trains were applied right before the acquisition module to suppress the static tissue and the slow venous flow with properly designed saturation and passbands. The susceptibility to inhomogeneity in the main static field, B_0, was somewhat alleviated, by incorporating a single refocusing pulse within each velocity encoding step, to around ±80 Hz of the Larmor frequency for peripheral MRA at 1.5T (237). Through paired and phase-cycled refocusing pulses, the immunity to off-resonance was further improved to around ±200 Hz for cerebral MRA (238) and peripheral MRA (239) at 3.0T. A combination of an SSI pulse with a preset delay and a VSS pulse train has been successfully demonstrated for cerebral MRA at 3.0T to provide superior background tissue suppression and separate intracranial arterial and venous blood (240).

In this study (241), we aimed to construct NCE abdominal MRA protocols at 3.0T with a large spatial coverage that do not require special planning and thus may be better suited for clinical applications. This is the first study to apply VSS and the combination of SSI and VSS pulse trains to abdominal MRA with a requirement of large field-of-view (FOV) necessitating insensitivity to B_0 and B_1 inhomogeneity. A combination of VSI and VSS pulse trains are proposed as an alternate of the combination of SSI and VSS pulse trains to alleviate the sensitivity to the speed of arterial blood flow. The protocols utilized advanced VSS pulse trains for the suppression of static tissue and the SSI or VSI module with an inversion delay time to null the venous signal for arteriography. The feasibility of the VS-MRA pulse trains was qualitatively evaluated by comparing truncated VS-MRA images of the renal area with the limited FOV provided by the commercial renal bTrance method. Abdominal arteriography applying various acquisition modules with VSS pulse trains and SSI or VSI preparation pulses were compared with quantitative evaluations among a group of healthy young- to middle-aged volunteers.

5.2 Methods

5.2.1 Pulse Sequences

Variations of the VS-MRA protocols were performed with the pulse sequence diagrams shown in Fig. 5.1a. VS-MRA sequences were triggered by respiratory bellows to minimize motion artifacts.

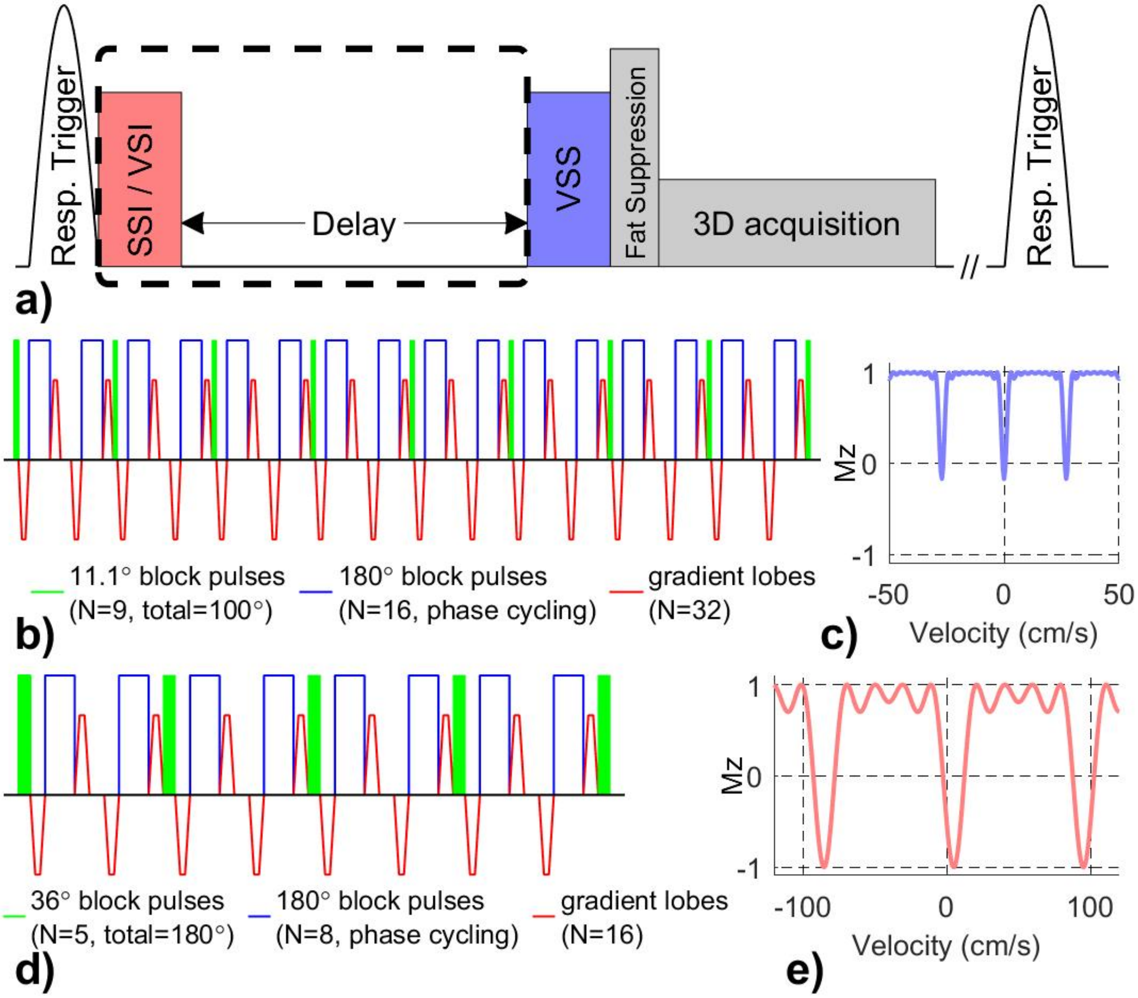

Figure 5.1: a) Diagram of the abdominal VS-MRA sequences. A Fourier-transform based velocity-selective saturation (VSS) pulse train is placed right before fat suppression and 3D acquisition modules to suppress static tissue. A spatially-selective inversion (SSI) or a velocity-selective inversion (VSI) pulse with a delay (dashed box) is applied to null venous blood signal for arteriography. Respiratory triggering is used before preparations. b) The diagram of the VSS pulse train and c) its corresponding velocity-selective profile. Note that Mz for tissue (v = 0 cm/s) should be close to 0 when taking into account the T2 effect. d) The diagram of the VSI pulse train and e) its corresponding velocity-selective profile.

A Fourier-transform based VSS pulse train was placed right before fat suppression and 3D bSSFP acquisition modules to suppress static tissues. The VSS pulse train, as detailed in (238), is composed of nine excitation pulses (11.1° block pulses) with eight velocity-encoding steps (11 ms each step) interleaved with paired and phase-cycled block refocusing pulses and gradient lobes with alternating polarity (29.0 mT/m, 0.5 ms duration, 0.2 ms ramp time). This 88 ms VSS pulse train is illustrated in Fig. 5.1b. The paired and phase-cycled (MLEV-16 scheme, (242)) refocusing through the velocity-encoding steps enabled robustness within ±200 Hz B_0 off-resonance and ±0.2 B_{1+} scales. Its velocity-selective profile (Fig. 5.1c) was generated through numerical simulations of the Bloch equations using Matlab (MathWorks, Inc., Natick, MA, USA). The targeted saturation band was within ±3.0 cm/s with periodical aliasing sidebands every 27 cm/s due to the limited Fourier velocity encoding steps (number of excitation pulses). Velocity-encoding gradients were applied along 45° between left-right (LR) and foot-head (FH) directions. Note that the accumulation of nine of 11.1° pulses yields an effective flip angle of 100° for static tissue to compensate for T2 relaxation during the VSS pulse train.

As described in (240), for obtaining arteriography, an adiabatic SSI pulse (HSn (136,243), n = 4, β = 4, 20 ms, bandwidth = 2500 Hz) was applied with an inversion delay to null the venous blood signal. During the inversion delay, fresh blood signal from the proximal aorta washes into the imaging volume and fills the major abdominal and iliac arteries, depending on the flowing velocity.

Alternatively, instead of the SSI pulse, a VSI pulse train was used to reduce the sensitivity to transit time in the large arteries (235). The VSI pulse train (Fig. 5.1d) contains five excitation pulses (36° block pulses) with four velocity-encoding steps (11 ms each step) and gradient lobes (8.8 mT/m, 0.5 ms duration, 0.2 ms ramp time). The inversion band was designed to select velocities between -11.0 and 21.0 cm/s along a diagonal line in the coronal plane, where positive velocity values stood for movement from foot and left directions to the head and right directions. This was to invert magnetization from large venous vessels and static tissue (contribute to small veins after the inversion delay) and not perturb the spins of large arterial vessels (contribute to small or distal arteries after the inversion delay). Due to the periodic properties of the velocity-selective profile, the inversion band repeated every 90 cm/s (Fig. 5.1e).

5.2.2 Imaging Protocol

Experiments were performed on a 3.0T scanner (Ingenia, Philips Medical Systems, Best, The Netherlands) using the body coil for RF transmission (maximum B_{1+} amplitude 13.5 μT) and a 32-channel chest-array coil for signal reception. The maximum strength of the gradient coil was 40 mT/m and the maximum slew rate was 200 mT/m/ms. A total of 14 healthy volunteers (age range: 24-60 years old, 6 males and 8 females) were enrolled after providing informed consent in accordance with the approved Institutional Review Board protocol. Volunteer consent for publishing their images with their age and gender information was also obtained.

For each VS-MRA protocol, a SPIR module (spectral presaturation with inversion recovery) was applied right before the acquisition train for fat suppression. A 120 mm-thick coronal imaging slab with a FOV of 300 (FH) × 400 (LR) mm^2 (Fig. 5.2a, the yellow box) was acquired with LR as the phase-encoding direction and a resolution of 1.4 (FH) × 1.4 (LR) × 2.0 (anterior-posterior, AP) mm^3. The slab was reconstructed to 0.78 (FH) × 0.78 (LR) × 1.00 (AP) mm^3 by zero-padding.

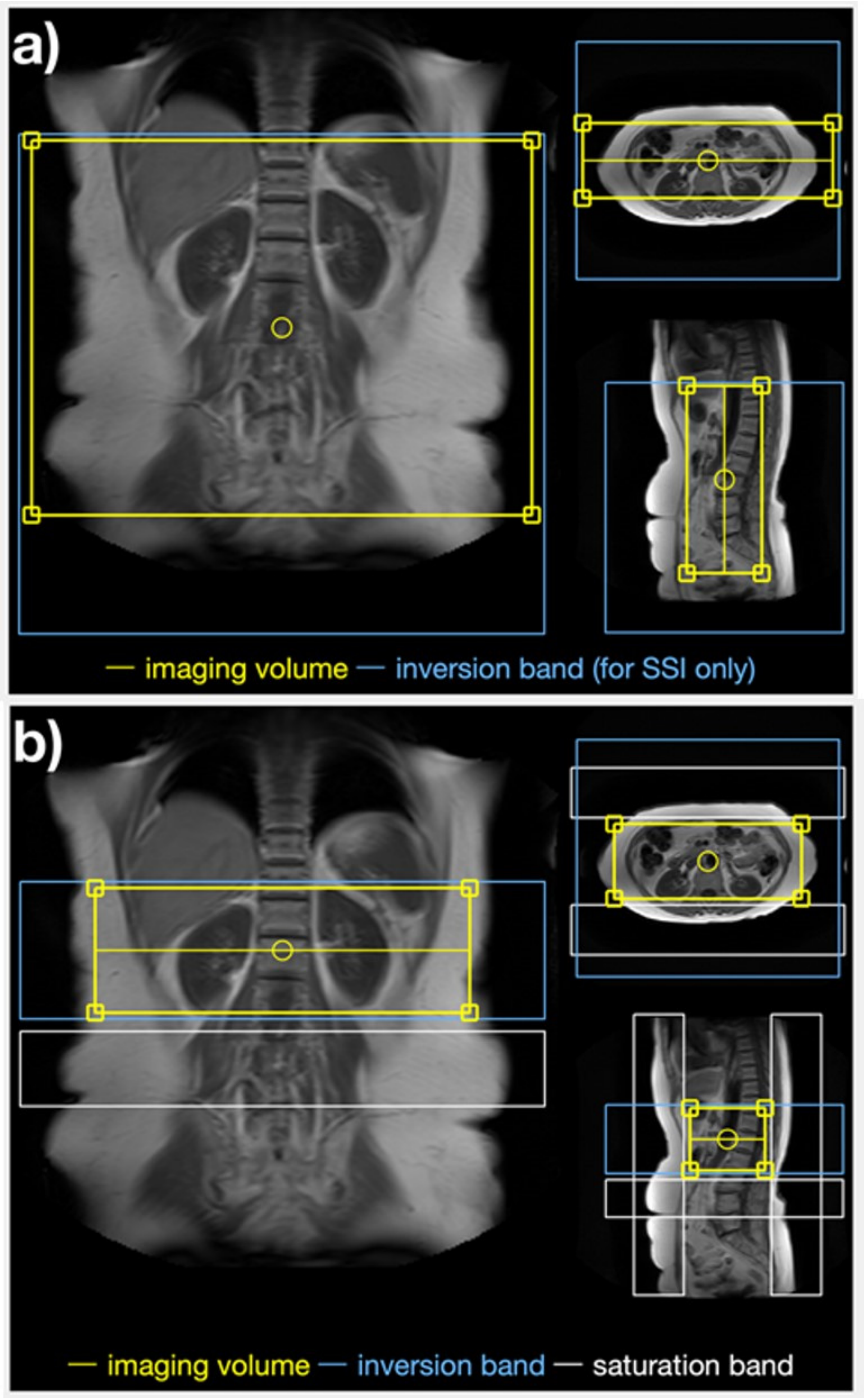

Figure 5.2: Positioning of the MRA sequences used in this study. The yellow boxes indicate the imaging volumes for a) the different abdominal VS-MRA protocols with VSS, SSI+VSS, or VSI+VSS preparations, all with a 300 mm spatial coverage in the foot-head (FH) direction; and (b) the vendor-provided SSI-based renal MRA protocol (bTrance), with a 100 mm coverage in FH direction. The blue boxes indicate the inversion bands applied in a) the SSI-VSS prepared abdominal MRA scans and b) the SSI prepared renal MRA scans, both with default inversion delays of 1200 ms. The white boxes in b) indicate the saturation bands applied for venous or fat suppression right before the acquisition.

The SSI pulse covered the imaging volume with 100 mm extension in the FH direction (Fig. 5.2a, the blue box) to mitigate contamination of the venous blood signal stemming from within the imaging volume as well as that inflowing from the inferior vena cava (IVC). A multi-shot 3D bSSFP acquisition module was used with a radial low-high profile ordering (244) that acquired k-space lines according to an ascending order of their radius from the k-space center. The bSSFP acquisition started with an α/2 excitation pulse applied with a TR/2 period to quickly stabilize the signal from the transient phase after magnetization preparation (245), and was followed by alternating ±α excitation pulses separated by TR. The parameters were: TR / TE = 4.7 / 2.2 ms; flip-angle α = 80°; readout bandwidth = 1330 Hz/pixel. 70 image k-space lines were acquired for each shot in an acquisition window of 330 ms. The compressed sensing technique (16,246,247) was used with an acceleration factor of 8. A minimal shot-interval was set at 3.5 s and the total scan duration was around 3-4 minutes depending on the individual breathing cycle.

VS-MRA with different sequence modules and acquisition methods were first evaluated in three of the volunteers (1 male, 45 years old; 2 females, 25 and 54 years old). To inspect the effect of tissue suppression at 3.0T using the combination of inversion and VSS together, we performed scans with SSI+VSS, VSI+VSS, SSI only (35), and VSI only (235) arteriography. To compare the performance with bSSFP and turbo field echo (TFE) acquisitions which have been used previously for cerebral MRA at 3.0T (238,240), we also tested these in this abdominal MRA study. With matched FOV and resolution, the parameters for

TFE were: TR / TE = 10.0 / 2.6 ms; flip angle α = 10°; readout bandwidth = 266 Hz/pixel; TFE factor = 70 k-space lines. Second-order B_0 shimming with the Pencil-Beam method (Philips) and patient-adaptive RF shimming using two parallel transmission channels as provided by the vendor, were both applied to mitigate the effect of the inhomogeneous B_0/B_1 field of the large abdomen volume at 3.0T.

The VS-MRA method with only the VSS pulse train as well as with additional SSI or VSI preparations were used in studies of nine of the healthy volunteers (45±15 years old, 4 females) for comparison. These scans were all acquired with bSSFP acquisition. The default inversion delay times were 1200 ms for SSI and 700 ms for VSI preparations as used in (235). In a subgroup of eight subjects, the data were acquired with delay times of [1100, 1200, 1300] ms for SSI+VSS arteriography, and [600, 700, 800] ms for VSI+VSS arteriography, respectively, in order to evaluate the inversion delays following the SSI and VSI modules. Given that the T1 of in vivo venous blood at 3.0T is about 1.8 s (248,249), the nulling time of venous blood should be around 1250 ms with perfect inversion and a shot-interval of 3.5 s. Respirational triggering introduces shot-interval variations depending on the breathing cycle. The nulling time after the VSI pulse should be shorter than the SSI pulse considering that the inversion degree of the VSI pulse train was sensitive to B_1 inhomogeneity (240,250). Among a subgroup of seven subjects, a reference scan without applying any of the VSS, SSI, or VSI preparation pulses was also acquired with the same acquisition parameters to compare the signal from arteries, veins, and the static tissue.

A conventional respiratory triggered SSI-based renal MRA protocol (bTrance, Philips) was also acquired for these nine subjects, for comparison. An axial imaging volume with FOV = 300 (LR) × 120 (AP) × 100 (FH) mm^3 (Fig. 5.2b, the yellow box), AP as the phase-encoding direction, resolution = 1.5 (LR) × 1.5 (AP) × 2.0 (FH) mm^3, was reconstructed to 0.75 (FH) × 0.75 (LR) × 1.00 (AP) mm^3 after zero-filling as above. The SSI pulse inverted the 100 mm imaging slab with an inversion delay of 1200 ms (Fig. 5.2b, the blue box). Before acquisition, three saturation pulses were applied with one 80 mm thick axial slab below the imaging volume in order to reduce the downstream signal from the IVC, and two coronal slabs with 60 mm thickness or more were saturated to suppress anterior and posterior subcutaneous fat (Fig. 5.2b, the three white boxes). A pair of 1-3-3-1 fat-suppression binomial pulses (ProSet, Philips) was also applied for water-only acquisition. Multi-shot 3D bSSFP acquisition module was applied in linear profile ordering that acquired the k-space lines sequentially from one side to the other side of the k-space. The acquisition parameters were: TR / TE = 6.7 / 3.4 ms, flip angle $\alpha = 27°$; readout bandwidth = 1330 Hz/pixel; TFE factor = 73 kspace-lines (with 9 dummy echo included); SENSE acceleration factor = 2.2. A minimal shot-interval was set as 1.4 s and the total scan duration was around 6 minutes. Note that the bTrance protocol can only cover the renal area (100mm in FH direction) and is unsuitable for coverage of the whole abdomen (300mm in FH direction), the intended target of the VS-MRA sequences. Thus, comparisons of bTrance and the VS-MRA methods were limited to the renal area.

Lastly, a 2D phase-contrast (PC) velocity mapping (Q-flow, Philips) was acquired from each subject to measure aortic and IVC flow velocities at 20 phases through a cardiac cycle. The Q-flow map was obtained within one breath-hold with cardiac gating triggered by a peripheral-pulse-unit (PPU). A slice with 8 mm thickness was placed axial and about 5 mm distal to the lower renal branch of the aorta with FOV = 350 (LR) × 300 (AP) mm^2 and resolution = 2.0 (LR) × 2.0 (AP) mm^2.

5.2.3 Quantitative Assessment

A quantitative assessment of the efficacy of the VSS, SSI+VSS, and VSI+VSS preparation modules was performed. Experimental data were analyzed using Matlab. Twelve circular regions of interest (ROIs) were manually drawn on the coronal maximum-intensity-projection (MIP) images at the hepatic level, the renal level, the aortic bifurcation, and the iliac bifurcation. Four ROIs were drawn on the descending abdominal aorta and iliac arteries, four on the IVC and iliac veins, and the remaining four on background static tissue at each level.

Relative signal ratios between the signal intensities of MRA images acquired with VSS, SSI+VSS, and VSI+VSS preparation pulses and the corresponding reference scans acquired without using any preparation pulses, were quantified for each ROI. The relative contrast ratios between signal intensities from arterial blood and static tissue (artery-to-tissue) were calculated as (the arterial signal – the static tissue signal) / arterial signal, as measured on the VSS full-angiogram, and the SSI+VSS and VSI+VSS arteriograms. The relative contrast ratios between the signal intensities of arterial and venous blood (artery-to-vein) were also computed as (arterial signal – venous signal) / arterial signal measured from the SSI+VSS and VSI+VSS arteriograms. The artery-to-tissue and artery-to-vein relative contrast ratios were also measured for the bTrance protocol in coronal MIP images acquired at the renal level using the same ROIs.

5.3 Results

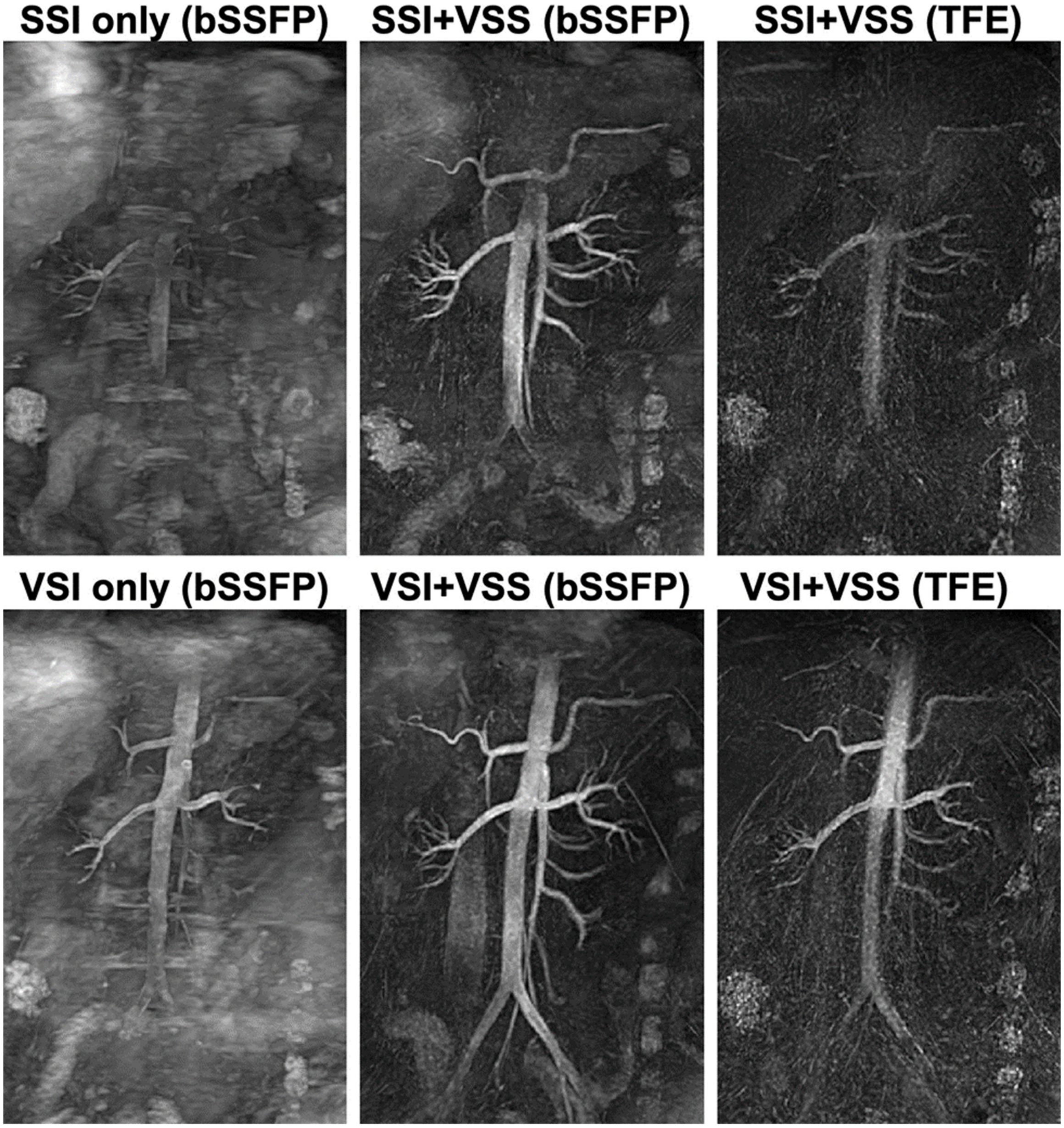

Figure 5.3: Coronal MIP arteriography from a 25-year-old female using SSI (top row) and VSI (bottom row) preparations. Comparisons are made between sequences applying SSI or VSI only with bSSFP acquisition (left column), a combination of SSI or VSI with VSS using bSSFP (middle column) and TFE (right column) acquisitions.

Fig. 5.3 shows the arteriograms of a 25-year-old female with different sequence modules utilizing SSI (top row) and VSI (bottom row) preparations. When not applying the VSS pulse trains immediately before the acquisitions, residual background tissue from imperfect nulling obscured the vessel signal in the coronal MIP for the sequences using SSI or VSI alone (left column). The combination of inversion and VSS pulses revealed arterial structures with much-improved tissue suppression (middle column). Replacing bSSFP with TFE yielded lower arterial signal (right column). In this example, compared to the SSI based arteriograms (top row), the VSI based ones (bottom row) depicted more signal in the proximal aorta, distal iliac arteries, and their small branches.

Results of a 24-year-old female using SSI+VSS with [1100, 1200, 1300] ms delay times (top row) and VSI+VSS with [600, 700, 800] ms delay times (bottom row) are shown in Fig. 5.4. Since SSI+VSS arteriography is totally inflow based, longer delay times led to a better depiction of distal iliac arteries and small arterial branches. For VSI+VSS, the signal in distal branches was much less dependent on the delay times. Both methods displayed increasing contamination from iliac veins and IVC with longer delays, most likely due to the inflow of upstream venous blood spins that were inadequately inverted by the SSI or VSI pulses. The adiabatic SSI pulse produced more uniform background tissue suppression than the VSI pulse train. Tissue recovery with longer delay times was not apparent because the VSS pulse train was applied immediately before the data acquisition.

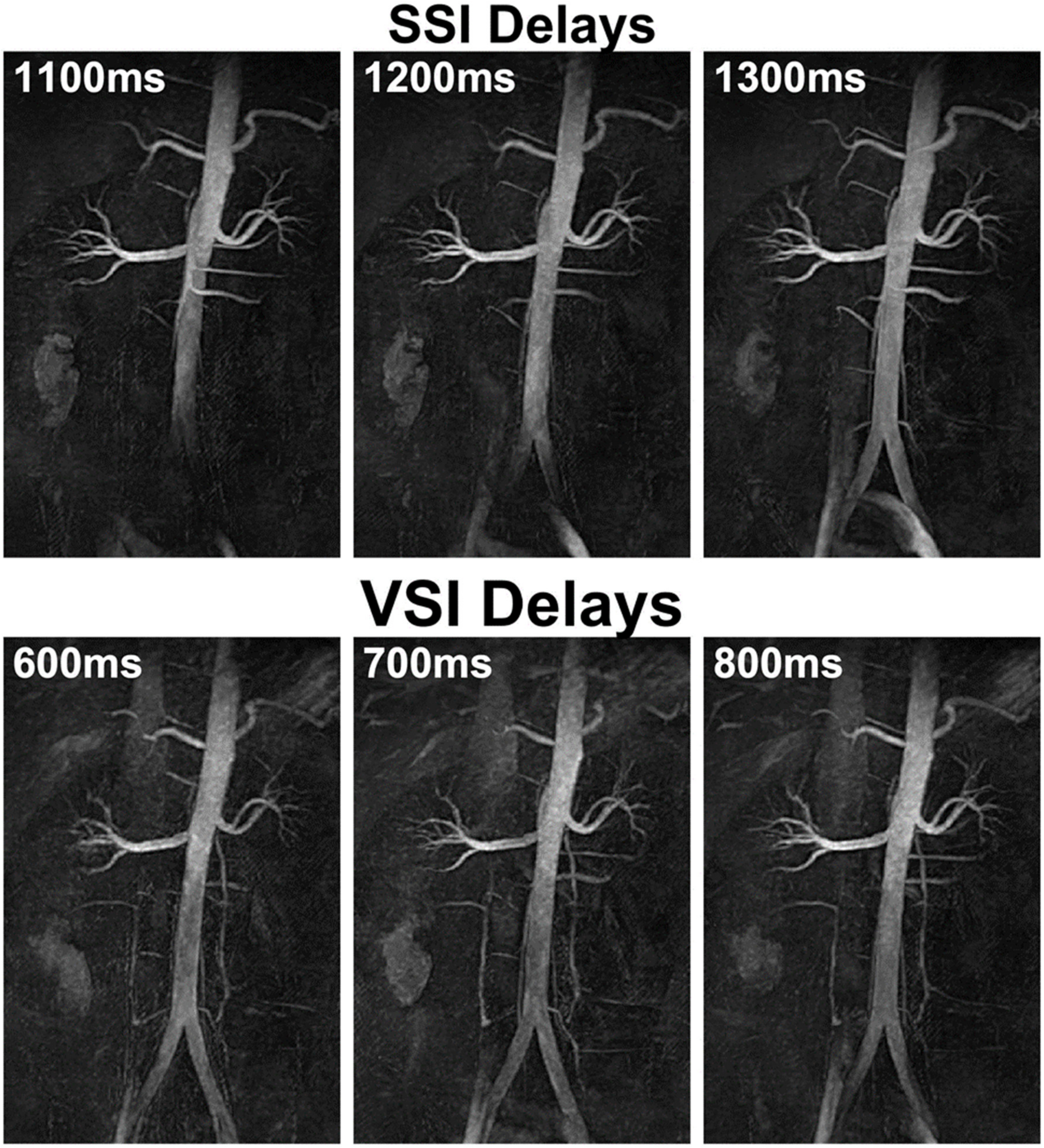

Figure 5.4: Coronal MIP arteriography from a 24-year-old male using SSI+VSS (top row) and VSI+VSS (bottom row) preparations with various inversion delays.

Fig. 5.5 exhibits the coronal MIPs of the reference scans (1st column), VSS based angiograms (2nd column), and SSI + VSS and VSI + VSS based arteriograms (3rd and 4th columns) in three cases: **I**: a 25-year-old female (top row); **II**: a 33-year-old male (middle row); **III**: a 55-year-old female (bottom row). One representative axial slice of the corresponding source images of each of the three cases is displayed Fig. 5.6.

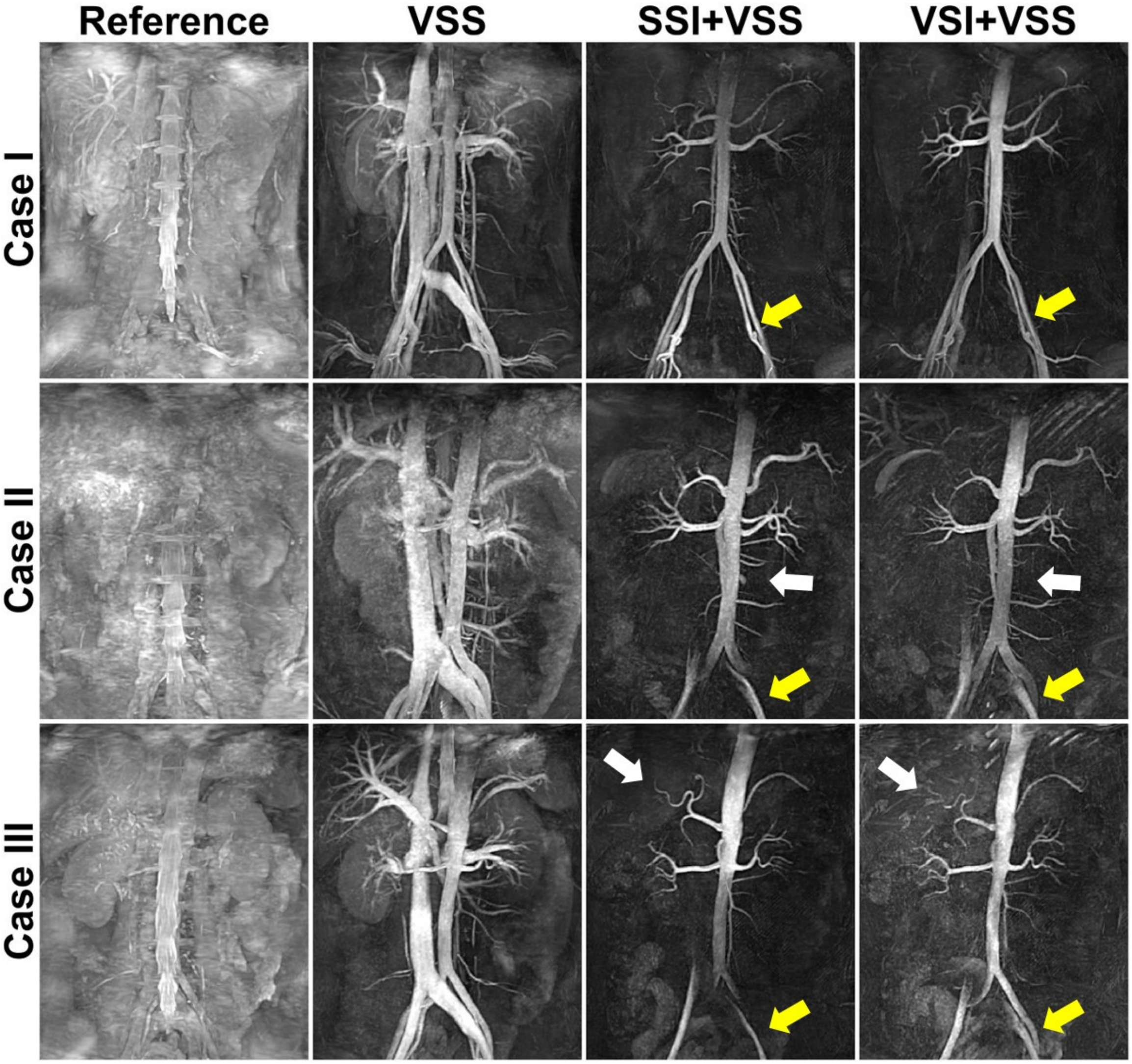

Figure 5.5: Coronal MIP images of the reference scans without applying any of the VSS, SSI, or VSI preparation pulses (1st column); full angiograms of both arteries and veins using the VSS pulse train for static tissue suppression (2nd column); arteriograms using SSI+VSS sequence (3rd column) and VSI+VSS sequence (4th column), from a 25-year-old female (case I: top row), a 33-year-old male (case II: middle row), and a 55-year-old healthy female (case III: bottom row), respectively. Yellow arrows point at the left common iliac artery. White arrows point at the abdominal aorta in case II and the hepatic arteries in case III.

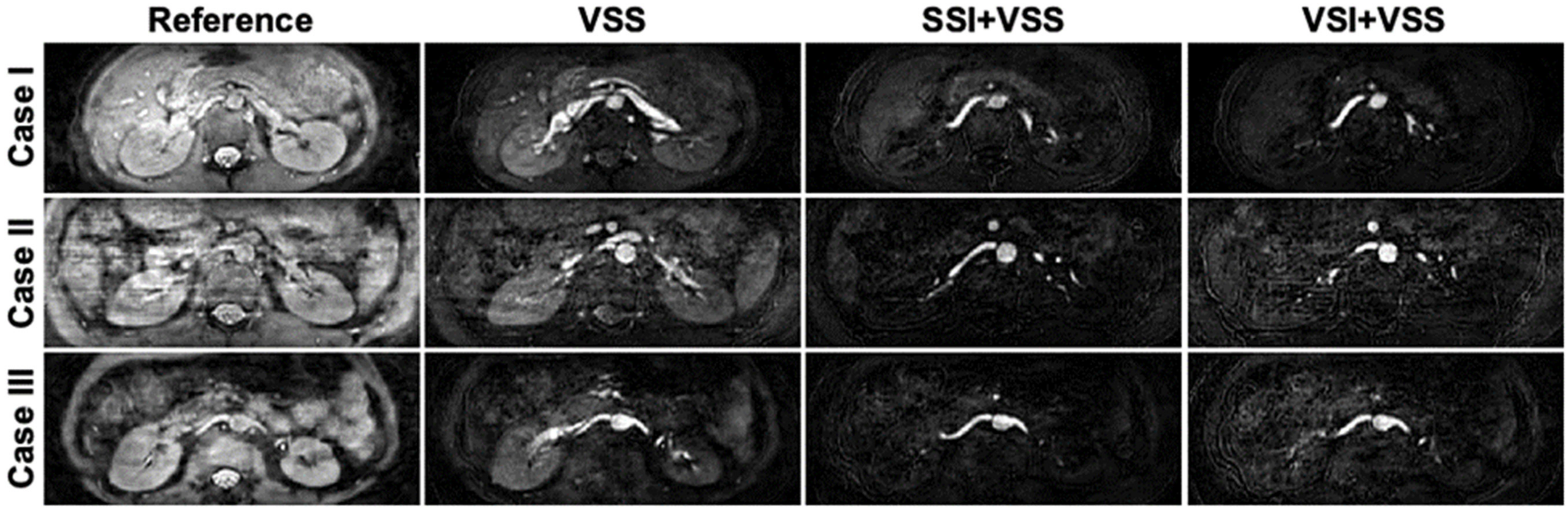

Figure 5.6: One representative axial slice from the source images of the three cases of Fig. 5.5, displaying the reference scans (1st column); full angiograms using the VSS pulse train for static tissue suppression (2nd column); arteriograms using SSI+VSS sequence (3rd column) and VSI+VSS sequence (4th column).

For all three cases, the VSS-only sequences greatly enhanced blood contrast with visualization of the major abdominal vasculature, including the descending aorta and iliac arteries, the IVC, the portal venous system, the hepatic, renal and splenic vessels, and many small, secondary branches. The SSI + VSS and the VSI + VSS scans largely nulled the venous blood signal except for some residual signal in iliac veins. These scans provide visualization of the aorta and its major branches including the celiac trunk, common hepatic and splenic arteries, superior and inferior mesenteric arteries, renal arteries, and the more diminutive spinal arteries. The VSI-based method produced better signal than the SSI method in the distal iliac arteries in cases II and III, likely reflecting the susceptibility of the inflow-based SSI approach to the effects of a slower refreshment of downstream arterial blood in these older subjects (yellow arrows).

For the same three cases, Fig. 5.7 displays their axial MIP images acquired with SSI based renal MRA (bTrance, second column), and with the SSI/VSI+VSS based MRA. These are cropped from the renal portion (3rd and 4th columns) with the matched spatial coverage in the FH dimension (100 mm). Detailed renal artery branches were visualized in images from all three methods.

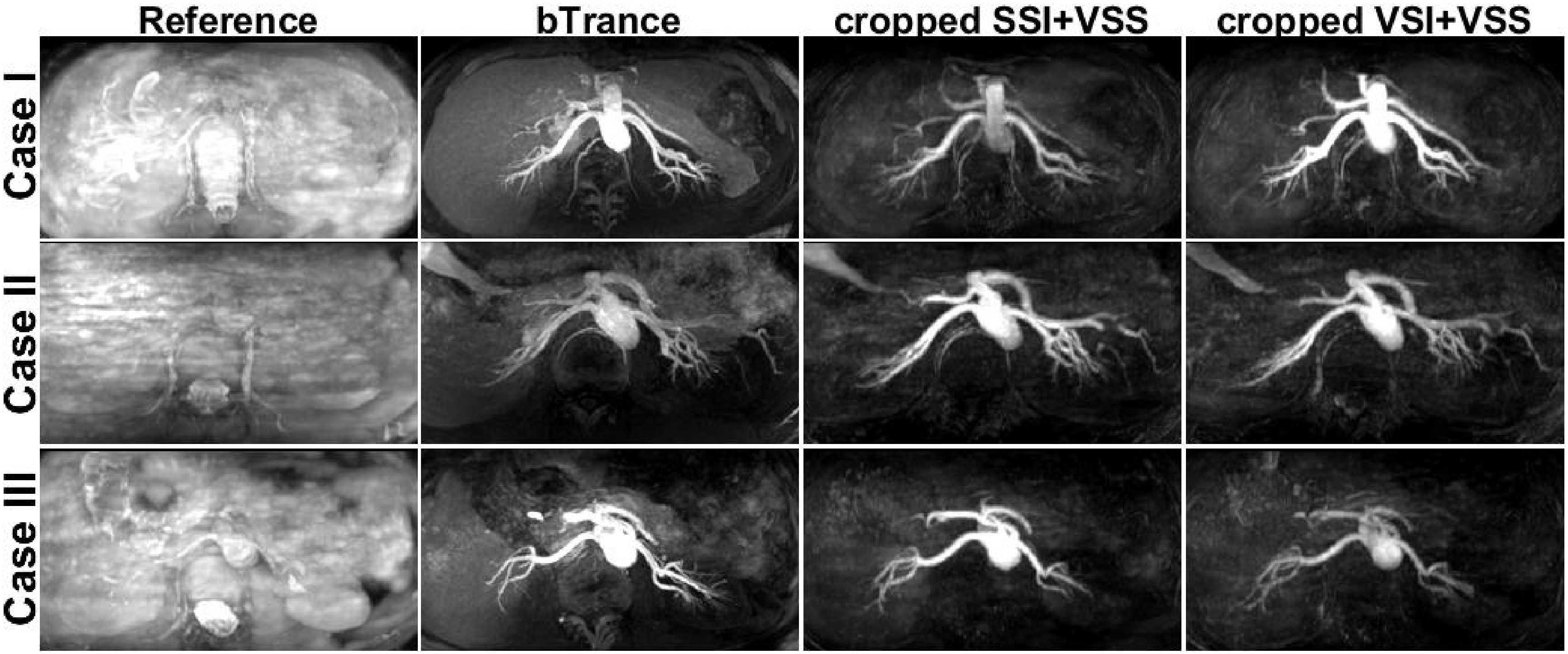

Figure 5.7: Axial MIP images from cases I, II, and III, showing renal arteriograms using bTrance (left column), SSI+VSS (middle column), and VSI+VSS (right column). VS-MRA results were cropped from 300 mm to 100 mm in the FH direction to match the spatial coverage of bTrance. Comparing to bTrance, our VS-MRA methods still delineated detailed renal artery branches, while achieved 3 times of the spatial coverage (300 mm vs. 100 mm) in almost half of the acquisition time (3-4 min vs. 6 min).

The averaged blood velocities of the aorta and IVC lumen through different cardiac phases of an R-R interval measured from these three cases with the additional Q-flow sequence are shown in Fig. 5.8.

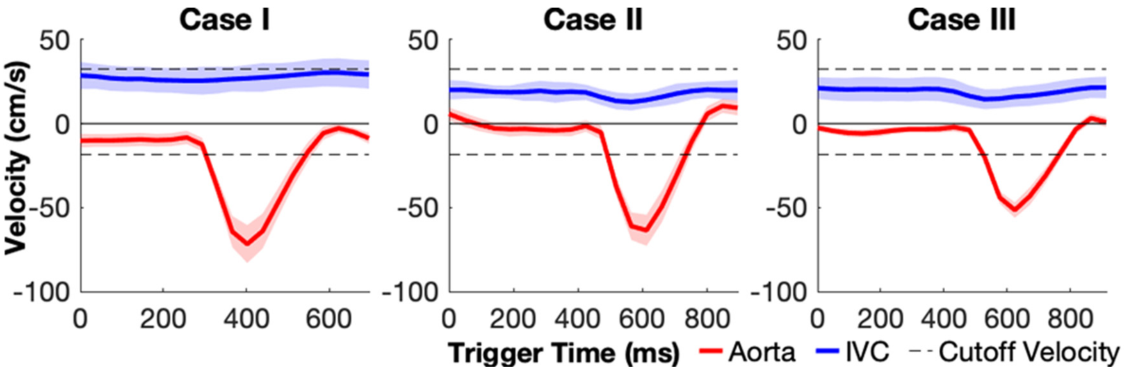

Figure 5.8: The averaged blood velocities of the descending aorta (red) and the ascending IVC (blue) lumen through different cardiac phases during an R-R interval measured from cases I, II, and III. The inversion band for the applied VSI pulse train ([-15.7, 30.0] cm/s along the FH direction) is indicated as the range between the dashed lines.

As expected, in the descending aorta, blood reached peak velocity at the systolic phase (case I: -75 ± 4 cm/s; case II: -65 ± 4 cm/s; case III: -55 ± 4 cm/s.), but maintained low velocities (below 10 cm/s) during diastole. In the ascending IVC, blood flow was relatively constant (case I: 27 ± 4 cm/s; case II: 24 ± 4 cm/s; case III: 20 ± 4 cm/s.) showing minimal pulsation effects. The inversion band applied in the VSI pulse train ([-15.7, 30.0] cm/s along the FH direction, dashed lines) fell mostly between the blood velocities in the aorta and IVC.

The ROIs of arteries (#1, 2, 3, 4), veins (#5, 6, 7, 8) and tissues (#9, 10, 11, 12), placed at hepatic level, renal level, aortic and iliac bifurcations respectively, are exhibited on a coronal MIP image of the VSS prepared MRA (Fig. 5.9). The diameters of the circular ROIs were 7.8 mm, except for those on the smaller iliac arteries (#4) and veins (#8), which were 6.3 mm. The tissue ROI #9 for the hepatic level was drawn at the right liver lobe, avoiding portal veins. The left and right kidney ROIs (#10, 11) were averaged from tissue at the renal level. ROI #12 represented the background tissue for comparing signal levels at both the aortic and iliac bifurcations.

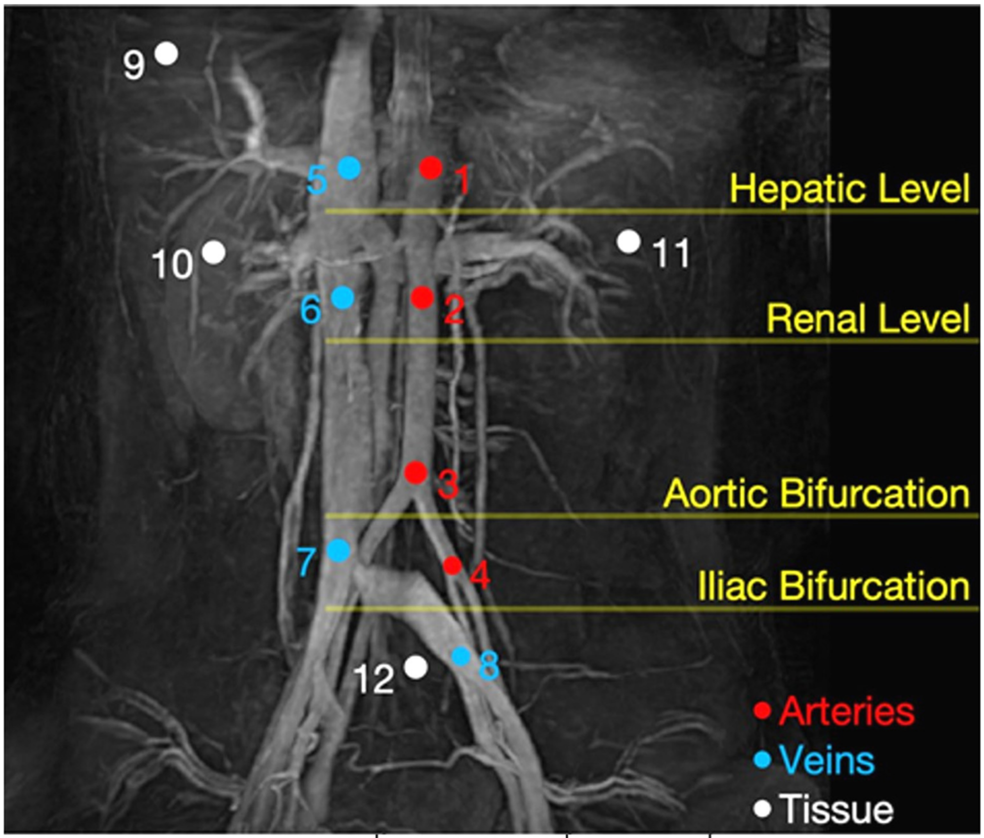

Level	Arteries	Veins	Background
Hepatic	1	5	9
Renal	2	6	(10+11)/2
Aortic Bifurcation	3	7	12
Iliac Bifurcation	4	8	12

Figure 5.9: The ROIs drew for the quantitative assessment of relative signal and contrast ratios in major abdominal vascular segments on a coronal MIP image acquired with the VSS method.

The measured relative signal ratios of different ROIs between the scans with VSS, SSI+VSS, and VSI+VSS preparations and without any preparations (the reference scans) averaged across seven subjects are listed in Table 5.1.

Tissue	**Location**	**VSS / Reference**	**(SSI+VSS) / Reference**	**(VSI+VSS) / Reference**
Arteries	Hepatic Level	0.49±0.16	0.38±0.17	0.38±0.12
	Renal Level	0.55±0.12	0.37±0.14	0.31±0.09
	Aortic Bifurcation	0.55±0.18	0.27±0.12	0.31±0.17
	Iliac Bifurcation	0.53±0.13	0.15±0.11	0.22±0.10
Veins	Hepatic Level	0.60±0.18	0.13±0.05	0.16±0.05
	Renal Level	0.61±0.15	0.11±0.04	0.12±0.04
	Aortic Bifurcation	0.68±0.16	0.13±0.06	0.13±0.04
	Iliac Bifurcation	0.66±0.19	0.12±0.03	0.14±0.05
Static Tissue	Liver	0.16±0.05	0.10±0.03	0.11±0.03
	Right Kidney	0.30±0.08	0.11±0.04	0.11±0.02
	Left Kidney	0.23±0.08	0.09±0.02	0.08±0.02
	Below Iliac Branch	0.20±0.05	0.09±0.03	0.10±0.04

Table 5.1: The averaged relative signal ratios from different ROIs for different VS-MRA protocols. The ROIs are labeled in arteries, veins, and static tissue at various locations as shown in Fig. 5.9. The reference scans were acquired without applying any preparation pulses.

When VSS pulse trains were applied, 49-55% of the signal intensity in segments of the descending aorta and iliac arteries and 60-68% of signal in ascending IVC and iliac veins was preserved. About 16-30% of the signal at static tissue background were left. The signal intensity at the right kidney tissue was higher than the left side (0.30±0.08 vs. 0.23±0.08, paired t-test *P* = 0.02). When the SSI+VSS or VS+VSSI pulse trains were applied, only 11-13% (SSI+VSS) or 12-16% (VSI+VSS) of signal in major veins and 8-11% of signal in static tissue was left; the preserved arterial signal from proximal to distal levels was reduced from 38% to 15% (SSI+VSS) or from 38% to 22% (VSI+VSS), following a decreasing pattern (Table 5.1). The relative signal ratios of arteries and static tissue at the iliac bifurcation level were insignificant in SSI+VSS (t-test P = 0.34) but significant in VSI+VSS (t-test P = 0.03). As a result, the VSS pulse train preserves about 2-4 times more blood signal than the signal from static background tissue. The SSI+VSS and VSI+VSS pulse train preserve about 1.5-3 times more arterial blood signal than from venous blood and static background tissue.

The contrasts in the angiograms and arteriograms were quantitatively evaluated using the relative contrast ratios. The averaged relative contrast ratios of artery-to-tissue and artery-to-vein at four different levels on VSS angiogram, SSI+VSS and VSI+VSS arteriograms are shown in Fig. 5.10a and 5.10b, respectively. For VSS angiography, the artery-to-tissue relative contrast ratios were mostly above 0.60 except at the renal level (0.52). For SSI+VSS and VSI+VSS arteriography, these ratios increased to about 0.70 at hepatic (t-test $P = 0.045<0.05$ between SSI+VSS and VSS) and renal levels (t-test $P = 0.006<0.05$ between VSI+VSS and VSS) due to the better tissue suppression (Fig. 5.10a). The artery-to-tissue relative contrast ratio of the bTrance method at the renal level is similar to the SSI+VSS and VSI+VSS methods (t-test $P = 0.37>0.05$ between bTrance and SSI+VSS). At the iliac bifurcation level, the artery-to-tissue relative contrast ratio of SSI+VSS was lower than 0.20 whereas the VSI+VSS approach was around 0.46, with an improvement of 130% (Fig. 5.10a, t-test P = 0.03). Artery-to-vein relative contrast ratios follow the same decreasing pattern from proximal to distal levels (Fig. 5.10b). For both SSI+VSS and VSI+VSS, artery-to-vein relative contrast ratios were about 0.60 at hepatic and renal levels and about 0.50 at the aortic bifurcation level. The difference between SSI+VSS and VSI+VSS at these three levels are not significant (t-test *P* = 0.45, 0.18, and 0.77 at hepatic, renal, and aortic bifurcation levels, respectively). The artery-to-vein relative contrast ratio of the bTrance method at the renal level is about 0.35, significantly lower than VS-MRA methods (t-test *P* = 0.02 vs. bTrance and VSI+VSS, with Bonferroni correction due to reuse of the VSI+VSS ratios). At the iliac bifurcation level, this ratio of SSI+VSS was lower than 0 but VSI+VSS still yield a contrast of around 0.34 (Fig. 5.10b, t-test *P* = 0.03).

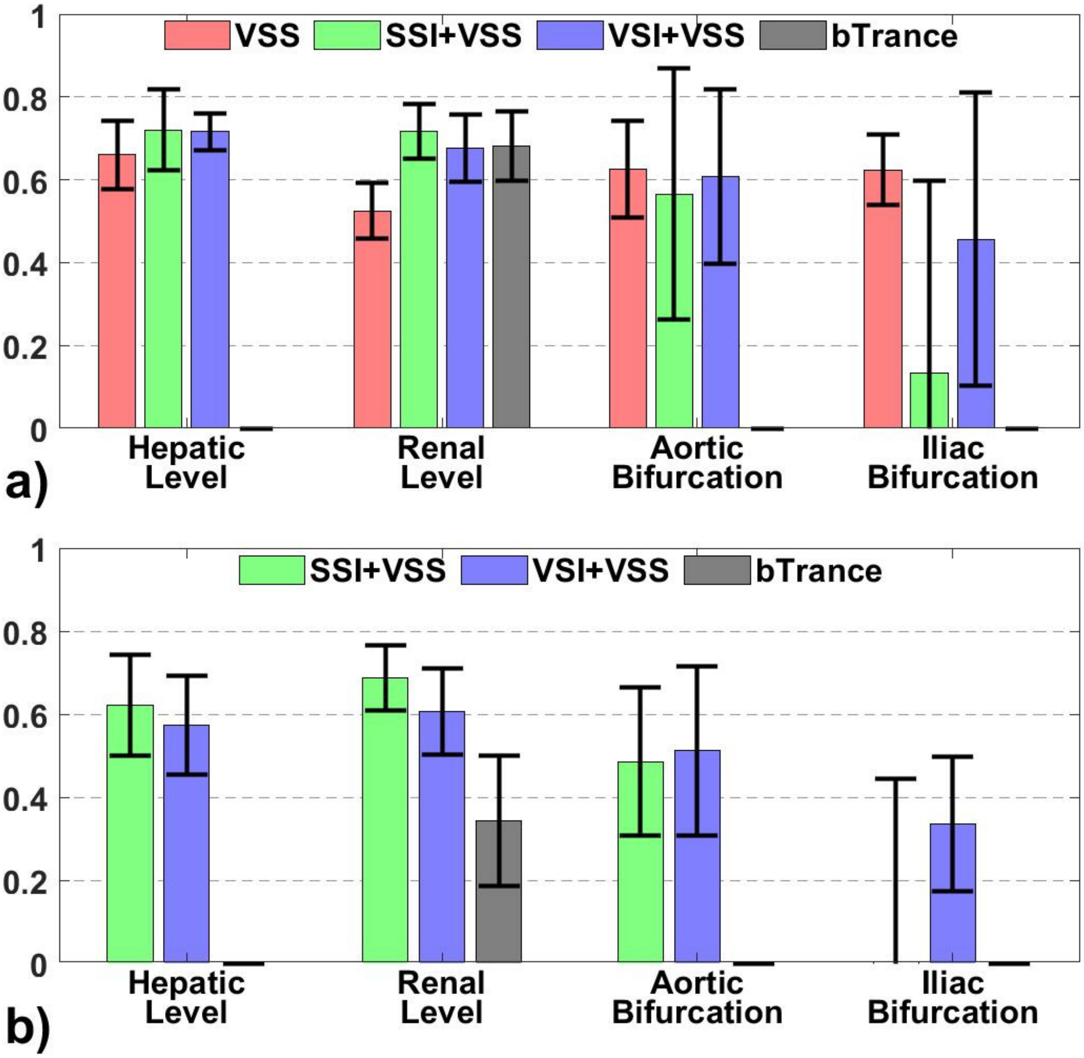

Figure 5.10: The averaged relative contrast ratios of a) artery-to-tissue at different vascular locations on VSS angiogram, SSI+VSS, and VSI+VSS arteriograms and b) artery-to-vein on SSI+VSS and VSI+VSS arteriograms, respectively. The ratios of the VS-MRA methods are compared with the bTrance at the renal level.

5.4 Discussion

The feasibility of 3D abdominal VS-MRA at 3.0T with a large FOV was evaluated for the first time among a group of healthy young and middle-aged volunteers. The protocols under investigation utilized advanced VSS pulse trains immediately before image acquisition for suppression of static tissue. The SSI or VSI module with an inversion delay time was placed to null the venous signal for arteriography.

VSS angiography achieved high and stable artery-to-tissue contrast (mean>0.5, i.e., blood signal is more than twice as large as the tissue signal, SD≤0.2, Fig. 5.10) in all four levels from proximal to distal arteries. Arteriogram was obtained by incorporating the additional SSI or VSI pulse trains considering the clinical preference of arterial only images. Both SSI+VSS and VSI+VSS arteriography achieved high artery-to-tissue and artery-to-vein relative contrast (mean>0.5) at proximal levels from the liver level to aortic bifurcation (Fig. 5.10). These methods have comparable artery-to-tissue contrast and higher artery-to-vein contrast compared to the widely-used bTrance method when applied at the renal level (Fig. 5.10). The SSI prepared method is inflow based and thus the extent of the arterial segments being displayed, such as the bilateral iliac arteries, could be hampered by the slow velocity of arterial blood in some subjects (Figs. 5.4 and 5.5). In contrast, the arterial signal in distal branches was less dependent on the arterial inflowing speed for the VSI based approach than the SSI based approach, as reflected in both representative cases (Figs. 5.4 and 5.5) and the quantitative evaluation of the artery-to-tissue relative contrast ratios within the group (Fig. 5.10).

Blood velocity in the aorta of the subjects with normal cardiovascular functions is reportedly correlated with heart rate, age, gender, and body size, etc. (251). Older subjects tend to have slower flow velocity (Fig. 5.8) and thus might benefit more from the VSI based method.

When compared to reference scans, applying only VSS pulse trains was found to reduce signal in half in segments of the descending aorta and iliac arteries (Table 5.1). The signal drop was mainly attributed to T2 relaxation and pulsation during the 88 ms VSS pulse train (238). To alleviate signal loss in the arterial blood, shorter pulse durations and a better gradient system are required.

Here, the velocity-selective gradients were applied along a 45° angle to both LR and FH directions, as aorta, IVC, iliac arteries and veins are largely in the FH direction, and common hepatic artery, splenic artery and vein, renal arteries and veins are primarily in the LR direction. All of these vessels have velocity components projected along the velocity-encoded direction. In addition, the portal arterial system, which mainly supplies the liver, is approximately parallel to the chosen VSS gradient direction. A notable limitation of this implementation is that vessels flowing in the AP direction, such as the celiac trunk, might be poorly delineated. This could be avoided by choosing a velocity-selective direction slightly off the coronal plane and this will be evaluated in future work. The saturation band for the VSS pulse train, [-3.0, 3.0] cm/s, and the inversion band for VSI, [-11.0, 21.0] cm/s along the diagonal direction, were projected to be [-4.3, 4.3] cm/s and [-15.7, 30.0] cm/s along the LR and FH directions, respectively.

Note that the velocities of aortic blood during diastole recorded here were within the inversion band of the VSI sequence (Fig. 5.8). This might explain the lower signal in the aortic lumen and some distal arterial branches compared to SSI-based results as observed in cases II and III (Fig. 5.5, white arrows). ECG triggering of VSI at the systolic phase would avoid inverting the fast-moving arterial magnetization as done in (235).

One challenge of the VSI pulse train used in this study is that its effective inversion degree was sensitive to B_{1+} homogeneity, due to the use of hard pulses with low flip angles being played at the beginning of each velocity-encoding step for weighting of the excitation k-space. In contrast, SSI+VSS based arteriography using an adiabatic SSI pulse ensured robust suppression of static tissue and venous signal (Figs. 5.4 and 5.5). The relatively inhomogeneous background suppression and the shorter delay times for VSI based method (700 ms vs. 1200 ms) resulted from the inadequate inversion caused by B_1 inhomogeneity. Note that the severity of B_1 field inhomogeneity within the abdomen at 3T is associated with both body geometry and tissue composition (252,253). A larger body size with less fat fraction might induce more severe B_{1+} inhomogeneity due to the higher dielectric constant and RF wavelength in water-containing tissue vs. fat (252,253). In a recent cerebral VS-MRA study, nine 10° optimal composite (OCP) pulses for the VSS pulse train were designed to achieve uniform suppression of stationary tissue (240). For the VSI pulse train used in this study, five 36° OCP pulses could be applied for robust inversion, by tailoring to the B_{1+} inhomogeneities in the abdomen at 3.0T.

Another technical issue is the detrimental effect of inverting the blood within the heart caused by the SSI or VSI pulses, on reducing the signal from blood flowing into the proximal abdominal aorta (Fig. 5.5). For SSI, when carefully choosing the inversion slab to avoid overlapping with the heart apex, the venous blood from the cranial part of the liver, which is often in the same axial plane as the base of the heart, may not be adequately suppressed. For VSI, the contraction of the myocardium may fall into the inversion band of the velocity-selective yet spatially nonselective pulse train and result in unintended perturbation.

The images acquired by bSSFP in Fig. 5.3 appear to show higher SNR compared to the TFE acquisitions for our VS-MRA methods at 3.0T. Similar to previous implementations for cerebral or peripheral MRA (238–240,254), the bSSFP readout in this work utilized low-high profile ordering to acquire the center of k-space right after the VSS pulse train. This was to capture the maximal contrast between the flowing signal in the passband and the static tissue signal in the saturation band.

A disadvantage of bSSFP is that it is susceptible to B_0 field inhomogeneity effects (222), especially near the lung-liver interface. In this study, the use of a second-order B_0 shimming and a patient-adaptive B_1 shimming sufficed to achieve high-quality bSSFP based abdominal MRA on our 3.0T system. The B_0 shimming volume applied was the same as the imaging volume in AP and FH directions but only wide enough to cover both kidneys in the LR direction.

It is worth mentioning that the compressed sensing technique is well-suited for VS-

MRA due to its sparse nature, and the acceleration factor of 8 obtained here reduced the acquisition duration for the large FH FOV (300 mm) to a time window of 3-4 min. In contrast, the SSI based bTrance renal MRA with only one-third of the spatial coverage in the FH direction (100 mm) provided by the vender has a SENSE factor of 2.2 in the AP direction and took almost twice as long (6 min).

Respirational triggering at the exhale phase sufficed to ensure insensitivity to respiratory movement as well as the associated variations of the B_0 or B_1 field inhomogeneities, but at the cost of lengthened acquisition time depending on the breathing rate. Advanced imaging and reconstruction methods such as the use of radial or spiral trajectories could potentially allow continuous acquisition during free breathing and thus further improve imaging efficiency.

Chapter 6 Physiology change in real-time MRI up to 100Hz

6.1 Introduction

Real-time (RT) MRI (255) has been achieved with radial fast low angle shot (FLASH) acquisition and total-variation (TV) regularized nonlinear inversion reconstruction (256). The data is highly undersampled for RT acquisition and immediately reconstructed on powerful multiple graphical processing units (GPU). RT images were utilized in studies of dynamic MRI, including throat imaging during speaking (257) and cardiac imaging (258). RT MRI was able to be acquired at up to 100 frames per sec (fps) (259).

As well as capturing structural movement, the RT image series can also show temporal intensity fluctuations. For example, intensity changes in RT MRI at 30 and 100 fps was able to reveal a 6 Hz fast movement of the tongue in elite horn players (260). Real-time images are also subject to changes due to physiological motion and perfusion. In traditional functional MRI, physiological changes were usually assumed stable or periodic, and data acquired were averaged over time including repeated scans.

Physiological changes that affect the signal intensity can be analyzed by signal decomposition methods such as Fourier transformation (FT) or principal component analysis (PCA). For example, perfusion- and ventilation-weighted images have been extracted from structural lung scans by spectral separation of the respiratory and cardiac frequency components (261). However, the types of physiological information that can be extracted from signal fluctuations detectable in RT MRIs is presently very limited (262,263).

In this work, we extract physiological information from real-time datasets acquired in RT MRI by FT, PCA, and using perfusion models. Pharyngeal RT MRI during speaking is analyzed to reveal spectral patterns on different muscles involved with speech; RT cerebral and cardiac data acquired from healthy subjects are decomposed to synthesize images with physiological contrast; and cardiac data acquired from patients with wall motion abnormalities are processed by FT and PCA to distinguish healthy and diseased myocardium.

6.2 Methods

6.2.1 Data acquisition and analysis

RT MRI data were acquired from a 3T Siemens Prisma Scanner (Siemens Healthineers, Germany). Online reconstruction was performed on a bypass computer (‘sysGen/TYAN Octuple-GPU’, Sysgen, Bremen) with 8 GPUs (GeForce GTX 580, TITAN, Nvidia, Santa Clara). RT pharyngeal MRI were acquired at 25 and 55 fps while speaking in 2 healthy subjects (25 and 30 years old, 1 female). RT cerebral MRI at 100 fps was acquired together with a peripheral pulse unit (PPU) and respiratory monitoring with no task in a healthy subject (25 years old, female). Left ventricular (LV) short-axis and long-axis RT cardiac MRIs were acquired at 30 fps at rest for 4 healthy subjects (50 ± 16 years old, 2 female) and 100 fps for 2 healthy subjects (65 and 57 years old, 1 female).

A patient (50 years old male) with wall motion abdominally was scanned at 30 fps. The acquisition parameters were: flip angle (FA)=8°; TR / TE = 2.1 / 1.33 ms (for 25 fps), 2.22 / 1.46 ms (30 fps), 2.02 / 1.28 ms (55 fps) and 2 / 1.26 ms (100 fps); in-plane resolution = 1.3 – 1.6 mm 2D isotropic; in-plane field of view (FOV) = 192 – 320 mm 2D isotropic, these being varied among different subjects and targets; slice thickness = 6 mm.

The FT is an efficient way to extract and analyze periodic time-domain signals. The Fast Fourier transform (FFT) method is used for the FT of the datasets. The spectrum of each image pixel provided by FT along the temporal dimension may reveal temporal physiological changes. A short-time Fourier transform (STFT) is used to extract physiological information that changes with time, by calculating the spectral information in segmentations from short time periods. The segmentation period of the STFT transform is 128 temporal frames.

PCA of the RT datasets was implemented with singular value decomposition (SVD). Real-time high temporal resolution images were vectorized to an x-t domain matrix and then analyzed by SVD. Decomposed images associated with the largest eight singular values–the principal components–were synthesized from the corresponding singular values and vectors. The weaker components were considered less important and/or were corrupted by noise. The spatial sum of the synthetic images associated with each component provided a time curve for each component. Most of these curves were periodic and correlated with breathing, the cardiac cycle, or their harmonics. The second-largest principal component in the full dataset always exhibited a T1 decay pattern, which was regarded as a T1-weighting component. The square-root of the-sum-of-the-squares (SSOS) along the temporal dimension of the synthesized decomposed images was used to show areas with the highest change in signal intensity.

As described in subsection 1.3.1 of Chapter 1, the image signal acquired with the FLASH sequence reaches a steady-state after several excitation pulses. The period between the first excitation pulse and before entering the steady-state is the transient-state. The real-time data sets acquired by FLASH started at the transient-state. Therefore, the data were segmented into transient-state frames and steady-state frames. Image series with both transient-state and steady-state were regarded as ’full datasets,’ containing information of anatomical structure, T1, and physiological changes. Truncated image series with only steady-state data are regarded as ’reduced datasets,’ containing no T1-encoding information while retaining anatomical structure and physiological information. FT and PCA analyses were applied to both full and reduced datasets. STFT itself transformed data on temporal segments and was only applied in full datasets.

For short-axis cardiac scans, the LV was segmented based on the active contour (SNAKEs) method in a semi-automatic process. An initial ROI of the LV epicardial border was manually drawn in a first time frame of the RT data. Precise segmentation of epicardial and endocardium borders was automatically calculated with SNAKE starting from the initial ROI. The SNAKEs method was also used to segmentation the subsequent frames using the final ROI of the previous frame as the initial ROI. Fig. 6.1 demonstrates the segmentation process in the first cardiac frame. The donut-shaped LV myocardium area was further dissected into 72 sectors and aligned according to their polar angle. Fig. 6.2A demonstrates the dissection with an example of 16 sectors. The dissection with 72 sectors was processed similarly. The signal within the aligned sectors was averaged and unwrapped to produce an angular-temporal plot, as shown in Fig. 6.2B. The angular-temporal plot was used for model-based calculations of myocardial perfusion in the following section. For quantitative FT analysis and PCA, each sector was further segmented into 15 smaller sectors along the radial dimension based on the distance from the ROI center.

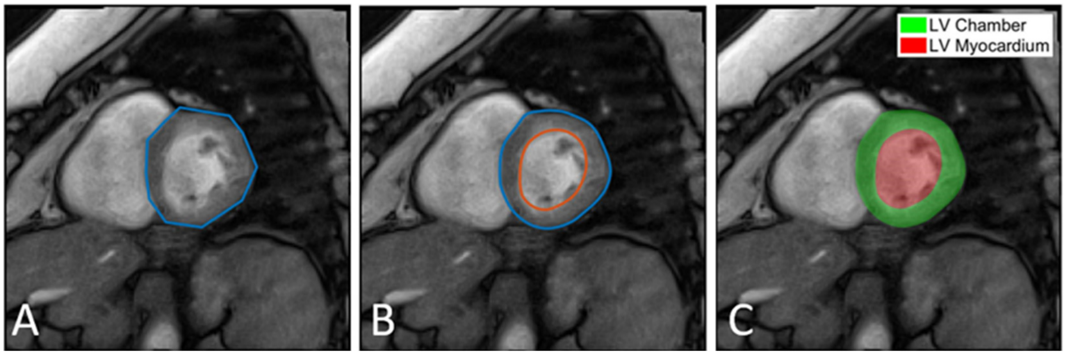

Figure 6.1: Initial manually-drawn epicardial borders (A), snakes contour (B), and segmentation (C) of the left ventricle of the first frame. Initial ROIs of other frames were set as the final contour of the previous slice.

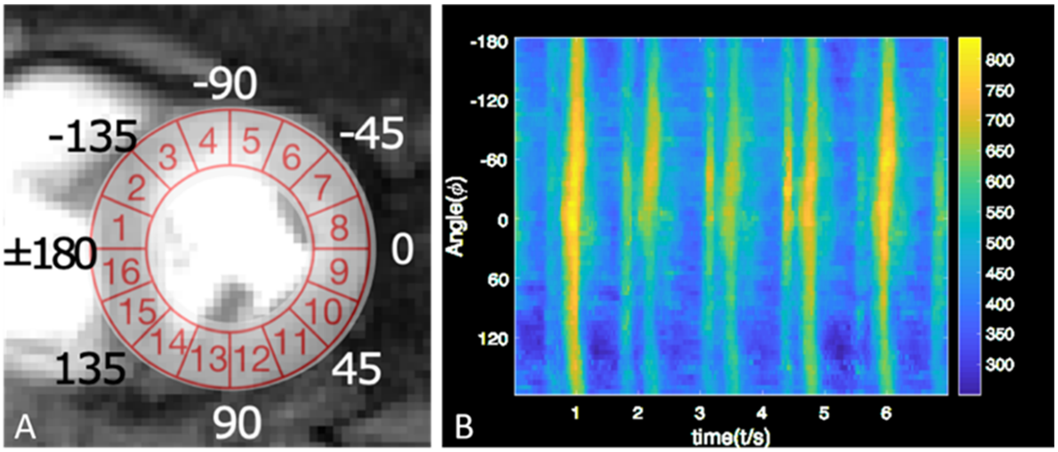

Figure 6.2: Donut-shaped left ventricle myocardium segmented into sectors corresponding to their polar angulation (A) and the unwrapped polar angle-temporal plot showing periodic signal change (B).

6.2.2 Perfusion model of RT cardiac MRI in left ventricular myocardium

The angular-temporal plot in Fig. 6.2B showed periodic signal fluctuation, which is correlated with the cardiac period and thought to be affected by cardiac motion and perfusion. A perfusion model is proposed in this section to extract the perfusion information. The description of this model starts with the equations of the signal in the transient-state and in the steady-state using the FLASH sequence.

Defining the signal intensity at an image pixel as M_k after the k^{th} RF excitation pulse, the pixel signal M_{k+1} after the $(k+1)^{th}$ pulse is a recurrent function of M_k with parameters TR, TE, T1, T2* and FA (θ), when the whole pixel remains in the imaging slice:

$$M_{k+1} = M_k e^{-\frac{TR}{T1}} \cos\theta + M^0 \left(1 - e^{-\frac{TR}{T1}}\right) e^{-\frac{TE}{T2^*}} \sin\theta. \qquad 6.1$$

Here, M^0 is the bulk magnetization in the pixel at equilibrium, θ is the flip angle of the FLASH sequence, and T_1 and T_2 are the lattice-spin and spin-spin relaxation times. Define:

$$E_1 = e^{-\frac{TR}{T1}}, E_2 = e^{-\frac{TE}{T2^*}} \qquad 6.2$$

Eq. 6.1 can be simplified:

$$M_{k+1} = M_k E_1 \cos\theta + M^0 (1 - E_1) E_2 \sin\theta. \qquad 6.3$$

When k is large enough, this signal will converge to a steady-state. The analytical solution of the steady-state FLASH signal intensity in the pixel, M_{ss}, is given by Eq. 6.4, obtained by solving Eq. 6.3 with M_{k+1} = M_k, assuming the transverse magnetization is completely dephased prior to the next excitation pulse. The expression was derived in the original paper (264):

$$M_{ss} = M_{ss}E_1 \cos\theta + M^0(1 - E_1)E_2 \sin\theta$$

$$M_{ss} = M^0 \frac{1-E_1}{1-E_1 \cos\theta} E_2 \sin\theta. \qquad 6.4$$

Consider the case where each of the real-time image frames is reconstructed from N radial projections, and the pixel signal of image frame t is $M_t = M_k$. Then, the pixel signal of image frame t+1, $M_{t+1} = M_{k+N}$, can be derived from the recurrent Eq. 6.3, as a function of M_t.

$$M_{k+N} = M_{k+N-1}E_1 \cos\theta + M^0(1 - E_1)E_2 \sin\theta$$

$$M_{k+N} = M_{k+N-1}E_1 \cos\theta + M^0 \frac{1-E_1}{1-E_1 \cos\theta} E_2 \sin\theta\,(1 - E_1 \cos\theta)$$

$$M_{k+N} - M^0 \frac{1-E_1}{1-E_1 \cos\theta} E_2 \sin\theta = \left(M_{k+N-1} - M^0 \frac{1-E_1}{1-E_1 \cos\theta} E_2 \sin\theta\right) E_1 \cos\theta$$

$$M_{k+N} - M^0 \frac{1-E_1}{1-E_1 \cos\theta} E_2 \sin\theta = \left(M_k - M^0 \frac{1-E_1}{1-E_1 \cos\theta} E_2 \sin\theta\right) (E_1 \cos\theta)^N$$

$$M_{k+N} = \left(M_k - M^0 \frac{1-E_1}{1-E_1 \cos\theta} E_2 \sin\theta\right) (E_1 \cos\theta)^N + M^0 \frac{1-E_1}{1-E_1 \cos\theta} E_2 \sin\theta$$

$$M_{t+1} = \left(M_t - M^0 \frac{1-E_1}{1-E_1 \cos\theta} E_2 \sin\theta\right) (E_1 \cos\theta)^N + M^0 \frac{1-E_1}{1-E_1 \cos\theta} E_2 \sin\theta. \qquad 6.5$$

Because $M^0 \frac{1-E_1}{1-E_1 cos\theta} E_2 sin\theta$ is actually the same as the analytical value of the steady-state signal, M_{ss} (Eq. 6.4). We can simplify Eq. 6.5 to:

$$M_{t+1} = (M_t - M_{ss})(E_1 \cos\theta)^N + M_{ss}. \tag{6.6}$$

Note that M_{ss} used here is defined as the steady-state signal $M^0 \frac{1-E_1}{1-E_1 cos\theta} E_2 sin\theta$, as calculated from Eq. 6.4 based on the values of $M^0, E_1, E_2 \text{ and } \theta$ for the tissue in the pixel. M_{t+1} and M_t can still be in the transient-state and differ from M_{ss}.

The previous equations are all based on the assumption that the whole pixel is always in the imaging slice. However, in the myocardium, this assumption needs to be modified due to cardiac motion and blood perfusion. In the following derivations, we assume that the signal in a pixel is a mixture of muscle signal and blood signal; that the muscle in the myocardium is affected by cardiac motion; and that the blood signal is affected both by motion and myocardial blood flow (MBF, perfusion measured as perfuse blood volume per unit of myocardial mass per time). Both the motion and the perfusion effects are regarded as spins moving from outside to inside the pixel. There are two steps to calculate the perfusion component. First, the total amount of spins that move into the imaging slice is calculated without distinguishing between cardiac motion and perfusion or flow. Second, we consider only the muscle signal in order to calculate the effect of motion. Perfusion is then calculated by subtracting the spins move in by motion from all spins move into the pixel.

In the first step, consider a pixel with mixed muscle and blood with signal M_t^{m+b} at frame t. The equilibrium signal of this pixel is denoted as $M^{0,m+b}$, in the absence of motion or perfusion. A steady-state signal M_{ss}^{m+b} is calculated from Eq. 6.4. This is only affected by the T1 and T2* value, and the TR/TE/FA used in the protocol, and not by transient motion or perfusion. Suppose that $T1^{m+b}$ is the T1 value of this pixel and $E_1^{m+b}$is the corresponding E_1value from Eq. 6.2. $T1^{m+b}$ is measured in the myocardium from a separate T1 mapping scan. Because the duration between frame t and t+1 (τ, temporal resolution) is very short, we assume that the speed (v) of through-plane cardiac motion (the speed component perpendicular to the imaging plane; motion within the plane does not affect the MRI saturation state of in-plane spins) and the perfusion (MBF) is constant in this period. If the volume of muscle moving into this pixel during frame t to t+1 due to motion is $Vnew_{mo}^{m+b}$ and the volume of perfused blood is $Vnew_{per}^{m+b}$, then:

$$Vnew_{mo}^{m+b} = \delta_x \delta_y v \tau, \text{ and}$$

$$Vnew_{per}^{m+b} = MBFm\tau = MBF\rho\delta_x\delta_y\delta_z\tau. \qquad 6.7$$

Here, δ_x and δ_y are the in-plane imaging pixel sizes and δ_z is the slice thickness. m is the mass of the pixel, and ρ is the specific gravity of the myocardium in the pixel. For simplicity, we assume the same proton density and specific gravity for muscle and blood, which are only slightly different. At frame t+1, the fraction of new spins moving into this pixel f_{mo+per}^{m+b} due to both motion and perfusion is:

$$f_{mo+per}^{m+b} = \frac{v\tau}{\delta_z} + MBF\rho\tau, \qquad 6.8$$

as compared to the pixel at time t. The new spins in frame t+1 experience their first excitation so their signal can be regarded as:

$$M_{t+1,mo+per}^{m+b} = f_{mo+per}^{m+b} M_1^{m+b}. \tag{6.9}$$

Here the signal $M_1^{m+b} = M^{0,m+b} E_2 \sin\theta$ is the signal after one excitation. The rest of the spins, with a fraction of $1 - f_{mo+per}^{m+b}$, remain in the pixel. The signal of these remaining spins can be derived from Eq. 6.6 as:

$$\widehat{M}_{t+1}^{m+b} = \left(M_t^{m+b} - M_{ss}^{m+b}\right)\left(E_1^{m+b}\cos\theta\right)^N + M_{ss}^{m+b}. \tag{6.10}$$

Thus their net contribution to the signal, $M_{t+1,static}^{m+b}$, is:

$$M_{t+1,static}^{m+b} = \left(1 - f_{mo+per}^{m+b}\right)\widehat{M}_{t+1}^{m+b}. \tag{6.11}$$

Note that $\widehat{M}_{t+1}^{m+b}$ in Eq. 6.10 is an inferred signal derived from M_t^{m+b} that is used for substitution like M_{ss} in Eq. 6.6. We will also use M with a hat for inferred signals later in subsection 6.2.2.

Combining Eq. 6.9 and 6.10, M_{t+1}^{m+b}, the signal of this pixel at frame t+1 is the summation of $M_{t+1,mo+per}^{m+b}$ and $M_{t+1,static}^{m+b}$:

$$M_{t+1}^{m+b} = M_{t+1,mo+per}^{m+b} + M_{t+1,static}^{m+b} = f_{mo+per}^{m+b} M_1^{m+b} + \left(1 - f_{mo+per}^{m+b}\right)\widehat{M}_{t+1}^{m+b}. \tag{6.12}$$

With M_{t+1}^{m+b} and M_t^{m+b} measured directly from the RT scans, the fraction f_{mo+per}^{m+b} can be calculated with Eq. 6.12 derived from Eq. 6.11:

$$f_{mo+per}^{m+b} = \frac{M_{t+1}^{m+b} - \widehat{M}_{t+1}^{m+b}}{M_1^{m+b} - \widehat{M}_{t+1}^{m+b}}. \tag{6.13}$$

Because $M_1^{m+b} = M^{0,m+b} E_2^{m+b} \sin\theta$, and M_{ss}^{m+b} is related to M_1^{m+b} via Eq. 6.4.

$$M_{ss}^{m+b} = M_1^{m+b} \frac{1 - E_1^{m+b}}{1 - E_1^{m+b} \cos\theta} \qquad 6.14$$

M_{ss}^{m+b} is estimated as the minimum value measured in the myocardium ROI, whereupon M_1^{m+b} is calculated from Eq. 6.14.

We cannot yet solve MBF from f_{mo+per}^{m+b} in Eq. 6.8 because the speed of motion, v, is still unknown. In the second step, we treat muscle and blood signals separately. We consider only the muscle to calculate the moving speed v, because all muscle spins that move into the pixel are a result of cardiac motion rather than perfusion. To separate muscle and blood, a new parameter r is introduced as the ratio of myocardial blood volume, which is treated as a constant. Then, the volume of new muscle moving into a pixel between frame t and t+1 ($Vnew_{mo}^{m+b}$) is:

$$Vnew_{mo}^{m} = (1-r)Vnew_{mo}^{m+b} = (1-r)\delta_x\delta_y v\tau, \qquad 6.15$$

The fraction of these new spins compared to existing muscle spins (blood spins excluded) f_{mo}^{m} due to motion is:

$$f_{mo}^{m} = \frac{(1-r)\delta_x\delta_y v\tau}{(1-r)\delta_x\delta_y\delta_z} = \frac{v\tau}{\delta_z}, \qquad 6.16$$

Recall that we assume identical proton density and specific gravity for blood and myocardium, so the volume ratio equals the mass ratio. Thus the initial signal ratio of inflowing blood and moving myocardial spins is also the same. The muscle (M_t^m) and blood (M_t^b) signal in the pixel at frame t should be:

$$M_t^m = (1-r)M_t^{m+b}, \quad M_t^b = rM_t^{m+b}. \tag{6.17}$$

Similar to Eq. 6.10, we can compute ($\widehat{M}_{t+1}^b$) and ($\widehat{M}_{t+1}^m$), the signal of remaining blood and muscle spins, respectively, derived from Eq. 6.6 are:

$$\widehat{M}_{t+1}^b = \left(M_t^b - M_{ss}^b\right)\left(E_1^b \cos\theta\right)^N + M_{ss}^b = \left(rM_t^{m+b} - M_{ss}^b\right)\left(E_1^b \cos\theta\right)^N + M_{ss}^b, \text{ and}$$

$$\widehat{M}_{t+1}^m = \widehat{M}_{t+1}^{m+b} - \widehat{M}_{t+1}^b. \tag{6.18}$$

Here, $E_1^b = e^{-\frac{TR}{T1^b}}$ and $T1^b$ is the blood T1, which is calculated from the left ventricular chamber signal measured in a separate T1 mapping scan, assuming that the T1 of blood is the same in the chamber and in the myocardium. M_{ss}^b is the steady-state signal of blood, which is calculated with Eq. 6.14 substituting M_1^{m+b} with M_1^b and E_1^{m+b} with E_1^b:

$$M_{ss}^b = M_1^b \frac{1-E_1^b}{1-E_1^b \cos\theta} = rM_1^{m+b} \frac{1-E_1^b}{1-E_1^b \cos\theta}. \tag{6.19}$$

Here we use $M_1^b = rM_1^{m+b}$ by substituting t=1 in Eq. 6.17. $\widehat{M}_{t+1}^m$ is calculated by subtraction in Eq. 6.18 rather than from the recurrent equations because the T1 value of muscle without blood is hard to measure. As with $\widehat{M}_{t+1}^{m+b}$, $\widehat{M}_{t+1}^b$ and $\widehat{M}_{t+1}^m$ are inferred signals calculated from M_t^{m+b}.

At frame t+1, the signals from new spins and from static spins are:

$$M_{t+1,mo}^m = f_{mo}^m M_1^m = f_{mo}^m (1-r) M_1^{m+b}, \text{ and } M_{t+1,static}^m = (1-f_{mo}^m)\widehat{M}_{t+1}^m. \tag{6.20}$$

Here we use $M_1^m = (1-r)M_1^{m+b}$ by substituting t=1 in Eq. 6.17.

Similar to Eq. 6.12, the muscle signal (M_{t+1}^m) is the summation of $M_{t+1,mo}^m$ and $M_{t+1,static}^m$, which is also $(1-r)M_{t+1}^{m+b}$ by substituting t=t+1 in Eq. 6.17.

$$M_{t+1}^m = (1-r)M_{t+1}^{m+b} = f_{mo}^m(1-r)M_1^{m+b} + (1-f_{mo}^m)\widehat{M}_{t+1}^m. \qquad 6.21$$

Therefore, we can derive f_{mo}^m from Eq. 6.12:

$$f_{mo}^m = \frac{(1-r)M_{t+1}^{m+b} - \widehat{M}_{t+1}^m}{(1-r)M_1^{m+b} - \widehat{M}_{t+1}^m}. \qquad 6.22$$

With f_{mo+per}^{m+b} and f_{mo}^m, we can calculate MBF, deriving from Eq. 6.8 and 6.16:

$$f_{mo+per}^{m+b} - f_{mo}^m = MBF\rho\tau,$$

$$MBF = \frac{f_{mo+per}^{m+b} - f_{mo}^m}{\rho\tau}. \qquad 6.23$$

In this study, we use ρ=1.05 g/ml. The temporal resolution τ is the production of TR and N, the number of projections per frame. We use r=0.089 in this work, based on published contrast-MRI measurements from healthy subjects at rest (265). With τ in ms, a scaling factor of 60000 ms/min is applied to obtain MBF in units of ml/g/min.

The following steps describe a possible protocol for quantifying myocardial blood flow (MBF) from RT cardiac images transformed into the polar angle-temporal domain.

1. Acquire a short axis T1-weighted image and calculate the T1 value of the myocardium with blood ($T1^{m+b}$) and the T_1 value of the chamber blood alone ($T1^{b}$).

2. Calculate corresponding E_1^{m+b} and E_1^{b} using Eq. 6.2.

3. Calculate the minimum signal in the myocardium ROI of the RT dataset which is taken as an estimate of M_{ss}^{m+b}, the steady-state of myocardium (muscle+blood).

4. Calculate M_1^{m+b} , the new inflowing muscle and blood signal, with Eq. 6.14.

5. Calculate M_{ss}^{b}, the steady-state blood signal, with Eq. 6.19 and blood volume ratio r=0.089.

6. Apply the segmentation described in subsection 6.2.1 and obtain the angular-temporal plot with T temporal frames and 72 angles.

7. For each angle ϕ and each frame 0≤t<T, measure the signal M_t^{m+b} at angle ϕ and time t in the angular-temporal plot and the signal M_{t+1}^{m+b} at angle ϕ and time t+1.

8. For each angle ϕ and each frame 0≤t<T, calculate $\widehat{M}_{t+1}^{m+b}$ from M_t^{m+b} and M_{ss}^{m+b} by Eq. 6.10.

9. For each angle ϕ and each frame 0≤t<T, calculate f_{mo+per}^{m+b}, the fraction of both in-moving tissue and inflowing blood at angle ϕ and between time t and t+1 from M_{t+1}^{m+b}, $\widehat{M}_{t+1}^{m+b}$, and M_1^{m+b} by Eq. 6.13.

10. For each angle ϕ and each frame 0≤t<T, calculate $\widehat{M}_{t+1}^{m}$ by Eq. 6.18 from M_{t+1}^{m+b}, M_t^{m+b}, and M_{ss}^{b}.

11. For each angle ϕ and each frame 0≤t<T, calculate f_{mo}^{m}, the fraction of in-moving myocardium at angle ϕ and time t by Eq. 6.22 from M_{t+1}^{m+b}, $\widehat{M}_{t+1}^{m}$, and M_1^{m+b}

12. For each angle ϕ and each frame 0≤t<T, compute MBF by Eq. 6.23 from f_{mo+per}^{m+b} and f_{mo}^{m}, with specific gravity ρ=1.05 g/ml.

6.3 Results

6.3.1 FT and STFT spectrum of RF pharyngeal data during speaking

Fig. 6.3 shows some regions of interest (ROIs) that were manually annotated on a 6mm sagittal frame a 55 fps RT image stream through the brain and pharynx of a healthy volunteer. Fig. 6.4 demonstrates FFT images of different frequencies of motion that occur, along with the STFT frequency spectra of the RT data acquired with the subject talking. The lip, tongue, and soft palate each show different frequency patterns. Though the medulla area is not directly involved in the speech process, some signal variations suggest a physiological change.

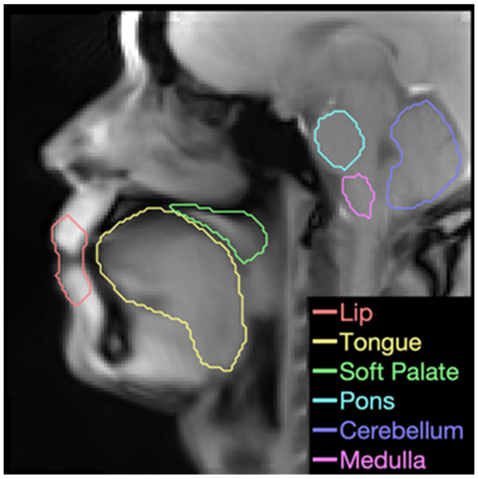

Figure 6.3: Annotated ROI of lip, tongue, soft palate, palatine tonsil, pons, and cerebellum on a sagittal pharyngeal MRI acquired at 55 fps.

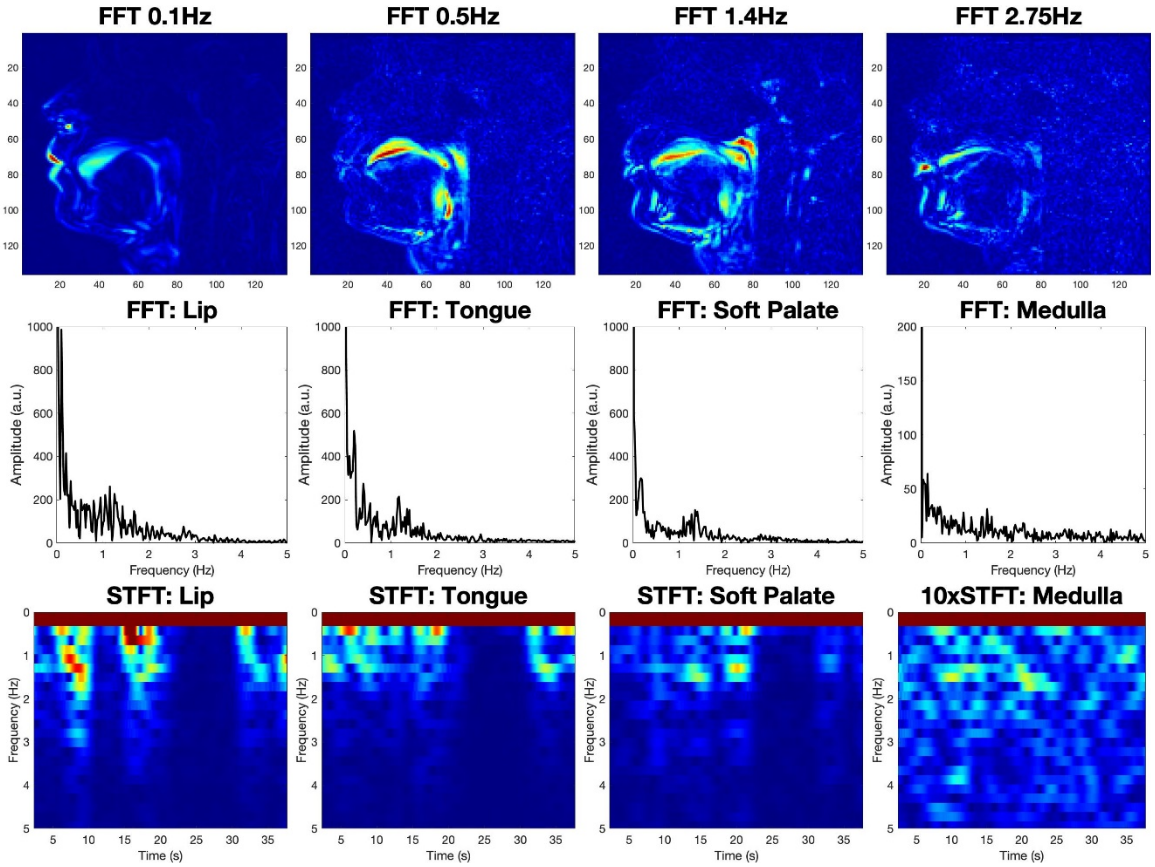

Figure 6.4: Fourier Transform of RT sagittal pharyngeal images sagittal acquired at 55 fps along the temporal dimension. (Top row) the images at four specific frequencies, (middle row) integral of FT magnitude within four different ROIs respectively, and (bottom row) short-term Fourier transform showing spectral-temporal magnitude. Intensities of images are scaled in each subfigure for better contrast of the spectrum.

6.3.2 FT and PCA of RT cardiac and cerebral data

Fig. 6.5 shows the integral of an FT spectrum of the whole image FOV of RT heart and brain datasets. Several peaks can be observed in the spectrum. The peak at around 0.25 Hz is attributed to respiration. Similarly, the peak at around 1 Hz is correlated with the cardiac cycle. 1-3 harmonics of the respiration and cardiac peaks are also identifiable in the spectrum. In all four 30 fps and two 100 fps cardiac datasets, the respiratory and cardiac frequencies are consistent with the apparent diaphragm displacement rate associated with breathing and contraction rates. In brain images, the frequency spectra showed similar peaks consistent with breathing and the heart rate as evidenced in monitoring data acquired from a PPU and a respiration belt. Interestingly, brain data showed a peak at the respiratory frequency, though not directly involved in respiratory motion.

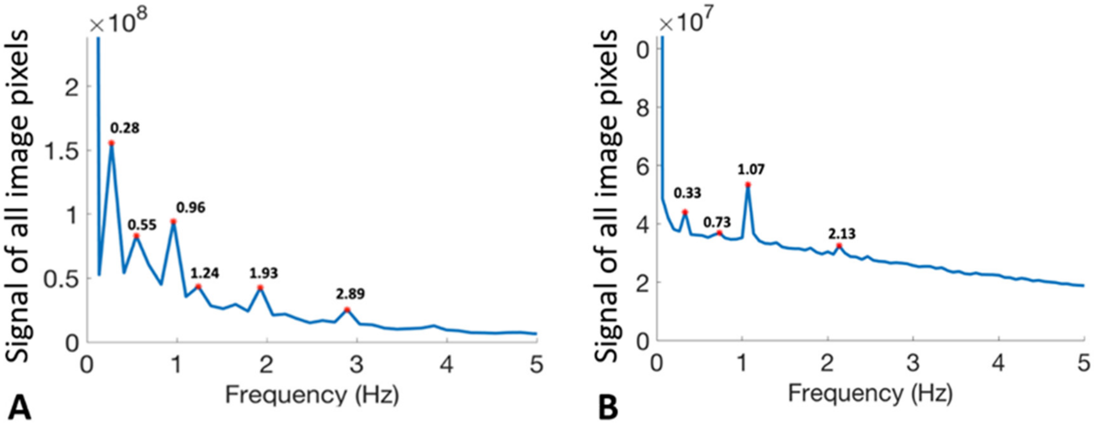

Figure 6.5: The superposition of the spectrum along space dimensions of a 30 fps RT heart reduced dataset (A), and a 100 fps RT brain reduced dataset (B), both show several peaks. In (A), a 0.28 Hz peak is attributed to respiration, and a 0.96 Hz peak is assigned to the cardiac cycle period. The respiration peak has an apparent harmonic at 0.55 Hz. The cardiac peak has two apparent harmonic peaks at 1.89 and 2.89 Hz. The 1.24 Hz peak (not the cardiac peak) has no harmonics. Similarly, in (B) 0.33 Hz is the respiratory frequency and 1.07 Hz is the cardiac frequency.

Figure 6.6 shows the FT results of RT cardiac (A) and cerebral (B) images corresponding to detected peak amplitudes at the respiratory and cardiac frequencies and their harmonics from the reduced dataset. Images at different frequencies show different enhancement patterns. The cardiac images (Fig. 6.6A) at the respiratory frequency and its harmonics are influenced by respiration so the most affected area of the liver appears brighter than other parts of the image. The images at the cardiac frequency and its harmonics are most influenced by heart motion, blood flow in the ventricular chambers, and perfusion so those signals in the myocardium and some hepatic vessels appear brightest at these frequencies. In the brain (Fig. 6.6B), the respiratory signal is most intense at the frontal sinus, while blood vessels light up in the cardiac frequency images. The signal change at the respiratory frequencies in the sinus is most likely caused by blood oxygen level changing with respiration.

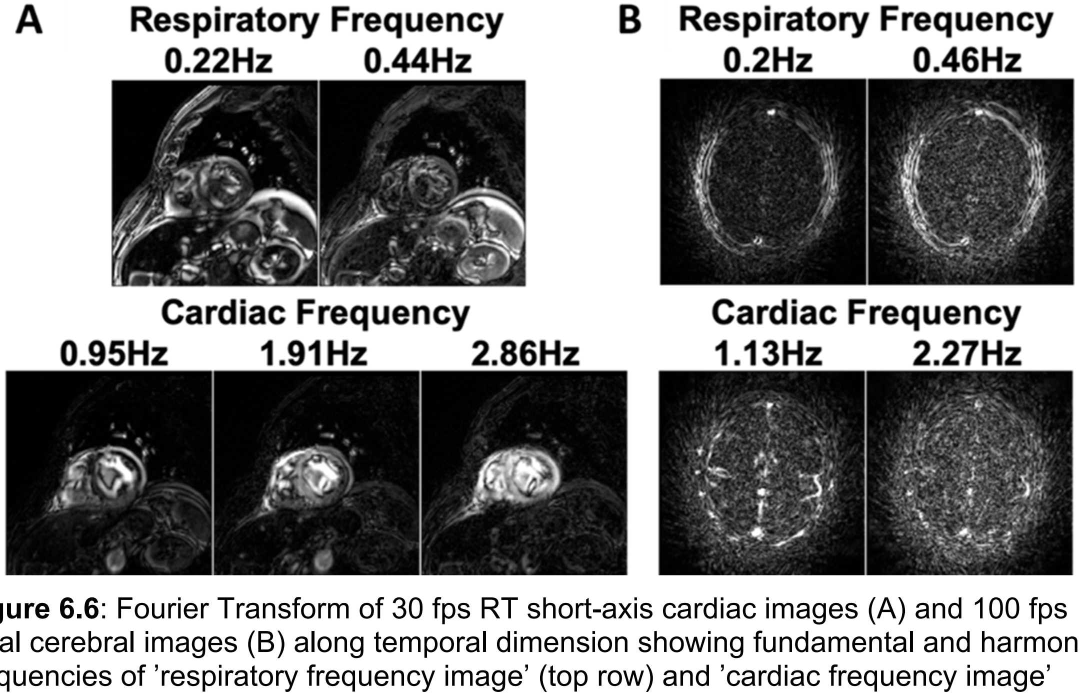

Figure 6.6: Fourier Transform of 30 fps RT short-axis cardiac images (A) and 100 fps axial cerebral images (B) along temporal dimension showing fundamental and harmonic frequencies of ’respiratory frequency image’ (top row) and ’cardiac frequency image’ (bottom row). Both data sets are from healthy volunteers.

PCA analysis of RT cerebral images (full datasets) are illustrated in Fig. 6.7 (component with the initial T1 decay to equilibrium in a transient-state) and Fig. 6.8 (a component at the heart rate exhibiting pulsatile blood flow). The images that correspond to the T1 decay component shown in Fig. 6.7 is heavily T1 weighted. Although it has a long T1, the signal in the sinus is bright due to fresh inflowing blood, generating a high steady-state signal from the FLASH sequence.

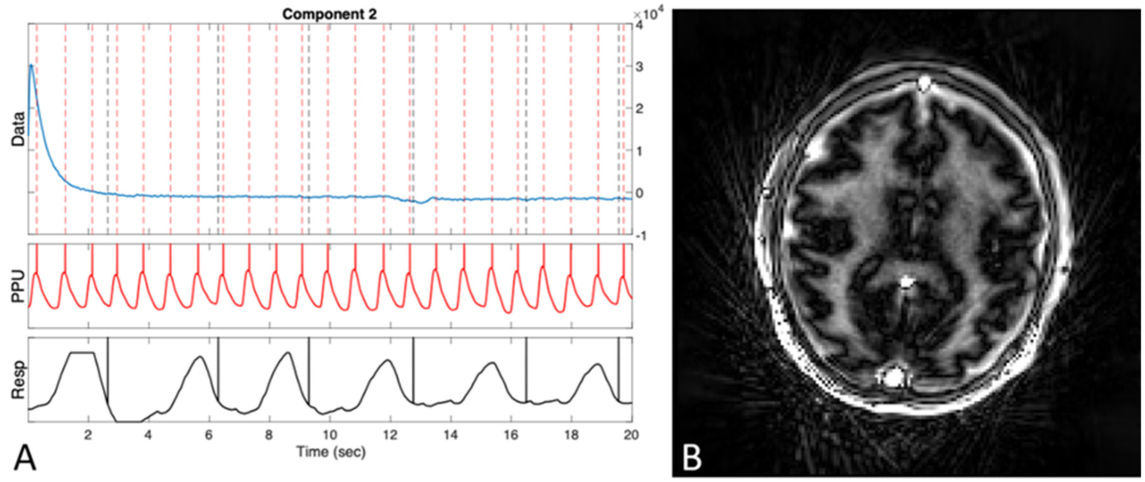

Figure 6.7: PCA analysis of 100 fps axial RT brain images showing the superposition signal evolution of the second-largest component (T1 decay) aligned with PPU and Respiration monitoring data (A). Corresponding images of the second-largest component showing T1 weighting with bright sinus signal (B). The image is the square-root of the sum-of-squares (SSOS) over all temporal frames.

Fig. 6.8, a more caudal slice, demonstrates an enhanced arterial signal with flow pulsation that follows the cardiac frequency. We can observe some vessels in this image (yellow arrows).

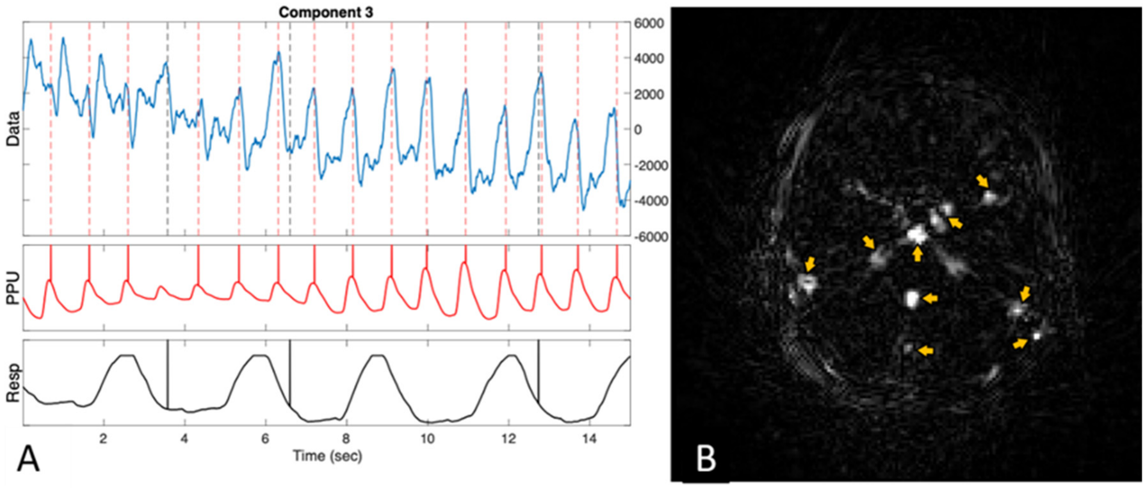

Figure 6.8: PCA analysis of 100 fps RT cerebral images showing the superposition signal evolution of the third-largest component (consistent with the PPU pattern) aligned with PPU and respiration monitoring data (A), and corresponding images of the third-largest component. Yellow arrows in (B) denote vessels.

6.3.3 Estimation of RT MBF with RT cardiac data

Fig. 6.9 shows the MBF estimated from the proposed model (Eq. 6.15) with a 30 fps RT cardiac dataset with the blood ratio r = 0.089. The MBF in diastolic phases (~1 ml/g/min) are generally higher than MBF in systolic phases (0.6 -1 ml/g/min). The average MBF of this subject of this slice is 0.88 ± 0.25 ml/g/min. The systolic and diastolic MBF is 0.80 ± 0.27 ml/g/min and 0.90 ± 0.24 ml/g/min, respectively. Figure 6.10 shows another case with 100 fps RT cardiac data. Although the signal is noisier, the pattern along the cardiac cycle is similar to the 30 fps case. The average MBF of this subject of this slice is 0.77 ± 0.45 ml/g/min. The systolic and diastolic MBF is 0.68 ± 0.4 ml/g/min and 0.81 ± 0.47 ml/g/min, respectively. The MBF mean values of the two datasets are comparable. The standard deviation of the 100 fps data is higher than the 30 fps data because the 100fps data is noisier.

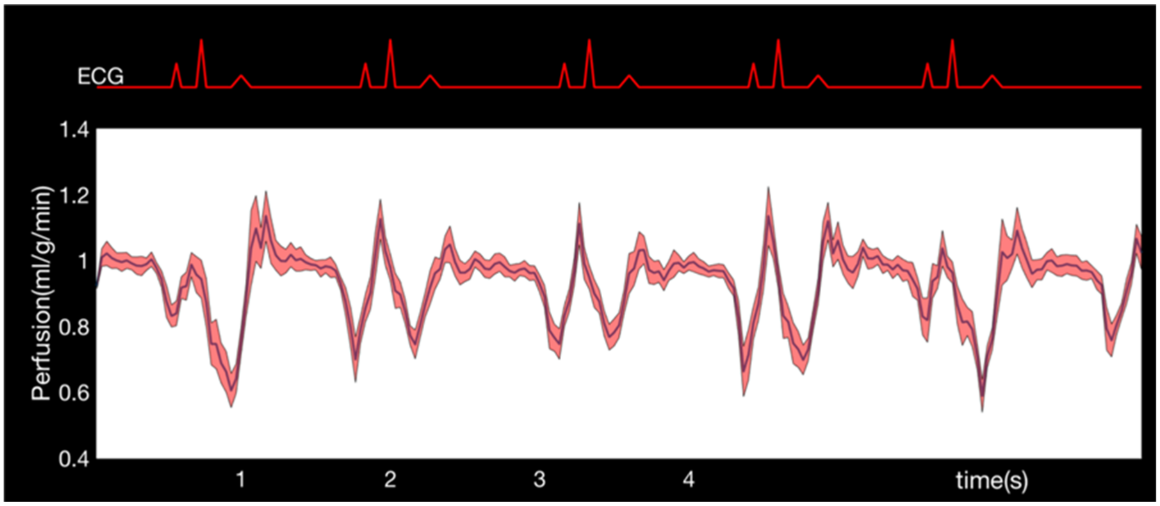

Figure 6.9: MBF Calculated from 30 fps RT cardiac data of a 65-year-old male with the proposed model. In this case, the blood ratio r=0.089 was used.

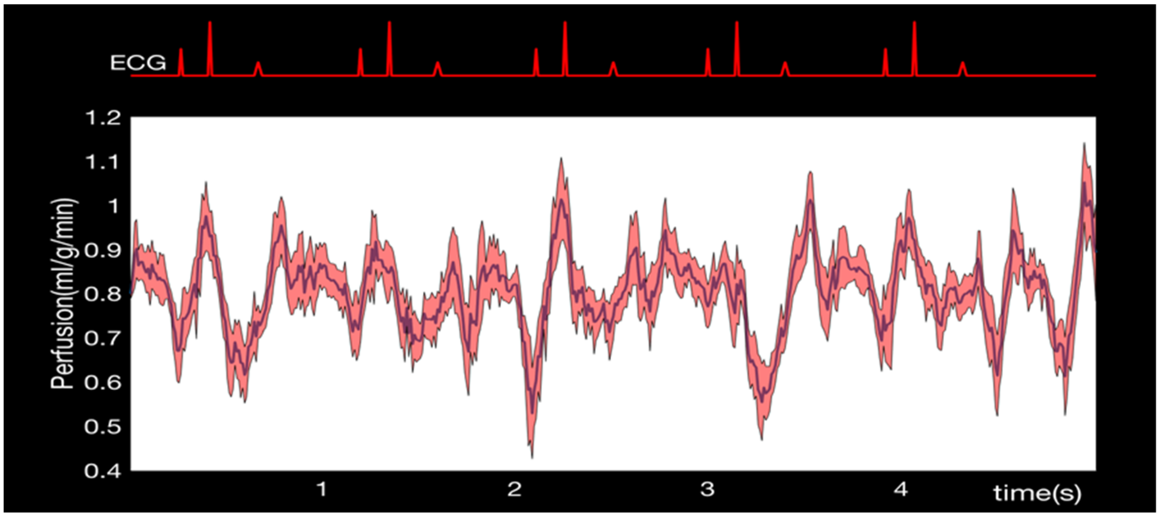

Figure 6.10: MBF Calculated from 100 fps RT cardiac data of a 57-year-old female with the proposed model. In this case, the blood ratio r=0.089 was used.

6.3.4 Patient results

Figure 6.11 demonstrates the analysis of the 30 fps cardiac RT data of a patient with wall motion abnormalities on the inferior left ventricular (LV) (wall yellow arrow). The signal difference between the normal and abnormal LV wall is not apparent in the static structural image (figure 6.11A), but the abnormality is clear in the angular-temporal map (figure 6.11B). In the FFT images (figure 6.11C), only small differences were observed in the 0 Hz (static signal) component, while the 1.35 Hz (cardiac frequency) component showed larger contrast between normal and diseased tissue. The principle component in the PCA decomposition also shows high contrast (figure 6.11D).

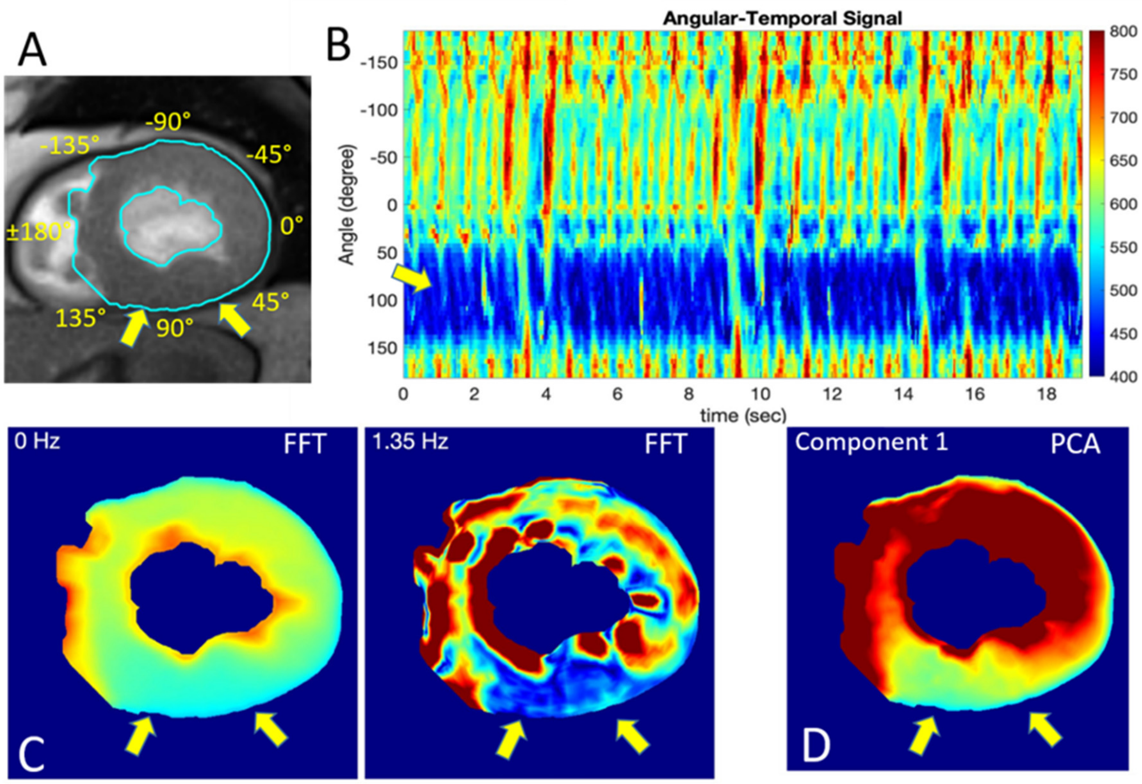

Figure 6.11: Structural data (A), angular-temporal map (B), and 0 Hz and 1.35 Hz short-axis images extracted by FFT from a 30 fps RT data stream acquired in a 50-year-old patient with wall motion abnormalities on the inferior LV wall. Part (D) is an image of the largest PCA. In (A), the region enclosed by the blue lines was segmented as the myocardial LV. Yellow arrows denote the abnormal LV wall.

6.4 Discussion

This chapter is a preliminary study to test whether high-speed RT MRI at up to 100 fps can capture temporal functional physiological information on timescales of up to 50 Hz. FT spectral, PCA decomposition techniques were applied and a model was developed to fit signal changes observed in myocardial tissue to motion and perfusion components. The feasibility of detecting high-speed physiological changes with RT MRI was tested on healthy volunteers with pharyngeal imaging during speaking, and with cerebral and cardiac datasets recorded at rest. The Fourier spectrum and PCA allowed the reconstruction of T_1-weighted, pulsation-weighted, and respiratory-weighted images. The MBF estimated from the perfusion model is around 0.6-1 ml/g/min at rest, assuming a blood volume ratio of r =0.089. This is comparable with published PET, contrast-enhanced MRI, and arterial spin labeling (ASL) scans, which yields average perfusion rates of 0.64-1.1ml/g/min(266–270). The MBF temporal patterns in each cardiac cycle are similar to the flow patterns of the left anterior descending artery (LAD) and the right coronary artery (RCA) that supply LV myocardium (271). The blood volume ratio r used here may change in different cardiac phases and with disease and other physiological factors, which will require further investigation. However, in patients with focal abnormalities, measurements from uninvolved tissue can serve as an internal control for comparison. Cardiac data from one patient with wall motion abnormalities showed FT and PCA decomposition images suggesting that the methods may be suitable for differentiating healthy and dysfunctional myocardium. In particular, focal perfusion abnormalities could be identified by changes in the area of abnormal wall motion relative to surrounding uninvolved tissue.

Physiological signals obtained from RT MRI suffer from noise and artifacts introduced by the imaging technique as well as that which is inherent in the source of physiological fluctuation. Although acquired from a high signal-to-noise ratio (SNR) 3T scanner, the data still requires averaging to increase the SNR. Traditionally, multiple repeated scans were averaged to obtain higher SNR in functional studies such as perfusion and spectroscopy. This prolongs scan time and is generally contrary to the goal of providing high temporal resolution RT MRI but may be useful for increasing the SNR for analysis of repetitive motion such as in the heart. In this work, averaging was applied to either multiple consecutive temporal frames, for example, the STFT transform, or within an ROI (sector) using the angular-temporal domain applied to short-axis RT cardiac MRI. The number of temporal frames in STFT was set to 128, balancing the resolution of the frequency, SNR of the spectrum, and the temporal resolution. 72 sectors were picked for the angular-temporal image as a tradeoff between the resolution in the angular dimension and SNR. Data can be acquired at up to 100 fps technically. Nevertheless, RT images with <100 fps temporal resolution but higher SNR are also studied in this work.

In the perfusion model, the unsaturated fresh blood signal S_0 was estimated from the dataset. An alternative way of measuring S_0 is to perform a separate scan with the same FA, TE, and spatial resolution as the FLASH sequence but with long TR (>5s). This scan would require breath-hold and cardiac triggering due to long TR and would add scan time.

This is a preliminary study and the number of cases is limited for both healthy subjects and patients, and more studies comparing measurements obtained by

FT and PCA analysis need to be conducted. In future studies, the perfusion model would also need to be validated on more subjects and against an independent method of measuring myocardial perfusion, which may include animal studies.

Chapter 7 Conclusions and Future Works

7.1 Conclusions

MRI has abundant controllable parameters and provides images with different kinds of physiological information. There are many potential clinical applications of MRI that benefit if the scan time is shortened. This dissertation explores the usage of accelerated and real-time MRI on parametric mapping, velocity mapping, angiography, and perfusion quantification. There are several efforts described in this dissertation that provide guides for existing fast imaging methods, proposes and develop new fast imaging methods using accelerated MRI, and explores novel uses for real-time MRI datasets.

First, we explored the effects of undersampling and iterative reconstruction in 3D whole-heart T2 parametric mapping. The selected reconstruction approaches exploit the redundancy in images that are similar, except for variations in contrast. We found that the parametric maps were more sensitive to undersampling than the raw images used in fitting the parameters, implying that for relaxometry, selection of the approach and acceleration factor can be critical. Traditional sensitivity encoding (SENSE) with equally-spaced (ES) sampling could only be considered as viable at low acceleration factors (≤3). However, for acceleration factors larger than 3, model-based SENSE and joint-sparsity SENSE reconstruction using variable density random (VDR) sampling were found to be more robust and better at preserving parametric T2 maps. We have submitted a journal paper manuscript on this work.

Second, we introduced a T2-prepared 3D stack-of-spiral gradient echo (GRE) pulse sequence for T2 mapping with high isotropic resolution, whole-brain coverage, and clinically acceptable scan time. Simulation results show that a non-linear 2-parameter fitting weighted by image intensities was optimal to reduce sensitivity to wide B_1 inhomogeneity and to low signal-to-noise ratio (SNR). We proposed an iterative model-based reconstruction method, which jointly utilized the model, data consistency, and spatial sparsity. This method achieved reasonable T2 estimation with an in-plane acceleration factor of 5 (root mean square error = 3.1% in simulations and = 8.2% in vivo). We also appended a cerebrospinal fluid (CSF) nulling module to the T2-prepared GRE sequences to suppress CSF partial volume effects and potentially ameliorate lesion detection. This work was performed in collaboration with Ruoxun Zi, M.S. We contributed equally. Ruoxun contributed to simulation, data processing, and the combination of the model-based reconstruction with compressed sensing (CS). My contribution included manipulating in-vivo scans, implementing scan sequences and protocols, and implementing fast non-linear T2 fitting and image reconstruction methods. This work resulted in a journal publication (272).

For velocity mapping, we developed and validated a novel single breath-hold coronary phase contrast (PC) MRI technique with both high temporal (<21 ms) and spatial resolution (0.8 mm) in the third project. To achieve high resolution, a golden angle (GA) rotated spiral acquisition sequence was combined with k-t sparse SENSE reconstruction. Gaps in k-space that occur after the binning of GA-rotated data into cardiac frames, were filled in by using a new-shifted binning method and the proposed triggered GA scheme, leading to a reduction of aliasing artifacts due to undersampling, resulting in improved image quality. Peak systolic velocity (PSV), peak diastolic velocity (PDV), coronary flow volume, and the cross-sectional area acquired with the proposed triggered GA scheme exhibited excellent intra-scan (0.92≤intraclass correlation (ICC)≤0.99) and high inter-scan (0.78≤ICC≤0.91) and intra-observer (0.91≤ICC≤0.98) reproducibility. We have submitted a journal paper manuscript on this work.

In the fourth project, we developed 3D non-contrast-enhanced abdominal MRA sequences for large spatial coverage at 3.0T, using a combination of velocity-selective saturation (VSS) pulse train and spatially selective inversion (SSI) or velocity-selective inversion (VSI). The CS technique was applied to accelerate the large field-of-view (FOV) scans, taking advantage of the image sparsity in angiograms. Both SSI+VSS and VSI+VSS arteriography delineated the arterial segments above the aortic bifurcation. We found that the VSI-based approach was less sensitive to slow arterial inflow than the SSI based approach and demonstrated better performance on bilateral iliac arteries. This work also resulted in a journal publication (241).

Finally, we studied the potential of capturing temporal functional and physiological information from high-speed real-time (RT) MRI at up to 100 fps. Spectral patterns of speech organs during speaking was detected with Fourier transform (FT). The FT and principal component analysis (PCA) allowed the reconstruction of T1-weighted, pulsation-weighted, and respiration-weighted images of healthy volunteers and a patient with wall motion abnormality. The RT myocardium blood flow (MBF) was calculated from a proposed perfusion model on healthy volunteers. The project is still ongoing and is planned for journal paper submission in the first half of 2021.

7.2 Future Works

7.2.1 T1 mapping using 3D stack-of-spiral GRE acquisition and model-based sparse reconstruction

The T2 mapping methods in this dissertation are applicable to similar scenarios, such as T1 mapping. In fact, we are presently testing the application of the stack-of-spiral gradient-echo (GRE) sequence and model-based sparse reconstruction (272) for brain T1 mapping with saturation recovery (SR) or inversion recovery (IR). We can obtain images with different T1 weighting with the stack-of-spiral gradient echo (GRE) method combined with the SR sequence. Fig. 7.1 demonstrates four of the fully-sampled T1-weighted spiral images from an initial attempt applying this sequence. We can accelerate these images with the model-based sparse reconstruction in (272). The model for T1 mapping is Eq. 1.4.

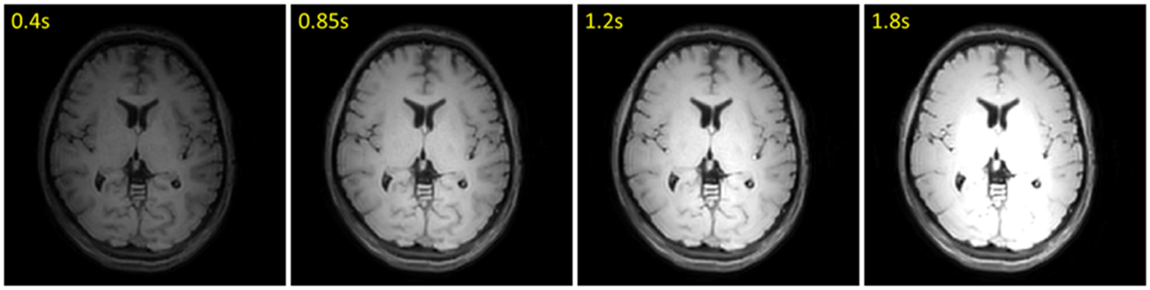

Figure 7.1: Stack-of-spiral brain images with different SR delays show different T1 weighting. Delay times after the saturation pulse are labeled on the top left of each image.

7.2.2 VSI based abdominal perfusion quantification

The velocity-selective (VS) abdominal angiography technique developed in Chapter 5 can be extended to obtain abdominal perfusion. We are applying the VSI technique for renal perfusion. The VSI ASL sequence as applied in an initial study of kidney perfusion is shown in Fig. 7.2. Because respiratory motion can corrupt the images, we started by using a 2D imaging sequence with a single gradient and spin echo (GRASE) acquisition, which is barely affected by intra-scan motion. Images at different respiratory phases were registered for non-rigid inter-scan motion before subtraction and averaging.

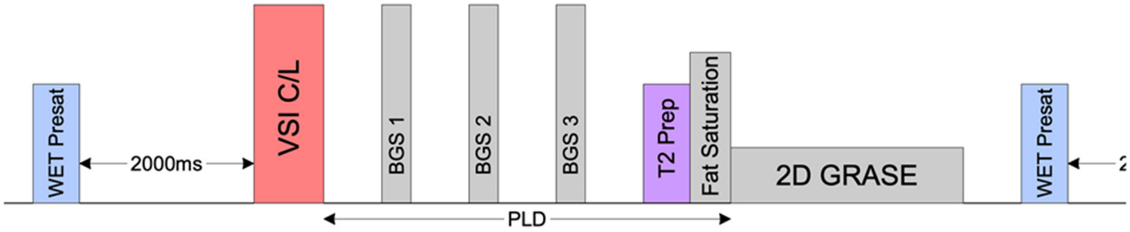

Figure 7.2: Pulse sequence of the VSI based renal perfusion. A water excitation pre-saturation pulse (WET) was applied with a 2000ms delay allowing arterial inflow. The VSI module (red) was then applied for control (velocity-compensated, for background subtraction) or labeled (velocity-encoded) images. During post labeling delay (PLD), three background suppression pulses were applied to increase temporal SNR. At the end of the PLD, a T2 preparation (T2 Prep) VSS module dephases flowing blood spins above 3cm/s. 2D gradient and spin echo (GRASE) was used for image acquisition.

The abdominal area suffers strong field inhomogeneity. In our initial attempt (Fig. 7.3), we tested fixed and adaptive shims available in the Philips scanners. We also tested three different post-labeling delays (PLDs): 0.6s, 0.9s, and 1.2s (Fig. 7.3). We obtained good quality renal perfusion-weighted images with distinct cortex-medulla contrast using adaptive shimming and PLD = 0.9s/1.2s.

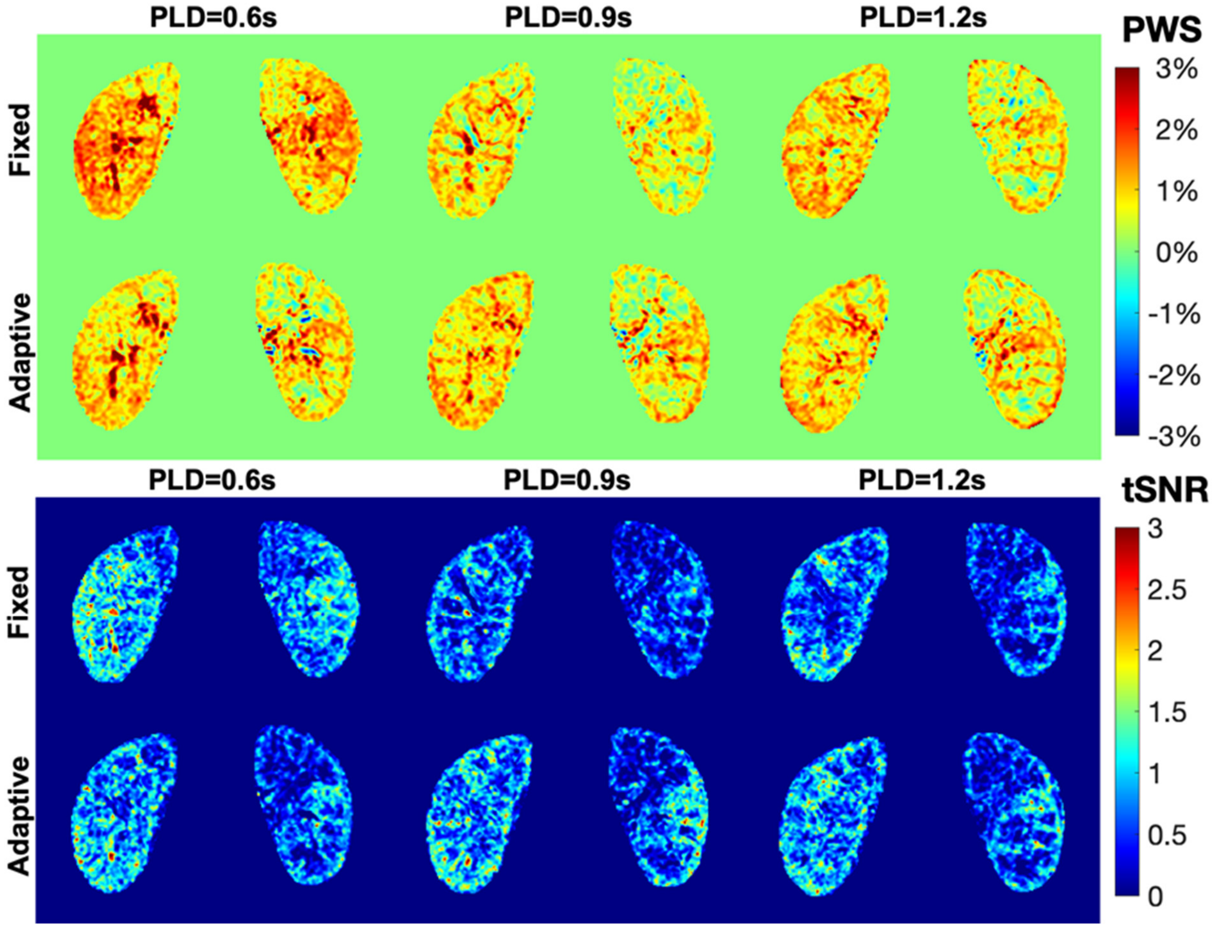

Figure 7.3: Renal perfusion-weighted signal (PWS) and temporal SNR (tSNR) results of a 59-years-old female subject with different PLDs at two B1 shimming conditions.

7.2.3 Accelerating velocity-selective (VS) angiography and perfusion with spiral acquisitions

We are accelerating velocity-selective (VS) angiography and perfusion with more efficient spiral acquisitions. An initial attempt at brain angiography is demonstrated in Fig. 7.4. The Cartesian acquisition is accelerated by a factor of 3 to match the scan time of the spiral acquisition, as spiral is more efficient than Cartesian k-space trajectories. Blurring induced by CS in the Cartesian scan is not observed in the spiral scan (yellow arrows). Nevertheless, the fully-sampled spiral scan can be further accelerated by incorporating CS. We plan to implement offline CS reconstruction for spiral imaging, which is currently not available on this vendor's platform.

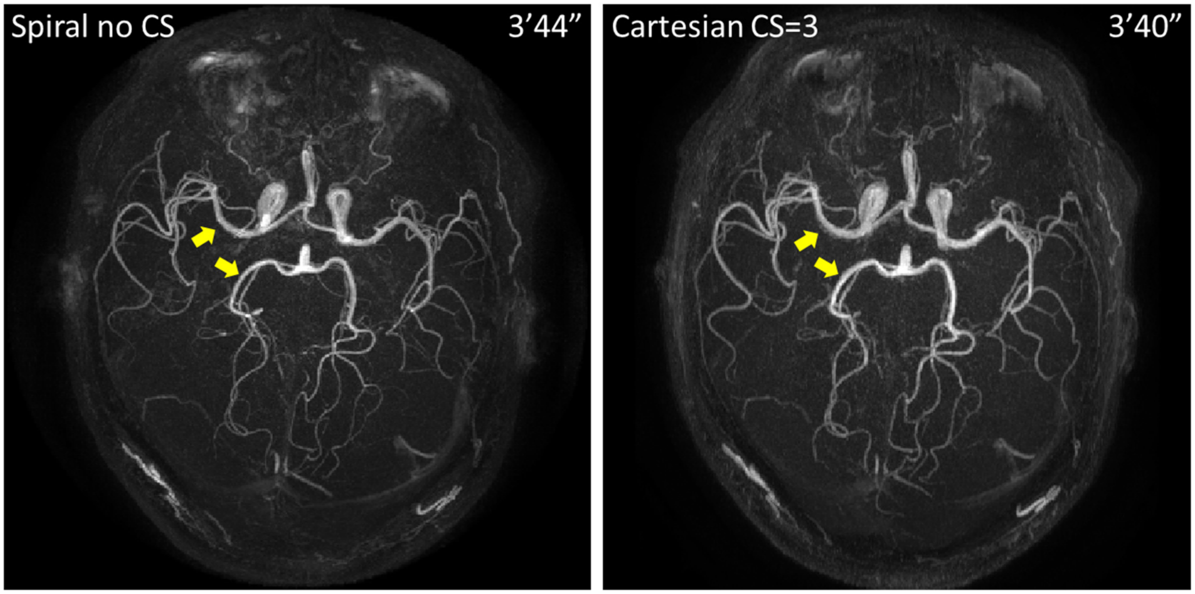

Figure 7.4: Stack-of-spiral (left) and Cartesian (right) SSI+VSS cerebral arteriography were acquired within similar scan times (indicated top right). The spiral acquisition is fully sampled, while the Cartesian acquisition is accelerated by 3 times using compressed sensing (CS). Blurring induced by CS accelerated is visualized in the Cartesian scan but not the spiral scan (yellow arrows).

Besides high sampling efficiency, spiral acquisitions reduce the dependence on the velocity encoding (VE) direction, explained as follows. The overall image contrast is determined by the center of k-space. Therefore, in a Cartesian image, the efficiency of blood contrast enhancement is dominated by the VE direction applied to the k-space line that crosses the center. Vessels perpendicular to that direction is usually poorly depicted. In the spiral acquisition, the center of k-space is repeatedly sampled in every spiral arm, so different VE directions can be applied to each arm. Fig. 7.5 compares the angiograms with one VE direction to that with multiple VE directions on a flow phantom. The flow phantom is cylindershaped and has 60 star-shaped ducts in the transverse plane that are curved to the foot-head (FH) direction at the border. Fluid can flow through the ducts. When using the FH direction (left column), the flow in axial ducts perpendicular to the VE direction has lower signals than the flow in the FH direction. If the LR direction is encoded (middle column), ducts in the AP direction (axial) are darker than the ducts in the LR direction. Ducts in the FH direction is also poorly depicted in the coronal MIP. The spiral image with multiple encoding directions (right column) has overall good image quality for all ducts.

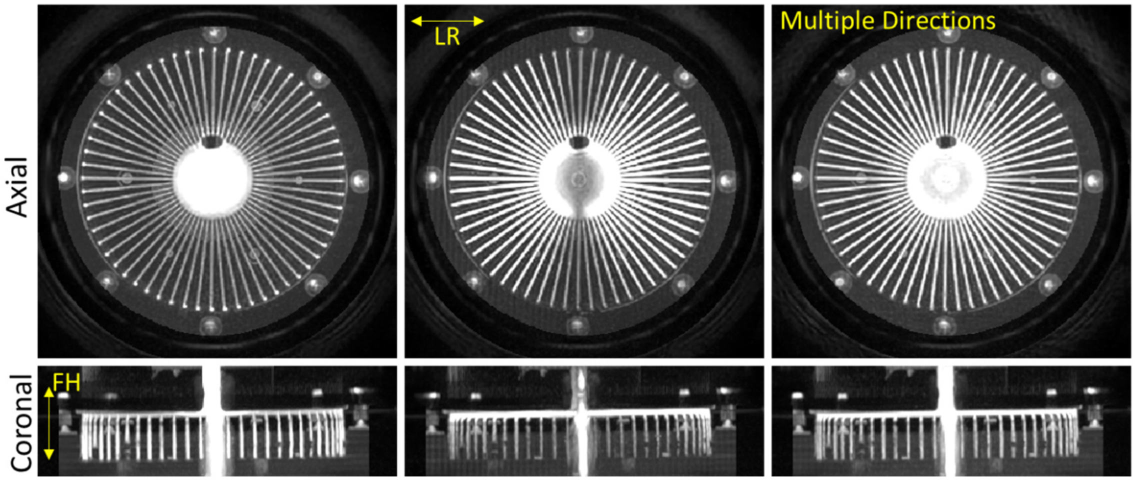

Figure 7.5: VSS angiography of a flow phantom with different VE directions (yellow arrows and labels). Fluid flows through 60 star-shaped ducts showing bright signal (white radial lines in axial images). The ducts are curves to the foot-head (FH) direction at the border of the phantom (outer tip of the radial lines in axial images). The ducts in the FH direction are parallel and aligned in a cylinder shape, the fluid in which show bright signal in coronal maximum intensity projection (MIP) images (thin parallel white lines). For angiograms with multiple VE directions (right), we applied three directions, FH, left-right (LR), and anterior-posterior (AP), interleaved to different spiral arms. Axial MIP images (Top row) show the 60 radial ducts (bright signal) in the axial plane. Coronal MIP (Bottom row) show ducts that are parallel to the FH direction.

The VSI based multiple-direction spiral technique also applies to perfusion scans. An initial attempt of this technique is demonstrated in Fig. 7.6.

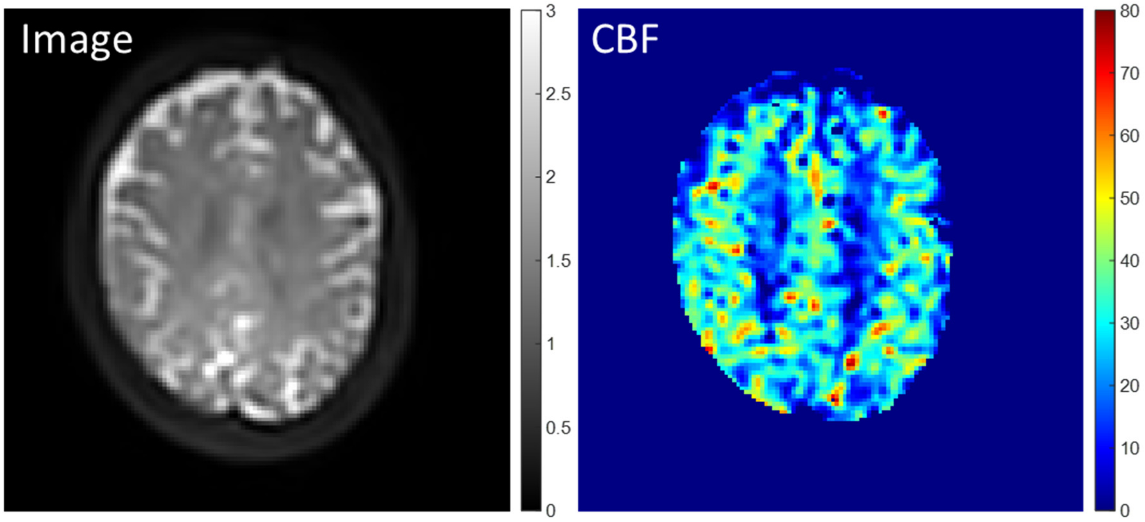

Figure 7.6: Structural image (left) and cerebral blood flow (CBF, ml/100g/min) perfusion map (right) of a brain dataset using VSI based arterial spin labeling (ASL) with stack-of-spiral acquisition and multiple VE directions.

7.2.4 Perfusion model in patients with wall motion abnormalities

RT perfusion has been calculated using the perfusion model and methods introduced in Chapter 6 in some patients with wall motion abnormalities. Fig. 7.7 demonstrates a regional analysis of perfusion in the initial patient whose images appear in Fig. 6.11. In the region of the wall motion abnormality (dark blue band in Fig. 6.11B), we see a ~30% reduction of myocardial blood flow (MBF) at rest, as compared to the uninvolved myocardium with normal wall motion (green-red bands in Fig. 6.11B). The reduced perfusion (MBF) in the dysfunctional area is consistent with a prior study showing reduced perfusion in hibernating myocardium (273). We are in the process of acquiring more patient data to evaluate the feasibility of this perfusion model along with the use of angular-temporal analysis for evaluating wall motion abnormalities, with quantitative comparisons.

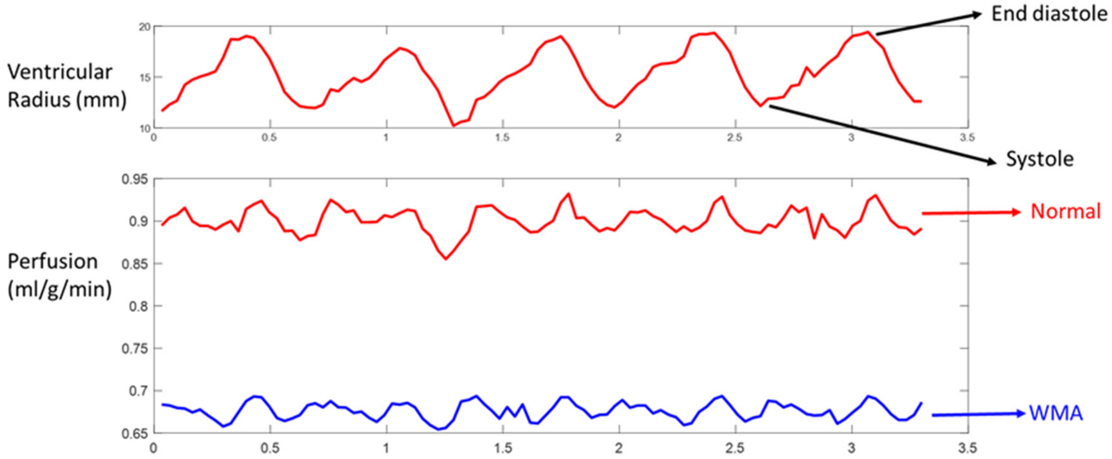

Figure 7.7: RT MBF calculated from a patient with wall motion abnormality (WMA) showed reduced perfusion in the WMA area than in the normal area. Perfusion values were calculated with the perfusion model given by subsection 6.2.2. The WMA area was manually selected based on the motion performance in the dynamic images. The T1 value of the normal and dysfunctional myocardium used in this model are calculated independently.

7.2.5 Novel contributions made in this dissertation and their potential benefits to MRI.

The accelerated parametric mapping methods offered in Chapters 2 and 3 cover the whole heart or brain in about 3 to 5 min and at high resolution (1-1.5 mm). Mapping without such acceleration can be as long as 20 minutes and/or low in resolution (2-3 mm). Shorter scan times are attractive in clinical applications due to a lower cost per unit patient scan-time, fewer motion artifacts, and less patient inconvenience and potential suffering in acute care settings. The high resolution parameter maps can improve the accuracy of diagnosis and segmentation of the area-at-risk in many cardiac and neurologic diseases, such as acute myocardial infarction, cardiac myocarditis, Alzheimer's disease, and multiple sclerosis (45–52,85,86,274–278).

The novel coronary phase contrast technique in Chapter 4 has a high spatial and temporal resolution, and high image quality compared to existing methods. Coronary flow metrics measured by the novel method are quantified in high accuracy and with a well-preserved temporal pattern and an excellent intra-scan reproducibility, which is especially suitable for paired rest and stress studies. This work can improve the accuracy of the diagnosis and the assessment of the severity of coronary stenosis by providing a more accurate measurement of coronary flow reserve (157–160) and measures of pressure gradients across coronary arteries (164). It can also help assess local endothelial dysfunction with high spatial and temporal resolution (161–163).

In Chapter 5, we developed a novel abdominal MRA technique with high resolution and large coverage. This technique is non-invasive and contrast-agent-free, which is especially suitable for screening and follow-up studies of many abdominal vasculature diseases (204). We are collaborating with radiologists to study the feasibility of this technique in the screening of abdominal vasculature diseases. Providing a larger coverage than existing MR techniques is attractive in screening settings because more area can be examined in one study. Moreover, compared to clinical ultrasound screening, MRA has high SNR in vessels that are deeply buried in the abdomen and is less sensitive to the operators' training and experience. We are working on further accelerating the scan-time and on implementing the technique on lower B_0 systems that could potentially offer reduced costs.

The RT data processing and decomposition in Chapter 6 explores the novel usage of high-speed MRI data: this system is the only one extant in the western hemisphere. More applications remain to be discovered, and are not limited to temporal weighting and RT perfusion mapping. We are considering potential applications of the techniques to the assessment of myocardial motion and perfusion in patients with wall motion abnormalities, and separately, studying swallowing patterns after throat surgical intervention to treat cancer which otherwise may not be able to be performed due to study time limitations.

We can also build MRI exams with primary structural and functional scans that can be completed in 10-20 minutes, with any or all of the techniques in Chapters 2 to 6. These MRI exams would be attractive in clinics by providing accelerated scan times at potentially lower cost, with the minimal safety issues associated with MRI compared to other modalities, and with high accuracy and reproducibility.

Appendix

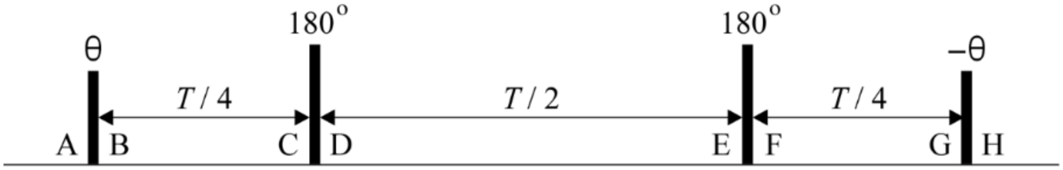

Figure A1: The sequence diagram of a T2 preparation module, which is typically composed of a hard pulse excitation (90º), followed by paired refocusing pulses (180º) and then a flip-back pulse (-90º). The flip angles of the hard pulses at the beginning or end of the T2 preparation module, although prescribed as 90°, are proportional to the B1 scales, $\theta = (\boldsymbol{B_{1+}}) \cdot \mathbf{90°}$**.**

The T2 preparation module (Fig. A.1) is typically composed of a hard pulse excitation (90º), followed by paired refocusing pulses (180º) and then a flip-back pulse (-90º). The refocusing pulses are relatively robust to B_1 inhomogeneities, being either composite or adiabatic pulses, so perfect 180º pulses are assumed in the following analytical derivation. In contrast, the flip angles of the hard (θ) pulses at the beginning or end of the T2 preparation module, although prescribed as 90°, are proportional to B_1:

$$\theta = (B_1 +) \cdot 90°$$

Assuming the longitudinal and transverse magnetization before T2 preparation (point A) are:

$$M_{z,A} = M^0, M_{xy,A} = 0$$

where M^0 is the equilibrium magnetization at fully recovery.

After the first pulse, the magnetizations become:

$$M_{z,B} = M^0 cos\theta, M_{xy,B} = M^0 sin\theta$$

The formula of T1 recovery and T2 decay are:

$$M_z(t) = M^0 + (M_z(0) - M^0)e^{-t/T1} \tag{A.1}$$

$$M_{xy}(t) = M_{xy}(0)e^{-t/T2} \tag{A.2}$$

where $M_z(t)$ and $M_{xy}(t)$ are the longitudinal and transverse magnetizations at time = t , respectively.

T2 weighting is set by the duration of the T2 preparation module (T). The longitudinal magnetizations before each of the following pulses are:

$$M_{z,C} = M^0(1 + (cos\theta - 1)e^{-T/4T1}))$$

$$M_{z,E} = M^0(1 - 2e^{-T/2T1} - (cos\theta - 1)e^{-3T/4T1})$$

$$M_{z,G} = M^0(1 - 2e^{-T/4T1} + 2e^{-3T/4T1} + (cos\theta - 1)e^{-T/T1})$$

And the transverse magnetization before the flip-back pulse is:

$$M_{xy,G} = M^0 sin\theta e^{-T/T2}$$

Therefore, the longitudinal magnetization at the end of T2 preparation is:

$$M_{z,H} = M_{z,G} \cos(-\theta) - M_{xy,G}\, sin(-\theta)$$

$$= M^0(sin^2\theta e^{-T/T2} + cos\,\theta\,(1 - 2e^{-T/4T1} + 2e^{-3T/4T1} + (cos\,\theta - 1)e^{-T/T1})))$$

$$\approx M^0\left(sin^2\theta e^{-\frac{T}{T2}} + cos^2\theta\right), when\, T \ll T1 \qquad \text{A.3}$$

In addition to the T2 weighting, the signal after T2 preparation also has dependence on the B_1 scale and T1 relaxation. If θ is equal to 90°, it becomes pure T2 dependent as desired:

$$M_{z,H} = M^0 e^{-T/T2} \qquad \text{A.4}$$

Note that Eq. A.3 does not deviate significantly if the number of refocusing pulses applied in the T2 preparation module is more than 2, as done in the current study (simulation analysis results not shown).

Bibliography

1. Ferreira VM, Piechnik SK, Dall'Armellina E, et al. Non-contrast T1-mapping detects acute myocardial edema with high diagnostic accuracy: a comparison to T2-weighted cardiovascular magnetic resonance. J Cardiovasc Magn Reson 2012;14:42.

2. Giri S, Chung Y-C, Merchant A, et al. T2 quantification for improved detection of myocardial edema. J Cardiovasc Magn Reson 2009;11:56.

3. Deoni SCL. Quantitative Relaxometry of the Brain: Topics in Magnetic Resonance Imaging 2010;21:101–113.

4. Margaret Cheng H-L, Stikov N, Ghugre NR, Wright GA. Practical medical applications of quantitative MR relaxometry. J. Magn. Reson. Imaging 2012;36:805–824.

5. Moran PR, Moran RA, Karstaedt N. Verification and evaluation of internal flow and motion. True magnetic resonance imaging by the phase gradient modulation method. Radiology 1985;154:433–441.

6. Clarke GD, Eckels R, Chaney C, et al. Measurement of Absolute Epicardial Coronary Artery Flow and Flow Reserve With Breath-Hold Cine Phase-Contrast Magnetic Resonance Imaging. Circulation 1995;91:2627–2634.

7. Edelman RR, Mattle HP, Atkinson DJ, Hoogewoud HM. MR angiography. AJR. American journal of roentgenology 1990;154:937–946.

8. Chen Q, Stock KW, Prasad PV, Hatabu H. Fast magnetic resonance imaging techniques. European Journal of Radiology 1999;29:90–100.

9. Listerud J, Einstein S, Outwater E, Kressel HY. First principles of fast spin echo. Magnetic resonance quarterly 1992;8:199–244.

10. Haase A, Frahm J, Matthaei D, Hanicke W, Merboldt K-D. FLASH imaging. Rapid NMR imaging using low flip-angle pulses. Journal of Magnetic Resonance (1969) 1986;67:258–266.

11. Carr HY. Steady-State Free Precession in Nuclear Magnetic Resonance. Phys. Rev. 1958;112:1693–1701.

12. Mansfield P. Multi-planar image formation using NMR spin echoes. Journal of Physics C: Solid State Physics 1977;10:L55–L58.

13. Mansfield P, Pykett IL. Biological and medical imaging by NMR. Journal of Magnetic Resonance (1969) 1978;29:355–373.

14. Ahn CB, Kim JH, Cho ZH. High-Speed Spiral-Scan Echo Planar NMR Imaging-I. IEEE Trans. Med. Imaging 1986;5:2–7.

15. Deshmane A, Gulani V, Griswold MA, Seiberlich N. Parallel MR imaging. J. Magn. Reson. Imaging 2012;36:55–72.

16. Lustig M, Donoho D, Pauly JM. Sparse MRI: The application of compressed sensing for rapid MR imaging. Magn. Reson. Med. 2007;58:1182–1195.

17. Lingala SG, Hu Y, DiBella E, Jacob M. Accelerated Dynamic MRI Exploiting Sparsity and Low-Rank Structure: k-t SLR. IEEE Trans. Med. Imaging 2011;30:1042–1054.

18. Pedersen H, Kozerke S, Ringgaard S, Nehrke K, Kim WY. *k-t* PCA: Temporally constrained *k-t* BLAST reconstruction using principal component analysis: *k-t* BLAST Using PCA. Magn. Reson. Med. 2009;62:706–716.

19. Wedeen V, Meuli R, Edelman R, et al. Projective imaging of pulsatile flow with magnetic resonance. Science 1985;230:946–948.

20. Busse RF, Hariharan H, Vu A, Brittain JH. Fast spin echo sequences with very long echo trains: Design of variable refocusing flip angle schedules and generation of clinicalT2 contrast. Magn. Reson. Med. 2006;55:1030–1037.

21. Koch KM, Rothman DL, de Graaf RA. Optimization of static magnetic field homogeneity in the human and animal brain in vivo. Progress in Nuclear Magnetic Resonance Spectroscopy 2009;54:69–96.

22. Buonocore MH, Gao L. Ghost artifact reduction for echo planar imaging using image phase correction. Magn. Reson. Med. 1997;38:89–100.

23. Pruessmann KP, Weiger M, Scheidegger MB, Boesiger P. SENSE: sensitivity encoding for fast MRI. Magnetic Resonance in Medicine: An Official Journal of the International Society for Magnetic Resonance in Medicine 1999;42:952–962.

24. Griswold MA, Jakob PM, Heidemann RM, et al. Generalized autocalibrating partially parallel acquisitions (GRAPPA). Magn. Reson. Med. 2002;47:1202–1210.

25. Pruessmann KP, Weiger M, Börnert P, Boesiger P. Advances in sensitivity encoding with arbitrary *k* -space trajectories: SENSE With Arbitrary *k* -Space Trajectories. Magn. Reson. Med. 2001;46:638–651.

26. Rudin LI, Osher S, Fatemi E. Nonlinear total variation based noise removal algorithms. Physica D: nonlinear phenomena 1992;60:259–268.

27. Gamper U, Boesiger P, Kozerke S. Compressed sensing in dynamic MRI. Magn. Reson. Med. 2008;59:365–373.

28. Winkelmann S, Schaeffter T, Koehler T, Eggers H, Doessel O. An Optimal Radial Profile Order Based on the Golden Ratio for Time-Resolved MRI. IEEE Trans. Med. Imaging 2007;26:68–76.

29. Chan RW, Ramsay EA, Cheung EY, Plewes DB. The influence of radial undersampling schemes on compressed sensing reconstruction in breast MRI. Magn. Reson. Med. 2012;67:363–377.

30. Noll DC, Nishimura DG, Macovski A. Homodyne detection in magnetic resonance imaging. IEEE Trans. Med. Imaging 1991;10:154–163.

31. Look DC, Locker DR. Time Saving in Measurement of NMR and EPR Relaxation Times. Review of Scientific Instruments 1970;41:250–251.

32. Messroghli DR, Radjenovic A, Kozerke S, Higgins DM, Sivananthan MU, Ridgway JP. Modified Look-Locker inversion recovery (MOLLI) for high-resolutionT1 mapping of the heart. Magn. Reson. Med. 2004;52:141–146.

33. Chow K, Flewitt JA, Green JD, Pagano JJ, Friedrich MG, Thompson RB. Saturation recovery single-shot acquisition (SASHA) for myocardial T_1 mapping: SASHA for T_1 Mapping. Magn. Reson. Med. 2014;71:2082–2095.

34. Foltz WD, Al-Kwifi O, Sussman MS, Stainsby JA, Wright GA. Optimized spiral imaging for measurement of myocardialT2 relaxation. Magn. Reson. Med. 2003;49:1089–1097.

35. Katoh M, Buecker A, Stuber M, Günther RW, Spuentrup E. Free-breathing renal MR angiography with steady-state free-precession (SSFP) and slab-selective spin inversion: Initial results. Kidney International 2004;66:1272–1278.

36. Shin T, Worters PW, Hu BS, Nishimura DG. Non-contrast-enhanced renal and abdominal MR angiography using velocity-selective inversion preparation: Velocity-Selective Noncontrast Abdominal MRA. Magn Reson Med 2013;69:1268–1275.

37. Williams DS, Detre JA, Leigh JS, Koretsky AP. Magnetic resonance imaging of perfusion using spin inversion of arterial water. Proceedings of the National Academy of Sciences 1992;89:212–216.

38. Dai W, Garcia D, de Bazelaire C, Alsop DC. Continuous flow-driven inversion for arterial spin labeling using pulsed radio frequency and gradient fields: Pulsed Continuous Arterial Spin Labeling. Magn. Reson. Med. 2008;60:1488–1497.

39. Wong EC, Cronin M, Wu W-C, Inglis B, Frank LR, Liu TT. Velocity-selective arterial spin labeling. Magn. Reson. Med. 2006;55:1334–1341.

40. Alsop DC, Detre JA, Golay X, et al. Recommended implementation of arterial spin-labeled perfusion MRI for clinical applications: A consensus of the ISMRM

perfusion study group and the European consortium for ASL in dementia: Recommended Implementation of ASL for Clinical Applications. Magn. Reson. Med. 2015;73:102–116.

41. Look DC, Locker DR. Time Saving in Measurement of NMR and EPR Relaxation Times. Review of Scientific Instruments 1970;41:250–251.

42. Messroghli DR, Radjenovic A, Kozerke S, Higgins DM, Sivananthan MU, Ridgway JP. Modified Look-Locker inversion recovery (MOLLI) for high-resolutionT1 mapping of the heart. Magn. Reson. Med. 2004;52:141–146.

43. Piechnik SK, Ferreira VM, Dall'Armellina E, et al. Shortened Modified Look-Locker Inversion recovery (ShMOLLI) for clinical myocardial T1-mapping at 1.5 and 3 T within a 9 heartbeat breathhold. J Cardiovasc Magn Reson 2010;12:69.

44. Chow K, Flewitt JA, Green JD, Pagano JJ, Friedrich MG, Thompson RB. Saturation recovery single-shot acquisition (SASHA) for myocardial T_1 mapping: SASHA for T_1 Mapping. Magn. Reson. Med. 2014;71:2082–2095.

45. Weingärtner S, Akçakaya M, Basha T, et al. Combined saturation/inversion recovery sequences for improved evaluation of scar and diffuse fibrosis in patients with arrhythmia or heart rate variability: Improved Imaging of Scar/Fibrosis. Magn. Reson. Med. 2014;71:1024–1034.

46. Ferreira VM, Piechnik SK, Dall'Armellina E, et al. Non-contrast T1-mapping detects acute myocardial edema with high diagnostic accuracy: a comparison to T2-weighted cardiovascular magnetic resonance. J Cardiovasc Magn Reson 2012;14:42.

47. Giri S, Chung Y-C, Merchant A, et al. T2 quantification for improved detection of myocardial edema. J Cardiovasc Magn Reson 2009;11:56.

48. Kellman P, Hansen MS. T1-mapping in the heart: accuracy and precision. J Cardiovasc Magn Reson 2014;16:2.

49. Puntmann VO, Voigt T, Chen Z, et al. Native T1 Mapping in Differentiation of Normal Myocardium From Diffuse Disease in Hypertrophic and Dilated Cardiomyopathy. JACC: Cardiovascular Imaging 2013;6:475–484.

50. Sado DM, White SK, Piechnik SK, et al. Identification and Assessment of Anderson-Fabry Disease by Cardiovascular Magnetic Resonance Noncontrast Myocardial T1 Mapping. Circ Cardiovasc Imaging 2013;6:392–398.

51. Karamitsos TD, Piechnik SK, Banypersad SM, et al. Noncontrast T1 Mapping for the Diagnosis of Cardiac Amyloidosis. JACC: Cardiovascular Imaging 2013;6:488–497.

52. Bohnen S, Radunski UK, Lund GK, et al. Performance of T1 and T2 Mapping

Cardiovascular Magnetic Resonance to Detect Active Myocarditis in Patients With Recent-Onset Heart Failure. Circ Cardiovasc Imaging 2015;8.

53. Ding H, Fernandez-de-Manuel L, Schär M, et al. Three-dimensional whole-heart T_2 mapping at 3T: 3D Myocardial T_2 Mapping. Magn. Reson. Med. 2015;74:803–816.

54. Henningsson M, Botnar RM, Voigt T. 3D saturation recovery imaging for free breathing myocardial T1 mapping. J Cardiovasc Magn Reson 2013;15:P44, 1532-429X-15-S1-P44.

55. Nordio G, Bustin A, Henningsson M, et al. 3D SASHA myocardial T1 mapping with high accuracy and improved precision. Magn Reson Mater Phy 2019;32:281–289.

56. Guo R, Chen Z, Wang Y, Herzka DA, Luo J, Ding H. Three-dimensional free breathing whole heart cardiovascular magnetic resonance T1 mapping at 3 T. J Cardiovasc Magn Reson 2018;20:64.

57. Weingärtner S, Akçakaya M, Roujol S, et al. Free-breathing combined three-dimensional phase sensitive late gadolinium enhancement and T_1 mapping for myocardial tissue characterization: Integrated Sequence for 3D LGE Imaging and 3D T_1 Mapping. Magn. Reson. Med. 2015;74:1032–1041.

58. Nordio G, Henningsson M, Chiribiri A, Villa ADM, Schneider T, Botnar RM. 3D myocardial T_1 mapping using saturation recovery: 3D Free-Breathing Myocardial T_1 Mapping. J. Magn. Reson. Imaging 2017;46:218–227.

59. Yang H-J, Sharif B, Pang J, et al. Free-breathing, motion-corrected, highly efficient whole heart T_2 mapping at 3T with hybrid radial-cartesian trajectory: Whole Heart T_2 Mapping at 3T with Hybrid Radial-Cartesian Trajectory. Magn. Reson. Med. 2016;75:126–136.

60. Doneva M, Börnert P, Eggers H, Stehning C, Sénégas J, Mertins A. Compressed sensing reconstruction for magnetic resonance parameter mapping. Magn. Reson. Med. 2010;64:1114–1120.

61. Huang J, Chen C, Axel L. Fast multi-contrast MRI reconstruction. Magnetic Resonance Imaging 2014;32:1344–1352.

62. Samsonov A. Accelerated MR Parameter Mapping Using Robust Model-Consistency Reconstruction. In: Proceedings of the International Society for Magnetic Resonance in Medicine 23. Toronto, Ontario, Canada; 2015. p. 3711.

63. Lustig M, Donoho D, Pauly JM. Sparse MRI: The application of compressed sensing for rapid MR imaging. Magn. Reson. Med. 2007;58:1182–1195.

64. Otazo R, Candès E, Sodickson DK. Low-rank plus sparse matrix

decomposition for accelerated dynamic MRI with separation of background and dynamic components: L+S Reconstruction. Magn. Reson. Med. 2015;73:1125–1136.

65. Pruessmann KP, Weiger M, Börnert P, Boesiger P. Advances in sensitivity encoding with arbitrary k -space trajectories: SENSE With Arbitrary k -Space Trajectories. Magn. Reson. Med. 2001;46:638–651.

66. Brittain JH, Hu BS, Wright GA, Meyer CH, Macovski A, Nishimura DG. Coronary Angiography with Magnetization-PreparedT2 Contrast. Magn. Reson. Med. 1995;33:689–696.

67. Schär M, Vonken E-J, Stuber M. Simultaneous B_0 - and B_1 +-Map acquisition for fast localized shim, frequency, and RF power determination in the heart at 3 T. Magn. Reson. Med. 2010;63:419–426.

68. Schär M, Ding H, Herzka DA. Improvement in B1+ Homogeneity and Average Flip Angle Using Dual-Source Parallel RF Excitation for Cardiac MRI in Swine Hearts Fan X, editor. PLoS ONE 2015;10:e0139859.

69. Wang J, Kluge T, Nittka M, Jellus V, Kuehn B, Kiefer B. Parallel acquisition techniques with modified SENSE reconstruction mSENSE. In: Proceedings of the First Würzburg Workshop on Parallel Imaging Basics and Clinical Applications. Würzburg, Germany; 2001. p. 89.

70. Pruessmann KP, Weiger M, Scheidegger MB, Boesiger P. SENSE: sensitivity encoding for fast MRI. Magn Reson Med 1999;42:952–962.

71. Tsao J, Kozerke S, Boesiger P, Pruessmann KP. Optimizing spatiotemporal sampling fork-t BLAST andk-t SENSE: Application to high-resolution real-time cardiac steady-state free precession. Magn. Reson. Med. 2005;53:1372–1382.

72. Breuer FA, Blaimer M, Heidemann RM, Mueller MF, Griswold MA, Jakob PM. Controlled aliasing in parallel imaging results in higher acceleration (CAIPIRINHA) for multi-slice imaging. Magn. Reson. Med. 2005;53:684–691.

73. Breuer FA, Blaimer M, Mueller MF, et al. Controlled aliasing in volumetric parallel imaging (2D CAIPIRINHA). Magn. Reson. Med. 2006;55:549–556.

74. Marseille GJ, de Beer R, Fuderer M, Mehlkopf AF, van Ormondt D. Nonuniform Phase-Encode Distributions for MRI Scan Time Reduction. Journal of Magnetic Resonance, Series B 1996;111:70–75.

75. Tsai CM, Nishimura DG. Reduced aliasing artifacts using variable-density k-space sampling trajectories. Magn Reson Med 2000;43:452–458.

76. Greiser A, von Kienlin M. Efficientk-space sampling by density-weighted phase-encoding. Magn. Reson. Med. 2003;50:1266–1275.

77. Griswold MA, Jakob PM, Heidemann RM, et al. Generalized autocalibrating partially parallel acquisitions (GRAPPA). Magn. Reson. Med. 2002;47:1202–1210.

78. Nayak KS, Nishimura DG. Randomized trajectories for reduced aliasing artifact. In: Proceedings of the 6th Annual Meeting of ISMRM, Sydney, Australia. Sydney, Australia; 1998. p. 670.

79. Samsonov AA, Kholmovski EG, Parker DL, Johnson CR. POCSENSE: POCS-based reconstruction for sensitivity encoded magnetic resonance imaging. Magn. Reson. Med. 2004;52:1397–1406.

80. Bilgic B, Kim TH, Liao C, et al. Improving parallel imaging by jointly reconstructing multi-contrast data: Joint Reconstruction of Multi-Contrast Data. Magn. Reson. Med. 2018;80:619–632.

81. Vasanawala S, Murphy M, Alley M, et al. Practical parallel imaging compressed sensing MRI: Summary of two years of experience in accelerating body MRI of pediatric patients. In: 2011 IEEE International Symposium on Biomedical Imaging: From Nano to Macro. Chicago, IL, USA: IEEE; 2011. pp. 1039–1043.

82. Wang X, Roeloffs V, Klosowski J, et al. Model-based T $_1$ mapping with sparsity constraints using single-shot inversion-recovery radial FLASH: Model-Based T $_1$ Mapping With Joint Sparsity Constraints. Magn. Reson. Med. 2018;79:730–740.

83. Noll DC, Nishimura DG, Macovski A. Homodyne detection in magnetic resonance imaging. IEEE Trans. Med. Imaging 1991;10:154–163.

84. Otsu N. A Threshold Selection Method from Gray-Level Histograms. IEEE Trans. Syst., Man, Cybern. 1979;9:62–66.

85. Deoni SCL. Quantitative Relaxometry of the Brain. Topics in Magnetic Resonance Imaging 2010;21:101–113.

86. Margaret Cheng H-L, Stikov N, Ghugre NR, Wright GA. Practical medical applications of quantitative MR relaxometry. Journal of Magnetic Resonance Imaging 2012;36:805–824.

87. Pruessmann KP, Weiger M, Scheidegger MB, Boesiger P. SENSE: Sensitivity encoding for fast MRI. Magnetic Resonance in Medicine 1999;42:952–962.

88. Griswold MA, Jakob PM, Heidemann RM, et al. Generalized autocalibrating partially parallel acquisitions (GRAPPA). Magn. Reson. Med. 2002;47:1202–1210.

89. Donoho DL. Compressed sensing. IEEE Transactions on information theory 2006;52:1289–1306.

90. Block KT, Uecker M, Frahm J. Undersampled radial MRI with multiple coils. Iterative image reconstruction using a total variation constraint. Magn. Reson. Med. 2007;57:1086–1098.

91. Lustig M, Donoho D, Pauly JM. Sparse MRI: The application of compressed sensing for rapid MR imaging. Magn. Reson. Med. 2007;58:1182–1195.

92. Feng L, Grimm R, Block KT, et al. Golden-angle radial sparse parallel MRI: Combination of compressed sensing, parallel imaging, and golden-angle radial sampling for fast and flexible dynamic volumetric MRI. Magn. Reson. Med. 2014;72:707–717.

93. Doneva M, Börnert P, Eggers H, Stehning C, Sénégas J, Mertins A. Compressed sensing reconstruction for magnetic resonance parameter mapping. Magn. Reson. Med. 2010;64:1114–1120.

94. Velikina JV, Alexander AL, Samsonov A. Accelerating MR parameter mapping using sparsity-promoting regularization in parametric dimension: Accelerating MR Parameter Mapping. Magnetic Resonance in Medicine 2013;70:1263–1273.

95. Majumdar A, Ward RK. Accelerating multi-echo T2 weighted MR imaging: Analysis prior group-sparse optimization. Journal of Magnetic Resonance 2011;210:90–97.

96. Zhang T, Pauly JM, Levesque IR. Accelerating parameter mapping with a locally low rank constraint: Locally Low Rank Parameter Mapping. Magn. Reson. Med. 2015;73:655–661.

97. Zhao B, Lu W, Hitchens TK, Lam F, Ho C, Liang Z-P. Accelerated MR parameter mapping with low-rank and sparsity constraints: Fast MR Parameter Mapping with Sparse Sampling. Magn. Reson. Med. 2015;74:489–498.

98. Huang C, Graff CG, Clarkson EW, Bilgin A, Altbach MI. T2 mapping from highly undersampled data by reconstruction of principal component coefficient maps using compressed sensing. Magn. Reson. Med. 2012;67:1355–1366.

99. Sumpf TJ, Uecker M, Boretius S, Frahm J. Model-based nonlinear inverse reconstruction for T2 mapping using highly undersampled spin-echo MRI. Journal of Magnetic Resonance Imaging 2011;34:420–428.

100. Block KT, Uecker M, Frahm J. Model-Based Iterative Reconstruction for Radial Fast Spin-Echo MRI. IEEE Trans. Med. Imaging 2009;28:1759–1769.

101. Samsonov A. Accelerated MR Parameter Mapping Using Robust Model-

Consistency Reconstruction. In: Proceedings of the 23th Annual Meeting of ISMRM. Vol. 3711. Toronto, Canada; 2015.

102. Hilbert T, Sumpf TJ, Weiland E, et al. Accelerated T2 mapping combining parallel MRI and model-based reconstruction: GRAPPATINI. J. Magn. Reson. Imaging 2018;48:359–368.

103. Hilbert T, Schulz J, Marques JP, et al. Fast model-based T2 mapping using SAR-reduced simultaneous multislice excitation. Magn Reson Med 2019;82:2090–2103.

104. Guo Y, Lingala SG, Zhu Y, Lebel RM, Nayak KS. Direct estimation of tracer-kinetic parameter maps from highly undersampled brain dynamic contrast enhanced MRI: Direct Estimation of Tracer-Kinetic Parameter Maps. Magn. Reson. Med. 2017;78:1566–1578.

105. Wang X, Roeloffs V, Klosowski J, et al. Model-based T_1 mapping with sparsity constraints using single-shot inversion-recovery radial FLASH: Model-Based T_1 Mapping With Joint Sparsity Constraints. Magnetic Resonance in Medicine 2018;79:730–740.

106. Tamir JI, Uecker M, Chen W, et al. T_2 shuffling: Sharp, multicontrast, volumetric fast spin-echo imaging: T_2 Shuffling. Magnetic Resonance in Medicine 2017;77:180–195.

107. Mandava S, Keerthivasan MB, Li Z, Martin DR, Altbach MI, Bilgin A. Accelerated MR parameter mapping with a union of local subspaces constraint: Mandava et al. Magn. Reson. Med 2018;80:2744–2758.

108. Roeloffs V, Uecker M, Frahm J. Joint T1 and T2 mapping with tiny dictionaries and subspace-constrained reconstruction. IEEE Trans. Med. Imaging 2019;39:1008–1014.

109. Keerthivasan MB, Saranathan M, Johnson K, et al. An efficient 3D stack-of-stars turbo spin echo pulse sequence for simultaneous T2-weighted imaging and T2 mapping. Magn Reson Med 2019;82:326–341.

110. Qi H, Sun J, Qiao H, et al. Simultaneous T1 and T2 mapping of the carotid plaque (SIMPLE) with T2 and inversion recovery prepared 3D radial imaging. Magn. Reson. Med 2018;80:2598–2608.

111. Ahn CB, Kim JH, Cho ZH. High-Speed Spiral-Scan Echo Planar NMR Imaging-I. IEEE Trans. Med. Imaging 1986;5:2–7.

112. Lustig M, Donoho DL, Santos JM, Pauly JM. Compressed sensing MRI. IEEE signal processing magazine 2008;25:72–82.

113. Liao J-R, Pauly JM, Brosnan TJ, Pelc NJ. Reduction of motion artifacts in

cine MRI using variable-density spiral trajectories. Magn. Reson. Med. 1997;37:569–575.

114. Deoni SCL, Rutt BK, Peters TM. Rapid combined T1 and T2 mapping using gradient recalled acquisition in the steady state. Magn. Reson. Med. 2003;49:515–526.

115. Nguyen TD, Wisnieff C, Cooper MA, et al. T_2 prep three-dimensional spiral imaging with efficient whole brain coverage for myelin water quantification at 1.5 tesla: Myelin Quantification with T_2 prep 3D Spiral Imaging. Magn. Reson. Med. 2012;67:614–621.

116. Roccia E, Vidya Shankar R, Neji R, et al. Accelerated 3D T_2 mapping with dictionary-based matching for prostate imaging. Magn. Reson. Med 2019;81:1795–1805.

117. Colotti R, Omoumi P, Bonanno G, Ledoux J-B, van Heeswijk RB. Isotropic three-dimensional T2 mapping of knee cartilage: Development and validation. J. Magn. Reson. Imaging 2018;47:362–371.

118. Coolen BF, Poot DHJ, Liem MI, et al. Three-dimensional quantitative T1 and T2 mapping of the carotid artery: Sequence design and in vivo feasibility. Magn. Reson. Med. 2016;75:1008–1017.

119. van Heeswijk RB, Piccini D, Feliciano H, Hullin R, Schwitter J, Stuber M. Self-navigated isotropic three-dimensional cardiac T2 mapping. Magn. Reson. Med. 2015;73:1549–1554.

120. Ding H, Fernandez-de-Manuel L, Schär M, et al. Three-dimensional whole-heart T2 mapping at 3T: 3D Myocardial T2 Mapping. Magn. Reson. Med. 2015;74:803–816.

121. Mussard EPC, Hilbert T, Forman C, Meuli R, Kober T. High-resolution 3D T2 mapping of the Brain Using T2-prepared Cartesian Spiral Phyllotaxis FLASH and Compressed Sensing. In: Proceedings of the 25th Annual Meeting of ISMRM. Honolulu, USA; 2017.

122. Weidlich D, Sarah Schlaeger, Kooijman H, et al. T2 mapping with magnetization-prepared 3D TSE based on a modified BIR-4 T2 preparation. NMR in Biomedicine 2017;30:e3773.

123. Yuan J, Usman A, Reid SA, et al. Three-dimensional black-blood T2 mapping with compressed sensing and data-driven parallel imaging in the carotid artery. Magnetic Resonance Imaging 2017;37:62–69.

124. Peng X, Ying L, Liu Y, Yuan J, Liu X, Liang D. Accelerated exponential parameterization of T2 relaxation with model-driven low rank and sparsity priors (MORASA): Accelerated T2 Mapping with MORASA. Magn. Reson. Med.

2016;76:1865–1878.

125. Peng X, Liu X, Zheng H, Liang D. Exploiting parameter sparsity in model-based reconstruction to accelerate proton density and T2 mapping. Medical Engineering & Physics 2014;36:1428–1435.

126. Moré JJ. The Levenberg-Marquardt algorithm: implementation and theory. Numerical analysis 1978:105–116.

127. Spielman DM, Pauly JM, Meyer CH. Magnetic resonance fluoroscopy using spirals with variable sampling densities. Magn. Reson. Med. 1995;34:388–394.

128. Meyer CH, Hu BS, Nishimura DG, Macovski A. Fast Spiral Coronary Artery Imaging. Magn. Reson. Med. 1992;28:202–213.

129. Qin Q. Point spread functions of the T2 decay in k-space trajectories with long echo train. Magnetic Resonance Imaging 2012;30:1134–1142.

130. Samsonov AA, Kholmovski EG, Parker DL, Johnson CR. POCSENSE: POCS-based reconstruction for sensitivity encoded magnetic resonance imaging. Magn. Reson. Med. 2004;52:1397–1406.

131. Pruessmann KP, Weiger M, Börnert P, Boesiger P. Advances in sensitivity encoding with arbitrary *k* -space trajectories: SENSE With Arbitrary *k* -Space Trajectories. Magn. Reson. Med. 2001;46:638–651.

132. Liang D, Liu B, Wang J, Ying L. Accelerating SENSE using compressed sensing. Magn. Reson. Med. 2009;62:1574–1584.

133. Levitt MH, Freeman R, Frenkiel T. Broadband heteronuclear decoupling. Journal of Magnetic Resonance 1982;47:328–330.

134. Qin Q, Grgac K, van Zijl PCM. Determination of whole-brain oxygen extraction fractions by fast measurement of blood T2 in the jugular vein. Magn. Reson. Med. 2011;65:471–479.

135. Wong EC, Liu TT, Luh W-M, Frank LR, Buxton RB. T1 and T2 selective method for improved SNR in CSF-attenuated imaging: T2-FLAIR. Magnetic Resonance in Medicine 2001;45:529–532.

136. Hwang T-L, van Zijl PCM, Garwood M. Fast Broadband Inversion by Adiabatic Pulses. Journal of Magnetic Resonance 1998;133:200–203.

137. Qin Q. A simple approach for three-dimensional mapping of baseline cerebrospinal fluid volume fraction. Magn. Reson. Med. 2011;65:385–391.

138. Lu H, Nagae-Poetscher LM, Golay X, Lin D, Pomper M, van Zijl PCM. Routine clinical brain MRI sequences for use at 3.0 Tesla. J. Magn. Reson.

Imaging 2005;22:13–22.

139. Wansapura JP, Holland SK, Dunn RS, Ball WS. NMR relaxation times in the human brain at 3.0 tesla. J. Magn. Reson. Imaging 1999;9:531–538.

140. Pipe JG, Zwart NR, Aboussouan EA, Robison RK, Devaraj A, Johnson KO. A new design and rationale for 3D orthogonally oversampled k-space trajectories. Magn. Reson. Med. 2011;66:1303–1311.

141. Gurney PT, Hargreaves BA, Nishimura DG. Design and analysis of a practical 3D cones trajectory. Magn. Reson. Med. 2006;55:575–582.

142. Hu C, Peters DC. SUPER: A blockwise curve-fitting method for accelerating MR parametric mapping with fast reconstruction. Magn Reson Med 2019;81:3515–3529.

143. Winkelmann S, Schaeffter T, Koehler T, Eggers H, Doessel O. An Optimal Radial Profile Order Based on the Golden Ratio for Time-Resolved MRI. IEEE Trans. Med. Imaging 2007;26:68–76.

144. Fessler JA, Sutton BP. Nonuniform fast fourier transforms using min-max interpolation. IEEE Trans. Signal Process. 2003;51:560–574.

145. Ma D, Gulani V, Seiberlich N, et al. Magnetic resonance fingerprinting. Nature 2013;495:187–192.

146. McGivney DF, Boyacıoğlu R, Jiang Y, et al. Magnetic resonance fingerprinting review part 2: Technique and directions. J Magn Reson Imaging 2020;51:993–1007.

147. Assländer J. A Perspective on MR Fingerprinting: A Perspective on MR Fingerprinting. J Magn Reson Imaging 2020.

148. Ben-Eliezer N, Sodickson DK, Block KT. Rapid and accurate T2 mapping from multi-spin-echo data using Bloch-simulation-based reconstruction. Magn. Reson. Med. 2015;73:809–817.

149. Ben-Eliezer N, Sodickson DK, Shepherd T, Wiggins GC, Block KT. Accelerated and motion-robust in vivo T2 mapping from radially undersampled data using bloch-simulation-based iterative reconstruction. Magn. Reson. Med. 2016;75:1346–1354.

150. Visser F, Zwanenburg JJM, Hoogduin JM, Luijten PR. High-resolution magnetization-prepared 3D-FLAIR imaging at 7.0 Tesla. Magn. Reson. Med. 2010;64:194–202.

151. Hennig J. Multiecho imaging sequences with low refocusing flip angles. Journal of Magnetic Resonance (1969) 1988;78:397–407.

152. Jiang Y, Ma D, Keenan KE, Stupic KF, Gulani V, Griswold MA. Repeatability of magnetic resonance fingerprinting T $_1$ and T $_2$ estimates assessed using the ISMRM/NIST MRI system phantom: Repeatability of MR Fingerprinting. Magn. Reson. Med. 2017;78:1452–1457.

153. Keenan KE, Biller JR, Delfino JG, et al. Recommendations towards standards for quantitative MRI (qMRI) and outstanding needs. J. Magn. Reson. Imaging 2019;49:e26–e39.

154. Moran PR, Moran RA, Karstaedt N. Verification and evaluation of internal flow and motion. True magnetic resonance imaging by the phase gradient modulation method. Radiology 1985;154:433–441.

155. Edelman RR, Manning WJ, Gervino E, Li W. Flow velocity quantification in human coronary arteries with fast, breath-hold MR angiography. J. Magn. Reson. Imaging 1993;3:699–703.

156. Keegan J, Firmin D, Gatehouse P, Longmore D. The application of breath hold phase velocity mapping techniques to the measurement of coronary artery blood flow velocity: Phantom data and initialin vivo results. Magn. Reson. Med. 1994;31:526–536.

157. Gould KL, Lipscomb K, Hamilton GW. Physiologic basis for assessing critical coronary stenosis. The American Journal of Cardiology 1974;33:87–94.

158. Clarke GD, Eckels R, Chaney C, et al. Measurement of Absolute Epicardial Coronary Artery Flow and Flow Reserve With Breath-Hold Cine Phase-Contrast Magnetic Resonance Imaging. Circulation 1995;91:2627–2634.

159. Hundley WG, Lange RA, Clarke GD, et al. Assessment of Coronary Arterial Flow and Flow Reserve in Humans With Magnetic Resonance Imaging. Circulation 1996;93:1502–1508.

160. Sakuma H, Blake LM, Amidon TM, et al. Coronary flow reserve: noninvasive measurement in humans with breath-hold velocity-encoded cine MR imaging. Radiology 1996;198:745–750.

161. Hays AG, Hirsch GA, Kelle S, Gerstenblith G, Weiss RG, Stuber M. Noninvasive visualization of coronary artery endothelial function in healthy subjects and in patients with coronary artery disease. J. Am. Coll. Cardiol. 2010;56:1657–1665.

162. Hays AG, Iantorno M, Soleimanifard S, et al. Coronary vasomotor responses to isometric handgrip exercise are primarily mediated by nitric oxide: a noninvasive MRI test of coronary endothelial function. Am. J. Physiol. Heart Circ. Physiol. 2015;308:H1343-1350.

163. Maroules CD, Chang AY, Kotys-Traughber MS, Peshock RM. Coronary

Endothelial Dysfunction in Women With Type 2 Diabetes Measured by Coronary Phase Contrast Flow Velocity Magnetic Resonance Imaging: Journal of Investigative Medicine 2015;63:856–861.

164. Deng Z, Fan Z, Lee S-E, et al. Noninvasive measurement of pressure gradient across a coronary stenosis using phase contrast (PC)-MRI: A feasibility study: Pressure Gradient Measurement Across a Coronary Artery. Magnetic Resonance in Medicine 2017;77:529–537.

165. Hofman MBM, Visser FC, Van Rossum AC, Vink GQM, Sprenger M, Westerhof N. In Vivo Validation of Magnetic Resonance Blood Volume Flow Measurements with Limited Spatial Resolution in Small Vessels. Magn. Reson. Med. 1995;33:778–784.

166. Schär M, Soleimanifard S, Bonanno G, Yerly J, Hays AG, Weiss RG. Precision and accuracy of cross-sectional area measurements used to measure coronary endothelial function with spiral MRI. Magnetic Resonance in Medicine 2019;81:291–302.

167. Hofman MBM, Wickline SA, Lorenz CH. Quantification of in-plane motion of the coronary arteries during the cardiac cycle: Implications for acquisition window duration for MR flow quantification. J. Magn. Reson. Imaging 1998;8:568–576.

168. Marcus JT, Smeenk HG, Kuijer JP, Van der Geest RJ, Heethaar RM, Van Rossum AC. Flow profiles in the left anterior descending and the right coronary artery assessed by MR velocity quantification: effects of through-plane and in-plane motion of the heart. J Comput Assist Tomogr 1999;23:567–576.

169. Keegan J, Gatehouse P, Yang GZ, Firmin D. Interleaved spiral cine coronary artery velocity mapping. Magn Reson Med 2000;43:787–792.

170. Keegan J, Gatehouse PD, Mohiaddin RH, Yang G-Z, Firmin DN. Comparison of spiral and FLASH phase velocity mapping, with and without breath-holding, for the assessment of left and right coronary artery blood flow velocity. J Magn Reson Imaging 2004;19:40–49.

171. Keegan J, Raphael CE, Parker K, et al. Validation of high temporal resolution spiral phase velocity mapping of temporal patterns of left and right coronary artery blood flow against Doppler guidewire. Journal of Cardiovascular Magnetic Resonance 2015;17.

172. Brandts A, Roes SD, Doornbos J, et al. Right coronary artery flow velocity and volume assessment with spiral K-space sampled breathhold velocity-encoded MRI at 3 tesla: Accuracy and reproducibility. Journal of Magnetic Resonance Imaging 2010;31:1215–1223.

173. Bernstein MA, King KF, Zhou ZJ. Handbook of MRI pulse sequences. Amsterdam ; Boston: Academic Press; 2004.

174. Pruessmann KP, Weiger M, Börnert P, Boesiger P. Advances in sensitivity encoding with arbitrary k-space trajectories. Magn Reson Med 2001;46:638–651.

175. Heidemann RM, Griswold MA, Seiberlich N, et al. Direct parallel image reconstructions for spiral trajectories using GRAPPA. Magn. Reson. Med. 2006;56:317–326.

176. Lustig M, Donoho D, Pauly JM. Sparse MRI: The application of compressed sensing for rapid MR imaging. Magn Reson Med 2007;58:1182–1195.

177. Adluru G, Awate SP, Tasdizen T, Whitaker RT, DiBella EVR. Temporally constrained reconstruction of dynamic cardiac perfusion MRI. Magn. Reson. Med. 2007;57:1027–1036.

178. Gamper U, Boesiger P, Kozerke S. Compressed sensing in dynamic MRI. Magn Reson Med 2008;59:365–373.

179. Winkelmann S, Schaeffter T, Koehler T, Eggers H, Doessel O. An optimal radial profile order based on the Golden Ratio for time-resolved MRI. IEEE Trans Med Imaging 2007;26:68–76.

180. Chan RW, Ramsay EA, Cheung EY, Plewes DB. The influence of radial undersampling schemes on compressed sensing reconstruction in breast MRI. Magn. Reson. Med. 2012;67:363–377.

181. Otazo R, Kim D, Axel L, Sodickson DK. Combination of compressed sensing and parallel imaging for highly accelerated first-pass cardiac perfusion MRI. Magn Reson Med 2010;64:767–776.

182. Kim D, Dyvorne HA, Otazo R, Feng L, Sodickson DK, Lee VS. Accelerated phase-contrast cine MRI using k-t SPARSE-SENSE. Magn Reson Med 2012;67:1054–1064.

183. Feng L, Grimm R, Block KT, et al. Golden-angle radial sparse parallel MRI: combination of compressed sensing, parallel imaging, and golden-angle radial sampling for fast and flexible dynamic volumetric MRI. Magn Reson Med 2014;72:707–717.

184. Yerly J, Ginami G, Nordio G, et al. Coronary endothelial function assessment using self-gated cardiac cine MRI and *k* - *t* sparse SENSE: Coronary Endothelial Function Assessment Using Self-Gated Cardiac Cine MRI. Magnetic Resonance in Medicine 2015.

185. Bonanno G, Hays AG, Weiss RG, Schär M. Self-gated golden angle spiral cine MRI for coronary endothelial function assessment: Self-Gated Spiral Cine MRI. Magnetic Resonance in Medicine 2018;80:560–570.

186. Krämer M, Herrmann K-H, Biermann J, Reichenbach JR. Retrospective

reconstruction of cardiac cine images from golden-ratio radial MRI using one-dimensional navigators: 1D Navigator Golden-Ratio Radial Cine Imaging. Journal of Magnetic Resonance Imaging 2014;40:413–422.

187. Edelman RR, Giri S, Murphy IG, Flanagan O, Speier P, Koktzoglou I. Ungated radial quiescent-inflow single-shot (UnQISS) magnetic resonance angiography using optimized azimuthal equidistant projections: Ungated Quiescent-Inflow Single-Shot MRA. Magnetic Resonance in Medicine 2014;72:1522–1529.

188. Kawaji K, Foppa M, Roujol S, Akçakaya M, Nezafat R. Whole Heart Coronary Imaging with Flexible Acquisition Window and Trigger Delay Guo Y, editor. PLOS ONE 2015;10:e0112020.

189. Han F, Zhou Z, Rapacchi S, Nguyen K-L, Finn JP, Hu P. Segmented golden ratio radial reordering with variable temporal resolution for dynamic cardiac MRI: Segmented Golden Ratio Radial Reordering for Cardiac MRI. Magnetic Resonance in Medicine 2016;76:94–103.

190. Schär M, Bonanno G, Hays AG, et al. Golden-Angle Spiral Sparse Parallel-Imaging for Coronary Lumen Area Measurements in Short Breath-Holds. In: Washington, D.C.; 2017. p. P321.

191. Dumoulin CL, Hart HR. Magnetic resonance angiography. Radiology 1986;161:717–720.

192. Zhu D, Bonanno G, Weiss RG, Schär M. Phase contrast coronary blood velocity mapping with both high temporal and spatial resolution using Golden Angle rotated Spiral k-t Sparse Parallel imaging (GASSP). In: Proc of 27th Meeting, ISMRM. Montreal, Canada; 2019. p. 1951.

193. Zhu D, Schär M. Reducing k-space gaps of golden angle rotated spiral MRI binned into cardiac frames applied to flow measurements of the coronary arteries. In: Proceedings of the 28th Annual Meeting of ISMRM. virtual; 2020. p. 2259.

194. Spielman DM, Pauly JM, Meyer CH. Magnetic resonance fluoroscopy using spirals with variable sampling densities. Magn Reson Med 1995;34:388–394.

195. Tsai CM, Nishimura DG. Reduced aliasing artifacts using variable-density k-space sampling trajectories. Magn Reson Med 2000;43:452–458.

196. Pipe JG, Zwart NR. Spiral trajectory design: A flexible numerical algorithm and base analytical equations: Spiral Trajectory Design. Magnetic Resonance in Medicine 2014;71:278–285.

197. Feinstein JA, Epstein FH, Arai AE, et al. Using cardiac phase to order reconstruction (CAPTOR): A method to improve diastolic images. J. Magn.

Reson. Imaging 1997;7:794–798.

198. Nunan D, Sandercock GRH, Brodie DA. A quantitative systematic review of normal values for short-term heart rate variability in healthy adults. Pacing Clin Electrophysiol 2010;33:1407–1417.

199. Schär M, Ding H, Herzka DA. Improvement in B1+ homogeneity and average flip angle using dual-source parallel RF excitation for cardiac MRI in swine hearts. PLoS ONE 2015;10:e0139859.

200. Stuber M, Botnar RM, Danias PG, et al. Double-oblique free-breathing high resolution three-dimensional coronary magnetic resonance angiography. J. Am. Coll. Cardiol. 1999;34:524–531.

201. Börnert P, Koken P, Nehrke K, Eggers H, Ostendorf P. Water/fat-resolved whole-heart Dixon coronary MRA: an initial comparison. Magn Reson Med 2014;71:156–163.

202. Zwart NR, Pipe JG. Graphical programming interface: A development environment for MRI methods. Magnetic Resonance in Medicine 2014.

203. Noll DC, Pauly JM, Meyer CH, Nishimura DG, Macovski A. Deblurring for non-2D Fourier transform magnetic resonance imaging. Magn Reson Med 1992;25:319–333.

204. Laissy JP, Trillaud H, Douek P. MR angiography: noninvasive vascular imaging of the abdomen. Abdom Imaging 2002;27:488–506.

205. Hartung MP, Grist TM, François CJ. Magnetic resonance angiography: current status and future directions. J Cardiovasc Magn Reson 2011;13:19.

206. Prince MR. Gadolinium-enhanced MR aortography. Radiology 1994;191:155–164.

207. Prince MR, Narasimham DL, Stanley JC, et al. Breath-hold gadolinium-enhanced MR angiography of the abdominal aorta and its major branches. Radiology 1995;197:785–792.

208. Hany TF, Debatin JF, Leung DA, Pfammatter T. Evaluation of the aortoiliac and renal arteries: comparison of breath-hold, contrast-enhanced, three-dimensional MR angiography with conventional catheter angiography. Radiology 1997;204:357–362.

209. Kuo PH, Kanal E, Abu-Alfa AK, Cowper SE. Gadolinium-based MR Contrast Agents and Nephrogenic Systemic Fibrosis. Radiology 2007;242:647–649.

210. Sadowski EA, Bennett LK, Chan MR, et al. Nephrogenic Systemic Fibrosis: Risk Factors and Incidence Estimation. Radiology 2007;243:148–157.

211. McDonald RJ, McDonald JS, Kallmes DF, et al. Intracranial Gadolinium Deposition after Contrast-enhanced MR Imaging. Radiology 2015;275:772–782.

212. Gulani V, Calamante F, Shellock FG, Kanal E, Reeder SB. Gadolinium deposition in the brain: summary of evidence and recommendations. The Lancet Neurology 2017;16:564–570.

213. FDA Drug Safety Communication: FDA warns that gadolinium-based contrast agents (GBCAs) are retained in the body; requires new class warnings. https://www.fda.gov/drugs/drug-safety-and-availability/fda-drug-safety-communication-fda-warns-gadolinium-based-contrast-agents-gbcas-are-retained-body. Accessed May 16, 2018.

214. Hope MD, Hope TA, Zhu C, et al. Vascular Imaging With Ferumoxytol as a Contrast Agent. American Journal of Roentgenology 2015;205:W366–W373.

215. Finn JP, Nguyen K-L, Han F, et al. Cardiovascular MRI with ferumoxytol. Clinical Radiology 2016;71:796–806.

216. Granata V, Cascella M, Fusco R, et al. Immediate Adverse Reactions to Gadolinium-Based MR Contrast Media: A Retrospective Analysis on 10,608 Examinations. BioMed Research International 2016;2016:1–6.

217. Miyazaki M, Lee VS. Nonenhanced MR Angiography. Radiology 2008;248:20–43.

218. Miyazaki M, Isoda H. Non-contrast-enhanced MR angiography of the abdomen. European Journal of Radiology 2011;80:9–23.

219. Miyazaki M, Sugiura S, Tateishi F, Wada H, Kassai Y, Abe H. Non-contrast-enhanced MR angiography using 3D ECG-synchronized half-Fourier fast spin echo. Journal of Magnetic Resonance Imaging 2000;12:776–783.

220. Miyazaki M, Takai H, Sugiura S, Wada H, Kuwahara R, Urata J. Peripheral MR Angiography: Separation of Arteries from Veins with Flow-spoiled Gradient Pulses in Electrocardiography-triggered Three-dimensional Half-Fourier Fast Spin-Echo Imaging. Radiology 2003;227:890–896.

221. Spuentrup E, Manning WJ, Börnert P, Kissinger KV, Botnar RM, Stuber M. Renal Arteries: Navigator-gated Balanced Fast Field-Echo Projection MR Angiography with Aortic Spin Labeling: Initial Experience. Radiology 2002;225:589–596.

222. Scheffler K, Lehnhardt S. Principles and applications of balanced SSFP techniques. Eur Radiol 2003;13:2409–2418.

223. Miyazaki M, Akahane M. Non-contrast enhanced MR angiography: Established techniques. J. Magn. Reson. Imaging 2012;35:1–19.

224. Coenegrachts KL, Hoogeveen RM, Vaninbroukx JA, et al. High-Spatial-Resolution 3D Balanced Turbo Field-Echo Technique for MR Angiography of the Renal Arteries: Initial Experience. Radiology 2004;231:237–242.

225. Herborn CU, Watkins DM, Runge VM, Gendron JM, Montgomery ML, Naul LG. Renal Arteries: Comparison of Steady-State Free Precession MR Angiography and Contrast-enhanced MR Angiography. Radiology 2006;239:263–268.

226. Maki JH, Wilson GJ, Eubank WB, Glickerman DJ, Millan JA, Hoogeveen RM. Navigator-Gated MR Angiography of the Renal Arteries: A Potential Screening Tool for Renal Artery Stenosis. American Journal of Roentgenology 2007;188:W540–W546.

227. Maki JH, Wilson GJ, Eubank WB, Glickerman DJ, Pipavath S, Hoogeveen RM. Steady-state free precession MRA of the renal arteries: Breath-hold and navigator-gated techniques vs. CE-MRA. J. Magn. Reson. Imaging 2007;26:966–973.

228. Shonai T, Takahashi T, Ikeguchi H, Miyazaki M, Amano K, Yui M. Improved arterial visibility using short-tau inversion-recovery (STIR) fat suppression in non-contrast-enhanced time-spatial labeling inversion pulse (Time-SLIP) renal MR angiography (MRA). J. Magn. Reson. Imaging 2009;29:1471–1477.

229. Pei Y, Shen H, Li J, et al. Evaluation of Renal Artery in Hypertensive Patients by Unenhanced MR Angiography Using Spatial Labeling With Multiple Inversion Pulses Sequence and by CT Angiography. American Journal of Roentgenology 2012;199:1142–1148.

230. Pei Y, Li F, Shen H, et al. Optimal Blood Suppression Inversion Time Based on Breathing Rates and Heart Rates to Improve Renal Artery Visibility in Spatial Labeling with Multiple Inversion Pulses: A Preliminary Study. Korean J Radiol 2016;17:69.

231. Shimada K, Isoda H, Okada T, et al. Non-contrast-enhanced hepatic MR angiography with true steady-state free-precession and time spatial labeling inversion pulse: Optimization of the technique and preliminary results. European Journal of Radiology 2009;70:111–117.

232. Shimada K, Isoda H, Okada T, et al. Non-contrast-enhanced MR angiography for selective visualization of the hepatic vein and inferior vena cava with true steady-state free-precession sequence and time-spatial labeling inversion pulses: Preliminary results. J. Magn. Reson. Imaging 2009;29:474–479.

233. Shimada K, Isoda H, Okada T, et al. Non-contrast-enhanced MR portography with time-spatial labeling inversion pulses: Comparison of imaging with three-dimensional half-fourier fast spin-echo and true steady-state free-precession sequences. J. Magn. Reson. Imaging 2009;29:1140–1146.

234. Atanasova IP, Kim D, Lim RP, et al. Noncontrast MR angiography for comprehensive assessment of abdominopelvic arteries using quadruple inversion-recovery preconditioning and 3D balanced steady-state free precession imaging. J. Magn. Reson. Imaging 2011;33:1430–1439.

235. Shin T, Worters PW, Hu BS, Nishimura DG. Non-contrast-enhanced renal and abdominal MR angiography using velocity-selective inversion preparation: Velocity-Selective Noncontrast Abdominal MRA. Magn Reson Med 2013;69:1268–1275.

236. de Rochefort L, Maître X, Bittoun J, Durand E. Velocity-selective RF pulses in MRI. Magn. Reson. Med. 2006;55:171–176.

237. Shin T, Hu BS, Nishimura DG. Off-resonance-robust velocity-selective magnetization preparation for non-contrast-enhanced peripheral MR angiography: Off-Resonance-Robust VS Preparation for NCE MRA. Magn. Reson. Med. 2013;70:1229–1240.

238. Qin Q, Shin T, Schär M, Guo H, Chen H, Qiao Y. Velocity-selective magnetization-prepared non-contrast-enhanced cerebral MR angiography at 3 Tesla: Improved immunity to B0/B1 inhomogeneity. Magn. Reson. Med. 2016;75:1232–1241.

239. Shin T, Qin Q, Park J-Y, Crawford RS, Rajagopalan S. Identification and reduction of image artifacts in non-contrast-enhanced velocity-selective peripheral angiography at 3T: Artifact Reduction in Velocity-Selective Peripheral MRA at 3T. Magn. Reson. Med. 2016;76:466–477.

240. Li W, Xu F, Schär M, et al. Whole-brain arteriography and venography: Using improved velocity-selective saturation pulse trains. Magn. Reson. Med 2018;79:2014–2023.

241. Zhu D, Li W, Liu D, et al. Non-contrast-enhanced abdominal MRA at 3 T using velocity-selective pulse trains. Magn Reson Med 2020;84:1173–1183.

242. Levitt MH, Freeman R, Frenkiel T. Broadband heteronuclear decoupling. Journal of Magnetic Resonance (1969) 1982;47:328–330.

243. Tannús A, Garwood M. Improved Performance of Frequency-Swept Pulses Using Offset-Independent Adiabaticity. Journal of Magnetic Resonance, Series A 1996;120:133–137.

244. Holsinger AE, Riederer SJ. The importance of phase-encoding order in ultra-short TR snapshot MR imaging. Magn. Reson. Med. 1990;16:481–488.

245. Scheffler K. On the transient phase of balanced SSFP sequences. Magn. Reson. Med. 2003;49:781–783.

246. Lustig M, Donoho DL, Santos JM, Pauly JM. Compressed Sensing MRI. IEEE Signal Process. Mag. 2008;25:72–82.

247. Liang D, Liu B, Wang J, Ying L. Accelerating SENSE using compressed sensing: Compressed Sensing SENSE. Magn. Reson. Med. 2009;62:1574–1584.

248. Qin Q, Strouse JJ, van Zijl PCM. Fast measurement of blood T_1 in the human jugular vein at 3 Tesla: Blood T_1 in the Jugular Vein. Magn. Reson. Med. 2011;65:1297–1304.

249. Li W, Liu P, Lu H, Strouse JJ, van Zijl PCM, Qin Q. Fast measurement of blood T_1 in the human carotid artery at 3T: Accuracy, precision, and reproducibility: Fast Measurement of Arterial Blood T1 at 3T. Magn. Reson. Med. 2017;77:2296–2302.

250. Qin Q, van Zijl PCM. Velocity-selective-inversion prepared arterial spin labeling: Velocity-Selective-Inversion Prepared ASL. Magn. Reson. Med. 2016;76:1136–1148.

251. Garcia J, van der Palen RLF, Bollache E, et al. Distribution of blood flow velocity in the normal aorta: Effect of age and gender: Distribution of Blood Flow Velocity in Aorta. J. Magn. Reson. Imaging 2018;47:487–498.

252. Bernstein MA, Huston J, Ward HA. Imaging artifacts at 3.0T. J. Magn. Reson. Imaging 2006;24:735–746.

253. Merkle EM, Dale BM. Abdominal MRI at 3.0 T: The Basics Revisited. American Journal of Roentgenology 2006;186:1524–1532.

254. Shin T, Qin Q. Characterization and suppression of stripe artifact in velocity-selective magnetization-prepared unenhanced MR angiography. Magn Reson Med 2018;80:1997–2005.

255. Uecker M, Zhang S, Voit D, Karaus A, Merboldt K-D, Frahm J. Real-time MRI at a resolution of 20 ms. NMR Biomed. 2010;23:986–994.

256. Block KT, Uecker M, Frahm J. Undersampled radial MRI with multiple coils. Iterative image reconstruction using a total variation constraint. Magn. Reson. Med. 2007;57:1086–1098.

257. Niebergall A, Zhang S, Kunay E, et al. Real-time MRI of speaking at a resolution of 33 ms: Undersampled radial FLASH with nonlinear inverse reconstruction. Magn Reson Med 2013;69:477–485.

258. Zhang S, Joseph AA, Voit D, et al. Real-time magnetic resonance imaging of cardiac function and flow—Recent progress. 2014 2014;4:313–329.

259. Frahm J, Voit D, Uecker M. Real-Time Magnetic Resonance Imaging:

Radial Gradient-Echo Sequences With Nonlinear Inverse Reconstruction. Investigative Radiology 2019;54:757–766.

260. Iltis PW, Frahm J, Voit D, Joseph AA, Schoonderwaldt E, Altenmüller E. High-speed real-time magnetic resonance imaging of fast tongue movements in elite horn players. 2015 2015;5:374–381.

261. Bauman G, Puderbach M, Deimling M, et al. Non-contrast-enhanced perfusion and ventilation assessment of the human lung by means of fourier decomposition in proton MRI: Non-CE Functional Lung Imaging in ^{1} H MRI. Magn. Reson. Med. 2009;62:656–664.

262. Cox RW, Jesmanowicz A, Hyde JS. Real-Time Functional Magnetic Resonance Imaging. Magn. Reson. Med. 1995;33:230–236.

263. Zerhouni EA, Parish DM, Rogers WJ, Yang A, Shapiro EP. Human heart: tagging with MR imaging--a method for noninvasive assessment of myocardial motion. Radiology 1988;169:59–63.

264. Edelstein WA, Bottomley PA, Hart HR, Smith LS. Signal, noise, and contrast in nuclear magnetic resonance (NMR) imaging. J Comput Assist Tomogr 1983;7:391–401.

265. Nickander J, Themudo R, Thalén S, et al. The relative contributions of myocardial perfusion, blood volume and extracellular volume to native T1 and native T2 at rest and during adenosine stress in normal physiology. J Cardiovasc Magn Reson 2019;21:73.

266. Packard RRS, Huang S-C, Dahlbom M, Czernin J, Maddahi J. Absolute Quantitation of Myocardial Blood Flow in Human Subjects With or Without Myocardial Ischemia Using Dynamic Flurpiridaz F 18 PET. Journal of Nuclear Medicine 2014;55:1438–1444.

267. Koskenvuo JW, Sakuma H, Niemi P, et al. Global myocardial blood flow and global flow reserve measurements by MRI and PET are comparable. J. Magn. Reson. Imaging 2001;13:361–366.

268. Chan SY, Brunken RC, Czernin J, et al. Comparison of maximal myocardial blood flow during adenosine infusion with that of intravenous dipyridamole in normal men. Journal of the American College of Cardiology 1992;20:979–985.

269. Fritz-Hansen T, Hove JD, Kofoed KF, Kelbaek H, Larsson HBW. Quantification of MRI measured myocardial perfusion reserve in healthy humans: A comparison with positron emission tomography. J. Magn. Reson. Imaging 2008;27:818–824.

270. Zun Z, Varadarajan P, Pai RG, Wong EC, Nayak KS. Arterial Spin Labeled CMR Detects Clinically Relevant Increase in Myocardial Blood Flow With

Vasodilation. JACC: Cardiovascular Imaging 2011;4:1253–1261.

271. Duncker DJ, Merkus D. Regulation of coronary blood flow. Effect of coronary artery stenosis. Archives des maladies du coeur et des vaisseaux 2004;97:1244.

272. Zi R, Zhu D, Qin Q. Quantitative T2 mapping using accelerated 3D stack-of-spiral gradient echo readout. Magnetic Resonance Imaging 2020;73:138–147.

273. Kim S-J, Peppas A, Hong S-K, et al. Persistent Stunning Induces Myocardial Hibernation and Protection: Flow/Function and Metabolic Mechanisms. Circulation Research 2003;92:1233–1239.

274. Friedman SD, Shaw DW, Artru AA, et al. Regional brain chemical alterations in young children with autism spectrum disorder. Neurology 2003;60:100–107.

275. Frontal, temporal, and striatal proton relaxation times in schizophrenic patients and normal comparison subjects. AJP 1992;149:549–551.

276. Pitkanen A, Laakso M, Kalviainen R, et al. Severity of hippocampal atrophy correlates with the prolongation of MRI T sub 2 relaxation time in temporal lobe epilepsy but not in Alzheimer’s disease. Neurology 1996;46:1724–1730.

277. Bartzokis G, Sultzer D, Cummings J, et al. In Vivo Evaluation of Brain Iron in Alzheimer Disease Using Magnetic Resonance Imaging. Arch Gen Psychiatry 2000;57:47.

278. Larsson HBW, Frederiksen J, Petersen J, et al. Assessment of demyelination, edema, and gliosis byin vivo determination of T1 and T2 in the brain of patients with acute attack of multiple sclerosis. Magn. Reson. Med. 1989;11:337–348.

Curriculum Vitae

Contact Information:

Phone: (443)-813-6742 (Cell)
Email: dzhu12@jhmi.edu, dan.zhu.thu@hotmail.com
Address: 600 N Wolfe Street, Park Building, Room 315, Baltimore, Maryland, 21287 USA

Education:

B.S. 2010-2014	Department of Biomedical Engineering Tsinghua University
Ph.D. 2014-2020(expected) (mentor: Paul A. Bottomley)	Department of Biomedical Engineering Johns Hopkins University

Awards:

1. Second prize on National (Chinese) Olympiad Informatics in Provinces (NOIP), 2008
2. First prize on National (Chinese) High School Mathematical League, 2009
3. Second prize on China High School Biology Olympiad (CHSBO), 2009
4. Huang Songyi - He Shansheng Scholarship (award for outstanding academic performance at Tsinghua University), 2011
5. Huang Qianheng Scholarship (award for outstanding academic performance at Tsinghua University), 2012

Journal Paper Publications:

† indicates equal-contribution first authors

1. **Zhu D**, Li W, Liu D, Liu G, Pei Y, Shin T, Sedaghat F, Qin, Q. Non□contrast□enhanced Abdominal MRA at 3 T Using Velocity□selective Pulse Trains. *Magn Reson Med*, 2020, 84, 1173–1183.
2. Zi R†, **Zhu D**†, Qin Q. Quantitative T2 Mapping Using Accelerated 3D Stack-of-Spiral Gradient Echo Readout. *Magnetic Resonance Imaging*, 2020, 73, 138–147.
3. Kumar D, Nanga RPR, Thakuri D, Wilson N, Cember A, Martin ML, **Zhu D**, Shinohara RT, Qin Q, Hariharan, H, Reddy, R. Recovery Kinetics of Creatine in Mild Plantar Flexion Exercise Using 3D Creatine CEST Imaging at 7 Tesla. *Magn Reson Med*, 2021, 85, 802–817.

4. Xu F, Li W, Liu D, **Zhu D**, Schär M, Myers M, Qin Q, A Novel Spectrally Selective Fat Saturation Pulse Design with Robustness to B0 and B1 Inhomogeneities: A Demonstration on 3D T1-weighted Breast MRI 3T, *Magn Reson Imaging*, 2021, 75, 156–161.
5. Liu D, Li W, Xu F, **Zhu D**, Shin T, Qin Q, Ensuring Both Velocity and Spatial Responses Robust to B0/B1+ Field Inhomogeneities for Velocity-Selective Arterial Spin Labeling through Dynamic Phase-Cycling. *Magn Reson Med*, 2020; [Accepted].
6. **Zhu D**, Bonanno G, Hays AG, Weiss RG, Schär M, Phase contrast coronary blood velocity mapping with both high temporal and spatial resolution using triggered Golden Angle rotated Spiral k-t Sparse Parallel imaging (GASSP) with optimized binning. *Magn Reson Med*, 2020; [Revision].
7. **Zhu D**, Ding H, Zviman MM, Halperin H, Schär M, Herzka DA. Accelerating Whole-Heart 3D T2 Mapping: Impact of Undersampling Strategies and Reconstruction Techniques. *Plos One*, 2020; [Under Review].
8. Cao D, Paez AG, Miao X, Liu D, **Zhu D**, Gu C, Li Y, Mao D, Qin Q, Hua J, Evaluation of point-spread-function and signal-to-noise ratio in highly-accelerated Compressed Sensing-SENSE (CS-SENSE) and SENSE MRI. *Magn Reson Med*, 2020; [Under Review].

Invited Talks:

1. The Human Heart at 30 to 100 Hertz, the 20th retreat of the Division of MRI Research, Department of Radiology, Johns Hopkins University, 2017.
2. The Human Heart at 30 to 100 Hertz, Siemens seminar, Department of Radiology, Johns Hopkins University, 2018.
3. Non-Contrast-Enhanced Abdominal MRA at 3T using Velocity-Selective Pulse Trains, the 22nd retreat of the Division of MRI Research, Department of Radiology, Johns Hopkins University, 2019.
4. Phase contrast coronary blood velocity mapping with both high temporal and spatial resolution using Golden Angle rotated Spiral k-t Sparse Parallel imaging (GASSP), ISMRM Study Group on MR Flow and Motion Quantitation, 2019.

Conference Oral Presentations:

1. **Zhu D**, Uecker M, Cheng JY, Bi Z, Ying4, Lustig M, Calibration for Parallel MRI Using Robust Low-Rank Matrix Completion, *Proc ISMRM*, 2014, p741.
2. **Zhu D**, Huang F, Ning J, Chen F, Chen H, Sparse Radial k-T SPIRiT for Dynamic Liver Imaging, *Proc ISMRM*, 2015, p387.
3. **Zhu D**, Li W, Liu D, Liu G, Sedaghat F, Pei Y, Shin T, Qin Q, Non-Contrast-Enhanced Abdominal MRA at 3T using Velocity-Selective Pulse Trains,

SMRA, Nantes, France, 2019, p59

Conference Abstracts:

1. **Zhu D**, Zhou Z, Huang F, Ying K, Preliminary Study of Reusability of Optimized Trajectory for SENSE, *Proc ISMRM*, 2013, p2685.
2. Chen F, Huang F, **Zhu D**, Qi H, Ying K, Chen H, Highly Accelerated Cardiac Cine Imaging Using a Combination of K-T Group Sparse and SPIRiT, *Proc ISMRM*, 2014, p1566.
3. Peng C, **Zhu D**, Chen F, Ying K, k-T ESPIRiT for Accelerating Proton Resonance Frequency Shift MR Temperature Mapping, *Proc ISMRM*, 2014, p1567.
4. Qi H, Huang F, Cai X, **Zhu D**, Chen F, Yuan C, Chen H, K-T PCA GROWL: Sequential Combination of Partially Parallel Imaging and K-T PCA, *Proc ISMRM*, 2014, p1571.
5. Hu Y, Chen F, **Zhu D**, Peng C, Wang S, Ying K, Comparison of GRAPPA, SPIRiT and ESPIRiT for the Acceleration of Model-Based PRF Temperature Mapping, *Proc ISMRM*, 2014, p2355.
6. Jiang D, **Zhu D**, Chen S, Chen S, Ying K, Preliminary Study on Motion Correction in Model-Based MR Thermometry, *Proc ISMRM*, 2014, p2357.
7. **Zhu D**, Huang F, Chen F, Qi H, Ying K, Yuan C, Chen H, Comparison of K-T SPIRiT and K-T GRAPPA for Accelerating Cardiac DCE and CINE MRI Proc ISMRM, 2014, p2400.
8. Ning J, Zhang B, Li H, **Zhu D**, Huang F, Chen S. Koken P, Smink J, Chen H, Simultaneous Acquisition Sequence for High Accuracy Whole Liver Perfusion Quantification(SAHA), *Proc ISMRM*, 2015, p1526.
9. Chen F, Huang F, **Zhu D**, Ning J, Chen H, Accelerated Breath-Hold Liver Imaging Using Additional Information from Free-Breathing Acquisitions, *Proc ISMRM*, 2015, p3805.
10. NessAiver E, **Zhu D**, Blitz A, Herzka D, Improved Banding Removal for High Resolution BSSFP Imaging of the Inner Ear Using SENSE, *Proc ISMRM*, 2016, p1336.
11. **Zhu D**, Ding H, Halperin H, Herzka D, Accelerating High-Resolution Whole-Heart 3D T2 Mapping, *Proc ISMRM*, 2017, p3108.
12. **Zhu D**, Ding H, Halperin H, Herzka DA, Accelerated Whole-heart 3D T2 Mapping: Comparison of Reconstruction Strategies, *Proc SCMR*, 2017, p320.
13. **Zhu D**, Bonanno G, Weiss RG, and Schär M, Phase contrast coronary blood velocity mapping with both high temporal and spatial resolution using Golden Angle rotated Spiral k-t Sparse Parallel imaging (GASSP), *Proc ISMRM*, 2019, p1951

14. **Zhu D**, Li W, Liu G, Pei Y, Shin T, Qin Q, Non-Contrast-Enhanced Abdominal MRA at 3T using Velocity-Selective Pulse Trains, *Proc ISMRM*, 2019, p2062
15. **Zhu D**, and Schär M, Reducing k-space gaps of golden angle rotated spiral MRI binned into cardiac frames applied to flow measurements of the coronary arteries, *ISMRM Workshop on Data Sampling and Image Reconstruction*, Sedona, Arizona, 2020.
16. Zi R, **Zhu D**, Li W, and Qin Q, Quantitative T2 Mapping using Accelerated 3D Stack-of-Spiral GRE Acquisition, *ISMRM Workshop on Data Sampling and Image Reconstruction*, Sedona, Arizona, 2020.
17. **Zhu D**, and Schär M, Reducing k-space gaps of golden angle rotated spiral MRI binned into cardiac frames applied to flow measurements of the coronary arteries, *Proc ISMRM,* 2020, p2259.
18. Xu F, Li W, Liu D, **Zhu D**, Myers K, Shär M, Qin Q, A Novel Chemical Shift-Selective Fat Saturation RF Pulse Design with Robustness to B0/B1 Inhomogeneity: A Demonstration on Breast MRI at 3T, *Proc ISMRM,* 2020, p3227.
19. **Zhu D**, Liu D, Li W, Schär M, Qin Q, Free Breathing Renal Perfusion Imaging at 3T Using Velocity-Selective Inversion prepared Arterial Spin Labeling, *Proc ISMRM,* 2020, p3300.
20. Liu D, Li W, Xu F, **Zhu D**, Shin T, Qin Q, Improving Robustness to Field Imperfections for Velocity-Selective Inversion prepared Arterial Spin Labeling through Dynamic Phase-Cycling, *Proc ISMRM,* 2020, p3301.
21. Zi R, **Zhu D**, Li W, and Qin Q, Quantitative T2 Mapping using Accelerated 3D Stack-of-Spiral GRE Acquisition, *Proc ISMRM*, 2020, p3794
22. **Zhu D**, Steinberg T, Weiss RG, Voit D, Frahm J, Bottomley PA, Rapid physiological dynamics measured by real-time MRI at up to 100Hz: MR kinematography, *Proc ISMRM*, 2021 (Under Review)
23. **Zhu D**, Qin Q, Analytical Characterization and Comparison of Magnetization-Relaxation-Induced Point Spread Functions of TFE, bSSFP and TSE Acquisitions, *Proc ISMRM*, 2021 (Under Review)
24. Liu D, **Zhu D**, Li W, Qin Q, Prostate Perfusion Mapping using Fourier-Transform based Velocity-Selective Pulse Trains: Choice of Cutoff Velocity and Comparison with Brain, *Proc ISMRM*, 2021 (Under Review)
25. Xu F, **Zhu D**, Fan H, Lu H, Liu D, Li W, Qin Q,Velocity-Selective Inversion prepared Arterial Spin Labeling: Examination in a Commercial Perfusion Phantom, *Proc ISMRM*, 2021 (Under Review)

Teaching Experience:

Teaching Assistant	Mathematics of Deep Learning Biomedical Engineering, Johns Hopkins University	Fall 2018

Teaching Assistant	Systems Biology of the Cell Biomedical Engineering, Johns Hopkins University	Spring 2019

Professional Memberships:

2013: International Society for Magnetic Resonance in Medicine (ISMRM).

Skills:

1. 8-year pulse sequence programming experience on Philips MRI scanner.
2. 5-year pulse sequence programming experience on Siemens MRI scanner
3. Human scan experience on Philips (9 years) and Siemens (4 years) 3T system.
4. Experience in MRI raw data processing on Philips and Siemens scanners.
5. Substantial experience in MRI image reconstruction.
6. Experience in Graphical Programming Interface (GPI) for MRI data processing.
7. Substantial coding experience with Matlab, C++, and Python. Other coding languages: Java, C, and visual basic.